The University of Sheffield

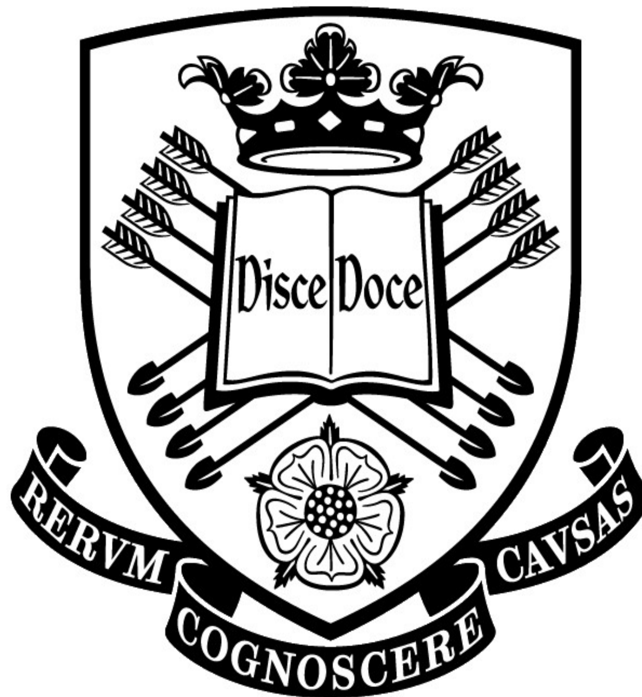

New Methods for Quantifying X-ray Spectra in
a Transmission Electron Microscope

by
M. C. Parri

A thesis submitted for the degree of Doctor of Philosophy
Department of Electrical and Electronic Engineering
January 2014

Abstract

In an effort to develop new methods of analysis and improving quantification accuracy in the transmission electron microscope (TEM) while using energy-dispersive X-ray spectroscopy (EDXS), several methods have been explored. Some of these methods have been applied to a sample that has a thin layer of some material embedded within a matrix of another material, while others can be applied to any sample that is homogeneous in chemical composition or nearly so.

For those methods that are applied to a thin layer embedded within a matrix, several conclusion can be drawn. While each of these methods works in simulations, only two ('absorption matching') provide reasonable results for experimental data. Unfortunately, these results differ considerably for the same sample. The other methods either prove to be so sensitive that the data scatter is too large to draw meaningful conclusions from, or so insensitive that any change of a useful magnitude would not be detected.

The remaining methods were found to give good results, particularly when used together. The X-ray intensity ratio from a pair of X-rays from a single spectrum (generally from the same element) can be used to calculate the sample thickness for that spectrum. The second method was a means of plotting a function of the Cliff-Lorimer *k*-factor as a function of thickness in order to better calculate the effect of absorption. Combined, these two methods can give considerably superior quantification of the chemical composition than when used alone.

Parts of this study have already been published in the conference proceedings listed on the following page.

Acknowledgement

There were many people who contributed to my work and deserve my thanks. First and foremost, my supervisor Dr. Thomas Walther, for the consistent assistance, keen insight and always having another suggestion on how to proceed. Dr. Ian Ross, for almost always being available to help and going out of his way to do so. Professor A. Cullis, for setting me on this path.

I would also like to thank my colleagues for miscellaneous assistance and advice over the years. In no particular order: Dr. D. Norris, Dr. H. Amari, Dr. L. Leonardo, Dr. Y. Qiu (who repeatedly helped with sample preparation), Mr. H. Y. Zhang (who three times helped with his FIB), Ms. A. Khani, Mr. S. Hussein.

Published work

Parri, M. C., & Walther, T. (2011). Quantification of series of X-ray spectra taken at different tilts in analytical transmission electron microscopy. *Journal of Physics: Conference Series*, *326*(1). doi:10.1088/1742-6596/326/1/012037

Parri, M. C., & Walther, T. (2012). Determining sample thickness in transmission electron microscopy using X-ray line intensity ratios. In D. J. Stokes, & J. L. Hutchison (Eds.), *15th European Microscopy Congress* Vol. 2 (pp. 645-646). Oxford: Royal Microscopical Society.

Parri, M. C., Qiu, Y., & Walther, T. (2012). Comparing experiment with theory of X-ray absorption in thin SiGe films. In D. J. Stokes, & J. L. Hutchison (Eds.), *15th European Microscopy Congress* Vol. 2 (pp. 693-694). Oxford: Royal Microscopical Society.

Parri, M. C., & Walther, T. (2012). Self-consistent absorption corrections for low-energy X-ray lines in energy-dispersive X-ray spectroscopy. In P. D. Nellist (Ed.), *Journal of Physics: Conference Series* Vol. 371 (pp. 012063-1-012063-4). Birmingham, UK: IoP Publishing. doi:10.1088/1742-6596/371/1/012063

Table of Contents

1 Introduction....4
2 Theory of X-ray production and detection in EDXS in an electron microscope....4
2.1 Introduction to EDXS in a TEM....4
2.1.1 Physical interactions of electrons with samples....5
2.1.2 Geometry of X-ray detector....7
2.1.3 Physics of X-ray detector....9
2.1.4 Detector window....11
2.1.5 Quantification of X-ray spectra in EDXS: principles....11
2.1.6 Other methods for quantification and thickness determination....14
2.1.6.1 Multigeometry and/or EELS determination of thickness....14
2.1.6.2 Absorption correction in ionic compounds....15
2.1.6.3 Discovering the depth of thin layers in an SEM by varying the beam voltage....15
2.1.6.4 φ(ρz) method....16
2.1.6.5 Thickness determination via increasing X-ray counts....16
2.1.6.6 Improvement to contamination spot size separation method....17
2.1.6.7 K/L ratio....17
2.1.6.8 Extrapolation method of absorption correction....18
2.1.6.9 Examples of situations where more accurate absorption correction is useful....18
2.1.7 Microcalorimeter....19
2.1.8 WDXS....19
3 Monte Carlo....20
3.1 Hurricane....20
3.2 Casino....20
3.3 EDAX Electron Flight Simulator (EEFS)....21
3.4 NISTMonte....21
3.5 PENELOPE....22
3.6 Comparison of absorption values of X-rays from Monte Carlo simulation programs....22
4 Equation for determination of the depth of thin layer within a matrix material....25
4.1 Description of method....25
4.1.1 Assumptions....26
4.1.2 Corrections....27
4.1.2.1 Livetime correction....27
4.1.2.2 Specimen Tilt correction....27
4.1.2.3 Beam Straggling....28
4.1.2.4 Shielding....29
4.1.3 Error determination....30
4.2 Detector Tilt Approach....30
4.3 Specimen Tilt Approach....34
4.3.1 Indium Simulations....34
4.3.2 Aluminium Simulations....42
4.4 Multiple thin layers within one matrix....45
4.5 λ calculation....50
4.5.1 Comparison of different methods for calculating λ....50
4.5.2 λ for normalised intensity....56
4.6 Total Sample Thickness by the Inversion Method....70
4.7 Quantification....75
4.8 Experimental Data....75
4.8.1 Conclusion....86
5 Other methods for determination of the depth of a thin layer in a matrix material....86

5.1 Chart comparison....86
5.2 Determination of the depth of a thin layer by matching absorption curves....91
5.2.1 Modelled absorption matching....91
5.2.2 Simulated absorption matching....96
5.3 Curve Fit....100
5.4 Piecewise curve fit....102
5.5 Conclusion....106
6 The use of X-ray intensity ratios to determine sample thickness....106
6.1 Experimental Analysis....117
6.2 Method for Determination of Thickness by Varying Take-off Angle....122
7 An improvement to the Cliff-Lorimer k-factors....127
7.1 Experimental analysis....135
7.1.1 Conclusion....145
8 Conclusion....145
9 References....145

1 Introduction

The purpose of this study is to develop new methods of quantifying energy-dispersive X-ray spectra in a transmission electron microscope with the intent of aiding both quantification of chemical composition and understanding of sample geometry. This is done in five parts:

Initially, several Monte Carlo programs were compared to discover which would be the most valid for the circumstances of this study, primarily in their modelling of X-ray absorption. While a direct comparison between experimental and simulation results is not valid, due to uncertainties in parameters such as fluorescence probabilities and absorption cross-sections, the general trends can be meaningfully compared.

The first new part would be to explore the use of an equation that permits the calculation of the depth of a thin layer within a matrix using characteristic X-ray intensity at different take-off angles. Knowledge of the depth of a thin layer would permit more accurate quantification, as the absorption correction of any method could be improved by knowing that all X-rays of a certain line originate from a particular depth and as such experience a specific amount of absorption. This amount of absorption could be quantified using well-known equations, with a resulting increase in the accuracy of quantifying chemical composition. There is an abundance of structures, such as thin semiconductor lasers for optoelectronics, that require a layer of material be present at a specific location: this method would assist in verifying this. Further, this method could in principle be extended into a more general metrological analysis tool.

Predominantly extended from the equation mentioned above, further work has been done on a number of miscellaneous methods that would permit not only calculation of the depth but also more direct quantification of the sample composition. Two of the methods are graphical, for a general estimate of the sample geometry, while the remaining three are intended for providing a numerical result of the depth of a thin layer within a matrix.

Many samples either do not possess such a thin layer or accurate knowledge of its particulars is not a vital part of any analysis. In such cases, improved quantification can be carried out by accurately determining the thickness of the sample, as it is the thickness, density and chemical composition which influences the degree of absorption. This can be done by calculating the intensity ratio of X-rays of different energies, matching this to what would be expected from prior experiments or simulations and thereby deriving the sample thickness. Some ratios allow more direct calculation of the chemical composition, as they do see little change with thickness.

The Cliff-Lorimer ratio method is heavily reliant on the *k*-factor for its accuracy. As such, any means of improving the accuracy of the *k*-factor is desirable. By considering the *k*-factor not as a constant for a specific microscope but as a variable which effectively changes with thickness, it is possible to calculate a self-consistent chemical composition. It is also possible to calculate a more accurate *k*-factor that can be applied to any sample within the same microscope and detector system. Of particular interest is how this method can be applied with any measure of thickness, such as detector deadtime or the method described in the above paragraph.

Three samples were examined for calculation of the depth of a thin layer in a matrix, while a further five chemically homogeneous samples were examined using the latter two methods.

2 Theory of X-ray production and detection in EDXS in an electron microscope

The original intent of electron microscopy was to surpass the resolution limit of optical light. It was found, however, that beyond simply allowing the user to image very small objects, electron microscopy also made it possible to gather, with appropriate detectors, various other kinds of information from the material being examined. This information can be analysed in order to achieve a quantitative understanding of the sample, thereby changing the microscope from a device which permits the viewing of the structure to a device which enables understanding the material on a far deeper level.

The information gathered can be loosely split into three categories: imaging, diffraction and spectroscopy, which could be by electron energy-loss spectroscopy (EELS) or energy-dispersive X-ray spectroscopy (EDXS). Imaging, as already mentioned, would allow the user to view small objects, where 'small' is often on the nanometre or Angstrom scale: far superior to optical microscopy. Diffraction utilises the wave-like nature of electrons more directly than imaging to form diffraction patterns of the atomic structure from nano-scale or larger regions, thereby understanding the crystal structure of the material. EELS exploits the energy dependent cross-sections of electrons interacting with atoms where electrons passing through the material lose an amount of energy, some of which is due to ionisation of core levels and thus reflects the chemical and electronic structure of the material. EDX detects the X-rays emitted from interactions (i.e. ionisation of shell electrons by those in the beam) with the atoms in the material to quantify its chemical composition.

There are two major alternatives by which an electron microscope would approach a sample: scanning/wide-field imaging and transmission/surface-excitation. A 'scanning' microscope would focus the beam on a small part of the sample at any given time and move the beam to analyse a different region, while a wide-field approach is to view the entire region of interest simultaneously. A 'transmission' microscope functions by utilising very high electron energies in conjunction with thin samples to ensure that the typical electron in the beam experiences little energy loss, meaning only a very few (generally zero or one) inelastic collisions and not so many elastic collision to have a significant effect (either singly or in total), which means that the typical electron statistically does not deviate far from its original path, and therefore behaves in a mathematically predictable manner (in that the first Born approximation can be applied). 'Surface-excitation' uses lower beam energies and generally much thicker (bulk) samples to limit the analysis to a fraction of the total sample thickness. The four kinds of electron microscopes are comprised of combinations of these alternatives:

- Transmission & wide-field: A transmission electron microscope (TEM) is often used for high-precision analysis, particularly in the spatial plane.
- Scanning & surface-excitation: Scanning electron microscopy (SEM) uses, with the primary advantage that imaging of the material surface is much easier and that much less (or no) sample preparation is required.
- Transmission & scanning:A scanning TEM (STEM) is a TEM which possesses the SEM capacity for a scanned focused electron probe, and to some extent combines the benefits of both.
- Wide-field & surface-excitation: The reflective electron microscope (REM) gathers information from elastically-scattered beam electrons, which can complement the SEM in such areas as determining the structure of crystals.

This work is primarily concerned with EDXS in a TEM, and so the other areas will only be mentioned in passing. In particular, the use of EDXS in SEM is common but will not be discussed in detail.

2.1 Physical interactions of electrons with samples

There are several ways that electrons interact with the material they travel through [1]. However, as this work is exclusively concerned with X-rays these other interactions will not be described in detail. In short, it is possible to categorise interactions broadly as either elastic or inelastic, where elastic forms the basis of imaging and diffraction while inelastic is responsible for EDXS and EELS.

An electron passing through the cloud of electrons which surround the nucleus of an atom will interact with this electron cloud. Most often, the interaction of the beam electrons with the nuclei takes the form of elastic scattering, and the incoming electron is simply deflected slightly with no particular result for the bound electron cloud. However, occasionally the interaction will be strong enough to eject one of the electrons from the cloud, thereby leaving a hole in one of the atomic shells. This hole can then be occupied by a higher-shell electron, emitting the energy difference required to conserve momentum and energy. This energy is either emitted isotropically as electromagnetic radiation or as an Auger electron. For the purpose of this work, transitions which result in Auger electrons are ignored. The energy level of each shell is determined by the nucleus, and as such the energy emitted from an electron jumping from one specific shell to another specific shell will also be discrete. Assuming that the energy is emitted as electromagnetic radiation, then this discreteness can be exploited, as each element has its own set of unique shells with unique energy levels, and therefore emits a unique 'family' of energies in the X-ray band. As such determining qualitatively which element(s) is/are in the material is simply a case of matching the resulting spectra to previously known X-ray 'families'. These 'element-specific' X-rays are known as 'characteristic X-rays'.

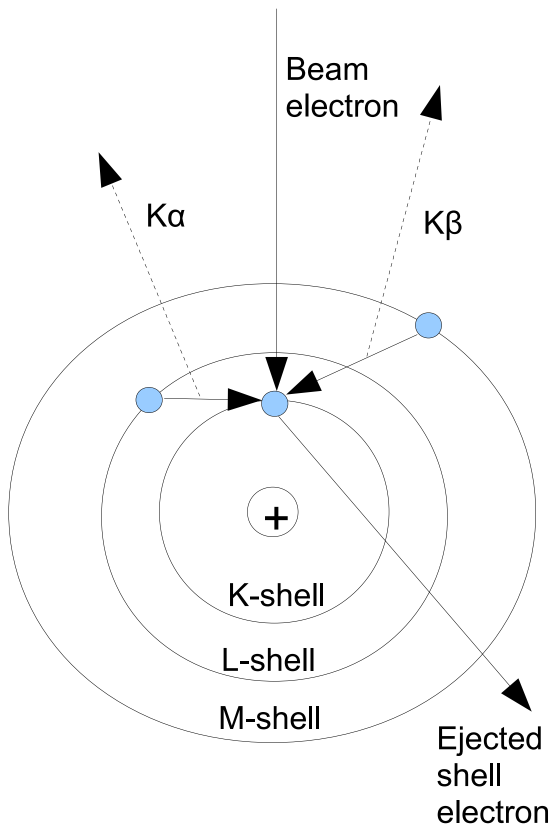

Figure 2.1.1: Diagram of characteristic X-ray emission. Note that the origin shell of the electron that falls into the hole created by the beam electron causes a change in the energy of the emitted X-ray, which is reflected by their different names. Superfluous electrons (those not in the shown interactions and the fate of the beam electron) have been omitted for clarity.

Unfortunately, there is another process which can result in an X-ray being emitted. If an incoming electron interacts not with the electron cloud but the electromagnetic field of the atomic nucleus then the fast primary electron will decelerate and/or be deflected by electromagnetic interactions with the screened nuclear potential. The energy lost is emitted as electromagnetic radiation. As there are innumerable possible angles and resulting velocities for the electron approaching the nucleus, the radiation emitted by this process is a continuum in energy. However, the statistical likelihood is that X-rays of lower energies are emitted far more often than higher, and as such the resulting X-ray output would, in theory, look like an exponentially decaying curve. The consequence of this is that the 'characteristic' X-rays appear as peaks on top of this background (or 'Bremsstrahlung') continuum, necessitating interpolation techniques to extract the number of characteristic X-rays by integration over some specific energy range.

However, there is still the issue of how X-rays interact with matter once they have been generated. An X-ray travelling through a material will have a certain probability of being absorbed, depending on the composition of the material and the X-ray's energy, where higher energy means it is less likely to be absorbed. The likelihood of being absorbed is not a simple curve with energy, however, as the atomic cross-section of an atom changes non-linearly with energy. The result of this is that some X-rays generated within the material will be absorbed before escaping, and as such cannot be detected. As the atomic cross-section for X-ray absorption (i.e. the probability of an X-ray being absorbed) is different for each X-ray energy and for each material it is not a simple matter to account for, as the number of X-rays detected does not reliably reflect the number generated. This is reflected in the Lambert-Beer law:

$$I_{Detected} = I_{Generated}\, e^{\frac{-D}{\lambda}} \qquad \text{Equation 2.1.1}$$

where I_{Detected} is the number of X-rays detected leaving the sample, $I_{\text{Generated}}$ is the number of X-rays

originally generated within the sample, D is the distance that the X-ray travels through the sample in the way to the detector and λ is the attenuation wavelength which in this thesis is defined as the amount of material necessary to reduce the X-ray intensity to $1/e$ of its original strength. Further, an absorbed X-ray can cause another to be fluoresced, which can confuse the situation if the fluoresced X-ray (with an energy slightly below the original X-ray) is of a similar energy to a characteristic X-ray from that material. In principle, this can be accounted for by recognising in which materials it will occur, and removing the supposed self-fluoresced X-rays from their new energy and adding them back onto their original characteristic peak. The details of these artefacts are described in section 2.3.

In summary, the information required is the number of 'characteristic' X-rays of all elements in the specimen, as they permit identification of elements within the sample. However, it is necessary to remove the intensity from the energy range of interest that comes from the background and account for absorption/fluorescence.

2.2 Geometry of X-ray detector

Despite the sheer flux of electrons in a typical electron beam (on the order of billions per second) X-ray fluorescence is a relatively rare event. For an X-ray of a specific energy to be emitted, first a shell electron must be ejected, which is uncommon. This is a result of the fact that primary electrons would be moving so quickly through a material that the interaction cross-section is very small. If the shell electron is ejected, then an electron from the correct shell for that particular emitted energy must fall into the newly vacated hole. Last, the resulting energy must be emitted as electromagnetic radiation instead of an Auger electron. Combined, these three requirements result in an efficiency that is extremely low. Those X-rays which are emitted do so isotropically which means that the most efficient method to gather these X-rays would be to have as many detectors as large as possible as close as possible. Assigning a numerical value to how many X-rays gathered out of all those generated (and which escape the sample) is described as the detector collection angle, generally defined by Ω. It is worth noting that while a large Ω gives the maximum number of X-rays being detected it also means a inferior spatial resolution, which can be important for methods like X-ray mapping. Generally, detectors are optimised for maximum count rate with a large Ω with spatial resolution being controlled by the size of the beam.

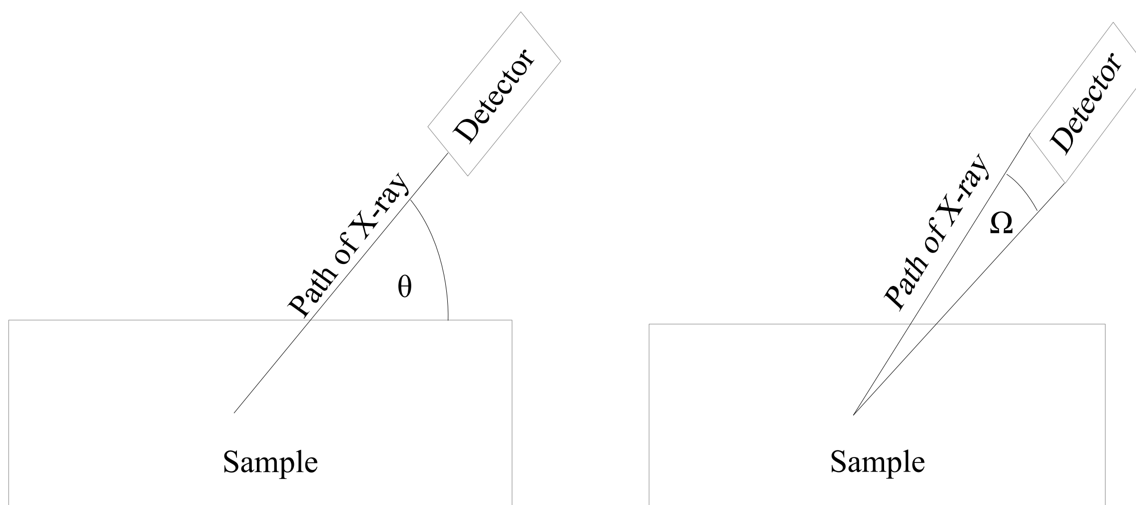

Figure 2.2.1: Diagrams defining take-off angle, θ, and collection angle, Ω.

As already mentioned, the more material the X-ray must travel through the greater the chance of it being absorbed. As such, minimising the amount of material it must travel through reduces absorption and hence reduces the necessity for correction, thereby increasing accuracy. Assuming that the sample is placed flat then situating the detector vertically above it would minimise the distance travelled. This, however, is not feasible as doing so would place the detector in the path of the electron beam. As a compromise, placing the detector at the highest possible angle from an imaginary horizontal line drawn through the sample is the most efficient. The detector's angle above a horizontal line drawn through the sample is defined as the take-off angle, θ. Changing this take-off angle can cause significant changes in the detected intensity.

There is generally very little additional space in the microscope in the area around the sample, as properly focussing the beam requires almost completely surrounding the sample with the objective lens. As such there is no guarantee that every X-ray which strikes the detector originates in the sample. X-rays from outside the sample can be generated almost anywhere, from the sample holder to an aperture. As one X-ray can fluoresce another, even parts outside the line of the electron beam are susceptible. To ensure that only a minimum of these spurious X-rays reach the detector, the detector is generally fitted with a collimator, which is a block of dense material with a hole of the correct size and shape so that only the sample itself is exposed to the detector in a direct line of sight. This block in often coated with a light element, so as to reduce fluorescence from the collimator. It is worth noting that despite this, some spurious X-rays will still be counted.

In addition to spurious X-rays, some of the beam electrons will experience what is known as 'back-scattering'. This occurs when the electron undergoes a collision so strong that its direction is changed by more than ninety degrees from the beam path. These backscattered electrons can travel in almost any direction, including into the detector, where they result in a 'false positive'. This can be mostly mitigated by installing a magnet on the collimator, which would deflect electrons but not X-rays.

As there is little space around the sample there is generally only one X-ray detector. The position of this detector is guided by three sometimes conflicting requirements: that it must be large, close to the sample and at the highest possible angle above the horizontal. The final compromise is generally

set by the manufacturer, with the user having no ability to change any of these three parameters. Any situation which requires changing the take-off angle can be accomplished by rotating the sample holder in place, which approximates the effect of moving the detector, with some side-effects which will be described later.

2.3 Physics of X-ray detector

There are three types of semiconductor X-ray detectors in general use available: lithium drifted silicon (Si(Li)), intrinsic germanium (IG) and silicon drift detectors (SDD). All three function by the same broad principle: converting X-ray energy into a proportional charge pulse. As all the experimental results in this work were obtained with a Si(Li), this section will go into some detail as to their operation. A brief mention of the advantages and disadvantages of the other two types will also be included.

As already mentioned, an X-ray travelling through a material has a certain probability of being absorbed by an inner shell electron and ejecting it from its position. If an X-ray is absorbed by a semiconductor (such as either silicon or germanium) then the number of electron-hole pairs generated (by 'multiple exciton generation') would be proportional to the energy of the high-energy X-ray. By applying a reverse bias across the large intrinsic area, these electron-hole pairs would be separated and gathered at the electrical contacts. As the bulk of the detector is both intrinsic and reverse biased there are very few conduction electrons in the intrinsic region, minimising spurious counts. Once an X-ray has been absorbed in the intrinsic region, discovering the energy of the incident X-ray is, in principle, a simple matter of counting electron-hole pairs generated before the next X-ray arrives, though this can give rise to an artefact known as a 'sum peak', described later.

The basic detector design is a large (in the order of 30mm^2 to 50mm^2) monolithic structure with electrical contacts on both ends. Unfortunately, the bulk of the material must be intrinsic (that is, not n- or p-doped) so that there is neither too rapid recombination of electron-hole pairs (as for p-doped) nor spurious pulses (for n-doped). Creating silicon of sufficient purity is not currently technologically possible, and so they are doped with lithium to cancel out the acceptor impurities and p-type behaviour. This doping is not perfectly effective, and so the regions of the detector between the effectively intrinsic material and the electrical contacts are effectively p-type. The p-type region which lies between the intrinsic region and the detector is often called the 'dead layer', as any X-ray which creates electron-hole pairs in this region will see the resulting charges recombine before being counted. This reduces the effective count rate [1].

The electronics which counts the electron pulses takes a finite time to work. During this time, no further inputs are permitted, meaning that the detector is effectively switched off. This time is called the 'dead time', and can be controlled to some extent by changing the degree of processing applied. Decreasing the 'dead time' would increase the number of X-rays detected (as the detector is 'off' for less time) but decreases the energy resolution (as the electronics would have less time to make a decision as to which energy range the pulse lies in) and as such is a compromise.

The lithium implantation is also one of the reasons that the detector must be cooled with liquid nitrogen. If it were not cooled the lithium atoms would diffuse, effectively destroying the intrinsic region and rendering the detector useless. Cooling is also necessary to reduce the thermally generated noise in both the detector and the processing electronics. Recent advances have reduced the requirements from liquid nitrogen (-196°C) for SiLi to Peltier cooling for SDD detectors (to ~-30°C).

There are several artefacts present in any detector. These are: escape peaks, internal fluorescence peaks and sum peaks. An escape peak comes about if some of an incident X-ray's energy is lost, most commonly by fluorescing a Si K-line X-ray that then exits the detector, taking its energy with it. As such, a false peak with an energy 1.74keV below the true value will arise if there are large numbers of a specific X-ray line. This is only a significant problem if there is another element which has a characteristic emission close to that value (e.g. In_L and Al_K). Internal fluorescence peaks generally originate from Si K X-rays being fluoresced in the dead zone by an incident X-ray. There is no way to differentiate between a Si K X-ray from the sample or from the detector. This is generally a fairly small peak, which does not have a particularly significant effect if the user is aware of the phenomenon and is not misled into thinking that its contribution is from the sample. A sum peak is a result of the processing method, where if two X-rays arrive almost simultaneously, then the detector cannot differentiate between them, and assumes that they are in fact a single X-ray with the sum of their energies. In a TEM thin sample, this would also not generally a problem for the wary user. For an SEM, where the samples are often much thicker, this can be a serious problem.

The significant difference between Si(Li) and IG detectors is their effectiveness with changing X-ray energy: a Si(Li) effectiveness decreases dramatically above ~20keV, as many such X-rays will pass straight through without being absorbed, while IG remains effective up to ~50keV while simultaneously giving somewhat better energy resolution. The only drawback to IG detectors is that Si(Li) are significantly easier to manufacture and have much better low-energy detection efficiency.

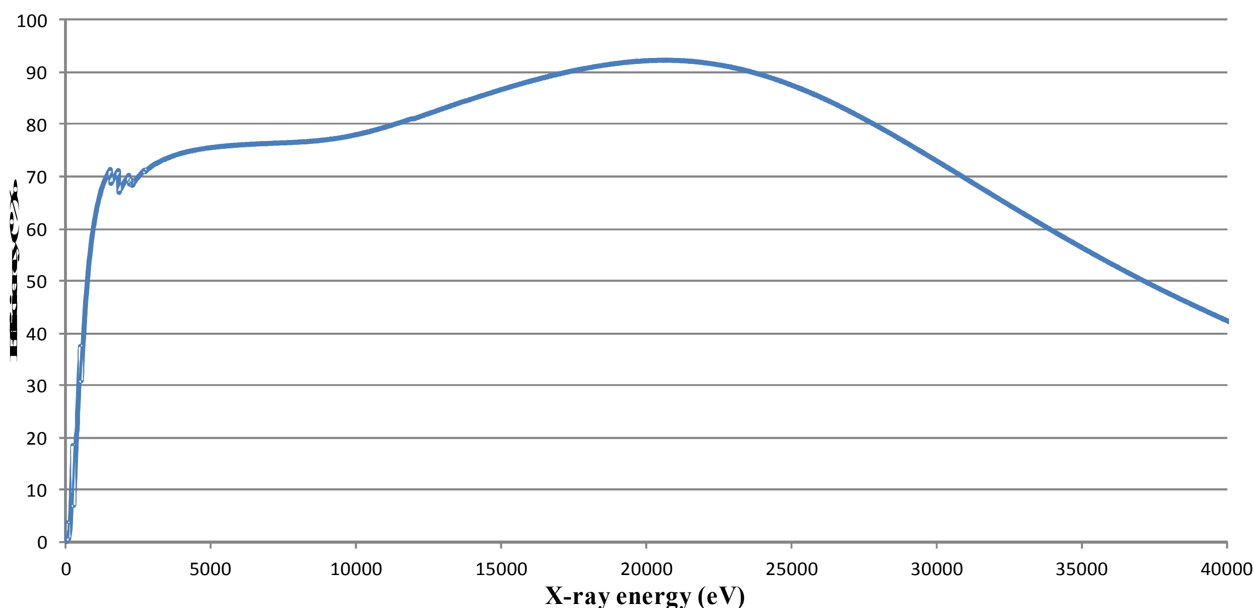

Figure 2.3.1: Detector efficiency for typical detector + window. Data calculated using DTSA II [2]. The data of this study was collected using a Oxford Instruments Si(Li) detector, model number 6498, serial number 31094-1380-01, and a Pentafet UTW. As no relevant values for this detector or window was available, the default values of DTSA II were used. Throughout this thesis, values calculated from this figure were used for detector efficiencies, for consistency.

The design of a SDD is radically different. Instead of a single monolithic region, the bulk of the detector is composed of n-type silicon, with concentric rings of p-type silicon radiating out from a single collection anode. Since the voltage is applied between the p-type regions and the single anode (where the physical separation is much smaller) a much lower voltage is required. Further, a

small anode has a much lower capacitance than the large one of the monolithic detector design, thereby permitting much higher throughput (on the order of ten to a hundred times more than for a monolithic Si(Li)). This higher throughput means that sum peaks are rare. Unfortunately, generating such a high count rate is generally not possible in most TEMs. While there is no lithium to diffuse there is no chance of lack of cooling destroying the detector, however, Peltier cooling to ~-30°C is still necessary to reduce thermal noise.

2.4 Detector window

The electron microscope must operate in a vacuum to maintain its effectiveness. However, this vacuum is not perfect, and over time contaminants can build up. For the majority of the microscope's interior, this is not that much of a problem, simply resulting in a slightly degraded vacuum, however the X-ray detector is particularly vulnerable as contamination both absorbs X-rays (and thereby reduces the detector's efficiency) but also the cooling causes contamination to build up much faster by condensation. The solution to this is to separate the detector from the microscope column while leaving a thin window to allow X-rays to pass through.

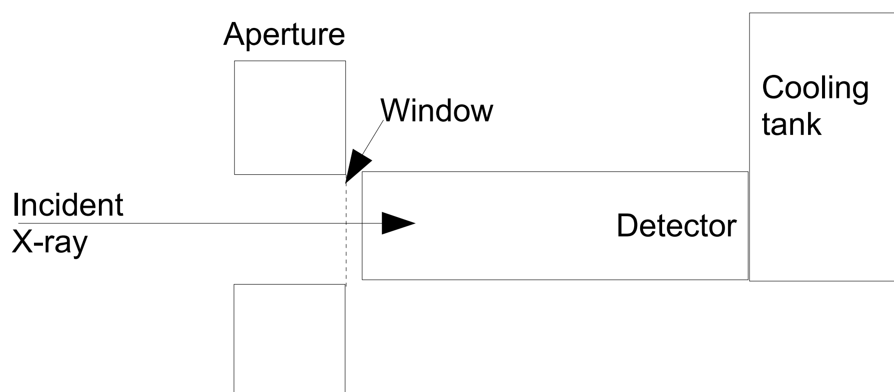

Figure 2.4.1: Diagram of EDX detector, showing detector window, aperture for blocking unwanted X-rays and electrons and the cooling tank.

The choice of material and thickness for this window is a compromise between maintaining the integrity of the vacuum and allowing the maximum number of X-rays to pass through. There are two types of windows in common use: beryllium windows and ultrathin polymer windows. A beryllium window will generally be ~12-25μm thick but still absorbs low-energy X-rays to a significant extent, so that X-rays with energies below ~0.6keV cannot be detected at all (this includes several elements which are potentially critical in some situations, like carbon and oxygen) and absorption is higher than for ultrathin windows up to approximately 1.7keV. An ultrathin window can range from less than a hundred to two hundred nanometres thick sheet of polymer, diamond or certain nitride compounds and gives significantly lower absorption at low energies and as such is vital for some studies. Some detectors can function effectively without a window, however this requires an extremely high quality vacuum.

The presence of the window both removes the detector cooling causing an increase in deposition buildup and reducing the possibility of ice buildup (which has a similar effect to contamination in that it absorbs X-rays) but also aids removing said contamination by evaporation and allowing the microscope's powerful vacuum pumps to remove the particles, as doing so requires heating, which is problematic for the detector but far less so for the microscope itself.

2.5 Quantification of X-ray spectra in EDXS: principles

To sum up, the output of EDXS is a spectrum which takes the form of a bremsstrahlung curve with detector artefacts, spurious X-rays and characteristic peaks superimposed. Obviously, correctly analysing this is non-trivial.

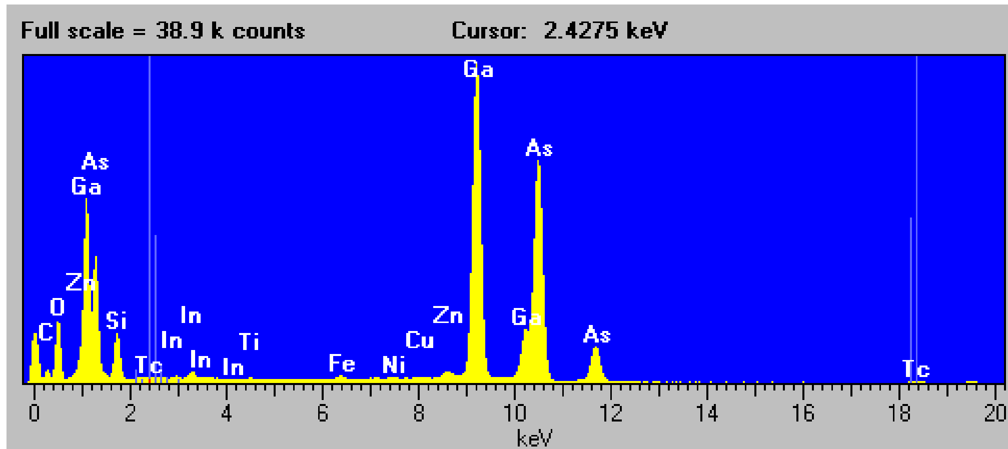

Figure 2.5.1: Example EDX spectra from a (In)GaAs sample. Note the Si_K peak at 1.740keV, which clearly originates in the detector as there is no silicon in this sample. The C_K and O_K peaks (0.282keV and 0.523keV, respectively) are likely from contamination, while the $Fe_{K\alpha}$ (6.400keV) and $Zn_{K\alpha}$ (8.631keV) are stray X-rays from the sample holder and the microscope itself. While the $Ga_{K\beta}$ line (10.263keV) is partially convolved with the $As_{K\alpha}$ (10.532keV) while the Ga_L and As_L lines (1.096keV and 1.282keV, respectively) are distinguishable at the top of the peaks but not at their base. This is a function of the processing time, with a longer time giving better separation.

Correctly removing detector artefacts and spurious X-rays is a matter of recognising what they are and subtracting them all from the spectrum. The difficulty with this approach arises when some artefact or spurious X-ray overlies a characteristic peak. When this occurs, the method is to either use a different characteristic peak for analysis or to attempt to remove the undesirable counts and analyse the remainder. Removing the undesirable counts is somewhat more difficult than it appears, however, as the strength of these detector artefacts and spurious X-rays changes from microscope to microscope and from sample to sample. As a rule, properly accounting for this problem is not particularly difficult for most X-ray lines, though Si_K and $Fe_{K,L}$ suffer most strongly from fluorescence by the detector and microscope column, respectively.

Aside from artefacts and spurious counts, it is also necessary to subtract the bremsstrahlung background. As the bremsstrahlung is not constant with energy, not doing so would cause some characteristic peaks to appear incorrectly high. As a first approximation, assuming the bremsstrahlung to be a linear interpolation between the beginning of the characteristic peak and the end is a good approximation, however this has problems when confronted with overlapping peaks. Given that a peak will be Gaussian in nature, with most peaks in the 0.5keV to 20keV range that is of most interest to microscopists being approximately 80eV to 180eV wide [1], it is reasonably straightforward to deconvolve the two, though doing so generally requires fairly sophisticated software that is commonly available.

One approach to quantification is the ZAF method [3], so called as it corrects for atomic number

(Z), absorption (A) and fluorescence (F). The difference in the atomic weight of the elements within the sample must be corrected for, as the backscattering and stopping power of each element affects the chance of X-ray fluorescence. Without this correction, a large difference between the atomic numbers of the elements within the sample would cause grossly erroneous results. The absorption correction takes into account the number of X-rays absorbed in the sample. Self-fluorescence within the sample must also be corrected for, by removing the estimated number of self-fluoresced X-rays from an intensity peak and adding them the original. Of the three, fluorescence is generally the most minor. The procedure begins by applying the equation

$$C_i = \frac{I_{sample}}{I_{standard}} \qquad \text{Equation 2.5.1}$$

where C_i is the concentration of a specific element as a percentage, and $I_{sample,standard}$ are the X-ray intensities from the sample and the pure-element standard (usually only available for SEM), respectively. Multiplying with the necessary terms for Z, A and F accounts for those effects, giving the total composition of that element. There are many different equations which can be used to determine the necessary terms, as the behaviour, for example, light elements can be radically different from that of heavier elements. After doing so for all X-ray lines of interest, the sum of the chemical concentrations is taken. If this result is not close to 100% (98% to 102% would be an acceptable range) then there is some error in the parameters that must be corrected. Assuming that this built-in error check passes, then the method re-calculates the ZAF values to arrive at new results for the compositions, then iteratively loops through this algorithm until the result converges. In this way the method arrives at the most appropriate result, ideally while avoiding errors.

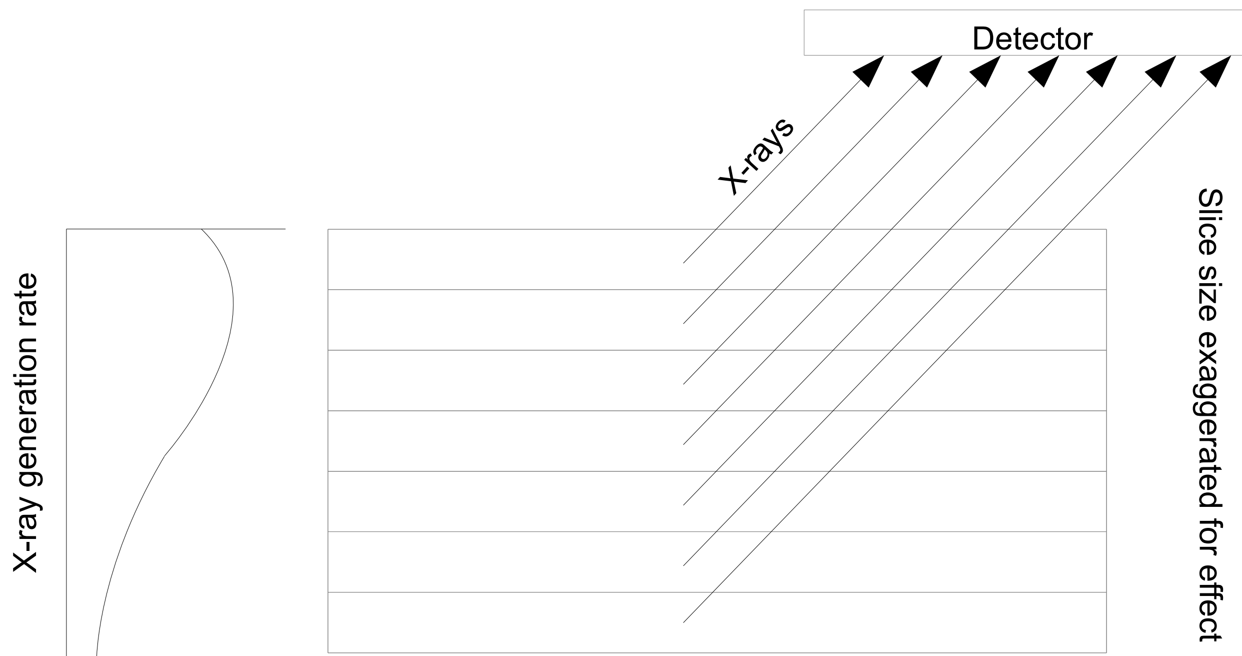

Figure 2.5.2: Sketch of φ(ρz) method, illustrating how each slice would be considered separately. Note that this is representative, and was not derived from actual data.

As mentioned, there are many different equations for deriving the corrections of the ZAF method. One of the most popular is known as the φ(ρz) approach, where the sample is divided into a number of arbitrarily thin slices and then each slice is dealt with separately for matters such as absorption. This would, in principle, give a superior view of the sample, though it is critically dependent on

accurate knowledge of how X-ray generation changes with depth, which in turn requires knowing both the sample composition and previously acquired data such as the stopping power of this material. Since the sample composition is necessary for the correction, an iterative approach is necessary.

Previously, the φ(ρz) approach had predominantly been used for bulk analysis in the SEM, typically with beam energies up to 40kV. However, a study conducted in 2003 [4] appears to demonstrate that the φ(ρz) approach is equally applicable to TEM analysis on the condition that the beam current can be measured: this means that knowledge of X-ray production yield as number of X-rays per electron would be required. As such, it appears to operate on those samples where the zeta-factor approach would also function. A significant advantage of this method is that the thickness naturally emerges from the equation, removing any necessity to calculate it independently.

The ZAF method, however, is dependent on having a pure-element sample on hand, which is obviously not ideal for TEM. Fortunately, scientific understanding of the physical processes involved has grown to the point where an entirely theoretical spectrum can, in principle, be used in place of the standard, though this does introduce some additional uncertainty. Further, the beam current must be stable over the period of time in which data is taken. If this is not the case, then the error check of summing compositions must be discarded [5].

A different approach to quantification is known as the Cliff-Lorimer method [6], which does not directly address the three factors as the ZAF method does but instead conflates most into a single '*k*-factor' term. This conflation is possible since TEM foils are so thin (tens of nanometres thick) that a great deal of simplification can be applied. One of these simplifications is to assume that X-ray generation is linear with thickness, contrary to the SEM where such would not be the case.

The essence of the method are the following equations:

$$\sum C_n = 100\% \quad \text{and} \quad C_j = \frac{\dfrac{I_j k_j a_j e_j}{A_j}}{\sum_n \dfrac{I_n k_n a_n e_n}{A_n}} \qquad \text{Equation 2.5.2}$$

where C_j are the percent compositions of elements, I_j are the detected counts from those elements, k_j is a sensitivity factor, a_j are corrections for absorption, e_j is the detector efficiency at that energy and A_j is the atomic weight of the relevant element which needs to be included when k_j is expressed as weight percentage. k_j, the *k*-factor, takes into account the differences between materials, microscopes and detectors, including such parameters as the chance of X-ray fluorescence. The *k*-factor is given with respect to that of a specific X-ray line, Si_K being the most common reference. If Si_K is the reference then it is defined as $k_{SiK}=1$. In principle, the only unknown should be $C_{j,n}$, which results in an algebraically simple, simultaneous equation problem. This approach is straightforward and in principle works fine. While it does not consider self-fluorescence this is generally not a problem. The chief difficulty is ensuring that the input parameters are correct, as variables like the detector efficiency can be incorrect by as much as ±10%. Given that this is not an iterative procedure there is no internal correction for such problems. While this method is gradually being supplanted by the zeta-factor method (below) it is still in common use.

As already mentioned, a major drawback of using *k*-factors is the need for a comparable standard. There is another approach, called the 'Zeta-factor method', initially developed in 1996 [7] by combining two other methods [8] [9], expanded in 1999 [10] and again in 2006 [11], which does not require compound standards, but can instead function with pure-element standards, which are much

easier to use.

If absorption and fluorescence are negligible (i.e. the thin-film approximation) then a characteristic X-ray line would increase with mass thickness, ρt. A term known as the zeta-factor, ζ, can then be defined as

$$\zeta = \frac{A}{N_0 Q b \omega i} \qquad \text{Equation 2.5.3}$$

where A is the atomic weight, N_0 is Avogadro's number, Q is the ionisation cross-section, b is the relative probability of a certain electron transition taking place after the inner-shell electron is ejected, ω is the probability of an X-ray being generated from that transition and i is the beam current. As there is no dependence on composition, density or thickness these factors can be ignored. This can then be used to establish the equation

$$\rho t = \zeta_A \frac{I_A}{C_A} \qquad \text{Equation 2.5.4}$$

where I_A is the X-ray intensity and C_A is the concentration. Then, the resulting calculation is similar to the Cliff-Lorimer method:

$$\rho t = \sum I_n \zeta_n \quad \text{and} \quad C_j = \frac{I_j \zeta_j}{\sum I_n \zeta_n} \qquad \text{Equation 2.5.5}$$

The drawback of this approach is that the beam current must be recorded with high accuracy, which is generally not possible in the typical TEM. This method exploits the fact that X-ray generation is proportional to the mass thickness to arrive at equations which are theoretically independent of sample thickness, density and composition. As a result, correcting for absorption is considerably more straightforward for the Zeta -factor method than for the Cliff-Lorimer method. Despite the advantages of the zeta-factor, the experimental results in this work are calculated with regard to the Cliff-Lorimer method, as the microscope available did not have the capability to measure the beam current in situ that the variable ζ requires.

2.6 Other methods for quantification

There has been much interest in improving the quality of compositional quantification over the years since quantification became feasible. This section describes a few of these methods and discusses their apparent usefulness in comparison to those developed in this thesis.

2.6.1 Absorption correction in ionic compounds

A method for correcting for absorption in ionic compounds was derived in 1994 [12], which exploits the fact that each atom would have an excess charge. Dependent on the assumption of sample charge neutrality (i.e. that summing all the anions and cations times their respective valence states gives a result of zero), this method does not depend on knowledge of the sample thickness and density and the detector take-off angle. Indeed, if two of these factors are known then the third to some degree of accuracy may be calculated as a result of quantification. Obviously, this assumes a degree of homogeneity which would render this method useless for a layered specimen structure.

This method functions by establishing various concentrations for the individual elements, projecting

how those concentrations would change with different mass-absorption lengths, then combining them to discover the only mass-absorption length which upholds charge neutrality (the accuracy of which calculation would obviously depend on the accuracy of the mass-absorption value), and therefore the absorption correction which yields the true composition. This requires processing the spectrum once for each element within the sample, and then again for the final result. Fortunately, it does function for complex system with multiple elements.

Plainly, the most significant disadvantage of this method is that it can only be used for ionic compounds. Beyond this, it seems to serve well enough and appears to suffer no significant drawback compared to the methods discussed in this thesis.

2.6.2 Discovering the depth of thin layers in an SEM by varying the beam voltage

This is a standard technique used in SEMs for determining the depth of a thin layer within a bulk material [13][14][15][16]. By varying the beam voltage the interaction volume will change which, if the variation in voltage is over the correct range, will cause more or fewer X-rays to be emitted from the layer of interest. If the user understands the behaviour of electrons in the material well enough (i.e. what kind of change can be expected from the interaction volume with varying voltage) then the reduction in the number of X-rays from the layer of interest can be correlated to its depth within the bulk material.

2.6.3 Extrapolation method of absorption correction

Originally developed in 1986 [17] and 1987 [18], then expanded in 1991 [19], this was an attempt to correct for absorption in the specimen. By taking measurements at several different thicknesses and plotting the resulting X-ray intensity ratios against either thickness or the intensity of a third X-ray line which does not suffer significant absorption, the absorption can to first order approximation be removed through linear extrapolation to zero thickness. Obviously, this is very similar to the method described in Chapter 7, though the report [19] indicates an interest more in accurate quantification for individual experiments rather than arriving at k-factors for general use. This method has been used with success [20]. It should be noted that the linear extrapolation is suggested to be used for any system, and as such may not be suitable for those specimens where the exponential decay with increasing thickness of an X-ray line has a significant effect. It is also worth noting that, like the method discussed in Chapter 7, a significant spread of thicknesses and a reasonably stable beam current are required for accurate quantification. This, however, can be overcome using the 'multigeometry' approach [19][8], which ensures that only a single thickness is required if the take-off angle can be varied sufficiently.

2.7 Methods for determination of sample thickness

2.7.1 Converged-Beam Electron Diffraction

While travelling though crystalline material, electrons will diffract in a similar manner to photons. In certain conditions, this diffraction leads to a phenomenon known as Kossel-Möllenstedt fringes which change as a function of sample thicknesss. The extent of this change is dependent on three

factors: the lattice parameters and atomic number of the material and the energy of the electron beam. The particulars of this relationship were first described in 1975 [21] and then detailed in 1981[22]. Fortunately, this method lends itself well to computerisation in that the changes are mathematically predictable.

This method is generally considered the most accurate, however the requirement for a undistorted, flat, crystalline area severely limits its use. It can, however, be carried out concurrently with other methods to give a self-consistent measurement of the thickness.

2.7.2 EELS plasmon

The EELS method of analysis is dependent on the inelastic interactions between beam electrons and sample material. Any specific electron would fall into three categories defined by the number of interactions: none, one or several. A thin sample would see most the electrons passing through without interacting, as the sample becomes thicker more electrons would interact, beginning with only one interaction on average but with a thick enough sample would multiple interactions would become commonplace. In this middle ground, where most electrons interact once, the relationship between those who do not interact and the total electron count is mathematically predictable [23], giving and accuracy of better than ±20%. If most electrons do not interact then the method loses sensitivity due to the insufficient number of electron in the remainder of the spectrum, while if many electron interact multiple times then the calculations become both more complex and less reliable.

2.7.3 Multigeometry and/or EELS determination of thickness

This method, developed in 1993 [24], attempts to correct for absorption iteratively without having to rely on knowing either the specimen thickness or mass absorption coefficients. If, while either changing the take-off angle or moving the beam to another region of the sample, the change in the amount of material the emitted X-rays would travel through can be accurately quantified, then in principle the degree of absorption can be modelled.

The only requirement is accurate knowledge of the amount of change and at least one X-ray line for which absorption can be neglected. Both of these conditions can be satisfied for samples which possess an X-ray line that is of sufficiently high energy compared to the thickness. For the first, it is worth noting that the absolute change is not necessary, only the relative change. If one has access to EELS, then this is readily achievable even when moving the beam from one region to another, further assuming that the sample is chemically homogeneous between the examined regions. The second condition can often be achieved, though it does impose a maximum thickness for which the method holds, dependent on the energies of the available X-rays. It should also be noted that EELS thickness determination experiences significantly larger errors beyond approximately 200nm sample thickness.

This method has been reported several times in the literature[25][26][27][28][29][30][31][32]. In particular, it is useful for those samples which are composed primarily of light elements with at least one hard X-ray line that is not strongly absorbed for the given sample thickness, and therefore can be used as a reference.

The chief disadvantage of this method is the requirement for multiple measurements. In cases where

the absorption correction is most necessary, i.e. light elements and therefore samples susceptible to knock-on beam damage, this can be a significant constraint, in particular with regards to counting statistics. The requirement for an X-ray line with negligible absorption is also of some difficulty, since it imposes a natural limitation on the maximum thickness for which this method can be used. It is worth noting that while the 'K/L ratio' method discussed in Chapter 6 prefers a hard X-ray (and the existence of such considerably simplifies the procedure) it is not strictly necessary to have such an X-ray line available.

2.7.4 Thickness determination via increasing X-ray counts

As previously described, the quantity of X-rays generated increases with sample thickness, linearly if the thickness is sufficiently small so that the beam electrons will not have lost significant energy. In principle, this relationship can be exploited to determine the thickness of the sample using only the X-ray spectrum, simply by observing how the X-ray intensity changes as the beam dose is increased while analysing the same area [33]. Obviously, this method is heavily dependent on calibration having been carried out for that particular microscope and detector, and rapidly becomes useless as the parameters (such as attempting to use a different detector) deviate further from those of the calibration. Correct calibration would allow determination of the absolute thickness, though this calibration must be very accurate. The biggest problem would be the beam current, as X-ray generation is also linearly dependent on the quantity of electrons, and as such a change in the current would be indistinguishable from a change in thickness. There is also the further difficulty that the X-ray line of interest (or more accurately the energy window, as this method functions equally well with bremsstrahlung) might experience absorption as thickness increases, thereby changing the apparent result. The logical solution is to use an energy window that is the highest possible for detection (19.5keV to 20keV, for example) while monitoring the beam current. Unfortunately, the bremsstrahlung and detector efficiency both decrease significantly at higher energies, and so statistical fluctuations could begin to dominate. As a result, this would be a compromise. Overall, this method appears to be inferior to the 'K/L ratio' method except when the ratio method cannot be used (no elements present with detectable K- and L-lines, for example). It should be noted that a characteristic X-ray peak is not strictly necessary for this process [34][35][36].

2.7.5 Improvement to contamination spot size separation method

The method of thickness determination known as 'contamination spot separation' was initially proposed some time ago [37]. This approach is reliant on the fact that a specimen that is not cooled builds up contamination relatively quickly while under electron bombardment in a TEM with poor vacuum. Having focussed the the beam on the sample for long enough this contamination will build up on both the upper and lower surfaces to the point where it would be visible with a less focused beam. Tilting the sample would then cause the contamination spots to move, where the extent of that motion would be dependent on the degree of tilt and, for the spot on the lower surface, the thickness of the sample. By knowing precisely how much the sample has been tilted by and measuring the apparent distance between the two spots, it is possible to use trigonometry to calculate the distance between them, and hence the thickness of the sample. Unfortunately, this method is known for somewhat overestimating the thickness, and some effort has been put into correcting this [38]. The degree of overestimation can be severe, up to a factor of three.

A slight modification to this method is to irradiate a line rather than a spot [39]. This retains the

effect of producing contamination on both surfaces while minimising the base broadening effect which seems to induce the overestimation of the spot method. This appears to function with good accuracy.

The obvious drawback of this method is that introducing this contamination changes the sample. If the region of interest is large, with many possible areas to investigate, then this is not a problem, however, a smaller region of interest could be rendered significantly less useful for further analysis, and as such would be a method that should be reserved for after all other methods have failed.

2.7.6 K/L ratio

The differential X-ray absorption (DXA) approach is straightforward in methodology. By taking the intensity ratio of two characteristic X-ray lines, preferably one which experiences significant absorption and one which does not, the thickness of the sample can be deduced. This is due to the fact that such a ratio would have a unique curve, where each point along the curve uniquely corresponds to a thickness. In principle, this would make thickness measurement trivial. There are, however, several significant problems with this: the sheer number of possible combinations (as each X-ray energy is absorbed differently in each material), the size of the errors inherent in acquiring that curve and the difficulty in making that curve universal, given the plethora of parameters associated with acquiring X-ray spectra.

This method was first proposed in 1979 [8], then expanded into a full-fledged quantification method in 1989 [40]. This method does have the obvious weakness of being dependent on there being two X-rays to compare. The zeta-factor method overcame this weakness [7]. While in principle those X-rays do not need to originate from the same element, this being the case would help as the user can be assured that any difference in detected intensities is due to differing fluorescence probabilities and absorption, as opposed to different quantities of each element in the sample.

Quantifying by this method is done iteratively. Considering that the available variables are the X-ray intensities, *k*-factors, chemical composition and the absorption correction. The X-ray intensities and *k*-factors are gathered during the experiment or determined beforehand, respectively, leaving only the chemical composition and the absorption correction. The absorption correction is a function of density, thickness and mass-absorption coefficients. All relevant mass-absorption coefficients can be determined from pre-existing stores of data (such as the NIST database), while the thickness is given by the DXA method. This leaves the density, which is a function of the chemical composition, which itself can be described by a percentage sum of all elements within the sample to 100%. Iterating back and forth would then give the correct values.

2.8 Microcalorimeter

Counting the resulting charge pulses is not the only way to determine the energy of an incoming X-ray. Another type of detector is also possible: the microcalorimeter, a type of detector that measures heat.

A material, upon absorbing an X-ray, will experience a rise in temperature proportional to the energy of the X-ray. It is this relationship that a microcalorimeter exploits. By necessity, a microcalorimeter is generally a small metal plate, as it needs to have high density (to absorb X-

rays), high thermal conductivity (to transmit the heat pulse quickly) and low 'background' heat (so that the detector quickly returns to the baseline). The method can deliver an energy resolution of approximately 5-10eV, which in some situations is sufficient to provide information about the chemical structure while theoretically providing a count rate similar to EDXS. There are several disadvantages, however: the small collection angle, which impairs counting statistics, the need to cool the detector using liquid helium instead of liquid nitrogen (a considerable difference), the fact that high-energy X-rays would either pass through the detector or, if absorbed, swamp it with a large pulse of heat thereby presenting such a high background that quantification would become impossible for some time, and the mechanical difficulties involved in attaching such a device to a TEM. Currently, microcalorimeters are not common and are only available for SEMs, not TEMs, mainly due to the effect of X-rays with an energy of >10keV.

2.9 WDXS

EDXS is based around the concept of detecting all X-rays and counting them based on their energy deposited in a suitable detector. Another approach is to sort the incoming X-rays by wavelength before allowing them into the detector: this is known as wavelength-dispersive X-ray spectroscopy (WDXS), a method where only X-rays of a specific narrow band of wavelengths are permitted into the detector.

WDXS is a general approach where, instead of allowing all X-rays to strike the detector and then attempting to differentiate their energies from each other, all incoming X-ray are filtered by a crystal diffractometer so that only those which lie within a small band of wavelength (and therefore energy) are admitted to the detector. The advantages of this is that the energy resolution can be made extremely high (~5-10eV is typical) while retaining high throughput due to the fact that the detector no longer needs to differentiate between X-rays of different energies and can be designed for maximum counting speed. Filtering the X-rays is accomplished by passing them through a crystal with known structure, so that Bragg diffraction causes the X-rays with the desired energy to be diffracted into the detector, while all others are intercepted by an aperture. Changing the desired energy for diffraction is a matter of mechanically rotating the crystal, which can introduce significant vibrations to the microscope. These vibrations, which necessitate correcting in an extremely sensitive system such as an electron microscope, in addition to the very small collection angle in comparison to EDXS, means that WDXS is not popular, despite its very high energy resolution. The differences between EDXS and WDXS can be summed up as EDXS acquires counts very fast with relatively poor energy resolution over the entire spectrum while WDXS counts much slower in a very narrow band but with much higher resolution. Presently, this is used only in SEMs with very low spatial resolution (on the order of a micrometer) and with very high probe current (~µA) for a good count rate, and as such is often used in metallography and mineralogy.

3 Monte Carlo Simulation Software

The principles of electron-atom interaction are well understood. Since each scattering or absorption event is independent of all others it is possible to sum the results of many such individual interactions for an overall average result [41]. Doing so analytically would be difficult: using a computer to simulate many such events in quick succession is a computationally far more efficient method. Of course, such a simulation would be dependent on correct parameters, both from the user and the programs' built-in values (such as fluorescence probabilities and X-ray absorption cross-sections)[42], and a capacity for the random numbers necessary to provide realistic fluctuations in the interactions between wave/particle and material.

First presented to the broader community for use with computers in 1949 [43], the approach is based on a concept first brought about in the nineteenth century as the ‘theory of sets’. The computer programs which permitted these calculations were initially written as part of the United States’ Manhattan Project, where they were used to model nuclear reactions. This class of simulation programs are known as 'Monte Carlo' programs, named after a casino where one of the inventors' uncle gambled. One of the earliest civilian uses was in 1972 [44].

Four different programs were used in the course of this report: Hurricane, Casino, NISTMonte and EDAX Electron Flight Simulator. Their primary characteristics are listed below, followed by a comparison intended to discover which is the most appropriate for use.

3.1 Hurricane

Designed for commercial use, the Hurricane [45] simulation program is theoretically capable of simulating an arbitrarily complex sample geometry and returning a wide variety of results, such as the X-ray intensities of different lines, the number of electron that transmit through the sample or are backscatterered or the number of events such as elastic scattering or plasmon generation. However, for the purposes of this project, where only X-ray generation and absorption simulation is necessary, its tendency to produce relatively few X-rays per incident electron and that in the output the number of said X-rays that are absorbed is limited to four decimal places is inconvenient.

Since the output is for absolute numbers of X-rays, simple Poisson statistics can be applied, allowing the user to readily estimate the error. Unfortunately, the time taken to simulate appreciably high numbers of X-rays can be very long, going some way to cancelling out this advantage. For example, 10^4 counts would result in 1% relative error, but even for a strong X-ray line (i.e. Likely to be generated) simulating this would take a day or more.

Hurricane is designed for high energies taking into account relativistically corrected cross-sections, but as shall be seen in Table 3.6.1 and Table 3.6.2, the absorption cross-sections appear to be too small. The final disadvantage is that some degree of instability in the running of the program is exhibited, particularly where high amounts of memory are required. As the samples most often under discussion tend to be moderately simple and as such can be reduced in size, this has not been of great concern.

Hurricane has been used several times in the literature. For example, it was used in 2009 to help determine the effects of the presence or absence of water in a polymer [46] where it was used to deduce the effects of charge accumulation, or in 2006 when it was used to provide comparison for the size of the interaction volume at low beam energy [47].

3.2 Casino

For a free software program, Casino [48] is remarkably useful. It only possesses the ability to simulate simple samples that take the form of layers, either horizontal or vertical, but as this is by far the most common geometry of interest it is of little concern here. The primary advantage of this program is that the amount of electrons required to achieve good reproducibility is such that most simulations can be run in minutes. Partially cancelling this advantage is that the output X-ray intensities are not absolute values but internally-consistent scaled numbers, and as such would

require repeated simulation to give a quantifiable error.

Since Casino was designed for SEM functionality, accurate simulation at high energies is not guaranteed. Despite this, it seems capable of producing reliable results at 200keV, as seen in Table 3.6.1 and Table 3.6.2.

Casino is also capable of simulating a tilted sample. This is relevant to this project, as described in section 3.5.1.

The capabilities of Casino are described in many journal publications. Most notably, its complete functionality was described in reports [49][50], which was updated in 2007 [51] when the new version was released. It has been used for many different applications, such as studying particles [52] or to explore the theory of electron backscattering at low energies [53].

3.3 EDAX Electron Flight Simulator (EEFS)

EEFS [54] is a program sold by EDAX as part of a SEM operator package. Designed to function in the ≤30keV range, it is not ideally suited for TEM simulation. Lacking the ability to simulate complex samples, having a 32,000 electron history per simulation limit and the results being truncated at 4 decimal places all contribute to ensure that it cannot be a mainstay program.

The only significant advantage that EEFS possesses is that it is extremely fast, with a typical simulation taking only seconds. This, however, is partly due to the maximum number of electrons per simulation limit. Extrapolating the simulation time up to match the number of histories typically used in Casino sees no significant difference.

Broadly, EEFS is mostly useful to acquire a first order estimate, and should not be trusted for more serious calculations which involve electrons moving at relativistic speeds. This can be seen in the literature, where very few reports use EEFS with a beam energy higher than 30keV [55][56][57]. This can be contrasted to CASINO, which is occasionally used for higher energy calculations.

3.4 NISTMonte

Developed by the National Institute of Science and Technology, NISTMonte [58] is by far the most flexible of the programs used. Capable of an arbitrarily complex sample, up to the limits of the computer's hardware, it can be used for any kind of simulation, no matter how obscure or convoluted.

Requiring somewhat higher numbers of electron histories than Casino, and consequently running slower, NISTMonte produces non-absolute intensity values, and hence several simulations are needed to quantify the error.

NISTMonte results tend to be accurate to some extent: absorption effects appear to be somewhat weaker than in experimental results: this appears to be a systematic effect, implying that it could be possible to simply multiply any calculated result by some factor to determine the correct answer. This is most obviously seen in Table 3.6.1 and Table 3.6.2.

The capabilities of NISTMonte have been adequately described in the following articles by the

author of the program [59][60].

3.5 PENELOPE

PENELOPE, "Penetration and ENErgy LOss of Positrons and Electrons", was developed at the University of Barcelona in 1996 [61] and then improved repeatedly up to 2011 [62]. PENELOPE, like NISTMonte, is capable of an arbitarily complex sample.

Running much slower than NISTMonte or CASINO, PENELOPE inevitably suffers problems when faced with a requirement for high statistical accuracy.

A report has shown that PENELOPE is more accurate in some situations than either NISTMonte or CASINO [63], though this paper indicates that the difference is not tremendously large.

Due to the difficulty in achieving good functionality with this program and the uncertain benefits of doing so, PENELOPE was not used in this thesis.

3.6 Comparison of absorption values of X-rays from Monte Carlo simulation programs

For the purposes of this project, there are fundamentally two properties that need to be correctly modelled for accurate Monte Carlo simulation: X-ray production yield and attenuation. If the former is incorrect, then any ratio of intensities of different X-ray lines will be suspect and comparison between simulated and experimental data will be difficult. If the latter is wrong, then the fundamental portion of the methodology of estimating absorption and calculating its effects on quantification of intensities cannot be determined. To this end, several attempts have been made to compare the programs used, to determine their suitability.

The method of comparison will be the determination of the variable λ from Equation 2.1.1 which is the slope of a linear least-squares fit of a ln Intensity vs. effective thickness curve, where its utility will be explained later. In this case, the calculation is done by simulating a thin layer capped by different amounts of material, as seen in Figure 3.6.1, and then calculating the slope of the resulting ln Intensity vs. thickness curve. This gives a distance in nanometres (assuming thickness is also in nanometres) for which the X-ray intensity would have fallen to 1/e (i.e.36%) of its original value. For the purposes of this comparison, all layers will be 10nm thick and composed of the pure element, and each program used their default models and parameters.

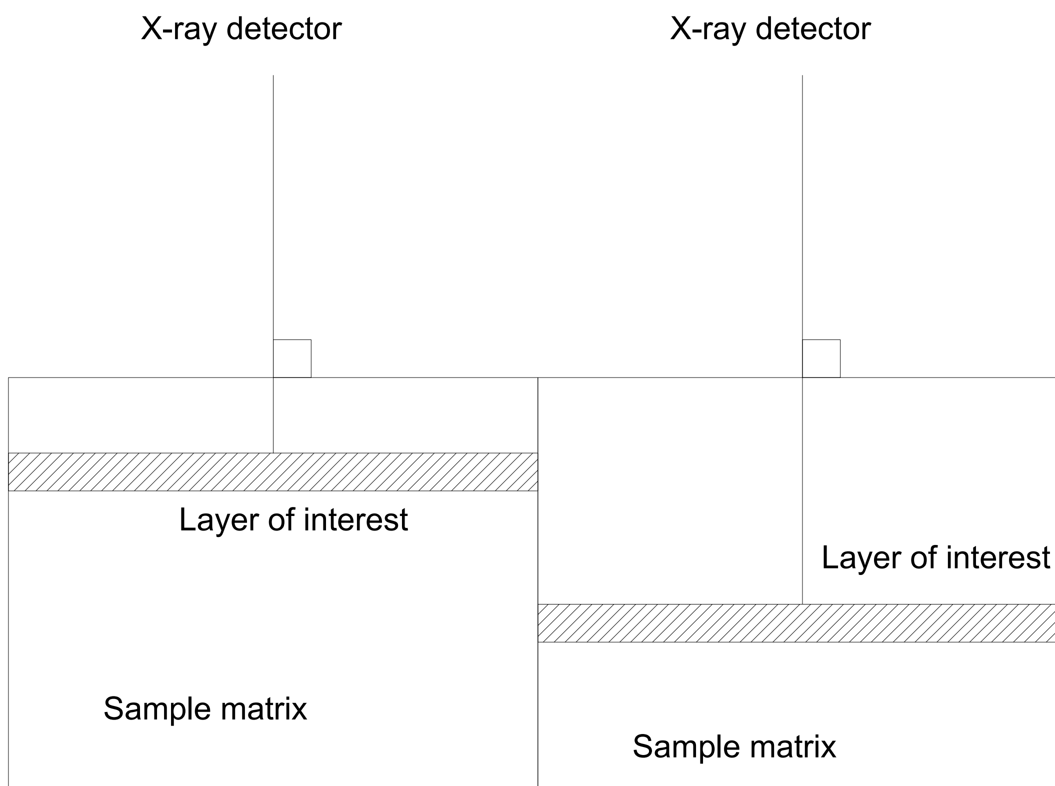

Figure 3.6.1: Diagram of change in sample for λ calculation.

GaN matrix (density 6.15gcm^{-3})										
X-ray Line	NISTMonte		EEFS		Hurricane		CASINO		Mean	
	λ	±	λ	±	λ	±	λ	±	λ	±
Mg_K	273.51	0.1	264.4	0.14	266	1	278	5	270	5
As_L	285.13	0.06	278.39	0.14	266	1	282.2	3	278	3
Al_K	373.03	0.14	341.6	0.2	343	1	352	3	352	3
Si_K	555.2	0.4	465.2	0.3	496	2	508	2	506	5
P_K	810.7	0.6	694.8	0.7	732	6	740	1	744	6
In_L	3397	9	2666	9	2669	18	2859	3	2900	20
Sb_L	4620	20	3420	14	3600	300	3766	4	3900	300
As_K	13250	190	8198	9	8500	600	12850	80	10700	800

Table 3.6.1: Comparison of calculated absorption-path length λ for different lines in GaN simulated with four different programs. The X-ray lines used are those of typical dopants, e.g. Mg or Si, and group III and group V elements that can substitute partially for Ga or N, respectively. Error is standard error of least-squares method.

GaAs matrix (density 5.316gcm^{-3})										
X-ray Line	NISTMonte		EEFS		Hurricane		CASINO		Mean	
	λ	±	λ	±	λ	±	λ	±	λ	±
N_K	144.15	0.01	134.43	0.05	140	3	138	4	139	5
Al_K	365.41	0.01	344.6	0.2	342	1	354	1	352	1
Si_K	502.52	0.01	419	0.3	470	10	468	1	460	10
P_K	725.65	0.02	625.9	0.5	670	10	668	4	672	11
In_L	2770.24	0.15	2393	9	2390	30	2551	2	2530	40
Sb_L	3627.3	0.3	3064	11	3010	40	3334	4	3290	50

Table 3.6.2: Comparison of calculated absorption-path length λ for different lines in GaAs simulated with four different programs. The X-ray lines used are those of typical dopants, e.g. P or Si, and group III and group V elements that can substitute partially for Ga or As, respectively. Error is standard error of least-squares method.

By comparing calculated λ values (as described in section 4.5) it is possible to describe the programs' relative absorption characteristics. Note that the stated error is the standard error calculated by the least-squares method.

Of note is that the different programs provide different scatter, with NISTMonte reproducing numerical values with sufficiently small error so as to disappear into rounding errors. Hurricane would require much longer processing times to achieve significantly better reproducibility, EEFS cannot by software limitation and Casino can run for the same amount of time as NISTMonte but would give more than five times the error. It is worth noting that while the CASINO values are generally close to the mean, this is not always the case, as seen for the As_K in GaN values.

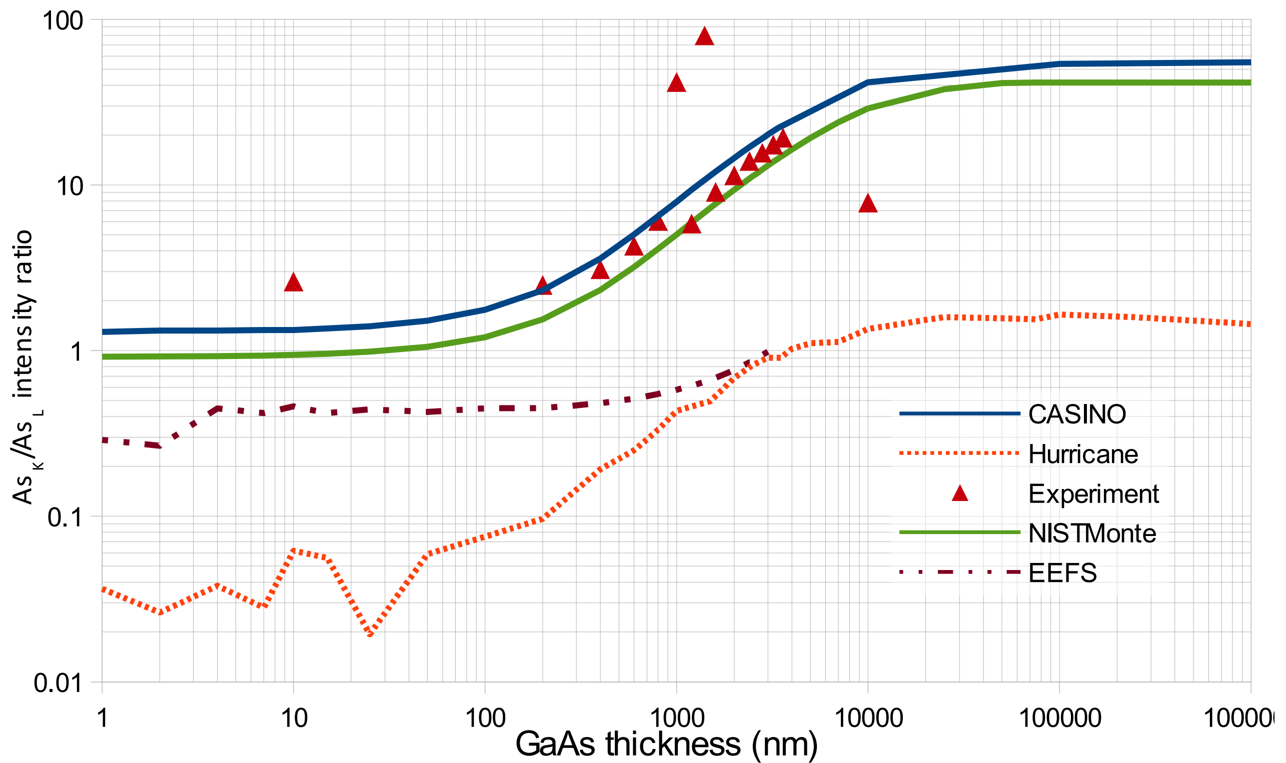

Figure 3.6.2: Comparison of As_K / As_L ratio in different thicknesses between four simulation programs and experimental results [64]. Note the double-log scale. Detector efficiencies applied to simulated data: As_L: 68%, As_K: 79%. Simulated sample homogeneous GaAs (density = 5.316gcm^{-3}), take-off angle constant = 90°.

Figure 3.6.2 is the result of a comparison between simulated and experimental data for a GaAs wedge sample of known varying thickness. As the sample thickness increases monotonically from the edge it is theoretically possible to determine the thickness of the sample by taking the ratio of As_K / As_L. It is clear that the closest correlation to the experimental results will likely be the most accurate program. The same trend is visible in all five curves, though EDAX Electron Flight Simulator cannot complete it because of a software limitation disallowing samples thicker than 3µm. Clearly, it is NISTMonte and Casino that agree rather well with the experimental results and as such are considered the most accurate, which appears to agree with a recent study [63].

4 Method for determination of the depth of thin layer within a matrix material by X-ray spectroscopy

4.1 Description of method

The ability to know the depth of a thin layer within a matrix is potentially very valuable. The most obvious way to do this is by creating a cross-section sample that is representative of the whole. Unfortunately, this is not always feasible, and as such a means of discovering the depth of a plan-view sample is described here. The most obvious use of this is to overcome the inherent assumption in the Cliff-Lorimer, ZAF or Zeta-factor methods that the sampled material is homogeneous, more specifically that X-rays originate equally from all depths. In cases where there is a large concentration instead of a homogeneous distribution of certain elements correcting for absorption can cause significant errors. It is expected that this approach would be useful for embedded quantum structures and certain forms of tomography.

A method for doing so was proposed in 2008 [65]. This is built on the model that the detected intensity (assuming a perfect detector) can be calculated by the Lambert-Beer law (Equation 2.1.1):

$$I_{Detected} = I_{Generated}\, e^{\frac{-D}{\lambda}}$$

where D is the amount of the material between the origin of the X-ray and the surface and λ is the attenuation wavelength (a value representing the distance a X-ray line can travel through a material before being reduced to 1/e % of its original intensity). This λ variable will initially be taken as given, with details of its calculation given in section in 4.5. I_{Detected} is given by the detector during experiment, λ would be calculated beforehand while both $I_{\text{Generated}}$ and D are unknowns. $I_{\text{Generated}}$ must always be eliminated by division: this is facilitated by the assumption that it does not change between analyses, provided the sample or beam conditions does not change significantly. In those cases where either the sample or the beam change then certain methods can be employed to compensate, such as that described in section 2.6.2. Through application of trigonometry and algebra D can be calculated using:

$$d = \frac{\lambda \ln \frac{I_1}{I_2}}{\operatorname{cosec}\theta_2 - \operatorname{cosec}\theta_1} = \frac{\lambda \ln \frac{I_1}{I_2}\left(\cos(\theta_1 - \theta_2) - \cos(\theta_1 + \theta_2)\right)}{4 \sin\left(\frac{\theta_1 - \theta_2}{2}\right) \cos\left(\frac{\theta_1 + \theta_2}{2}\right)} \qquad \text{Equation 4.1.1}$$

where $d = D/\sin\theta$ is the depth of the thin layer within the matrix, $\theta_{1,2}$ are two different take-off angles and $I_{1,2}$ are I_{Detected} for the respective take-off angles. Changing the take-off angle results in a change in absorption. This change in absorption is proportional to the change in the amount of material the X-rays travel through, and as such reflects the depth of the layer.

Equation 4.1.1 is used by analysing every possible combination of angles from the data set in order to arrive at the largest possible number of results, though (as explored later) some of these results may have to be discarded. Further variations and logical extrapolations on this method are discussed in section 4.8.

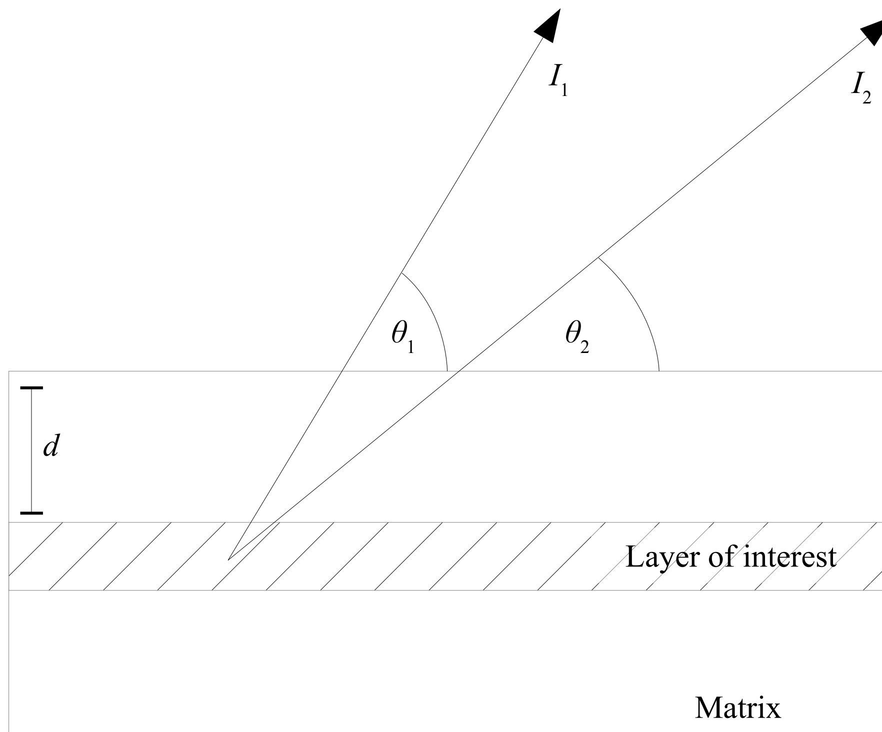

Figure 4.1.1: Diagram describing the variables of equation 4.1.1.

4.1.1 Assumptions

There are several assumptions in this model:

- That the embedded layer is sufficiently thin that self-absorption can be ignored and that all X-rays can be presumed to originate from a single point.
- That the embedded layer is homogeneous in its size, depth and composition over the entire area within which the electron beam interacts with the sample.
- That the region of the sample that the resulting X-ray travel through is sufficiently homogeneous that any change can be assumed to come from change in take-off angle.
- That the embedded layer is sufficiently deep so as to provide enough change in absorption over the range of take-off angles used.
- That sufficient X-rays are generated in the embedded layer so as to minimise statistical fluctuations.
- That there is only one thin layer.
- Either that the beam current remains constant or that any change in the number of X-rays generated can be normalised.

These assumptions can be summed up as: change of absorption by a predictable amount while holding all other parameters constant. As a rule, making sure that the same area is always examined even after changing the take-off angle is necessary. Closely monitoring the beam current can be avoided through normalisation with respect to a hard X-ray, though this introduces a dependency on total sample thickness.

4.1.2 Corrections

There are four corrections required for use of equation 4.1.1. These are the livetime correction, specimen tilt correction, beam straggling correction and the shielding correction. The beam straggling correction is required for calculation of λ: this is discussed in Section 4.5.

4.1.2.1 Livetime correction

Not all analysis is carried out with the same parameters. A obvious aspect to change is the detector livetime: how long the detector spends actively waiting to process X-rays. Measuring analysis length by the livetime ensures that the time for which the detector is active is always known. Increasing the livetime means that the detector is active for longer and that more X-rays are counted, which in turn means better counting statistics. It also, however, means that the analysis itself takes longer, which can be detrimental when facing issues such as sample drift and beam damage.

It is often necessary for the user to change the livetime to optimise the desired result from the analysis: this would often be necessary if the analysis is taking place in a region that is close to the border of effectiveness between two livetimes. These spectra will have a different number of total X-ray counts and therefore a change in the absolute value for the characteristic X-ray of interest. As equation 4.1.1 compares absolute values between spectra this can produce incorrect results. This can be resolved by dividing by the livetime, such that the values used in equation 4.1.1 are expressed in counts per seconds (i.e. the count rate for the X-ray of interest) or by dividing and multiplying each spectra to be analysed by the appropriate values so that they all have the same 'effective' livetime.

4.1.2.2 Specimen Tilt correction

Equation 4.1.1 requires that the only change be the take-off angle. In many microscopes, this is accomplished by tilting the specimen toward or away from the detector. However, doing this changes the size of interaction volume, as demonstrated in Figure 4.1.2.2.1. This increase in interaction volume causes a change in the number of X-rays generated, which would appear as a change in size, violating the second assumption described in Section 4.1.1.

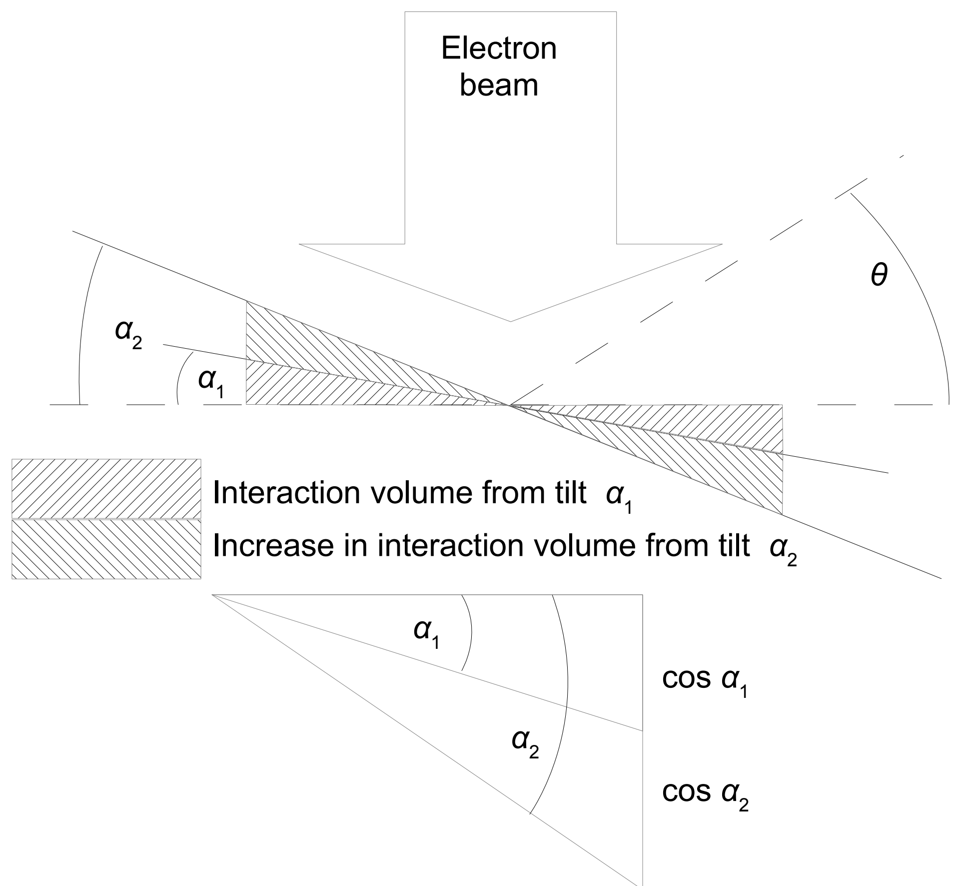

Figure 4.1.2.2.1: Diagram describing the geometry and the variables α, the specimen tilt, and θ, the take-off angle. Note that tilting the specimen causes a change in the interaction volume that is accounted for by the 'cos α' function of the lower part of the diagram.

Since the increase in interaction volume with tilt compared to the horizontal is cos α, then correcting for this increase simply requires multiplying the detected intensity with the cosine of the specimen tilt. In terms of of interaction volume, the sample would then have been reduced to its horizontal equivalent, with the only change being take-off angle.

4.1.2.3 Beam Straggling

Electrons travelling through material lose energy in several ways. If the amount of material travelled through changes then the average energy of the electrons changes. As the interaction cross-section of an atom changes with the energy of the incident electron, lower energy means a higher probability of interaction and therefore more X-ray fluorescence. This increase in interaction probability also means an increase in electron backscatter which in turn causes an increase in X-ray generation, often at fairly shallow depths: this effect is generally so small that it can be readily neglected.

With regard to using equation 4.1.1, the consequence of this is that tilting the specimen introduces a slight change in the amount of material travelled through, which cannot be compensated for as readily as the change in interaction volume. This can, in principle, be corrected for by normalising the detected intensity with respect to the generated intensity. This normalisation, however, is only available in simulations. Unfortunately, there does not appear to be a reliable way to account for this in experiments beyond increasing the beam energy. The point at which beam straggling becomes

relevant changes with material and beam energy, and as such the user should be aware that below a certain acceleration voltage the X-ray fluorescence becomes thickness dependent. This point can theoretically be determined by observing when the data deviates significantly from the expected curve (assuming that all parameters other than take-off angle remain the same).

4.1.2.4 Shielding

The shape of the sample holder is also relevant. As each sample holder has the sample positioned in a recess, it is necessary to consider whether some X-rays that should have reached the detector instead strike the side of the recess. This effect is referred to as 'shielding'. This can be accomplished by placing a test sample into he holder and then tilting it until the centre of the sample is no longer visible from the side. If the tilt is measured finely enough, a good estimate for the amount of shielding can be acquired. For both sample holders analysed (model number EM-31041), this angle was found to be ~10±2° and ~5±2°, where the difference between the centre of the sample and the far edge proved to be negligible. This can be interpreted as asserting that all X-rays leaving the sample at an angle of 10° or 5° or less from the sample's horizontal will be absorbed by the holder. Note that tilting the holder would cause the sample's horizontal to change from the absolute horizontal.

However, even for low take-off angles the detector will only be partially obscured by the specimen holder. Given knowledge of the detector's natural take-off angle, the degree of shielding, the radius or area of the detector and the collection angle it is possible to calculate the effect of changing take-off angle on the amount of X-rays blocked. The analytical calculation can be found in the appendix.

Determining the degree of shielding for a specific specimen holder is straightforward. Since it is assumed that this shielding occurs completely for a particular take-off angle (despite the fact that some hard X-rays would pass through the corner of the specimen holder's edge) then visual examination will suffice to determine at what angle the sample could no longer be seen. In the case of this attempt, the specimen holder was lined up with a specified point in space and then tilted until the centre of the holder was no longer visible. Then, it is a simple matter of measuring the degree to which it has been tilted.

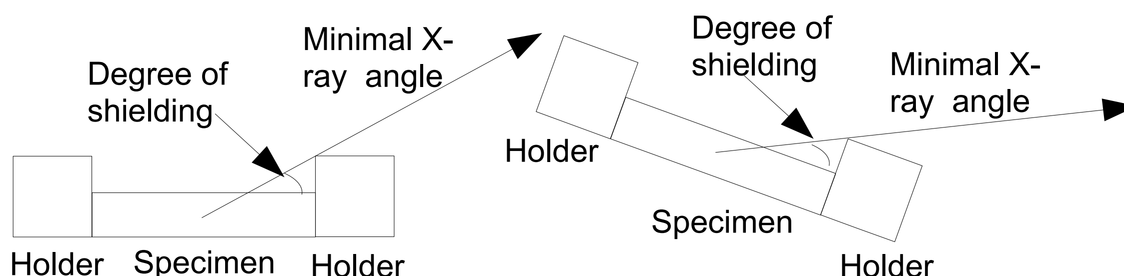

Figure 4.1.2.4.1: Demonstration of principle behind shielding.

Assuming a nominal, average take-off angle of 25°, degree of shielding as specified, nominal area of the detector =30mm^2 and collection angle = 0.12mrad, then the resulting change in the X-ray intensity is as seen in Figure 4.1.2.4.2. The curve of this graph indicates the proportion of X-rays generated by the sample that are not shielded by the sample holder, and does not account for any other effect. Proper comparison of simulations to experimental data requires that either the simulated data be multiplied with this curve or the experimental data divided by the curve. Doing so

would remove one source of disparity between the two data sets.

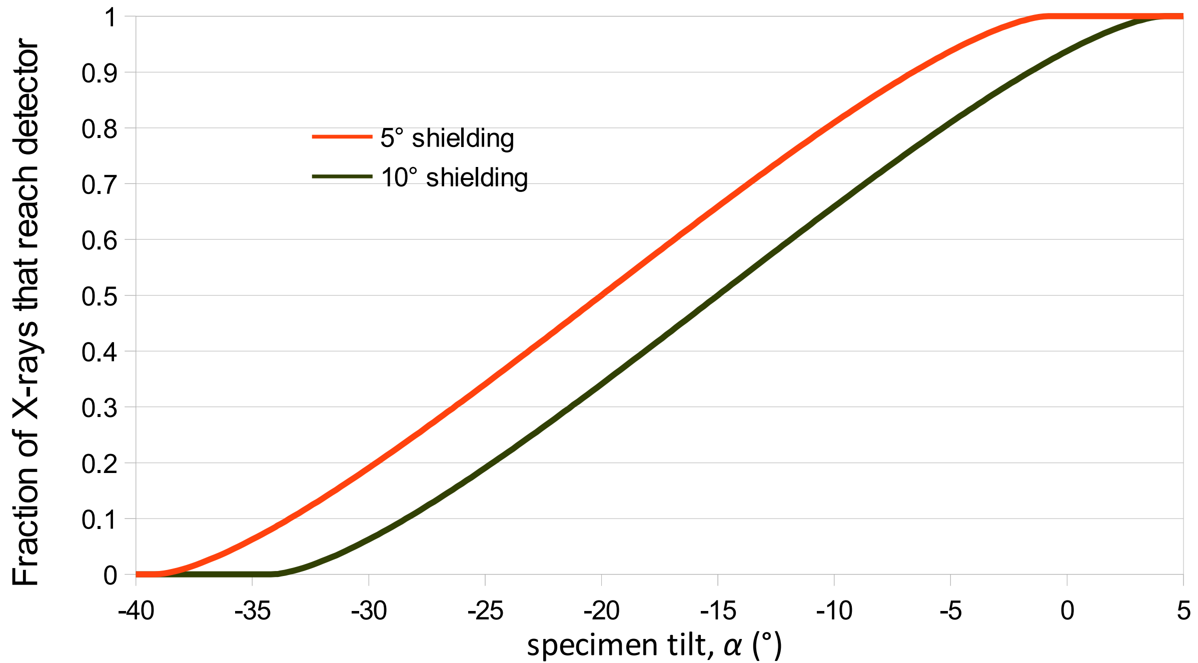

Figure 4.1.2.4.2: Projected effect of shielding by the specimen holder. Note that this effect is independent of changes in X-ray intensity due to take-off angle.

4.1.2.5 Detector solid angle

One of the core assumptions of this method is that the detector is a point. Physically, this is unrealistic, as the typical detector would be as large as possible in order to collect the greatest number of X-rays possible. A detector small enough in it's solid angle to effectively be a point would acquire almost no X-rays, and as such the atrocious statistics would offset any benefit from closer adherence to the method's assumptions.

Simulations imply that using a non-point detector has two effects: a possible increase in statistical fluctuations in the results (fairly small, in the order of 1%, if it exists at all) and an increase in the calculated depth, as the detector will to some extent appear analogous to a point detector with larger take-off angle. This latter effect is due to the fact that the portions of the detector that has a higher take-off angle will receive a larger portion of X-rays as a result of lesser absorption, but the detector does not record which part of itself received the X-ray and as such this effect cannot be removed.

In principle, correcting for this would be a matter of accurately simulating the detector used in the experiment with different variations of the calculated depth: this should give a reasonable estimate of the detector's effect on the result.

From a hardware perspective, a detector made of several independent sections which track X-rays separately would overcome this problem: this would be consistent with the design of a typical SDD.

4.1.3 Error determination

It can generally be assumed that the error in θ is negligible, as it is the difference between the two take-off angles that have a strong effect, not their absolute values. The error in equation 4.1.1 can be

given by

$$\Delta d=\sqrt{\left(\frac{\sqrt{\left(\frac{\Delta I_1}{I_1}\right)^2+\left(\frac{\Delta I_2}{I_2}\right)^2}}{\frac{I_1}{I_2}}\right)^2+\left(\frac{\Delta\lambda}{\lambda}\right)^2}$$ Equation 4.1.3.1

where $I_{1,2}$ are the intensities, d is the depth of the thin layer, λ is the attenuation wavelength described in section 4.1 and the character Δ denotes the error in the associated variable.

The error in λ will generally be known to the user before the experiment begins. The error in $I_{1,2}$ will be due to counting statistics and background subtraction. Typical experimental error appears to be in the range of 1-10%. Both of these errors can be mitigated by longer analysis time, a more intense beam and a thicker thin layer. A more intense beam could damage the sample, while longer analysis time may be hampered by available time on the microscope or the sample drifting such that the same region is no longer is being examined. This error estimation can be used to determine whether the analysis is worthwhile.

4.2 Detector Tilt Approach

The simplest application of equation 4.1.1 is in simulation with the change in take-off angle facilitated by moving the detector. For brevity, moving the detector instead of tilting the sample may be called the 'Detector Tilt' approach (despite the fact that the detector does not actually tilt).

Figure 4.2.1 shows simulated In_L detected intensity from a 5nm thick layer of InAs embedded at different depths within GaAs. The resulting curve is distinctive and appears to apply to any system with a thin layer, as it is the function of the change of absorption. It is worth noting that increasing the depth both changes the value of convergence and the slope as a result of there being a different amount of material to travel through before reaching the detector due to the changed thickness pf the overlayer. This is obviously due to the fact that X-rays from a shallower layer are not absorbed as much, and do not see as much of a change in the degree of absorption with changing take-off angle.

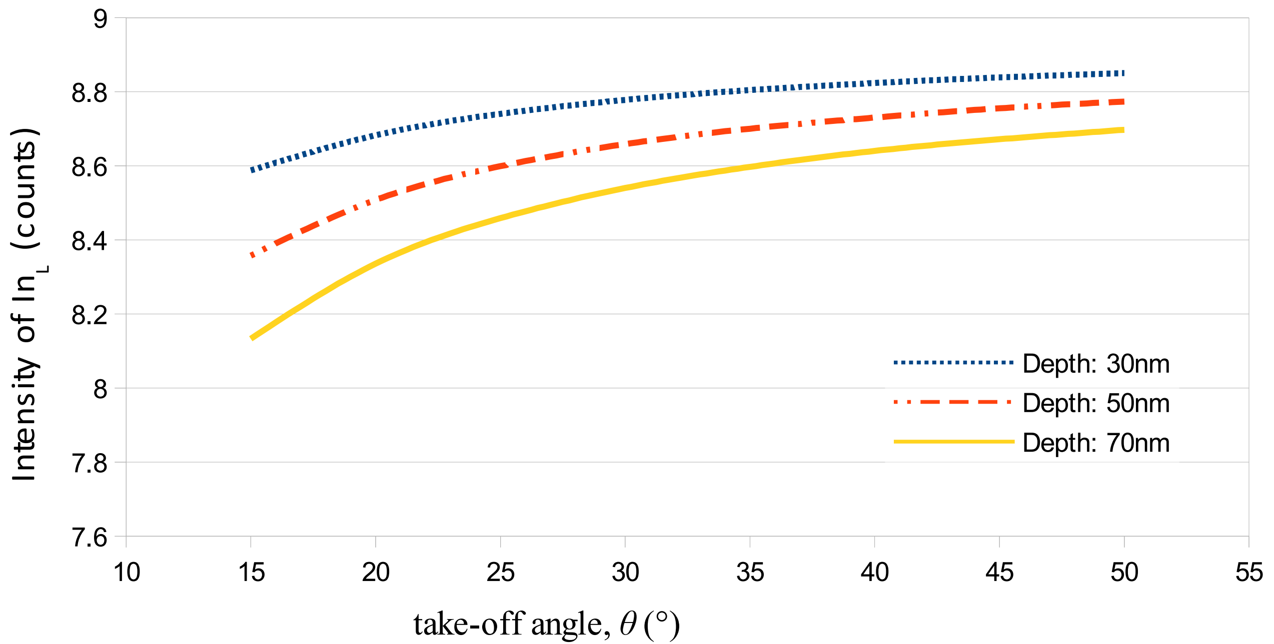

Figure 4.2.1: Intensity vs. take-off angle simulated for various overlayer thicknesses. Simulation run in NISTMonte at beam energy 197keV with 10^7 electron histories. Sample composition 5nm InAs (density = 6.51gcm^{-3}) at the bottom surface of 30, 50, and 70nm of GaAs (density = 5.316gcm^{-3}).

Figure 4.2.2 shows the calculated result from the 50nm deep embedded InAs, using a λ_{InL} value of 2770nm. The correct value would be 52.5nm, i.e. the depth plus half the thickness of the layer. It is clear that, while there is some scatter, the results are very uniform, with a mean of 52.6nm±1.0nm.

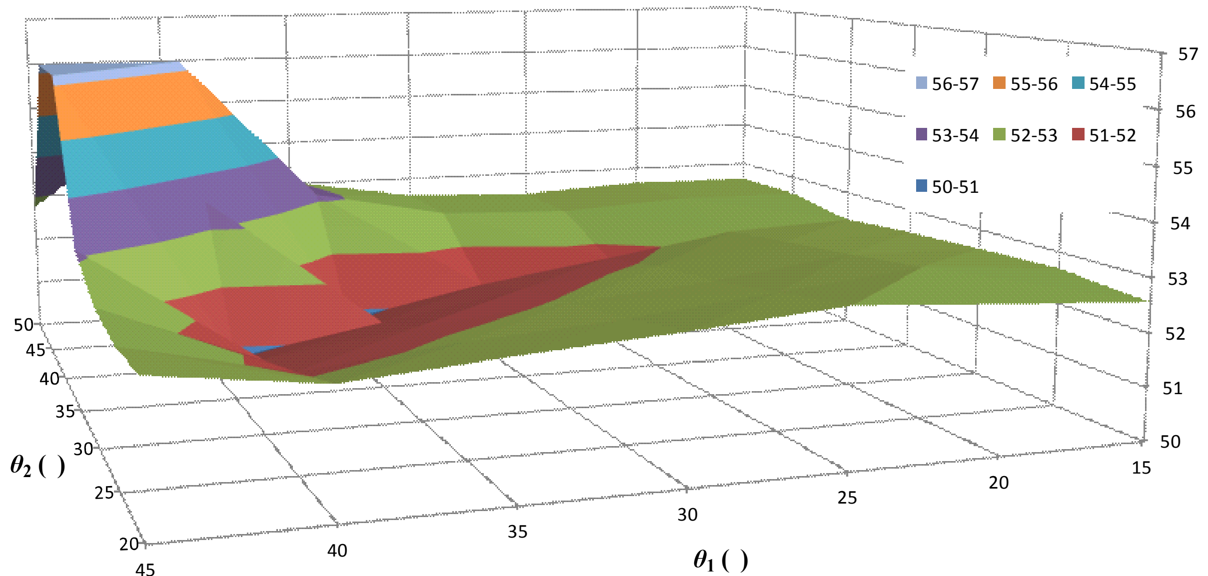

Figure 4.2.2: Calculated *d* (nm) from equation 4.1.1 for 5nm thick InAs layer at the bottom surface of 50nm of GaAs. Simulations run in NISTMonte at beam energy 197keV with 10^7 electron histories for two take-off angles θ_1 and θ_2.

Figure 4.3.1.2 and Figure 4.2.4 present this data in histogram form. Figure 4.3.1.2 uses the

internally consistent NISTMonte λ value of 2770 while Figure 4.2.4 uses the average value of all four Monte Carlo programs (2526). The Gaussian spread is clear, indicating that the method works with some statistical fluctuation. It is worth noting that the mean being slightly higher than expected (52.63±0.95nm as opposed to the true value of 52.5nm) while still being well within one standard deviation is typical, and implies that the calculated λ is slightly too high, possible due to a minor fault in the λ calculation method. This will be investigated later.

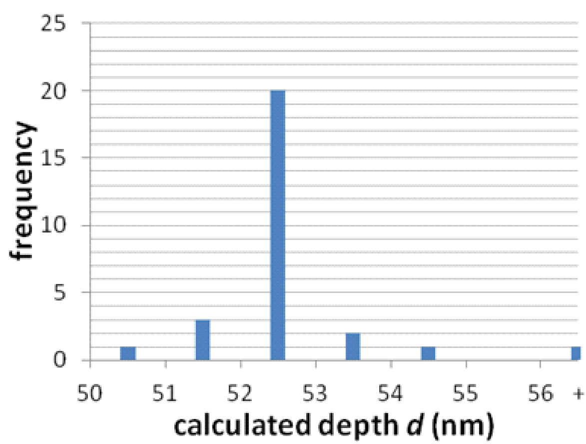

Figure 4.2.3: Histogram of simulated results from Error: Reference source not found using NISTMonte self-consistent λ = 2770nm value. Mean 52.63nm with a standard deviation of 0.95nm. Mean is 0.14 standard deviations away from true value of 52.5nm.

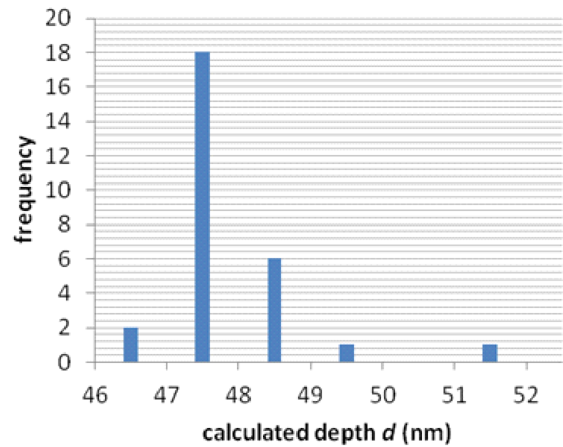

Figure 4.2.4: Histogram of simulated results using a λ = 2526nm value taken from the average of the four simulation programs. Mean 48.00nm with a standard deviation of 0.86nm.

Figure 4.2.5 is the equivalent simulation run in CASINO. The Gaussian spread is again visible, though even using either the average or the internally consistent λ value of 2525nm did not give the correct result. This is likely due to a function of the program's internal logic: re-running the simulation gave subtly different results. In this case, achieving d = 52.5nm would require a λ of 2312nm.

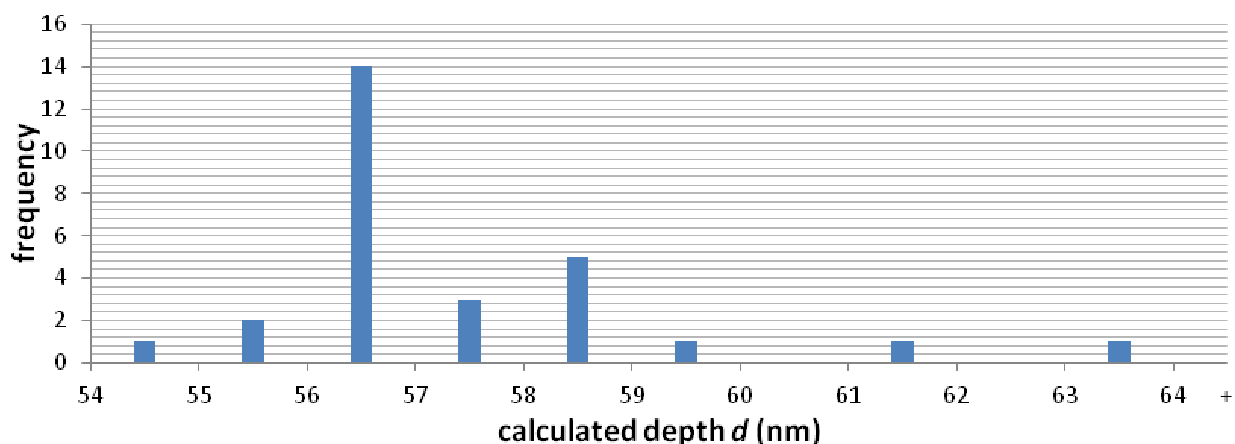

Figure 4.2.5: CASINO results for an equivalent simulation with λ = 2526nm. Mean is 57.34nm with a standard deviation of 1.83nm, 2.64 standard deviations from correct value.

Depth (nm)	Correct calculated depth, d (nm)	Average calculated d (nm)	Relative error ($d_{calculate} - d_{true}$) / standard deviation
10	12.5	12.5±0.8	0.1
30	32.5	32.7±0.3	0.6
50	52.5	52.6±1.0	0.1
70	72.5	72.7±0.6	0.3
90	92.5	92.7±1.1	0.2
110	112.5	112.7±0.8	0.2

Table 4.2.1: Average calculated depth in GaAs for various overlayer thicknesses. Error is standard deviation. Simulation run in NISTMonte at beam energy 197keV with 10^7 electron histories. Sample composition 5nm InAs (density = 6.51gcm^{-3}) at the bottom surface of the specified thickness of GaAs (density = 5.316gcm^{-3}). θ range of 15° to 50° inclusive in steps of 5°. λ = 2770nm

Table 4.2.1 shows the calculated depths for 5nm InAs embedded within a GaAs matrix at certain depths using NISTMonte's λ value for self-consistency. The trend for the calculated d to be slightly higher than the expected holds throughout, though there appears to be no discernible pattern in the magnitude of the error. Even for an overlayer thickness of 10nm (i.e. at depth 10nm) the method works despite the fact that the λ is much larger than this. This demonstrates that even very small changes in intensity can be used, provided there is sufficiently small statistical scatter. Of course, experimental results would not necessarily be accurate enough at this level, since it would require an exceptionally high signal to noise ratio.

4.3 Specimen Tilt Approach

4.3.1 Indium Simulations

As already mentioned, in transmission electron microscopes the take-off angle can be changed only by tilting the specimen. This causes a change in the interaction volume that must be accounted for. Figure 4.1.2.4.1 demonstrates the need for this in a GaAs matrix with 1nm of InAs buried 50nm deep. The 'Raw data' curve does not have any correction, while the 'Tilt-corrected' curve has only the tilt correction. It is obvious that not applying the tilt correction causes the resulting curve to differ tremendously from that expected from a change in take-off angle, due to the change in interaction volume. Specifically note the negative tilts, where the raw data is higher than it should be as a result of the tilt, despite the decrease in take-off angle.

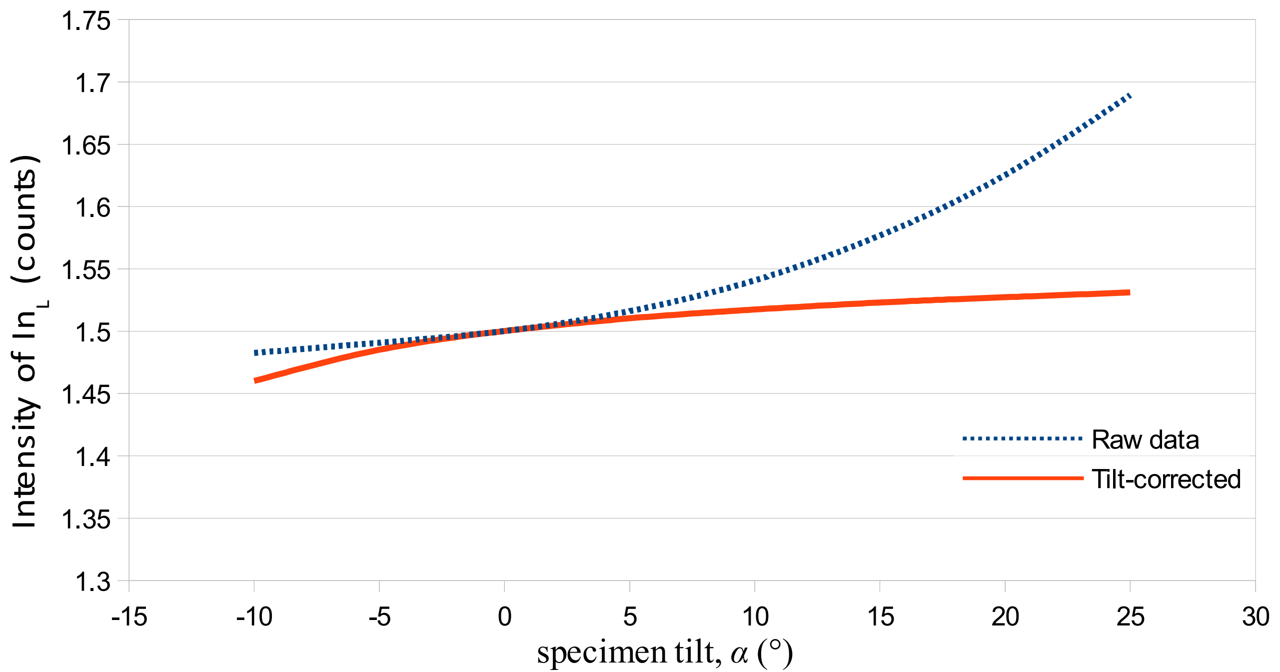

Figure 4.3.1.1: X-ray intensity vs. specimen silt for In_L in GaAs. Simulation run in NISTMonte at beam energy 197keV with 10^7 electron histories. $\theta = \alpha + 25°$. Sample is comprised of 1nm of InAs (density = 5.67gcm^{-3}) at the bottom surface of a 50nm thick GaAs (density = 5.316gm^{-3}) overlayer.

Figure 4.3.1.2 is a comparison between the 'Detector Tilt' model and the corrected 'Specimen Tilt', where both curves are normalised with respect to the +15° data point for ease of comparison. It is clear that the deviation between them increases with increasing take-off angle, more specifically that the deviation is numerically relevant even at +20° (i.e. -5° tilt), the first data point after the normalisation. This difference is most apparent in Table 4.3.1.1, specifically the 'Ratio' column, which contains the ratio of 'Specimen Tilt' over 'Detector Tilt'. In Figure 4.3.1.2, that ratio is also plotted against the vertical axis with the scale on the right.

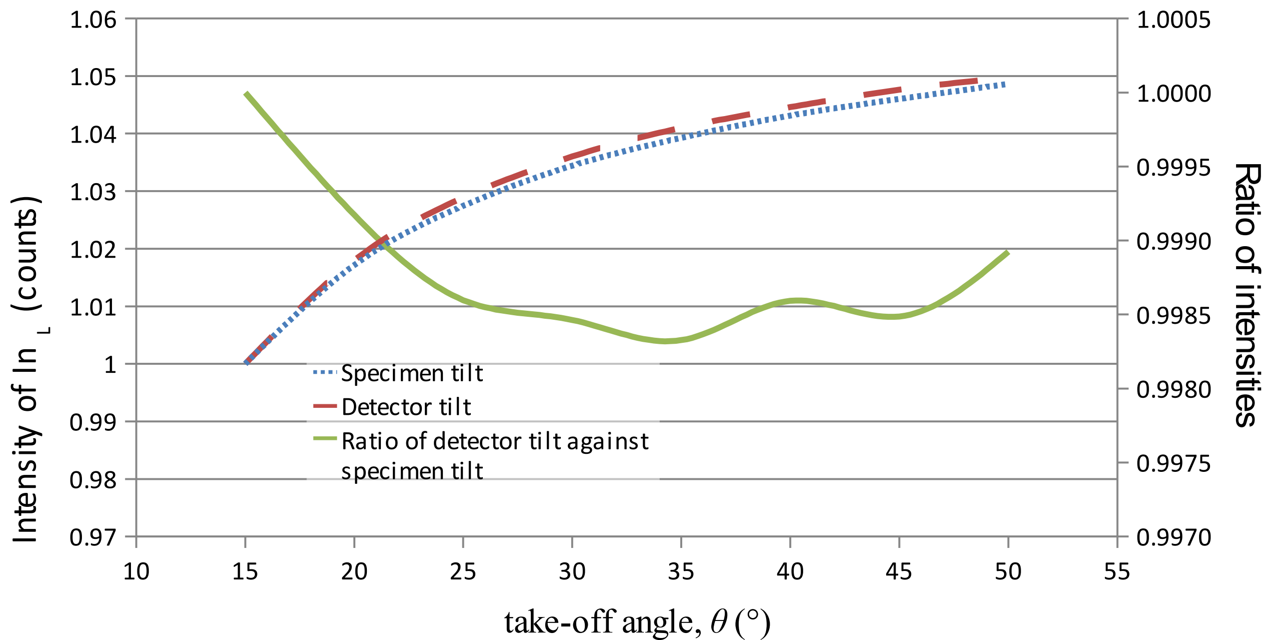

Figure 4.3.1.2: Simulated X-ray intensity vs. effective take-off angle for In_L in GaAs. The 'Ratio' curve is plotted against the vertical axis on the right. Simulation run in NISTMonte at beam energy 197keV with 10^7 electron histories. Effective $\theta = \alpha + 25°$. Sample is comprised of 1nm of InAs (density 5.67gcm^{-3}) at the bottom surface of a 50nm thick GaAs (density = 5.316gm^{-3}) overlayer.

θ [°]	Specimen tilt	Detector tilt	Ratio of specimen-over detector-tilt
15	1	1	1
20	1.017	1.018	0.999
25	1.027	1.029	0.999
30	1.034	1.036	0.998
35	1.039	1.041	0.998
40	1.043	1.045	0.999
45	1.046	1.048	0.998
50	1.049	1.050	0.999

Table 4.3.1.1: Numerical data from Figure 4.3.1.1.

Figure 4.3.1.3 is the same simulations as in Figure 4.3.1.1, extended to +65° tilt to show the effects of beam straggling. To the eye, it appears that the curve begins to significantly deviate at +55°, however the curve from +25° increases approximately linearly where it should converge at some value, indicating that there are differences even before the deviation is obvious. This implies that beam straggling due to 50nm GaAs begins to have a significant effect surprisingly early.

Figure 4.3.1.3 shows the consequence of increasing the beam energy by an order of magnitude. Here, the expected trend continues up to +65° without significant deviation, implying that beam straggling at this level has little to no effect. Unfortunately, as a 2MeV beam is beyond the reach of most electron microscopists this is not tremendously useful for many applications.

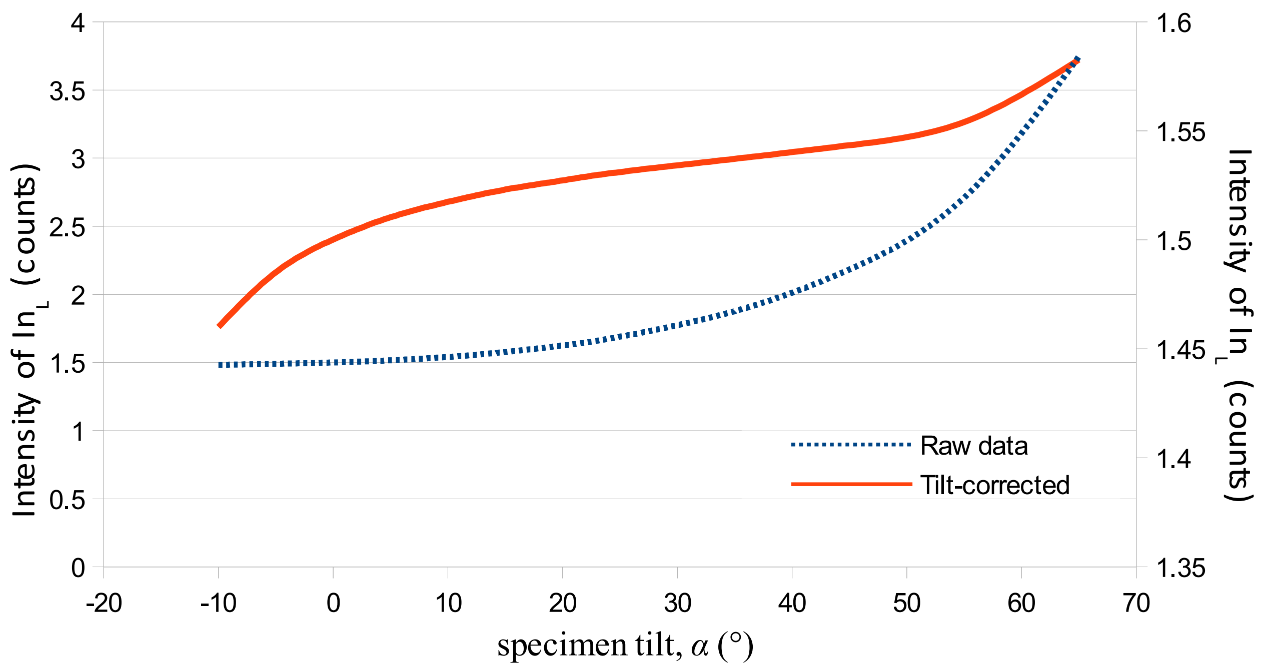

Figure 4.3.1.3: Simulation of X-ray intensity vs. Specimen Tilt for In_L in GaAs. Simulation run in NISTMonte at beam energy 197keV with 10^7 electron histories. $\theta = \alpha + 25°$. 'Raw data' is plotted against the vertical axis on the left, while 'Tilt-corrected' is against the vertical axis on the right. Sample is comprised of 1nm of InAs (density 5.67gcm^{-3}) at the bottom surface of a 50nm thick GaAs (density = 5.316gm^{-3}) overlayer.

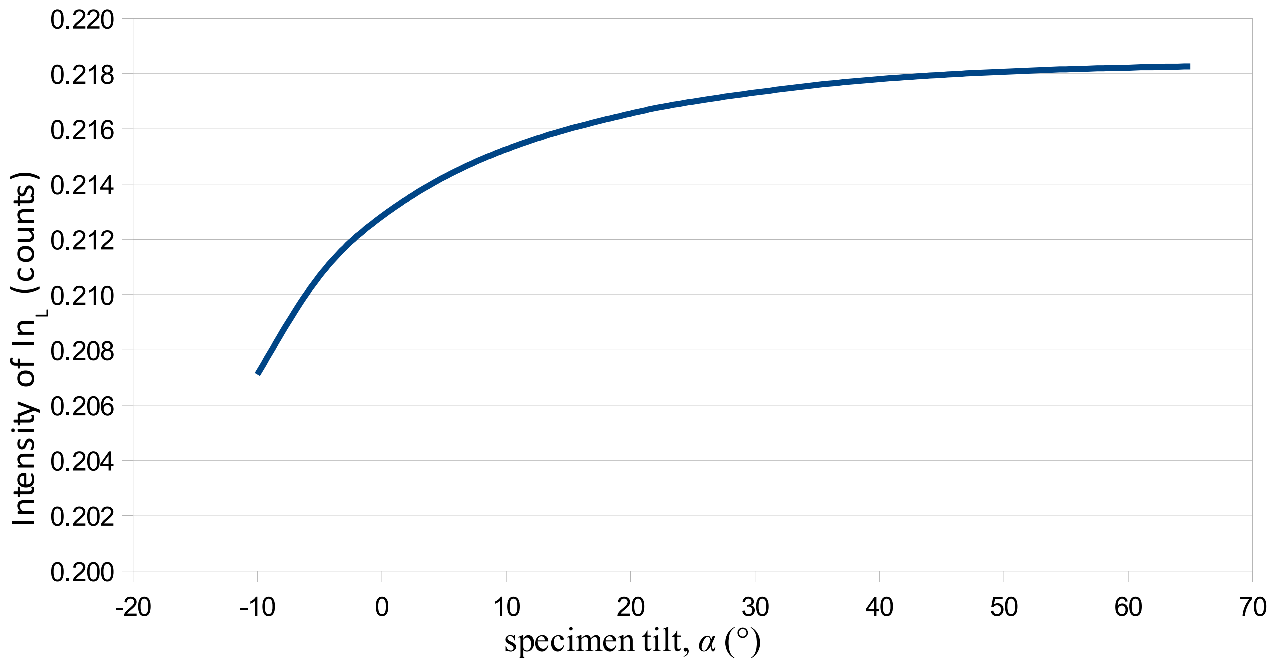

Figure 4.3.1.4: Simulation of X-ray intensity vs. Specimen Tilt for In_L in GaAs with a beam energy of 1970keV. Simulation run in NISTMonte for 10^7 electron histories. $\theta = \alpha + 25°$. Sample is comprised of 1nm of InAs (density 5.67gcm^{-3}) at the bottom surface of a 50nm thick GaAs (density = 5.316gm^{-3}) overlayer.

Figure 4.3.1.5 shows the calculated *d* values using the data in Figure 4.2.3 without tilt correction. It is obvious that these results are consistently incorrect, and more so with increasing tilt: note the

logarithmic vertical axis.

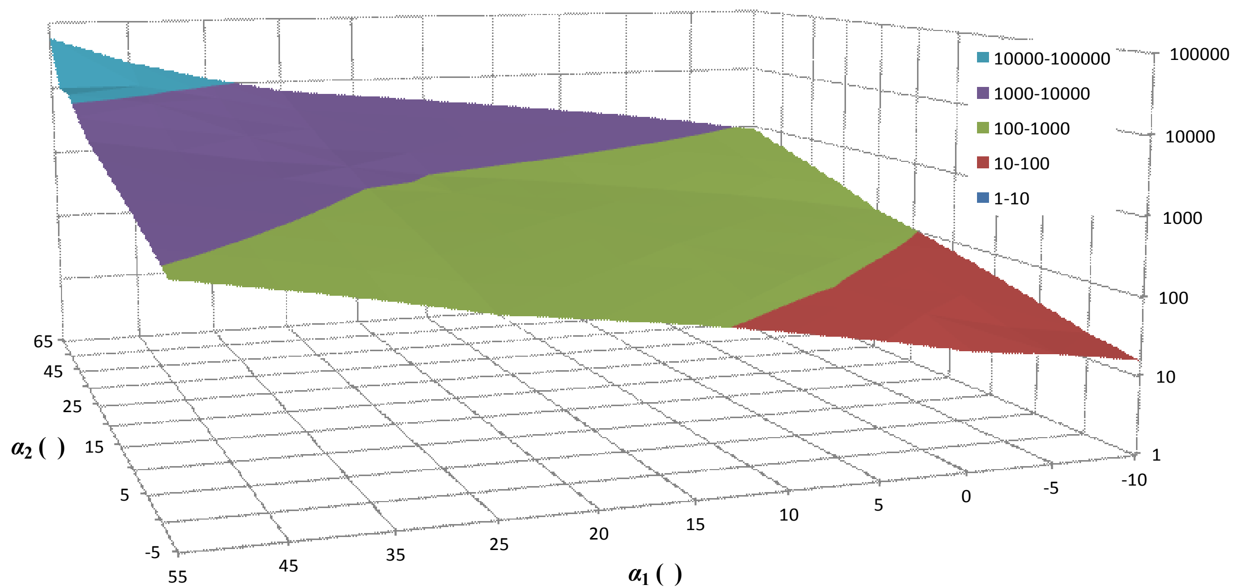

Figure 4.3.1.5: Calculated *d* (nm) results without applying geometric tilt correction, where the correct answer would be 50.5nm. Simulation run in NISTMonte at beam energy 197keV with 10^7 electron histories. $\theta_{eff} = \alpha + 25°$, where α is the specimen tilt towards the detector. Sample is comprised of 1nm of InAs (density 5.67gcm^{-3}) at the bottom surface of a 50nm thick GaAs (density = 5.316gm^{-3}) overlayer.

Figure 4.3.1.6 is again the data from Figure 4.2.3 but with tilt correction. The results here are far more consistent. Looking at the low tilt results (i.e. -10° to 10°) the results appear to be almost uniformly slightly lower than expected (in this case, 50.5nm) with only one which is significantly higher: this may be due to statistics. Moving into higher tilts, it is clear that using a low-tilt intensity in conjunction with a high-tilt intensity is better than two high-tilts. The significant deviation from the expected result in the 10°-15° value implies that beam straggling has an effect much sooner than expected, but that this effect is small enough to be almost negated by selecting using another data point which does not have significant beam straggling. Strictly, the point at which the results deviate too far would likely be +55°, however certain combinations before this give incorrect results. If the user is aware of this then those results that would be projected to be incorrect can, in principle, be ignored. Determining at which point beam straggling has an unacceptable effect is difficult, not least because said point is different for every system. This can be done crudely by simply being more willing to discount the higher tilt data points as outliers, however a more formal approach would require calculating how much more intensity was generated due to beam straggling (either through analytical calculation or Monte Carlo simulation) and then deciding how much of an effect on the data set is permissible.

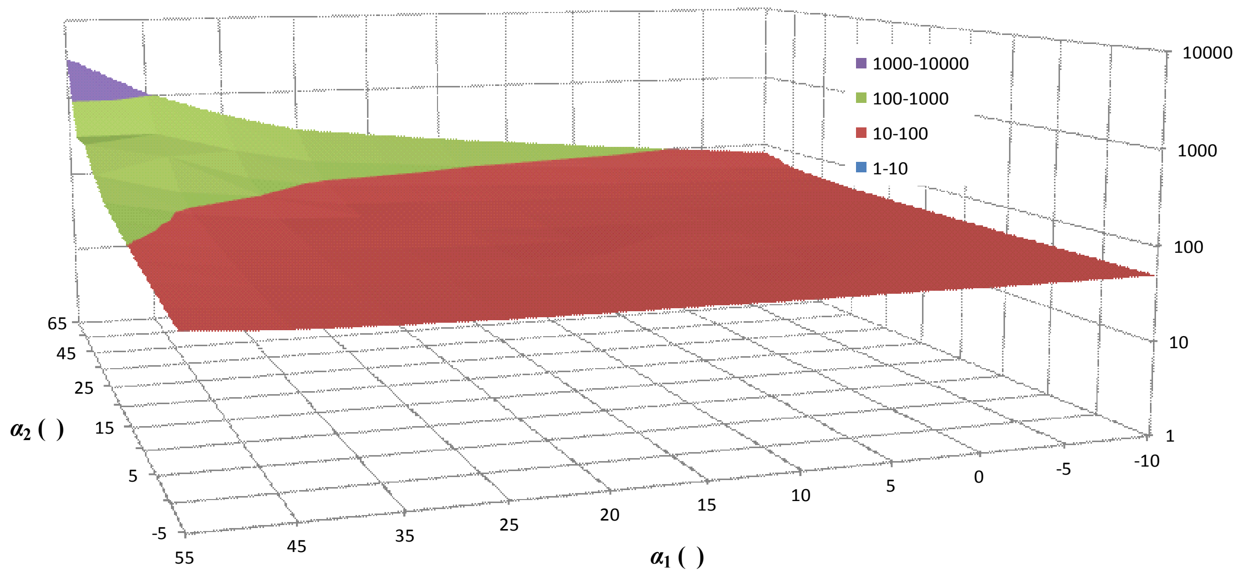

Figure 4.3.1.6: Calculated *d* (nm) results with applied tilt correction. Simulation run in NISTMonte at beam energy 197keV with 10^7 electron histories. $\theta = \alpha + 25°$, where α is the specimen tilt towards the detector. The correct answer is 50.5nm. Sample is comprised of 1nm of InAs (density 5.67gcm^{-3}) at the bottom surface of a 50nm thick GaAs (density = 5.316gm^{-3}) overlayer.

Figure 4.3.1.7 is the calculated *d* from Figure 4.3.1.3 for 1.97MeV. Here, the correct answers extend much further but still increasingly deviate at higher tilts. This implies that even a 2MeV beam is not enough to eliminate this effect in 50nm of GaAs. As a consequence, the user must be aware of this problem, regardless of beam energy.

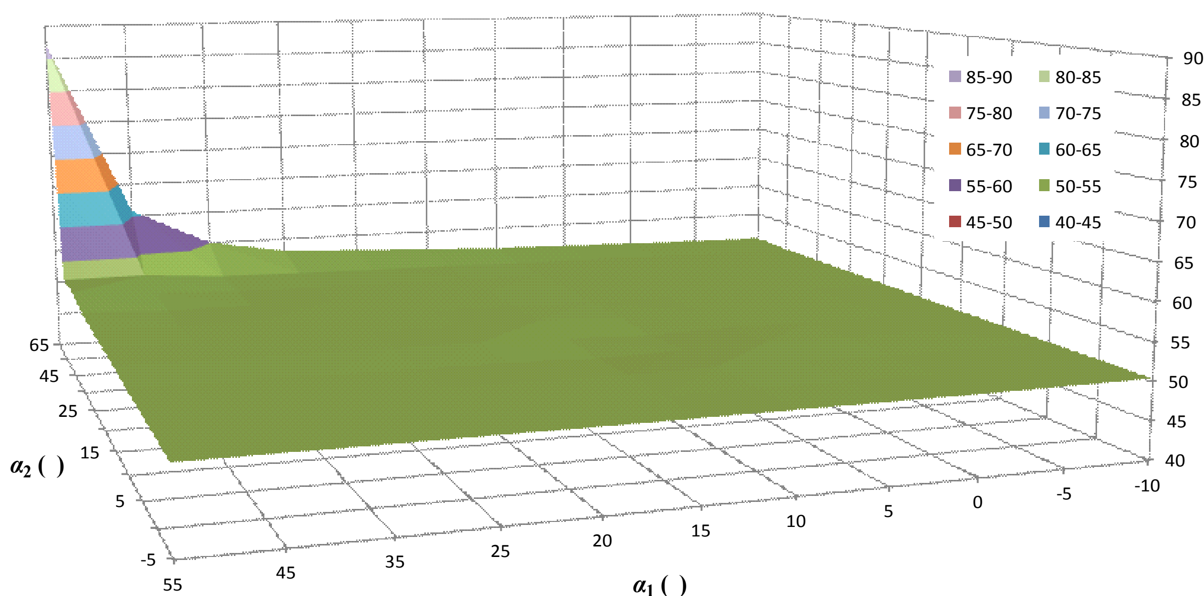

Figure 4.3.1.7: Calculated *d* (nm) results for 1970keV with tilt correction. Simulation run in NISTMonte at beam energy 1970keV with 10^7 electron histories. $\theta = \alpha + 25°$, where α is the specimen tilt towards the detector. The correct answer is 50.5nm. Sample is comprised of 1nm of InAs (density 5.67gcm^{-3}) at the bottom surface of a 50nm thick GaAs (density = 5.316gm^{-3}) overlayer.

Figure 4.3.1.4 summarises the results of Figure 4.3.1.6 in a histogram. In this context, the mean and the standard deviation are both too large to be accurate or useful, respectively. The notable

difference between this result and that of Figure 4.3.1.2 is that it is not Gaussian in nature: this difference exists due to the use of fairly high take-off angles introducing results that deviate increasingly from the correct answer. Without cherry-picking, it is difficult to justify rejecting many of the results based only on a-priori knowledge of the layer's depth (information which the user would obviously not possess in most experiments), however it is worth noting that with the exception of the '75+' channel the highest frequency lies in the '50 to 51' channel. This is very interesting, as it implies that simply calculating the mode of the reasonable results can give the correct answer, even if a straightforward averaging approach would not work.

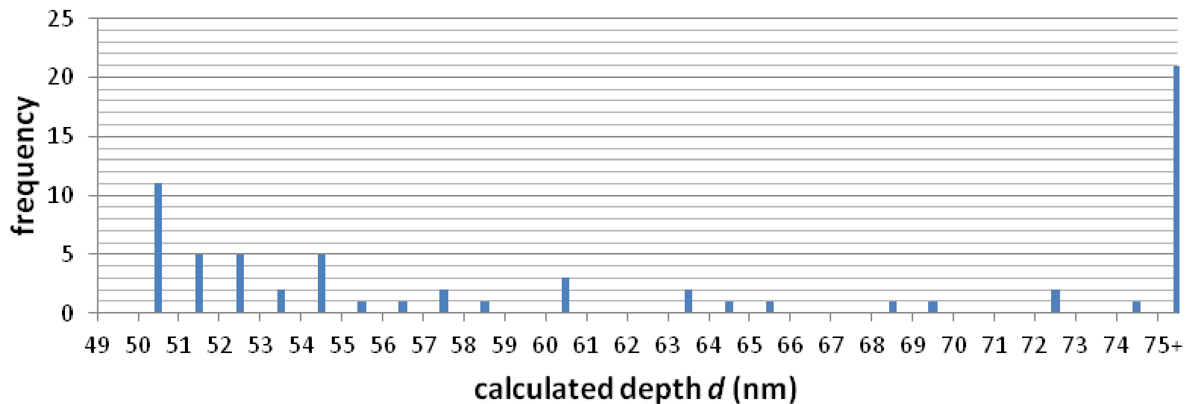

Figure 4.3.1.8: Histogram of Figure 4.3.1.6. The mean (discounting those obviously unreasonable, i.e. in the 75+ channel) is 56.36nm with a standard deviation of 6.93nm. Sample is comprised of 1nm of InAs (density 5.67gcm^{-3}) at the bottom surface of a 50nm thick GaAs (density = 5.316gm^{-3}) overlayer.

Figure 4.3.1.9 is the corresponding histogram of the results from Figure 4.3.1.7. In this case, the choice of channels causes a Gaussian curve that is skewed to the right where a simple average can work, if the user were to discount those values which are obviously incorrect . Again, however, the correct answer lies within the channel which has the highest frequency, and as such it is possible to avoid making an arbitrary choice as to which method to use.

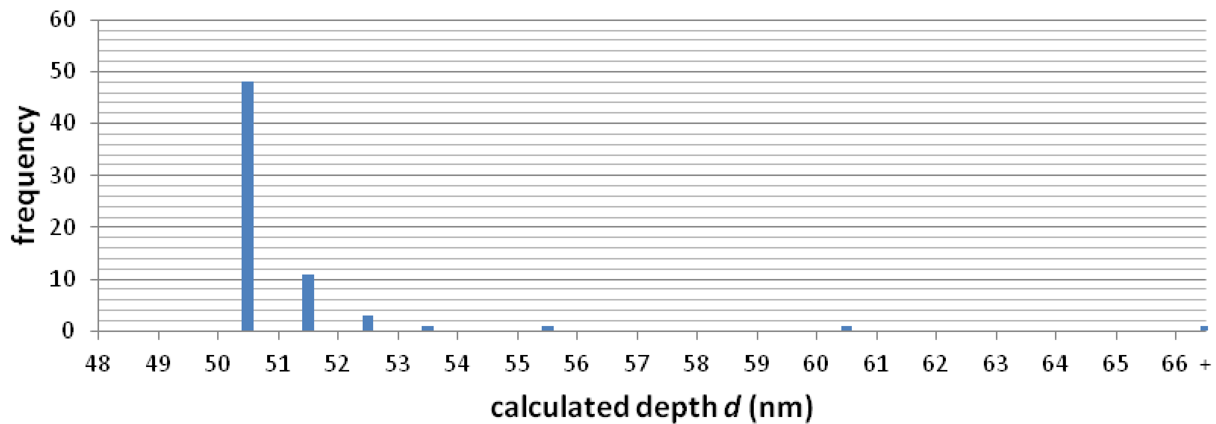

Figure 4.3.1.9: Histogram of Figure 4.3.1.7. The mean (discounting the two values greater than 56nm) is 50.88nm with a standard deviation of 0.76nm. Sample is comprised of 1nm of InAs (density 5.67gcm^{-3}) at the bottom surface of a 50nm thick GaAs (density = 5.316gm^{-3}) overlayer.

Table 4.3.1.2 shows the calculated *d* value for 1nm of InAs with various overlayer thicknesses of GaAs. for the 197keV data, there is considerable difference between results calculated including or excluding the +25° take-off angle data point, where +25° would be the most susceptible to beam straggling effects. This difference takes the form of a broadly consistent change in the calculated depth (approximately 1nm) and a significant increase in the standard deviation. This indicates that beam straggling has a small effect that is mainly independent of the overlayer thickness. This is obviously an interesting conclusion. This trend is not observed in the 2MeV case.

Overlayer thickness (nm)	Correct depth, *d* (nm)	Average calculated *d* (nm) including 25° value for 197keV	Average calculated *d* (nm) excluding 25° value for 197keV	Average calculated *d* (nm) excluding 25° value for 1.97MeV	Average calculated *d* (nm) including 25° value for 1.97MeV
10	10.5	10.8±0.6	11.3±1.4	10.43±0.13	10.47±0.18
30	30.5	32.0±1.5	32.4±1.7	30.5±0.6	30.5±0.6
50	50.5	51.5±1.4	53±3	50.44±0.13	50.49±0.16
70	70.5	71.6±1.5	73±3	70.41±0.09	70.41±0.08
90	90.5	91.7±1.7	93±3	90.4±0.3	90.4±0.3
110	110.5	112±2	113±3	110.31±0.11	110.5±0.5

Table 4.3.1.2: Average calculated depth in GaAs for various overlayer thicknesses with SpecTilt correction. Error is standard deviation. Conducted in NISTMonte for 10^7 electron histories and a θ range of -10° to +25° inclusive, in steps of 5°. Sample is comprised of 1nm of InAs (density 5.67gcm^{-3}) at the bottom surface of a GaAs (density = 5.316gm^{-3}) overlayer of the thickness listed in the first column.

4.3.2 Aluminium Simulations

Figure 4.3.2.1 shows equivalent results for Figure 4.3.1.1 using Al_K instead of In_L, where the InAs thin layer has been replaced with a pure aluminium thin layer and all other parameters kept constant. There is an obvious similarity between the two figures, though in Figure 4.3.2.1 the difference between the corrected and non-corrected for specimen tilt is significantly less pronounced.

The generated intensities of the InAs and pure Al layers are plotted in Figure 4.3.2.2. Here, we can see that while they are plotted against different scales (entirely expected, given their different fluorescence probabilities) there is very little difference in their forms. This indicates that the difference seen in the tilt-corrected data between the Al and In systems (Figure 4.3.2.1 and Figure 4.3.1.1, respectively) is due to differing absorption characteristics, and that the different fluorescence probabilities do not have any significant effect. It can be assumed that any X-ray under an appreciable amount of material would give a similar curve.

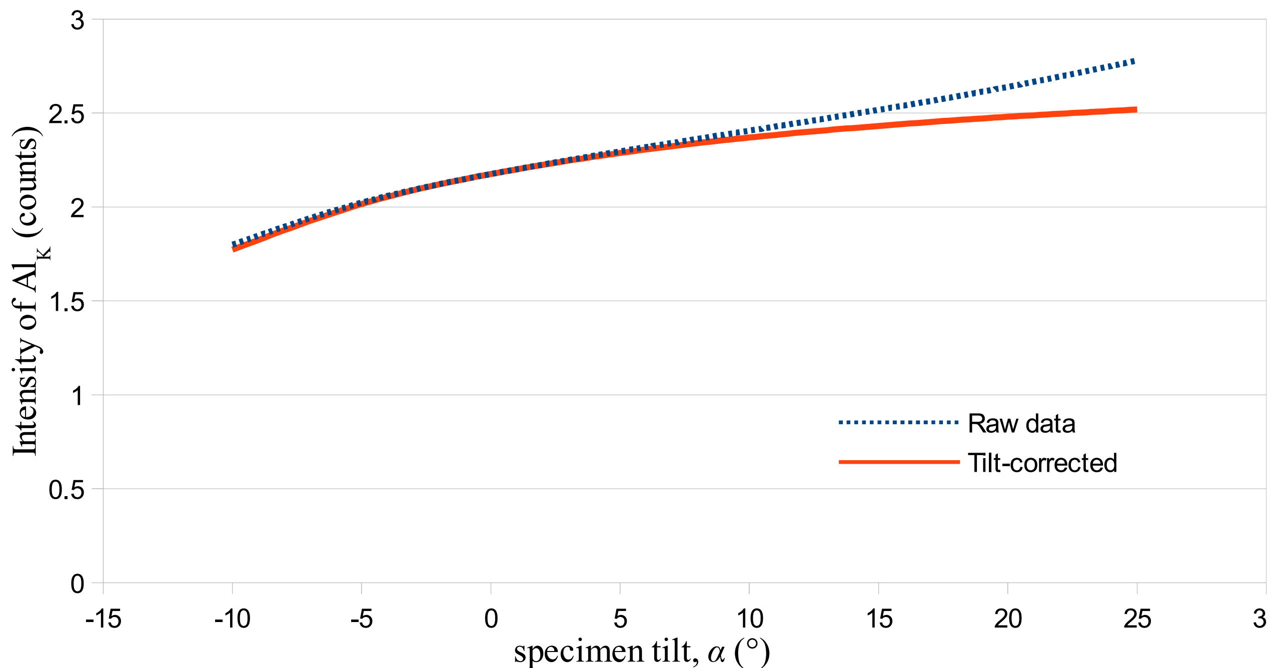

Figure 4.3.2.1: X-ray intensity vs. specimen tilt (α) for Al_K in GaAs. Correction applied is for specimen tilt. Simulation run in NISTMonte at beam energy 197keV with 10^7 electron histories. $\theta = \alpha + 25°$. Sample is comprised of 1nm of pure Al at the bottom surface of a 50nm thick GaAs (density = 5.316gm^{-3}) overlayer.

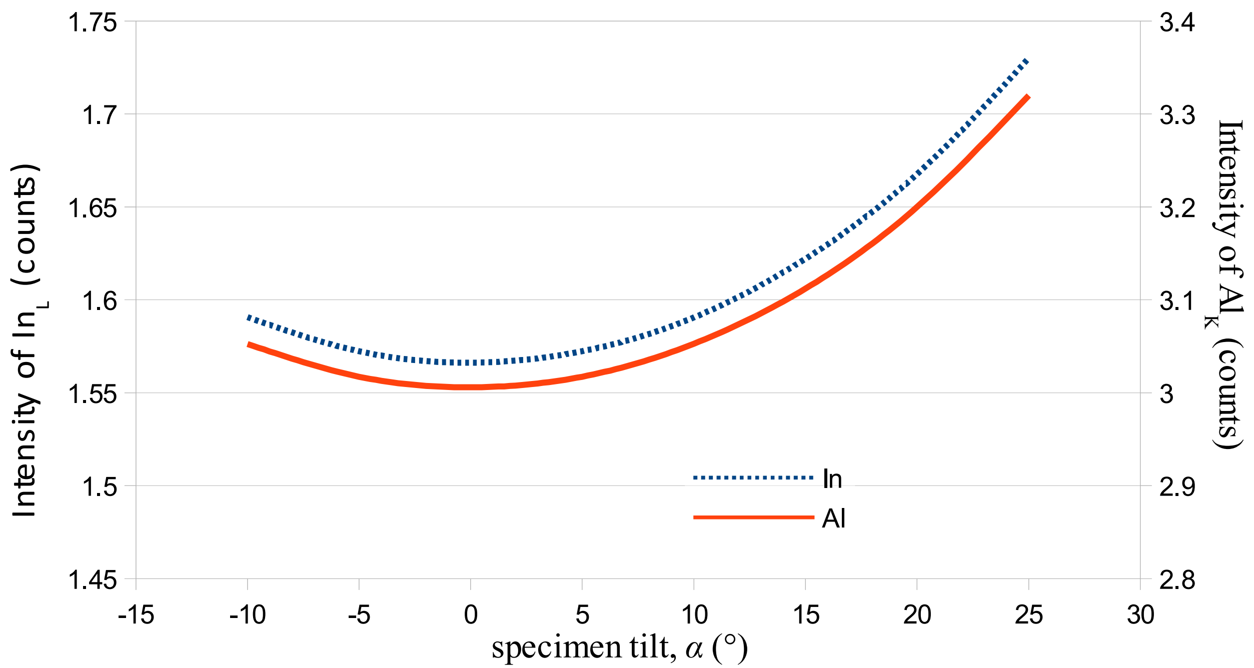

Figure 4.3.2.2: Comparison of generated (i.e. without absorption) X-ray intensities between In_L and Al_K in GaAs. Al_K is plotted against the vertical axis on the right. Simulation run in NISTMonte at beam energy 197keV with 10^7 electron histories. $\theta = \alpha + 25°$. Sample is comprised of 1nm of InAs (density 5.67gcm^{-3}) or 1nm of pure Al at the bottom surface of a 50nm thick GaAs (density = 5.316gm^{-3}) overlayer.

The calculated depths resulting from equation 4.1.1 is shown in Figure 4.3.2.3 using a λ value of 365nm. The majority of the results agree with the nominal values within error bars of <1nm. Interestingly, the effects of beam straggling do not appear until ~25° sample tilt, in contrast to ~15° for the InAs system seen in Figure 4.3.1.6, which could be due to the lower ionisation energy required for fluorescence of Al_K compared to In_L. This further indicates that a simple guideline would not function for reliably avoiding beam straggling, as it would differ in different materials.

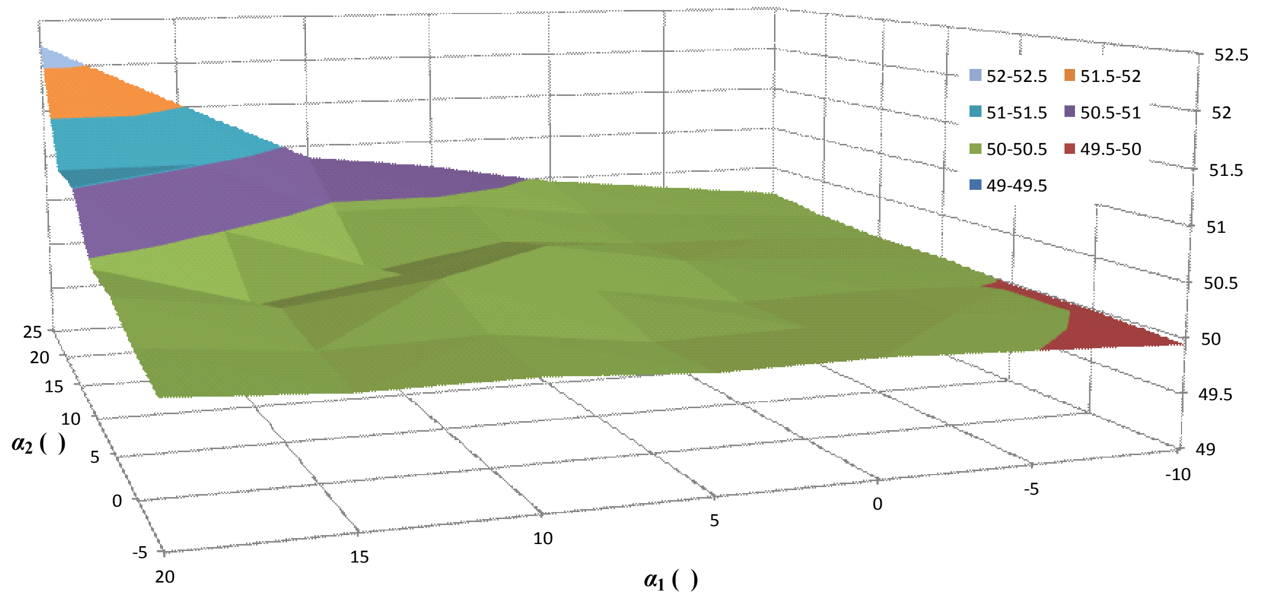

Figure 4.3.2.3: Calculated *d* (nm) results with applied tilt correction. Simulation run in NISTMonte at beam energy 197keV with 10^7 electron histories. θ = α +25°. The correct result would be 50.5nm. Sample is comprised of 1nm of pure Al at the bottom surface of a 50nm thick GaAs (density = 5.316gm^{-3}) overlayer. Mean is 50.35nm±0.52nm.

A comparison of average calculated *d* for different depths is given in Table 4.3.2.1, with the first column neglecting the +25° data point while the second includes it. This was done to test the effect of beam straggling. Unlike the In data shown in Table 4.3.1.2 the only difference between the two data sets is that the second column has a fractionally higher average depth and scatter. This is obviously different to the In system.

Overlayer thickness (nm)	Correct d (nm)	Excluding +25° data point	Including +25° data point
10	10.5	10.2±0.3	10.3±0.3
20	20.5	20.15±0.16	20.3±0.4
30	30.5	30.2±0.2	30.3±0.3
40	40.5	40.2±0.3	40.3±0.4
50	50.5	50.2±0.2	50.4±0.5
60	60.5	60.2±0.2	60.4±0.7
70	70.5	70.2±0.3	70.3±0.4
80	80.5	80.3±0.4	80.4±0.5
90	90.5	90.18±0.17	90.4±0.6
100	100.5	100.2±0.3	100.4±0.5
110	110.5	110.2±0.4	110.4±0.6
120	120.5	120.2±0.3	120.4±0.5

Table 4.3.2.1: Average calculated depth from Al_K in GaAs for various overlayer thicknesses. Error is standard deviation. Conducted in NISTMonte for 10^7 electron histories and a θ range of -10° to +25° inclusive, in steps of 5°. Sample is comprised of 1nm of pure Al at the bottom surface of a GaAs (density = $5.316gm^{-3}$) overlayer of the thickness listed in the first column.

4.4 Multiple thin layers within one matrix

One of the assumptions of this method is that there is only one thin layer with the specific element embedded within the matrix. If analysing an unknown sample, this assumption would not be justified, and as such it would be necessary to arrive at some manner of correction for these situations.

Figure 4.4.1 is a sketch of such a system, with the relevant variables marked.

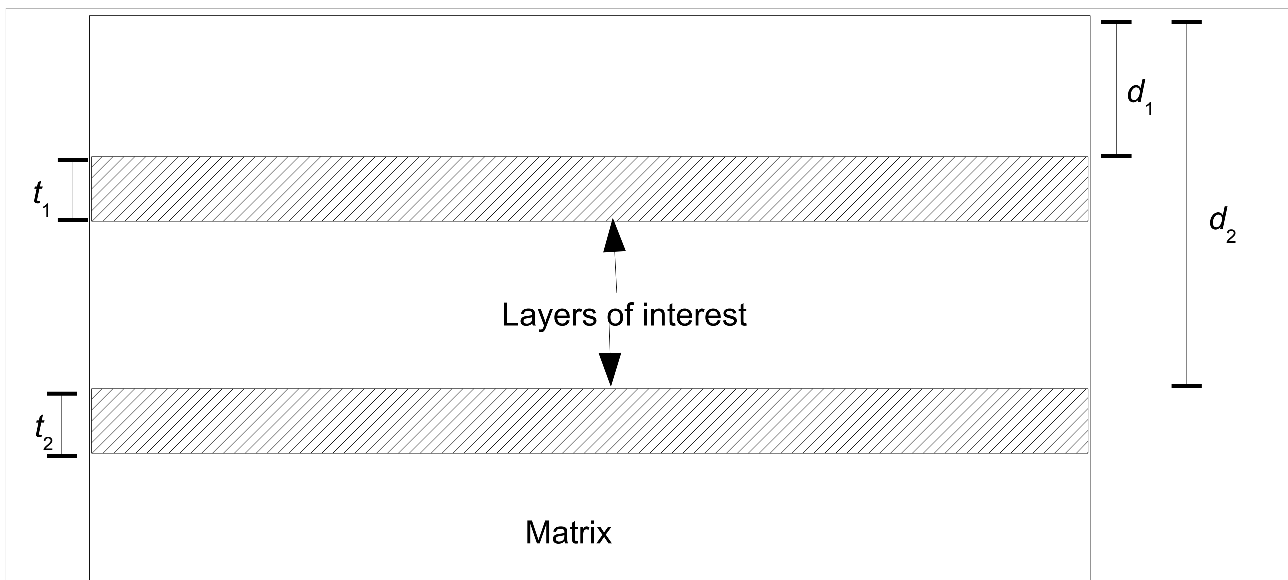

Figure 4.4.1: Sketch of multilayer system.

Table 4.4.1 shows the calculated depth from two pure indium layers embedded within a GaAs matrix using the 'Specimen Tilt' method. Comparing the t_1=1, d_1=0, d_2=120 and t_1=20, d_1=0, d_2=120 reveals that when the second layer is deeply buried, the first layer dominates, regardless of t_2. Looking at t_1=1, d_1=0, d_2=30 and t_1=20, d_1=0, d_2=30 shows that a shallower deeper layer has a much stronger effect on the calculated outcome, particularly for t_1=1 and t_2>5, as the increased counts caused by the thickness are not absorbed in the large depth as it was for d_2=120. Moving to t_1=1, d_1=30, d_2=120 and t_1=20, d_1=30, d_2=120, this trend is negated, with the change in t_2 having little to no effect. This is due to the fact that the first layer so strongly dominates the change in absorption. This contrasts with the d_1=0 results, which see very little absorption from the first layer which causes the change in absorption from the second layer to dominate. The t_1=1, d_1=100, d_2=180 and t_1=20, d_1=100, d_2=180 sets support this trend, as does the t_1=1, d_1=160, d_2=180 and t_1=20, d_1=160, d_2=180 sets.

It seems that the conclusion is this: if the two layers are separated by a certain amount of material then the thickness of the second layer is irrelevant, as the X-rays emitted from the first layer dominate the output. Beyond this, the calculated depth appears to be a weighted average that could, in principle, be used for more accurate total quantification even if it cannot be used to determine the exact depths of the two layers. This similarity is demonstrated in Figure 4.3.2.2, which compares the detected output from systems with multiple layers and those with only a single layer. The form of the curves is indistinguishable between the two systems.

t_1 = 1nm					
t_2 (nm)	d_1=0, d_2=120 (nm)	d_1=0, d_2=30 (nm)	d_1=30, d_2=120 (nm)	d_1=100, d_2=180 (nm)	d_1=160, d_2=180 (nm)
1	1.4±1.2	16.1±1.0	33±3	145±8	178±10
3	1.3±1.3	26±3	33±3	167±10	184±12
5	1.3±1.3	30±4	33±3	174±9	184±7
7	1.2±0.9	32±4	33±3	178±10	187±9
10	1.2±0.9	346±4	33±3	183±9	189±9
15	1.5±1.3	374±5	33±3	187±10	192±11
20	1.5±1.4	39±2	33±3	191±11	195±13

Table 4.4.1: Calculated depth from In_L from two layers of pure indium in GaAs (density = 5.316gcm^{-3}). Variables as specified in Figure 4.4.1. Simulation run in NISTMonte at beam energy 197keV with 10^6 electron histories. $\theta = \alpha$ +25°. 'Specimen tilt' method used, with tilts from -10° to +30° in steps of 10°.

t_1 = 20nm					
t_2 (nm)	d_1=0, d_2=120 (nm)	d_1=0, d_2=30 (nm)	d_1=30, d_2=120 (nm)	d_1=100, d_2=180 (nm)	d_1=160, d_2=180 (nm)
1	11±3	11.1±1.5	42±4	117±9	177±10
3	11±2	14±3	42±3	124±9	177±9
5	11±3	15±3	41±3	128±8	179±11
7	11±3	16±2	42±4	133±8	179±10
10	11±3	19±4	42±4	140±12	180±9
15	11±3	23±4	42±5	147±9	183±11
20	11±3	25±4	42±4	153±9	187±13
Continuation of Table 4.4.1					

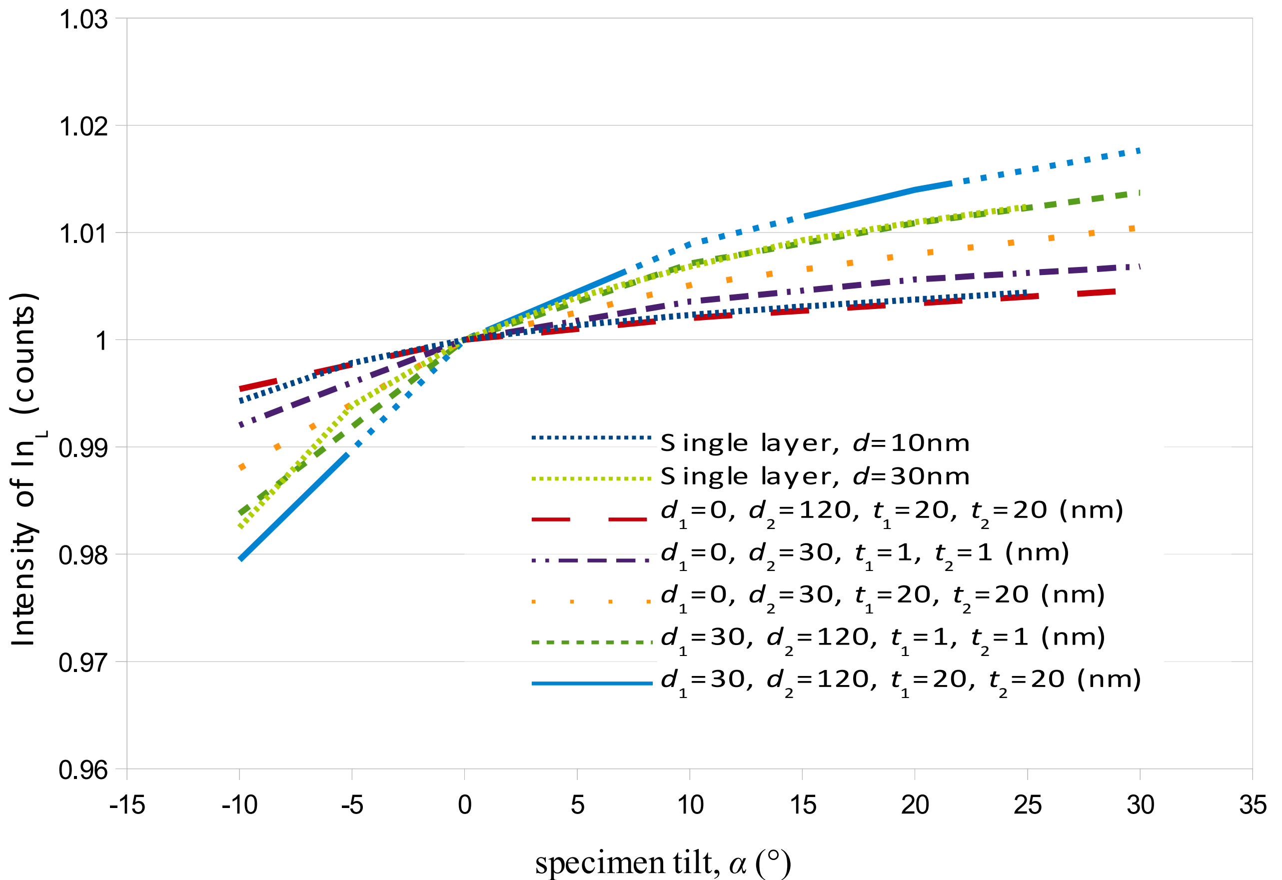

Figure 4.4.2: Comparison of calculated depth from In_L in GaAs of single layer and multiple layer systems. Variables as specified in Figure 4.4.1. Simulation run in NISTMonte at beam energy 197keV with 10^6 electron histories. $\theta = \alpha + 25°$. 'Specimen tilt' method used, with tilts from -10° to +30° in steps of 10°. Normalised against 0° tilt. Note that the 'Single layer, d=30nm' and 'd_1=30, d_2=120, t_1=1, t_2=1 (nm)' overlap to a significant extent.

Table 4.4.2 shows the results from running an identical set of simulations with 10^7 electron trajectories, an order of magnitude more than that of Table 4.4.1. Interestingly, there is no significant difference in either the calculated depths or the standard deviations. This implies that the statistical error is negligible compared to the systematic error introduced by having multiple layers.

t_2	d_1=100, d_2=180, t_1=1 (nm)	d_1=100, d_2=180, t_1=20 (nm)
1	145±8	118±8
3	167±10	124±8
5	174±10	129±9
7	179±11	133±8
10	183±10	139±9
15	188±10	147±10
20	191±11	154±10

Table 4.4.2: Equivalent of the relevant columns in Table 4.4.1 with 10^7 electron trajectories , to explore whether the error is systematic or statistical.

Table 4.4.3 is the aluminium equivalent of Table 4.4.1, in that it shows the calculated depths from different combinations of two layers of pure aluminium embedded within a GaAs matrix. The same broad patterns are visible, with the difference that the point at which changing the thickness of the second layer causes a significant change in the calculated depth is much smaller than for pure indium, which is presumably due to Al_K having significantly lower energy X-ray and hence higher probability of being absorbed.

	t_1 = 1nm				
t_2 (nm)	d_1=0, d_2=120 (nm)	d_1=0, d_2=30 (nm)	d_1=30, d_2=120 (nm)	d_1=100, d_2=180 (nm)	d_1=160, d_2=180 (nm)
1	41±6	13.7±0.8	64±4	132±4	170.0±1.8
3	72±6	21.3±0.8	88±4	152±3	174.7±1.4
5	86±6	23.9±0.7	97±3	161±3	176.3±1.2
7	93±5	25.3±0.6	102±3	165±2	177.2±0.9
10	100±4	26.5±0.7	107±3	169±2	178.0±1.4
15	106±3	27.6±0.6	111±2	172±2	178.7±1.2
20	109±3	28.1±0.6	113.0±1.9	174.2±1.7	179.2±1.4

Table 4.4.3: Calculated depth from Al_K for two layers of pure aluminium in GaAs (density = 5.316gcm^{-3}). Simulation run in NISTMonte at beam energy 197keV with 10^6 electron histories. $\theta = \alpha +25°$. 'Specimen tilt' method used, with tilts from -10° to +30° in steps of 10°.

t_1 = 20nm					
t_2 (nm)	d_1=0, d_2=120 (nm)	d_1=0, d_2=30 (nm)	d_1=30, d_2=120 (nm)	d_1=100, d_2=180 (nm)	d_1=160, d_2=180 (nm)
1	3.4±0.8	1.1±0.4	33.1±0.8	103.0±1.1	161.0±0.9
3	8.5±1.4	1.9±0.3	37.2±1.2	106.9±1.6	160.9±1.0
5	13±2	2.6±0.5	40.9±1.6	110.1±1.9	161.2±1.1
7	17±3	3.2±0.3	44.2±1.8	113.1±1.9	161.1±1.3
10	23±3	4.0±0.4	48±2	117±2	161.2±1.1
15	31±4	5.0±0.4	54±2	121.8±2.0	161.3±1.1
20	37±4	5.9±0.4	59±3	1269±2	161.3±1.0

Continuation of Table 4.4.3

Table 4.4.4 shows the results for a three layer In system, where the notation is logically extended from the two layer method. Introducing a third layer does not break the pattern, in that the calculated depth is a weighted average of the multiple layers, with changing the thickness of the third layer only causing a statistically significant change in the calculated depth when the third layer is either sufficiently thin or sufficiently deep so as to be negligible compared to the first and/or second layer(s). This can be readily seen by comparing the 'd_1=10, d_2=50, d_3=90, t_1=1, t_2=1 (nm)' to 'd_1=10, d_2=50, d_3=90, t_1=20, t_2=1 (nm)' results, where increasing the thickness of the first layer causes a change in the thickness of the third layer to have an effect on the calculated depth. This pattern is not visible for the 'd_1=10, d_2=50, d_3=90, t_1=20, t_2=20 (nm)' results, as the increased thickness of the second layer has a much stronger effect than the thickness of the third layer and hence the effect of change in the third layer becomes negligible compared to the statistical variation. Similar trends are seen in other simulations with different values for the depths and thicknesses (not shown here). Given that the same trend is visible in a system with either two or three layers, it is reasonable to assume that a similar comparison to a single layer is valid, and that this trend likely continues to systems with more than three layers.

	d_1=10, d_2=50, d_3=90 (nm)								
	t_1=1 (nm)			t_1=10 (nm)			t_1=20 (nm)		
t_3 (nm)	t_2=1nm	t_2=10nm	t_2=20nm	t_2=1nm	t_2=10nm	t_2=20nm	t_2=1nm	t_2=10nm	t_2=20nm
1	32±3	52±6	59±7	26±5	41±10	52±12	25.3±1.9	32.5±2.0	41±4
3	31±3	53±4	60±5	36±4	47±8	50±8	32±9	36±4	48±10
5	33±5	52±7	60±3	42±2	47±5	53±8	39±10	42±6	51±15
7	31±4	53±4	62±10	49±8	52±8	55±5	43±9	45±7	48±5
10	33±5	51±3	59±8	55±5	55±4	57±3	47±10	49±7	52±11
15	29±3	50±3	61±6	65±4	61±6	62±6	53±6	54±5	56±10
20	33±4	51±5	61±7	71±6	69±9	69±8	58±4	58±7	58±5

Table 4.4.4: Calculated depth from In_L from three layers of pure indium in GaAs (density = 5.316gcm^{-3}). Variables as specified in Figure 4.4.1. Simulation run in NISTMonte at beam energy 197keV with 10^6 electron histories. $\theta = \alpha$ +25°. 'Specimen tilt' method used, with tilts from -10° to +30° in steps of 10°.

	d_1=10, d_2=50, d_3=150 (nm)								
	t_1=1 (nm)			t_1=10 (nm)			t_1=20 (nm)		
t_3	t_2=1nm	t_2=10nm	t_2=20nm	t_2=1nm	t_2=10nm	t_2=20nm	t_2=1nm	t_2=10nm	t_2=20nm

(nm)									
1	31±3	53±6	59±5	21±5	36±6	45±3	23±2	30.1±1.7	40±3
3	34±3	53±3	64±13	17±6	34.9±1.4	47±6	24±6	32±7	40±4
5	33±4	56±6	61.3±10.0	19±3	36.6±5.2	46±4	22±4	35.1±10.0	42±7
7	34±10	50±4	60±7	17.8±1.2	40±12	47±4	19±4	31±8	41±4
10	35±6	50.6±1.0	61±10	19±4	34±5	46±4	24±4	34±4	40±7
15	34±9	53±7	60±8	20±6	35±4	48±10	22.6±1.6	33±9	40±5
20	32±1.7	54±7	57.4±0.7	21±6	35±4	51±11	23±3	34±10	42±8

Table 4.4.4 Continued.

4.5 Calculation of λ for use in equation 4.1.1

4.5.1 Comparison of different methods for calculating *λ*

As described in section 4.1, the variable λ, the attenuation wavelength, defines the thickness of material that would reduce the intensity of the relevant X-ray line to 1/e of it's original value. The value calculated by equation 4.1.1 is heavily dependent on λ being correct, and as such this section describes the difficulties associated with its calculation. Previously, this has been taken as given, but as seen in this section its calculation is non-trivial. As a reminder, if the natural log of the intensity ratio is plotted against the effective thickness (i.e. D/sinθ) then λ would be the slope of that curve. This slope is linear and can be accurately fitted with linear least squares regression, as given by the following equations:

$$y=mx+b \qquad Slope=m=\frac{N\cdot\sum_{i=0}^{i=n}(x_i y_i)-\sum_{i=0}^{i=n}x_i\cdot\sum_{i=0}^{i=n}y_i}{N\cdot\sum_{i=0}^{i=n}x_i^2-\left(\sum_{i=0}^{i=n}x_i\right)^2} \qquad Intercept=b=\frac{\sum_{i=0}^{i=n}y_i-m\cdot\sum_{i=0}^{i=n}x_i}{N}$$

where N is the total number of data points and x_i,y_i are the *i*th value of that axis.

Any method for changing the effective depth while holding all other parameters constant would work to determine the characteristic X-ray absorption length, λ. This gives the user two options: the 'Depth Variation' method or the 'Take-off Angle Variation' method.

The 'Depth Variation' method uses a series of samples with thin layers embedded within the matrix material where the part of the composition that changes is the overlayer thickness, ideally distributed over a range of thickness. The difficulty with this is obvious: manufacturing a single sample with a thin layer at a very well known depth is costly, manufacturing many would take tremendous resources. Given that knowledge of the depth is most reliably acquired through creation of a cross-section sample this would require two samples for each data point. This is obviously undesirable from a practical standpoint.

The other method, 'Take-off Angle Variation', instead relies on changing the take-off angle. This causes a change in the effective depth and hence results in the required curve. This method would require only two samples: a cross-section to determine the depth of the thin layer and another to carry out the analysis on. As previously mentioned, most microscopes cannot change the take-off angle by moving the detector and must instead rely on tilting the sample to achieve the same effect. This means that this method suffers from the same difficulties as the 'Specimen Tilt' approach

described in section 4.3. While the increase in interaction volume can be readily corrected, the result of beam straggling is somewhat more difficult. In simulations, this can be accounted for by dividing the detected intensity by the generated intensity, which has the dual function of removing the effect of beam straggling and statistical fluctuations in the generated intensity, leaving the change in the effective take-off angle the only variable. While this is obviously impossible in experiment it does serve to give a self-consistent estimate of the experimental result, which in theory are proportional to the experimental by some consistent factor given by the electron dose, as any simulation is likely to differ from experiment in parameters such as detector efficiency (perfect in simulations, not in experiment) or fluorescence probabilities.

Table 4.5.1.1 is the calculated λ values for In_L in GaAs using the 'Depth Variation' method. The result with and without correcting for beam straggling is shown. The various depths were chosen to correspond to effective take-off angles (as defined by $D/\sin\theta$), for later direct comparison to the 'Take-off Angle Variation' method. The non-corrected result has higher error and R^2, as expected, but it also has significantly higher λ, which is quite surprising. Comparing this result to that obtained by only considering either the shallowest six or shallowest three data points gives the expected result, as trending toward the corrected value is to be expected when discounting those data points which experience the effect of straggling most strongly. The increase in the error is to be expected, given that analysing fewer data points increases the proportional effect of statistical fluctuations.

Previously, 'beam straggling' has been taken to mean as a result of tilting the sample. However, straggling would occur in any occasion where the amount of material that the beam travels through changes between data points. While fairly slight, this would have an effect if the thin layer is made deeper in order to calculate λ as in Table 4.5.1.1, which would lead to the change in calculated λ seen for the non-corrected results. The change in the corrected value as fewer data points are used is interesting. The fact that the result calculated from using only the three shallowest data points has slightly higher R^2 than that from the full range and comparable error while the result from six data points has higher error and worse R^2 could be due to chance.

effective take-off angle (°)	actual depth (nm)		from all 8 depths	from 25° to 50°	from 40° to 50°
15	42.42574		without correcting for beam straggling		
20	45.96194	λ (nm)	3027	3000	2800
25	50.56102	$\Delta\lambda$ (nm)	10	30	40
30	56.66202	R^2	0.9999	0.9996	0.9998
35	65		corrected for beam straggling		
40	76.90155	λ (nm)	2768.5	2725	2750.2
45	95.02364	$\Delta\lambda$ (nm)	1.1	3	1.1
50	125.5704	R^2	1.0000	1.0000	1.0000

Table 4.5.1.1: Results of λ calculation using the 'Depth Variation' method. Simulation run in NISTMonte at beam energy 197keV with 10^7 electron histories at constant take-off angle of 90°. Sample is comprised of 5nm of InAs (density = 5.67gcm^{-3}) at the bottom surface of a GaAs (density = 5.316gm^{-3}) overlayer of a thickness given in the second column.

Table 4.5.1.2 is the equivalent of Table 4.5.1.1 run with a beam energy of 1970keV to reduce the effect of beam straggling. Here, the error is small and the R^2 value is high, for both corrected and non-corrected results, though the corrected results are fractionally better, as expected. Reducing the

number of data points used causes an increase in the error and worsening of the R^2, though the non-corrected three data point result appears to experience the same exceptionally high R^2 value as Table 4.5.1.1's corrected three data point result. Given that the λ calculated from the corrected full range has slightly worse R^2 than that of the non-corrected three data point result, it is clear that R^2 alone cannot be used as the only criterion. As the default position, however, it is logical to use the result gained from applying the relevant correction and considering the full range of data available to be the correct choice. The fact that this result roughly agrees with the equivalent for 197keV is also encouraging.

effective take-off angle (º)	actual depth (nm)		from all 8 depths	from 25° to 50°	from 40° to 50°
15	42.42574		non-corrected for beam straggling		
20	45.96194	λ (nm)	2774.0	2775	2783.9
25	50.56102	$\Delta\lambda$ (nm)	0.9	3	1.6
30	56.66202	R^2	1.0000	1.0000	1.0000
35	65		corrected for beam straggling		
40	76.90155	λ (nm)	2771.6	2731	2715
45	95.02364	$\Delta\lambda$ (nm)	0.8	3	17
50	125.5704	R^2	1.0000	1.0000	1.0000

Table 4.5.1.2: Results of λ calculation using the 'Depth Variation' method with 1970keV beam energy. Simulation run in NISTMonte at beam energy 197keV with 10^7 electron histories at constant take-off angle of 90°. Sample is comprised of 5nm of InAs (density = 5.67gcm^{-3}) at the bottom surface of a GaAs (density = 5.316gm^{-3}) overlayer of a thickness given in the second column.

The results of an equivalent simulation conducted using the 'Detector Tilt' model are shown in Table 4.5.1.3. Take-off angles where chosen to allow direct comparison to Table 4.5.1.1 and Table 4.5.1.2, with parameters of the sample being held constant. While there is no beam straggling, the straggling correction also functions to remove some part of the statistical fluctuations, as already mentioned, and as such is also carried out here. The results from the use of fewer data points for comparison retains the trend of increasing error and worsening R^2. Most interestingly, the calculated λ is significantly different when compared to the assumed correct value seen in Table 4.5.1.2's corrected full range result. Further, normalising with respect to generated intensity causes the result to deviate further rather than converge. This is discussed in Table 4.5.1.4

take-off angle (°)	effective depth (nm)		from all 8 depths	from 25° to 50°	from 40° to 50°
15	42.42574		non-corrected for beam straggling		
20	45.96194	λ (nm)	2785	2750	2900
25	50.56102	$\Delta\lambda$ (nm)	11	3	130
30	56.66202	R^2	0.9999	0.9997	0.9979
35	65		corrected for beam straggling		
40	76.90155	λ (nm)	2798.3	2798	2779
45	95.02364	$\Delta\lambda$ (nm)	0.8	2	6
50	125.5704	R^2	1.0000	1.0000	1.0000

Table 4.5.1.3: Results of λ calculation using the 'Detector Tilt' method. Simulation run in NISTMonte at beam energy 197keV with 10^7 electron histories. Sample is comprised of 5nm of InAs (density = 5.67gcm^{-3}) at the bottom surface of a 30nm GaAs (density = 5.316gm^{-3}) overlayer. θ is given in the first column.

Table 4.5.1.4 shows the results from the same simulation run three times. In this case, the full range of data points was used and no correction was applied. The variation between the results is not significant, as they lie within less than two standard deviations from each other. The corrected full range value of the first iteration, seen in Table 4.5.1.3, lies at the approximate average of all three values. Considering this average and the degree of scatter, this implies that the effect of beam straggling is significant enough that it must be considered. Indeed, it could be proposed that calculation of λ via the 'Detector Tilt' method is superior to the 'Depth Variation' methods, as it more closely resembles typical experimental conditions.

	iteration 1	iteration 2	iteration 3		
λ	2785	2803	2793	Mean λ	2794
$\Delta\lambda$	11	8	8	Standard error	6
R^2	0.9999	0.9999	1.0000		

Table 4.5.1.4: Results of λ calculations using the 'Detector Tilt' method. Simulation run in NISTMonte at beam energy 197keV with 10^7 electron histories.Sample is comprised of 5nm of InAs (density = 5.67gcm^{-3}) at the bottom surface of a 30nm GaAs (density = 5.316gm^{-3}) overlayer. θ varies from 15° to 50° in steps of 5°.

Table 4.5.1.5 is the same simulation run with 1970keV. The result is significantly different from the non-corrected 197keV results, however it is extremely close to the corrected 197keV result, and remains so whether it is corrected or not. This could be due to the fact that the beam experiences only little straggling whether the amount of material changes thickness or not. The effect of this straggling would be to cause a Gaussian distribution in the energy range of the beam electrons. As a result of this, the size of the absorption cross-sections (and therefore the fluorescence probabilities) would have an additional factor increasing the statistical fluctuations. This effect would be far more significant with a beam energy of 197keV than 1970keV, as the higher energy electrons would interact less and as such would not lose energy so quickly.

take-off angle (º)	effective depth (nm)		from all 8 depths	from 25° to 50°	from 40° to 50°
15	42.42574		non-corrected for beam straggling		
20	45.96194	λ (nm)	2798.1	2800	2781
25	50.56102	$\Delta\lambda$ (nm)	1.4	4	11
30	56.66202	R^2	1.0000	1.0000	1.0000
35	65		corrected for beam straggling		
40	76.90155	λ (nm)	2798.3	2795	2783
45	95.02364	$\Delta\lambda$ (nm)	0.9	3	18
50	125.5704	R^2	1.0000	1.0000	1.0000

Table 4.5.1.5: Results of λ calculation using the 'Detector Tilt' method and beam energy 1970keV. Simulation run in NISTMonte with 10^7 electron histories. Sample is comprised of 5nm of InAs (density = 5.67gcm^{-3}) at the bottom surface of a 30nm GaAs (density = 5.316gm^{-3}) overlayer. θ is given in the first column.

Table 4.5.1.6 is the 'Specimen Tilt' equivalent of the previous simulation. In this case, correction for specimen tilt and for beam straggling are handled separately. It is worth noting that correcting for straggling also corrects for tilt, and as such there is no need to apply both. In this case the sets of results are for -10° to +25° (limited tilt range) and -10° to +65° (wider tilt range). A direct comparison between the Limited Tilt-Corrected results and the full range non-corrected results from Table 4.5.1.3 indicates roughly similar errors and R^2, while the calculated λ values are somewhat different. Correcting for straggling brings λ closer to the values calculated previously.

Considering the total range of data points causes the tilt-corrected results to be very different, with a large error and low R^2. However, the full range while correcting for straggling gives results much closer to the expected. This upholds what was seen previously about how beam straggling has an effect with significant sample tilt.

specimen tilt (º)	effective thickness (nm)
-10	125.5704
-5	95.02364
0	76.90155
5	65
10	56.66202
15	50.56102
20	45.96194
25	42.42574
35	37.52777
45	34.58578
55	33.00136
65	32.5

	limited, tilt range (-10° to+25°)	
	tilt-Corrected	straggling-Corrected
λ	2773	2795.06
$\Delta\lambda$	14	0.14
R^2	0.9998	1.0000

	total, tilt range (-10° to+65°)	
	tilt-Corrected	straggling-Corrected
λ	2230	2794.61
$\Delta\lambda$	200	0.3
R^2	0.9279	1.0000

Table 4.5.1.6: Results of λ calculation using the 'Specimen Tilt' method. Simulation run in NISTMonte at beam energy 197keV with 10^7 electron histories. $\theta = \alpha + 25°$. Sample is comprised of 5nm of InAs (density = 5.67gcm^{-3}) at the bottom surface of a 30nm GaAs (density = 5.316gm^{-3}) overlayer. α is given in the first column.

The 1970keV beam energy equivalent to the results of Table 4.5.1.6 are shown in Table 4.5.1.7. It is clear that the 'Limited Tilt-Corrected' results are much superior to that seen in Table 4.5.1.6, most obviously in that the error is lower and the R^2 higher, but also in that the λ value has shifted toward that expected given previous results. The difference between the 'Limited' and the 'Total' results has also decreased, as expected.

specimen tilt (º)	effective thickness (nm)
-10	125.6
-5	95.0
0	76.9
5	65.0
10	56.7
15	50.6
20	46.0
25	42.4
35	37.5
45	34.6
55	33.0
65	32.5

	Limited, tilt range (-10° to+25°)	
	Tilt-Corrected	Straggling-Corrected
λ	2795.4	2796.1
$\Delta\lambda$	1.4	0.5
R^2	1.0000	1.0000

	Total, tilt range (-10° to+65°)	
	Tilt-Corrected	Straggling-Corrected
λ	2789	2795.8
$\Delta\lambda$	4	0.4
R^2	1.0000	1.0000

Table 4.5.1.7: Results of λ calculation for In_L using the 'Specimen Tilt' method at beam energy 1970keV. Simulation run in NISTMonte with 10^7 electron histories. $\theta = \alpha + 25°$. Sample is comprised of 5nm of InAs (density = 5.67gcm^{-3}) at the bottom surface of a 30nm GaAs (density = 5.316gm^{-3}) overlayer. α is given in the first column.

Figure 4.5.1.1 compares the calculated λ values for In_L values from each method, with the 'sub-methods' of 'Specimen Tilt' also considered, as this is the most representative of typical

experimental conditions. It is clear that the 197keV 'Specimen Tilt' result has the largest error with the 197keV 'Detector Tilt' error slightly less. This difference can be attributed to the effects of beam straggling resulting from the changing amount of material travelled through when the sample is tilted. The fact that the straggling-corrected 197keV 'Variable Depth' and its 1970keV non-corrected equivalent disagree with the result from 'Specimen/Detector Tilt' further implies that the two models are not exact equivalents, even when straggling correction is used. This difference is, however, fairly small, and likely to be negligible in experiment.

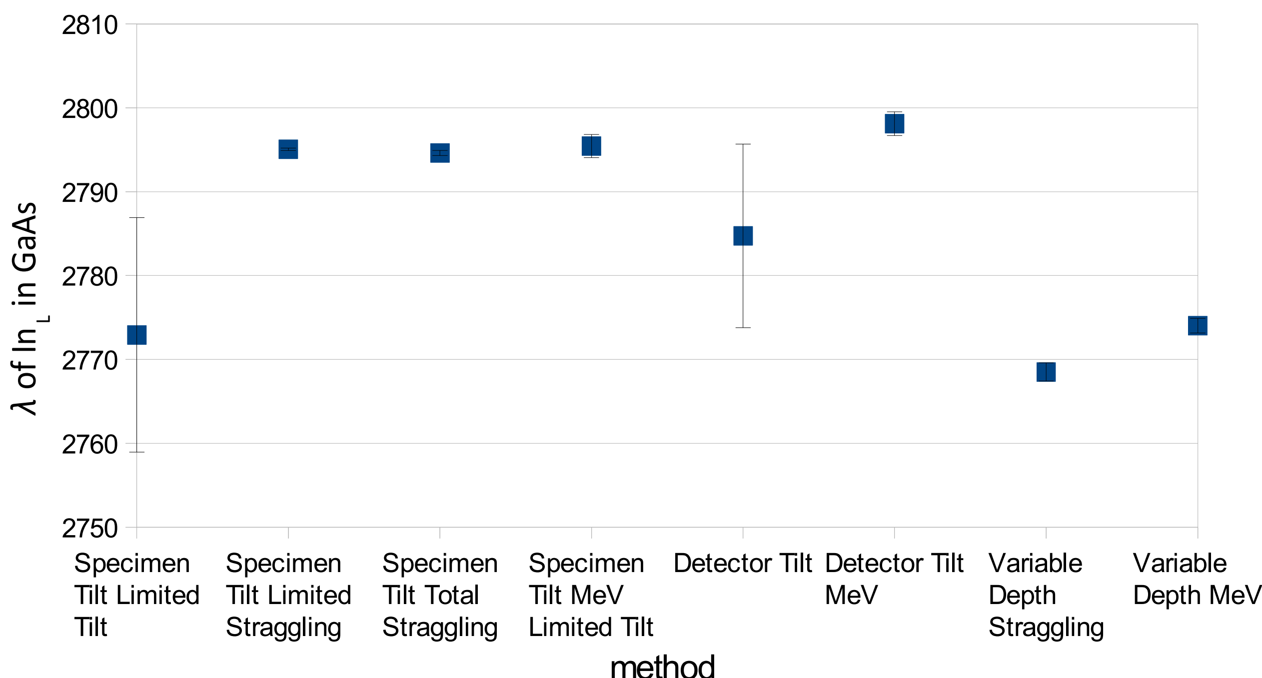

Figure 4.5.1.1: Comparison of λ values and their errors for the different methods. Mean is 2785.42 with a standard error of 4.25.

4.5.2 Calculation of λ using normalised X-ray intensity

Sometimes the intensity of the X-ray line of interest deviates from the expected curve due to inconsistency in the sample or experimental conditions, such as a change in beam current. This can often be resolved by normalising with respect to another X-ray line, ideally one that experiences negligible absorption. A good example of this would be an indium rich layer in GaAs, where the In_L can be normalised with respect to As_K, which for most typical TEM sample thicknesses does not suffer appreciable absorption. In an ideal situation, this would not have an effect on the resulting calculation, however, even a tiny change in detected intensity would potentially cause difficulty. As seen in Figure 4.5.2.1, even a fairly hard X-ray like As_K (10.543keV) experiences some intensity change with specimen tilt.

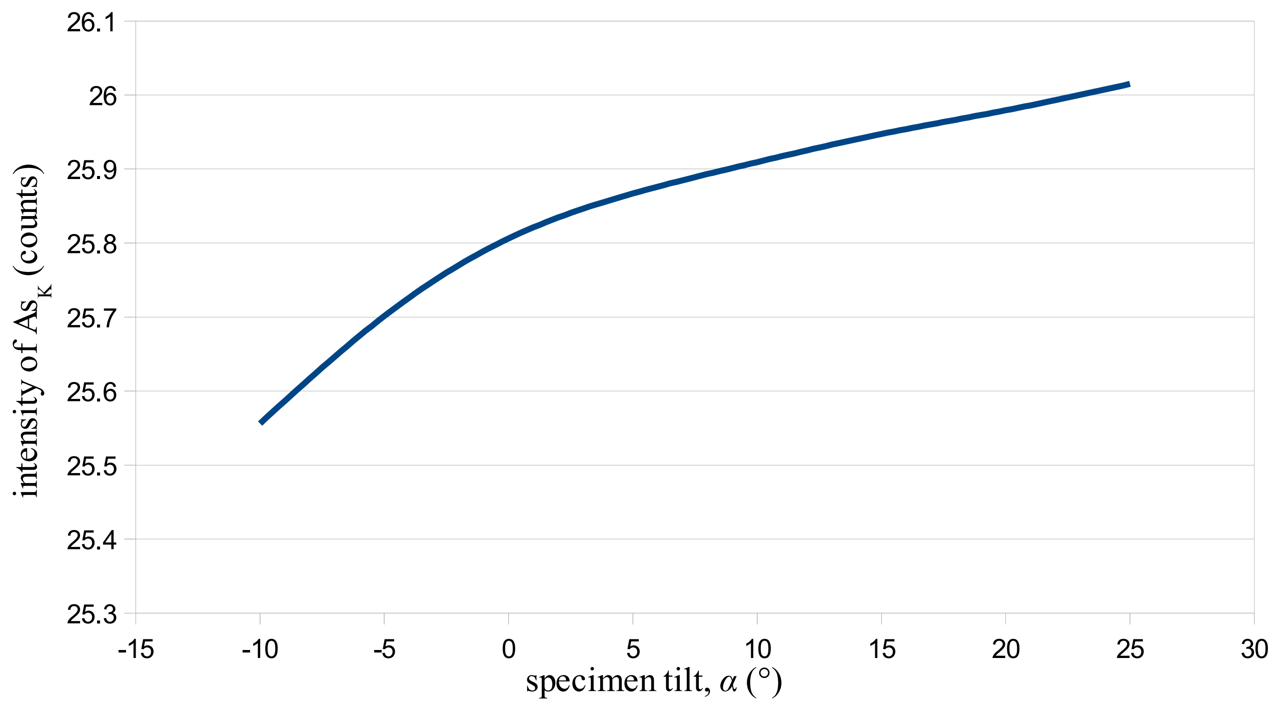

Figure 4.5.2.1: As_K intensity from GaAs sample. Note the small change in the absolute magnitude of the y-axis. Simulation run in NISTMonte at beam energy 197keV with 10^7 electron trajectories. $\theta = \alpha + 25°$. Correction for tilt was applied. Sample is comprised of 210nm of GaAs (density = 5.316gcm^{-3}) with a 5nm thick layer of pure indium embedded 50nm deep within the matrix.

A comparison of In_L and In_L/As_K is shown in Figure 4.5.2.2. The difference between the form of the two curves is obvious, with the In_L/As_K having a much weaker curvature.

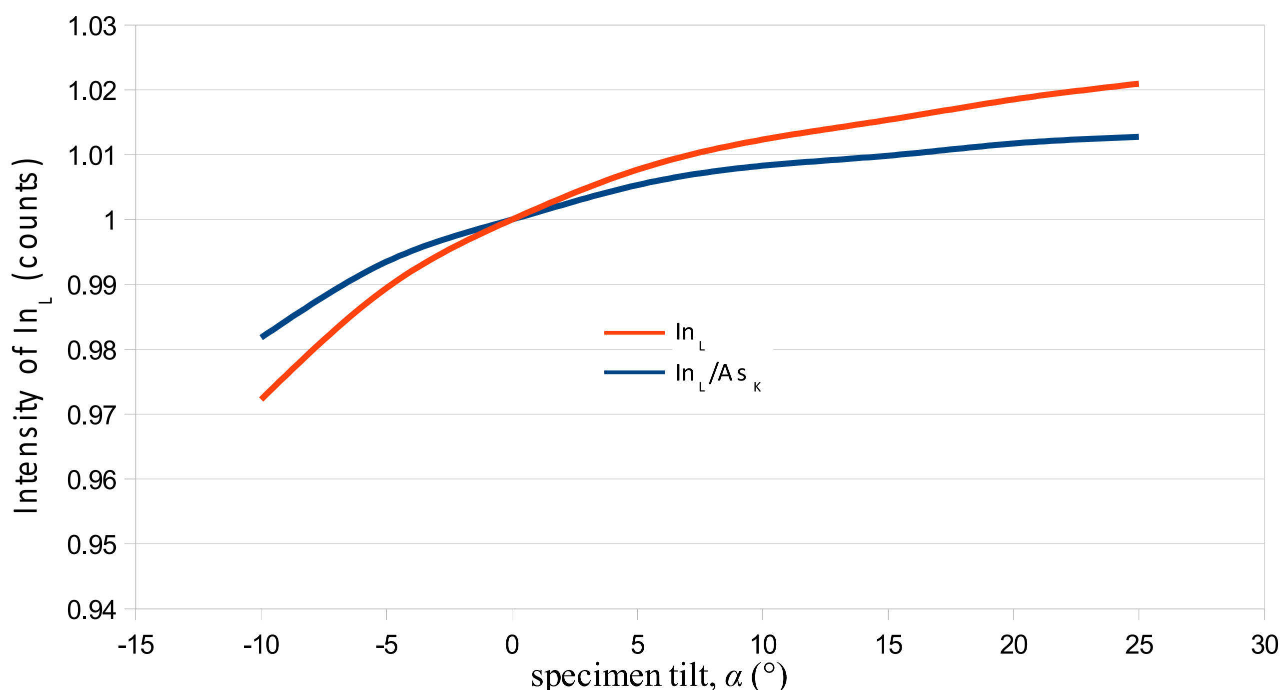

Figure 4.5.2.2: Comparison of In_L intensities and In_L/As_K intensity ratio against specimen tilt, both normalised to unity at zero tilt. Simulation run in NISTMonte at beam energy 197keV with 10^7 electron trajectories. $\theta = \alpha + 25°$. Correction for tilt was applied. Sample is comprised of 210nm of GaAs (density = 5.316gcm^{-3}) with a 5nm thick layer of pure indium embedded 50nm deep within the matrix.

This change in curvature can be accounted for by calculating the λ for the ratio and using that in equation 4.1.1. This difference in listed in Table 4.5.2.1, which compares the calculated λ values in different materials for In_L and the normalised counterparts. The normalisation universally increases the λ, with the change being smaller the higher the energy of the normalising X-ray line. This can be readily seen by comparing the results for AlSb and AlAs. Normalising with respect to Sb_K (26.3591keV) causes a much smaller proportional change than when As_K (10.543keV) is used: this is due to the fact that while both experience little absorption, and therefore change with take-off angle, the higher energy X-ray experiences even less absorption than the lower energy X-ray. An interesting exception to this is GaAs, which sees As_K (10.543keV) cause a greater change than Ga_K (9.251keV), despite being higher energy. Recalling that one X-ray can significantly fluoresce another if there is little difference in their energies, a simulation was run for a layer of pure indium in hypothetical ZnNi, which has a similar range of X-ray energies ([Zn_K: 8.63886, Ni_K: 7.47815keV) despite not being a semiconductor material and hence not otherwise relevant to this discussion. The same trend is visible, which indicates that self-fluorescence is the cause of this discrepancy.

matrix material	X-ray line	λ (nm)	$\Delta\lambda$ (nm)	R^2
AlSb (ρ = 4.26gcm^{-3})	In_L	4590	80	0.9983
	In_L/Sb_L	4950	70	0.9990
AlAs (ρ = 3.81gcm^{-3})	In_L	3670	40	0.9994
	In_L/As_K	4190	20	0.9998
BAs (ρ =	In_L	2900	40	0.9988

5.22gcm^{-3})	In_L/As_K	3307	19	0.9998
GaAs (ρ = 5.316gcm^{-3})	In_L	2755	20	0.9997
	In_L/As_K	4290	60	0.9986
	In_L/Ga_K	3280	40	0.9992
GaN (ρ = 6.15gcm^{-3})	In_L	3010	20	0.9997
	In_L/Ga_K	3620	30	0.9996
GaP (ρ = 4.138gcm^{-3})	In_L	3440	40	0.9990
	In_L/Ga_K	4110	30	0.9997
ZnNi (ρ = 7.87gcm^{-3})	In_L	2240	40	0.9977
	In_L/Zn_K	5600	300	0.9811
	In_L/Ni_K	3050	120	0.9907

Table 4.5.2.1: Comparison of calculated λ for In_L and their normalised counterparts in different matrix materials. Specimen tilt method used, with tilt (α) ranging from -10° to +25° in steps of 5°. Sample was 5nm of pure indium embedded 50nm within a 210nm thick matrix of the stated material and density.

An equivalent set of simulations was also run with indium replaced with aluminium. The result of this is shown in Table 4.5.2.2. The same trends are again visible, in that using higher energy for normalisation causes less change in the calculated λ. The difference between normalisation with respect to As_K and Ga_K also persists, for the same reason as previously.

matrix material	X-ray line	λ (nm)	$\Delta\lambda$ (nm)	R^2
BAs (ρ = 5.22gcm^{-3})	Al_K	435.9	0.8	1.0000
	Al_K/As_K	442.8	0.5	1.0000
GaAs (ρ = 5.316gcm^{-3})	Al_K	381.9	0.7	1.0000
	Al_K/As_K	401.4	0.4	1.0000
	Al_K/Ga_K	389.8	0.4	1.0000
GaN (ρ = 6.15gcm^{-3})	Al_K	384.8	0.8	1.0000
	Al_K/Ga_K	392	0.2	1.0000
GaP (ρ = 4.138gcm^{-3})	Al_K	680.5	0.9	1.0000
	Al_K/Ga_K	698.7	1.2	1.0000
InAs (ρ = 5.67gcm^{-3})	Al_K	474.4	0.7	1.0000
	Al_K/As_K	480.3	0.9	1.0000
	Al_K/Ga_K	496.2	0.9	1.0000
InSb (ρ = 5.775gcm^{-3})	Al_K	566.5	1.7	0.9999
	Al_K/In_K	575	0.9	1.0000
	Al_K/Sb_K	575.2	0.9	1.0000
InP (ρ =	Al_K	811	30	0.9999

5.12gcm^{-3})	Al_K/In_K	823	3	0.9999
InN (ρ = 6.81gcm^{-3})	Al_K	547	2	0.9999
	Al_K/In_K	554.3	1.1	1.0000

Table 4.5.2.2: Comparison of calculated λ for Al_K and their normalised counterparts in different matrix materials. Specimen tilt method used, with tilt (α) ranging from -10° to +25° in steps of 5°. Sample was 5nm of pure aluminium embedded 50nm within a 210nm thick matrix of the stated material and density.

The use of equation 4.1.1 is, as already mentioned, dependent on several assumptions. One of these assumptions is that absorption in the thin layer is negligible, more specifically that the only absorption of the X-ray line of interest is from the overlayer. The following section explores the validity of this assumption.

Table 4.5.2.3 lists the calculated λ values of the In_L X-ray line resulting from In or InAs layer of different thicknesses with an overlayer of 30nm GaAs. The apparent increase in λ with layer thickness is clear. λ is somewhat lower for thinner layers for the InAs only to increase to approximately the same value at 10nm thickness, though it should be noted that the magnitude of the error means that this cannot be taken as a trend. It is interesting that a tenfold increase in the thickness of the thin layer causes an apparent 2.1% change in λ. This implies that this change due to self-absorption may need to be accounted for in quantification, depending on the desired reproducibility. As a general rule, it seems that while a thicker layer does cause a change in λ, a thinner layer would require longer analysis for comparable statistical reproducibility, which may not be feasible. It is worth noting that this change due to self-absorption appears to be stronger than all other numerical effects, such as statistical fluctuations or beam straggling. This is due to the fact that the layer has a significantly different absorption cross-section than the matrix combined with the layer has a thickness that is not much less than that of the overlayer.

	pure indium				InAs		
t (nm)	1	5	10	t (nm)	1	5	10
λ	2753	2773	2790	λ	2740	2765	2797
$\Delta\lambda$	13	14	15	$\Delta\lambda$	17	13	15
R^2	0.9999	0.9998	0.9998	R^2	0.9998	0.9999	0.9998

Table 4.5.2.3: Calculated λ for In_L in GaAs for various thicknesses of pure indium or InAs for GaAs capping layer thickness 30nm. Simulation run in NISTMonte at beam energy 197keV with 10^7 electron trajectories. $\theta = \alpha + 25°$. Correction for tilt was applied. Sample is comprised of the specified thickness of either InAs (density = 5.67gcm^{-3}) or pure indium at the bottom surface of a 30nm GaAs (density = 5.316gm^{-3}) overlayer.

Figure 4.5.2.3 plots the In_L X-ray intensity from the simulations run for Table 4.5.2.3 against sample tilt, where Table 4.5.2.4 contains the ratios from the curves of In_L intensity from the pure indium system relative to that of the InAs system for each specimen tilt at each thickness. For ease of comparison, each curve has been normalised with respect to its -10° data point. It is clear from Figure 4.5.2.3 that the general form of each curve is the same, and that the curves for In and InAs for each layer thickness are very similar. Comparing the ratios of In over InAs is interesting: t = 1nm has what could be a minor trend to a value slightly greater than one with significant statistical noise, t = 5nm showing a consistent value of less than one and then t = 10nm giving a ratio that is always larger than one. This is logical: the t = 1nm curve can be understood as having significant

statistical uncertainty (as it is thinner than the other two thicknesses) in addition to experiencing a smaller change in self-absorption (and so the average value would be closer to one), and so does not contribute to the trend. Running the simulation again gives the same result to within statistical variation. This trend is a function of the exponential decay of X-ray intensity due to absorption, as the two materials display different absorption characteristics.

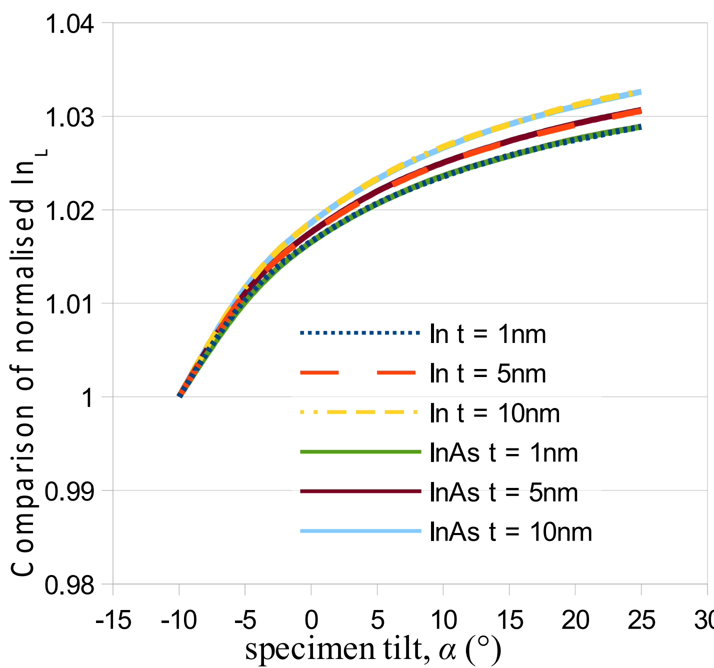

Figure 4.5.2.3: Comparison of ratios of normalised In_L series between pure indium and indium arsenide of different thicknesses. Note that each curve for pure indium is overlaying the equivalent for InAs.

	thickness, *t* (nm)		
specimen tilt, α (°)	1	5	10
-10	1.0000	1.0000	1.0000
-5	1.0003	1.0000	1.0001
0	1.0001	0.9999	1.0000
5	1.0000	0.9999	1.0001
10	0.9999	1.0000	1.0001
15	1.0001	0.9999	1.0000
20	0.9999	0.9999	1.0001
25	1.0000	0.9999	1.0001

Table 4.5.2.4: Normalised ratios of In_L intensity from the pure indium layer relative to that of the InAs layer of Figure 4.5.2.3 for their respective thicknesses. Sample is comprised of the specified thickness of either InAs (density = 5.67gcm^{-3}) or pure indium at the bottom surface of a 30nm GaAs (density = 5.316gm^{-3}) overlayer.

Figure 4.5.2.4 shows the calculated λ value from Table 4.5.2.3 in graphical form. The apparent trend for the pure indium result to have a higher initial value but a weaker slope is obvious, though the size of the error bars precludes any definitive assessment.

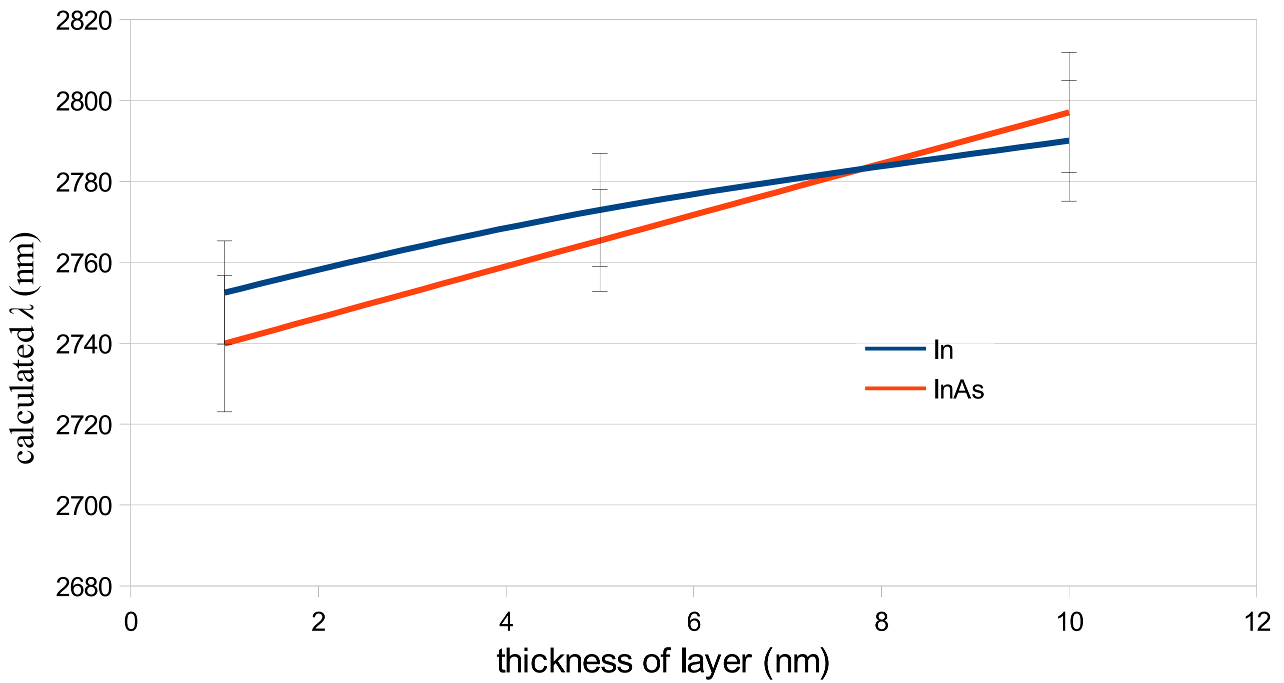

Figure 4.5.2.4: Calculated λ values for In_L X-ray line plotted against layer thickness. 'Specimen Tilt' method was used. Simulation run in NISTMonte at beam energy 197keV with 10^7 electron histories. $\theta = \alpha + 25°$. Correction for tilt was applied. Sample is comprised of the specified thickness of either InAs (density = 5.67gcm^{-3}) or pure indium at the bottom surface of a 30nm GaAs (density = 5.316gm^{-3}) overlayer.

The result of using these different λ is shown in Table 4.5.2.5 to calculate the depth of an In or InAs layer of different thicknesses buried beneath 30nm of GaAs. The difference between varying the λ with layer thickness ('Varying') to accommodate the thin layer self-absorption or using the average ('Average'), as would likely be done in an experiment where knowledge of the layer thickness is unlikely, is very small, well within standard deviations. This implies that for In or InAs, a change in the thickness of the thin layer can be ignored.

thickness, t (nm)	indium		indium arsenide	
	varying	average	varying	average
1	31.0±1.2	31.2±1.3	31.0±1.0	31.3±1.1
5	33.1±1.2	33.1±1.2	33.0±1.2	33.0±1.2
10	35.6±1.2	35.4±1.2	35.6±1.2	35.2±1.2

Table 4.5.2.5: Comparison of calculated d for layers of different thicknesses. Correct d is 30 + half thickness. 'Specimen Tilt' method was used. Simulation run in NISTMonte at beam energy 197keV with 10^7 electron histories. $\theta = \alpha + 25°$. Correction for tilt was applied. Sample is comprised of the specified thickness of either InAs (density = 5.67gcm^{-3}) or pure indium at the bottom surface of a 30nm GaAs (density = 5.316gm^{-3}) overlayer.

A similar test for different layer materials is shown in Table 4.5.2.6, again with a capping layer of 30nm GaAs. There are two comparisons of interest: between pure Al and AlAs (analogous to the In/InAs of Table 4.5.2.3), and between each pure material. The calculated λ values for the Al_K-line for Al and AlAs at 1nm thickness is very close, as there is too little material to exhibit their different absorption coefficients. The difference from the 10nm thick layer is significantly greater than that of the indium equivalent in Table 4.5.2.3, which is not surprising given that Al_K has lower energy than

In_L, and that introducing arsenic into aluminium would have a more significantly effect on the density (and therefore the absorption) than introducing arsenic into indium.

Comparing the relative change in calculated λ value between the different pure materials at different layer thicknesses, it seems that there is little difference with energy, with the exception of antimony, which has a relative change much smaller than its error. Sb_L seeing little difference from layer thickness is not surprising, given its high energy, however the relative constancy of the change in the other materials is unexpected. This can be understood to be a function of each pure material giving approximately the same relative change in self-absorption, where the AlAs compound has different behaviour because the presence of the As changes its characteristics while the Sb_L values experience statistically negligible change due to its much higher energy.

thickness, t (nm)	N_K	±sd	Al_K	±sd	Al_KAs	±sd	Si_K	±sd	P_K	±sd
1	145.99	0.09	369.8	0.3	367.3	0.3	508.1	0.7	733.2	1.2
4	153.37	0.06	388.1	0.3	375.6	0.2	533.4	0.5	770.3	1.0
7	160.39	0.04	405.7	0.3	383.1	0.2	557.6	0.5	805.4	1.1
10	167.41	0.04	423.2	0.2	390.4	0.3	581.2	0.6	839.6	0.9
% change	12.80		12.63		5.92		12.57		12.66	

Table 4.5.2.6: The effect of layer thickness on the λ values of various X-rays. 'Specimen Tilt' method was used. Simulation run in NISTMonte at beam energy 197keV with 10^7 electron histories. $\theta = \alpha + 25°$. Correction for tilt was applied. Sample is comprised of the specified thickness of either AlAs (density = 3.81gcm^{-3}) or the specified pure element at the bottom surface of a 30nm GaAs (density = 5.316gm^{-3}) overlayer. sd = standard error. '% change' is the percentage difference between t = 1nm and t = 10nm of each material, to illustrate the total change over this range of thicknesses.

thickness, t (nm)	Sb_L	±sd
1	3604	18
4	3600	20
7	3620	20
10	3610	30
% change	0.23	

Table 4.5.2.6 continued

Figure 4.5.2.5 is the equivalent of Figure 4.5.2.3 in comparing Al and AlAs instead of In and InAs, while Table 4.5.2.7 is the equivalent of Table 4.5.2.4. The same trend is visible, specifically that the curves for each thickness are very similar. The results of taking the ratio of the Al_K curves from the pure aluminium over the AlAs equivalent, shown in Table 4.5.2.7, show a consistent trend for the pure Al intensity over the compound AlAs. This is not a surprise, as the absorption cross-section of the compound has already been established as larger than that of the pure element.

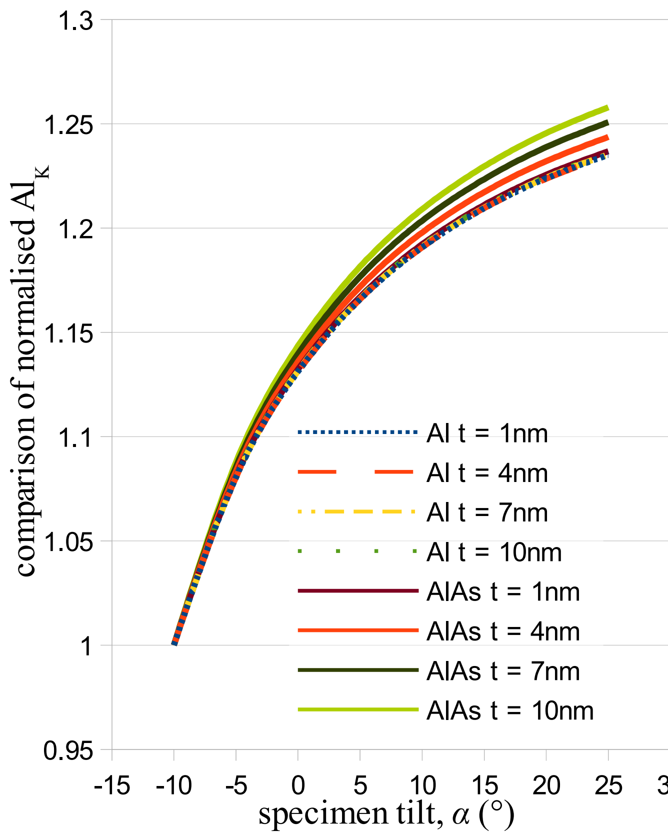

Figure 4.5.2.5: Comparison of ratios of AlK series between pure aluminum and aluminum arsenide. Note that all the pure aluminium and the 'AlAs t = 1nm' are superimposed on each other.

	thickness, *t* (nm)			
specimen tilt, *α* (°)	1	4	7	10
-10	1.0000	1.0000	1.0000	1.0000
-5	1.0006	1.0027	1.0046	1.0063
0	1.0009	1.0042	1.0072	1.0103
5	1.0011	1.0052	1.0091	1.0129
10	1.0012	1.0060	1.0104	1.0147
15	1.0013	1.0063	1.0113	1.0160
20	1.0014	1.0069	1.0119	1.0171
25	1.0014	1.0071	1.0125	1.0200

Table 4.5.2.7: Ratios of aluminium over aluminium arsenide from Figure 4.5.2.5 for their respective thickness. Sample is comprised of the specified thickness of either AlAs (density = 3.81gcm^{-3}) or pure aluminium at the bottom surface of a 30nm GaAs (density = 5.316gm^{-3}) overlayer.

Table 4.5.2.8 shows the results of using the thickness-specific ('Varying') or average ('Average') λ values for each material. Similar to Table 4.5.2.5 these calculation are performed for layers embedded under 30nm of GaAs, and as such the correct result would be 30nm plus half the thickness of the layer. The 'Varying' results perform exactly as expected, in that they give approximately the correct result for each material. The 'Average' calculations from all but the AlAs and Sb, however, give a similar result for each layer thickness, indicating that the constant λ value has a stronger effect than the changes in detected intensity from changing the layer thickness. For AlAs and Sb the 'Average' value is much closer to the 'Varying'. For AlAs this can be attributed to the higher self-absorption of the compound compared to the pure element, in that a change in the layer thickness has a much greater effect on the detected intensity. With Sb this can be understood as a result of the extremely high λ value, resulting in a negligible difference in absorption between the GaAs matrix and the Sb layer.

thickness, t (nm)	N_K		Al_K for pure Al		Al_K for AlAs	
	Varying	Average (λ =156.79)	Varying	Average (λ =396.67)	Varying	Average (λ =379.09)
1	30.56±0.10	32.82±0.11	30.60±0.17	32.82±0.18	30.58±0.14	31.56±0.14
4	32.04±0.07	32.75±0.07	32.07±0.18	32.78±0.19	32.06±0.11	32.36±0.11
7	33.53±0.06	32.78±0.06	33.57±0.14	32.82±0.14	33.56±0.11	33.24±0.11
10	35.03±0.06	32.81±0.06	35.06±0.14	32.86±0.13	35.09±0.18	34.07±0.17

Table 4.5.2.8: Comparison of calculated depth, d, for different materials with layers of different thicknesses. Correct d is 30nm + half thickness. 'Specimen Tilt' method was used. Simulation run in NISTMonte at beam energy 197keV with 10^7 electron histories. $\theta = \alpha + 25°$. Correction for tilt but not straggling was applied. Sample is comprised of the specified thickness of either AlAs (density = $3.81 gcm^{-3}$) or the specified pure element at the bottom surface of a 30nm GaAs (density = $5.316 gm^{-3}$) overlayer. 'Varying' λ is that given in Table 4.5.2.6.

thickness, t (nm)	Si_K		P_K		Sb_L	
	Varying	Average (λ =545.05)	Varying	Average (λ =787.12)	Varying	Average (λ =3608.88)
1	30.6±0.3	32.9±0.3	30.8±0.4	32.9±0.4	31.1±1.3	31.1±1.3
4	32.1±0.2	32.8±0.2	32.1±0.3	32.8±0.3	32.7±1.4	32.8±1.4
7	33.6±0.2	32.8±0.2	33.7±0.4	32.9±0.3	34.1±1.3	34.0±1.3
10	35.1±0.3	32.9±0.3	35.1±0.3	32.9±0.3	36±2	36±2

Table 4.5.2.8 continued.

Figure 4.5.2.6 shows the simulated results of calculating λ using the straggling-corrected 'Variable Depth' method in various matrices for different pure element thin layers. This is intended to demonstrate the difference between various materials, and in particular how λ changes with material density. It is clear that while there is a general trend for λ to decrease with increasing density, there is no easily discernible pattern. Instead, the λ values are significantly scattered around this broadly linear decrease, with the In_L and Sb_L results from BN being the most obviously different.

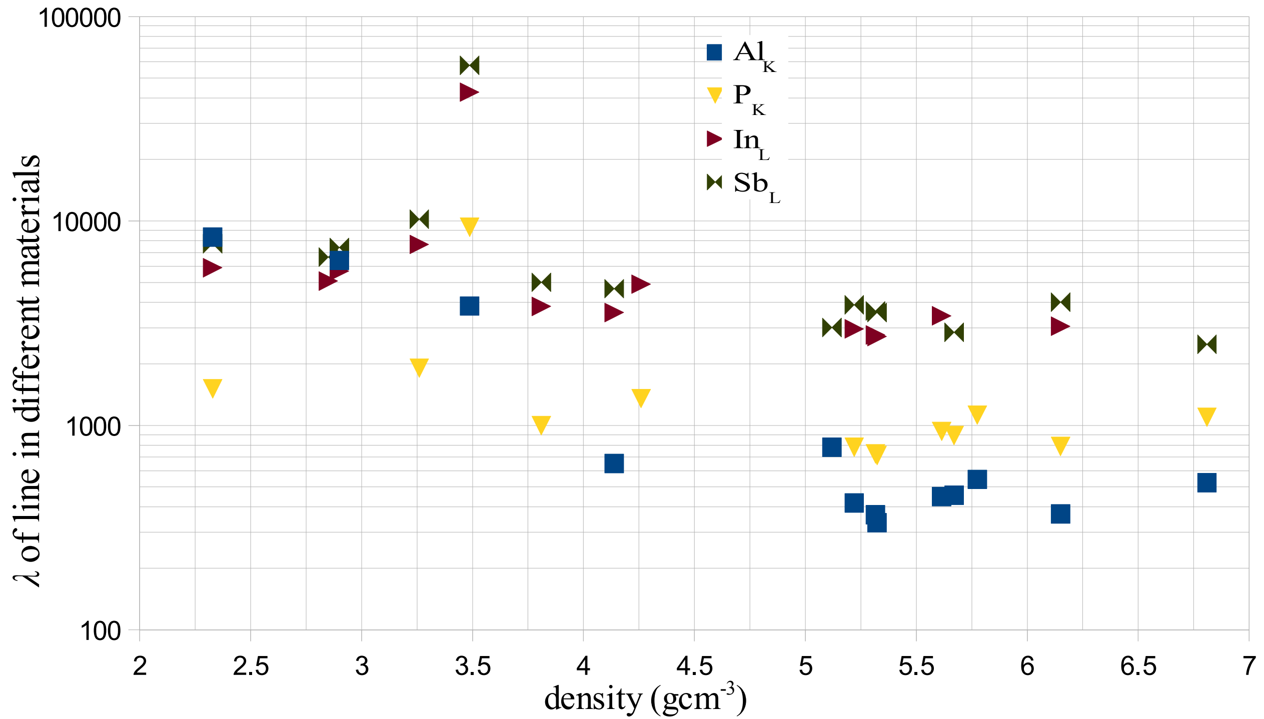

Figure 4.5.2.6: Calculated λ for four lines in a variety of substrates. ‘Variable Depth’ method used. Correction for straggling applied. Simulation run in NISTMonte at beam energy 197keV with 10^7 electron histories at constant take-off angle of $\theta = 90°$. Sample is comprised of 10nm of the specified pure element at the bottom surface of an overlayer that varies from 10nm to 190nm in steps of 10nm.

Figure 4.5.2.7 shows calculated λ values taken from the NIST XCOM database [66] for the same materials as Figure 4.5.2.6. These are calculated from the photoelectric absorption using the following equation:

$$\lambda = \frac{1}{\left.\frac{\mu}{\rho}\right]_{spec}^{A} \cdot \rho} \cdot \frac{1}{10^{-7}}$$

Equation 4.5.2.1

where $\left.\frac{\mu}{\rho}\right]_{spec}^{A}$ is the mass absorption coefficient in cm^2g^{-1}, ρ is the density in gcm^{-3} and the 10^{-7} converts the resulting value into nanometres. The results show a general trend for decreasing λ with increasing density remains, to broadly the same extent. The reasons for the difference is not clear, nor is which should be preferred. Obviously, using the λ value from a Monte Carlo program to calculate depth using data from that same program would give superior, self-consistent results, however determining which is the most valid experimentally requires considerable experimental data. Verifying which, if either, is correct could also be accomplished by the parameters used to arrive at the answers in in a Monte Carlo program, as doing so would leave only 'real world' effects (e.g. beam spreading) and eliminate any differences caused by variations in the absorption and density parameters.

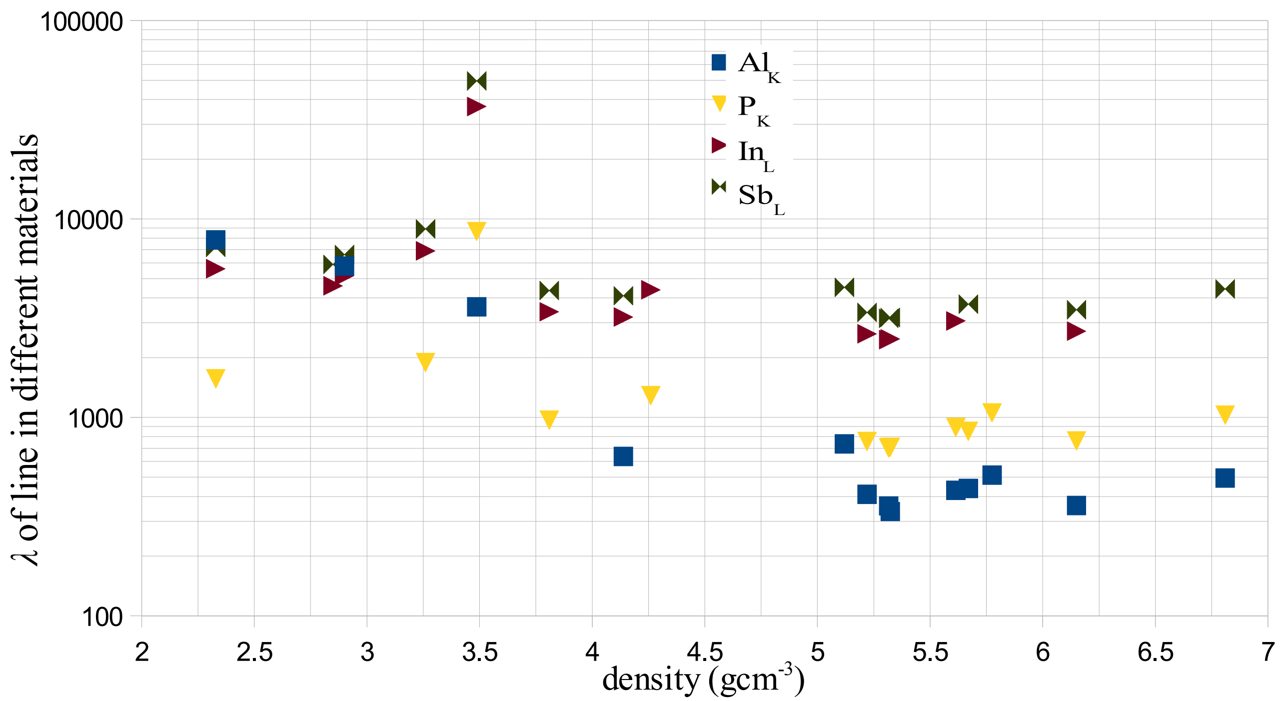

Figure 4.5.2.7: Calculated λ using equation 4.5.2.1 and photoelectric absorption coefficients taken from NIST XCOM [66].

Figure 4.5.2.8 show all possible ratio combinations using the X-ray lines from Figure 4.5.2.6. This is an attempt to determine if there exists any systematic ratio between the various materials, so that it might be possible to determine a reliable inference and from that calculate others. It is clear that In_L/Sb_L gives a strong trend for values near 0.763, with a slight difference for Al_N and B_N. P_K/In_L and P_K/Sb_L also give reasonably stable ratios for certain ranges of density, as does Al_K/P_K. Verifying whether these values are accurate would require comparison to experimental data, however it is worth noting that there is no particular reason to think that the approach is invalid, so that any of these the values themselves could be incorrect without invalidating the approach.

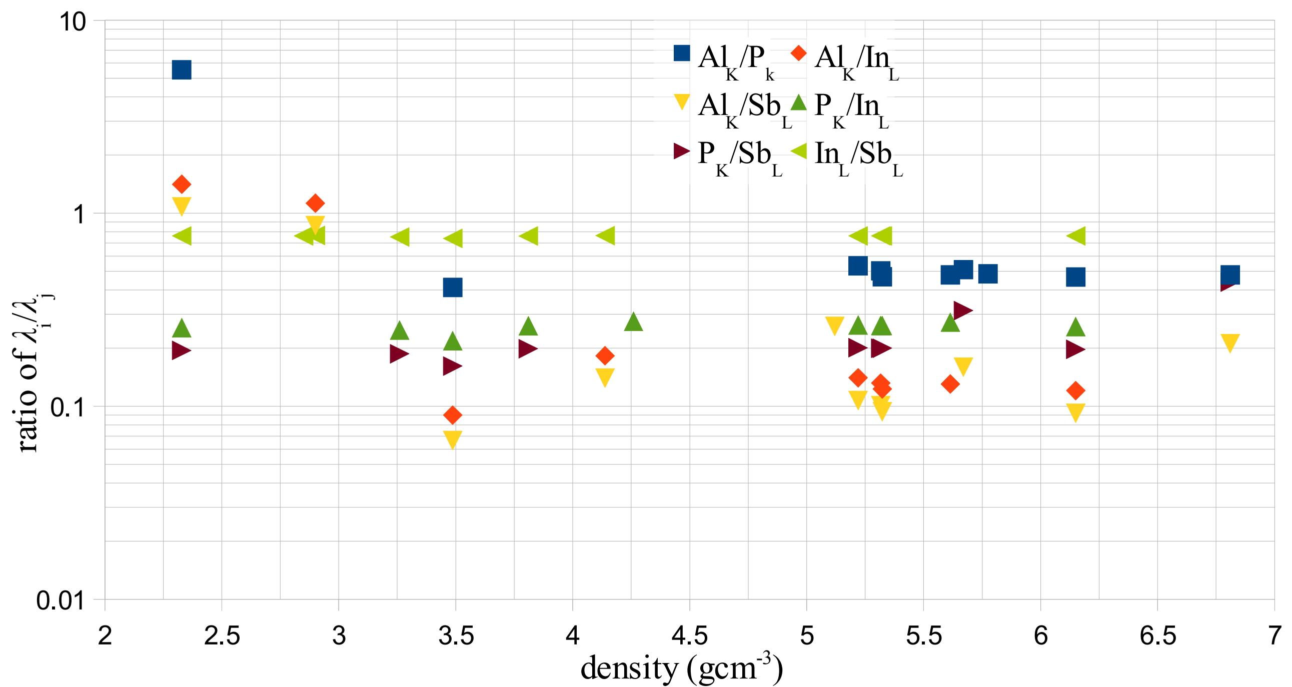

Figure 4.5.2.8: Graphical representation of Error: Reference source not found on a logarithmic scale, as a linear scale does not allow useful differentiation between series.

In general, the calculated λ shown in this section are likely incorrect by some constant factor but are correct in the trends seen between different materials and methods. This is typical of simulations, regardless of which Monte Carlo program is used. In terms of accuracy, Hurricane and NISTMonte, the programs that would be expected to give good results, instead give values that are too low and too high, respectively. 'Calibrating' these results, by comparing them to experimental values, noting the difference and then extrapolating to other values, would in principle allow the use of both to calculate λ values without direct comparison to experiment.

A typical TEM sample (i.e ~100nm) would likely provide enough change in absorption to calculate λ with good accuracy, regardless of the methods used. This is obvious in the calculation of λ for such X-ray lines as In_L while using a sample that is in many cases <100nm thick.

4.6 Total Sample Thickness by the Sample Flip Method

It is possible to utilise equation 4.1.1 to determine the total thickness of a sample that is homogeneous other than having a thin layer at a certain depth, if λ is known. This can be accomplished by taking a data series, inverting the sample and then taking another data series in the same region. In principle, the total sample thickness would then be the sum of the two resulting calculated depths of the thin layer.

Obviously, it is not quite so simple. The most prominent problem is that the same region must be analysed twice from different viewpoints. Inverting the sample would require removing and re-inserting the sample, which in turn would introduce slight changes in orientation. While these changes would be invisible to the naked eye, even a change of 1µm would cause considerable difficulty in locating the same region. This, of course, assumes that the region is readily identifiable from the inverted viewpoint, which would not be the case in most cases.

The data that follows was simulated using a 200nm GaAs sample. Part of the GaAs was replaced with either Al or In of varying thicknesses and depths, but the total sample thickness of 200nm remains constant. In this case, it was considered more expedient to specify the depth and the centre of the layer, i.e. a 5nm layer embedded 50nm within the sample occupies the depth range 47.5nm to 52.5nm.

		α_2 (°)						
		-5	0	5	10	15	20	25
α_1 (°)	-10	10.2	10.3	10.5	10.6	10.6	10.7	11.1
	-5		10.3	10.7	10.9	10.8	11.0	11.6
	0			11.4	11.4	11.2	11.5	12.3
	5				11.6	11.1	11.5	12.8
	10					10.6	11.5	13.5
	15						12.7	15.6
	20							19.5

Table 4.6.1: Calculated d (nm) results with applied tilt correction. Simulation run in NISTMonte at beam energy 197keV with 10^7 electron histories. $\theta = \alpha + 25°$. Sample is comprised of 1nm of pure indium 10nm deep inside a 200nm GaAs (density = 5.316gm^{-3}) matrix. Mean 11.7±1.9nm.

		α_2 (°)						
		-5	0	5	10	15	20	25
α_1 (°)	-10	189.5	188.8	189.4	189.7	190.3	191.2	191.8
	-5		187.8	189.4	189.8	190.8	192.3	193.2
	0			191.7	191.6	192.9	194.9	196.1
	5				191.5	193.8	196.9	198.3
	10					197.0	201.0	202.3
	15						206.4	206.3
	20							206.2

Table 4.6.2: Calculated d (nm) results with applied tilt correction. Simulation run in NISTMonte at beam energy 197keV with 10^7 electron histories. $\theta = \alpha + 25°$. Sample is comprised of 1nm of pure indium 10nm deep inside a 200nm GaAs (density = 5.316gm^{-3}) matrix. This is a companion table to Table 4.6.1. Mean 194.3±5.6nm.

Table 4.6.1 and Table 4.6.2 show the calculated depths for a 1nm thick In layer embedded 9.5nm and 189.5nm within the sample, respectively. These depths were chosen to mimic the effect of inverting the sample. The pattern of increasing deviation with take-off angle described in Section 4.3 also holds for this data set, as expected. Their summation is shown in Table 4.6.3.

		α_2 (°)						
		-5	0	5	10	15	20	25
α_1 (°)	-10	199.7	199.1	199.9	200.3	200.9	201.9	202.9
	-5		198.1	200.1	200.7	201.7	203.3	204.8
	0			203.1	203.1	204.1	206.3	208.3
	5				203.1	204.9	208.4	211.1
	10					207.5	212.5	215.8
	15						219.1	222.0
	20							225.7

Table 4.6.3: Summation of Table 4.6.1 and Table 4.6.2. Expected result = 200nm. Mean 206.0±7.2nm.

It is clear that summing the two depths does give the correct answer, though the effects of increasing take-off angle do give increasingly incorrect results. Increasing the thickness of the In layer to 5nm and 10nm gives the summed result seen in Table 4.6.4 and Table 4.6.5.

		α_2 (°)						
		-5	0	5	10	15	20	25
α_1 (°)	-10	198.1	198.8	199.2	199.8	200.5	201.1	202.3
	-5		200.1	200.3	201.2	202.2	203.0	204.8
	0			200.5	202.1	203.6	204.8	207.3
	5				204.4	206.1	207.4	210.8
	10					208.5	209.7	214.5
	15						211.3	219.1
	20							229.2

Table 4.6.4: Summation of depth calculation with tilt correction applied from 5nm pure indium embedded 10nm and 190nm within 200nm of GaAs (density = 5.316gcm^{-3}). Expected result = 200nm. Simulation run in NISTMonte at beam energy 197keV with 10^7 electron histories. $\theta = \alpha + 25°$. Mean 205.4±6.9nm.

		α_2 (°)						
		-5	0	5	10	15	20	25
α_1 (°)	-10	197.5	197.2	297.9	198.5	198.8	200.0	201.3
	-5		196.6	198.2	199.3	199.7	201.4	203.5
	0			200.6	201.6	201.8	204.3	207.1
	5				203.0	202.8	206.5	210.6
	10					202.5	209.3	215.0
	15						218.3	224.4
	20							232.5

Table 4.6.5: Summation of depth calculation with tilt correction applied from 10nm pure indium embedded 10nm and 190nm within 200nm of GaAs (density = 5.316gcm^{-3}). Expected result = 200nm. Simulation run in NISTMonte at beam energy 197keV with 10^7 electron histories. $\theta = \alpha + 25°$. Mean 204.7±8.6nm.

It is clear that while there is some systematic change in the extent of the deviation at higher take-off angles, the difference for lower take-off angles is negligible. This can be interpreted as it being reasonable to assume that a change in the thickness of the layer does not have a strong effect, though it should be noted that this situation is for $d \ll \lambda$. Looking at the means of the summations, it is clear that there is no significant difference for different thicknesses of the thin layer.

Table 4.6.6 and Table 4.6.7 are the Al equivalent of Table 4.6.1 and Table 4.6.2, in that they are for a 1nm AlAs film buried 10nm within a 200nm GaAs sample. Again the trend seen in Section 4.3.2 holds consistent, in that the effects of beam straggling are much less for Al than for In.

		α_2 (°)						
		-5	0	5	10	15	20	25
α_1 (°)	-10	10.0	10.1	10.1	10.1	10.1	10.2	10.2
	-5		10.1	10.1	10.1	10.2	10.2	10.3
	0			10.1	10.2	10.2	10.3	10.4
	5				10.3	10.3	10.5	10.5
	10					10.4	10.6	10.6
	15						10.9	10.8
	20							10.7

Table 4.6.6: Calculated d (nm) results with applied tilt correction. Simulation run in NISTMonte at beam energy 197keV with 10^7 electron histories. $\theta = \alpha + 25°$. Sample is comprised of 1nm of pure aluminium 10nm deep inside a 200nm GaAs (density = 5.316gm^{-3}) matrix. Mean 10.3±0.2nm

		α_2 (°)						
		-5	0	5	10	15	20	25
α_1 (°)	-10	189.7	189.8	189.8	189.8	189.9	190.0	190.1
	-5		189.8	189.9	189.9	190.1	190.2	190.4
	0			190.1	190.0	190.3	190.5	190.7
	5				190.0	190.4	190.8	191.1
	10					191.0	191.4	191.6
	15						191.9	192.0
	20							192.1

Table 4.6.7: Calculated *d* (nm) results with applied tilt correction. Simulation run in NISTMonte at beam energy 197keV with 10^7 electron histories. $\theta = \alpha + 25°$. Sample is comprised of 1nm of pure aluminium 10nm deep inside a 200nm GaAs (density = 5.316gm^{-3}) matrix. Mean 190.5±0.7nm.

Their summation is shown in Table 4.6.8. Clearly, the total thickness is very accurately calculated, with the previously noted exceptions of those data points significantly affected by beam straggling.

		α_2 (°)						
		-5	0	5	10	15	20	25
α_1 (°)	-10	199.8	199.8	199.9	200.0	200.0	200.2	200.3
	-5		199.9	200.0	200.0	200.2	200.5	200.6
	0			200.2	200.2	200.5	200.8	201.0
	5				200.2	200.7	201.2	201.5
	10					201.4	202.0	202.0
	15						202.8	202.8
	20							202.8

Table 4.6.8: Calculated *d* (nm) results with applied tilt correction. Summation of Table 4.6.6 and Table 4.6.7. Mean 200.8±1.0nm.

The summed results for a similar simulation where the Al layer thickness is changed to 5nm and 10nm respectively are shown in Table 4.6.9 and Table 4.6.10. The deviation from the correct value stems from the previously-explored change in λ with changing layer thickness. As described in Section 4.5, this change effects softer X-rays much more strongly than harder X-rays. This change causes an underestimation of the depth, particularly for the layer near the surface, which then results in the summed result being incorrect.

		α_2 (°)						
		-5	0	5	10	15	20	25
α_1 (°)	-10	195.8	195.8	195.9	196.0	196.0	196.2	196.3
	-5		195.8	195.9	196.1	196.2	196.4	196.6
	0			196.1	196.4	196.5	196.7	197.0
	5				196.7	196.8	197.1	197.4
	10					196.9	197.4	197.8
	15						198.1	198.5
	20							199.0

Table 4.6.9: Summation of depth calculation with tilt correction applied from 5nm pure aluminium embedded 10nm and 190nm within 200nm of GaAs (density = 5.316gcm^{-3}). Expected result = 200nm. Simulation run in NISTMonte at beam energy 197keV with 10^7 electron histories. $\theta = \alpha + 25°$. Mean 196.7±0.9nm.

		α_2 (°)						
		-5	0	5	10	15	20	25
α_1 (°)	-10	190.0	190.1	190.1	190.2	190.2	190.3	190.5
	-5		190.2	190.2	190.3	190.4	190.6	190.7
	0			190.2	190.4	190.6	190.8	191.0
	5				190.7	190.9	191.1	191.5
	10					191.2	191.6	191.9
	15						192.0	192.4
	20							192.9

Table 4.6.10: Summation of depth calculation with tilt correction applied from 10nm pure aluminium embedded 10nm and 190nm within 200nm of GaAs (density = 5.316gcm^{-3}). Expected result = 200nm. Simulation run in NISTMonte at beam energy 197keV with 10^7 electron histories. $\theta = \alpha + 25°$. Mean 190.8±0.8nm.

While the layer thickness is largely irrelevant when $d \ll \lambda$, the results of Table 4.6.9 and Table 4.6.10 indicate that such is not the case when d and λ are within an order of magnitude of each other. In this case, the means of the summations do change with layer thicknesses. This appears to be a function of the first analysis (i.e. for 10nm overlayer thickness) giving an underestimate of the depth which increases with the thin layer thickness. This is a result of self-absorption in the layer which would affect Al_K much more strongly than In_L.

Running a similar set of simulations for pure Al layers of 1, 5 and 10nm thickness embedded 50nm and 100nm within a GaAs sample gives an equivalent result. This includes the increased underestimation of the total thickness due to self-absorption, though this effect becomes less pronounced as the depth increases.

4.7 Quantification

As already mentioned, determining the depth of a thin layer in a thin foil sample can be used to achieve a more accurate quantification result. The difference between a homogeneous sample of some average chemical composition and one with an embedded thin layer is the extent of the

absorption, in that changing the take-off angle would cause different changes in the two samples. As such, it is logical to approach the problem of utilising the improved knowledge of the sample composition through the absorption correction.

This can be done by replacing the material's absorption correction used in the homogeneous approaches with the following equation:

$$a_j = e^{\frac{-D}{\lambda_j \sin\theta}}$$ Equation 4.7.1

where D = thickness of overlayer in nm, λ_j the absorption decay length in nm of X-ray line j in material of thickness D and given ρ and θ is the take-off angle.

4.8 Other methods of determining thin layer depth

4.8.1 Graphical comparison of change in X-ray intensity ratio with varying take-off angle

Using equation 4.1.1 is not the only way to calculate the depth of a thin layer. Another method, described in the following section, called 'Graphical comparison', attempts to compare the degree of absorption for two or three different X-ray intensities. By taking the ratio of an X-ray from the thin layer to another from the matrix and plotting that ratio against changing take-off angle, it is theoretically possible to determine the thickness of the matrix material above the thin layer. Specifically, the slope and *y*-intercept of the ratio can be compared to simulated data in order to deduce the depth of the embedded layer, while the absolute value at some consistent take-off angle (e.g. 0°) in conjunction with the depth reflects the chemical composition.

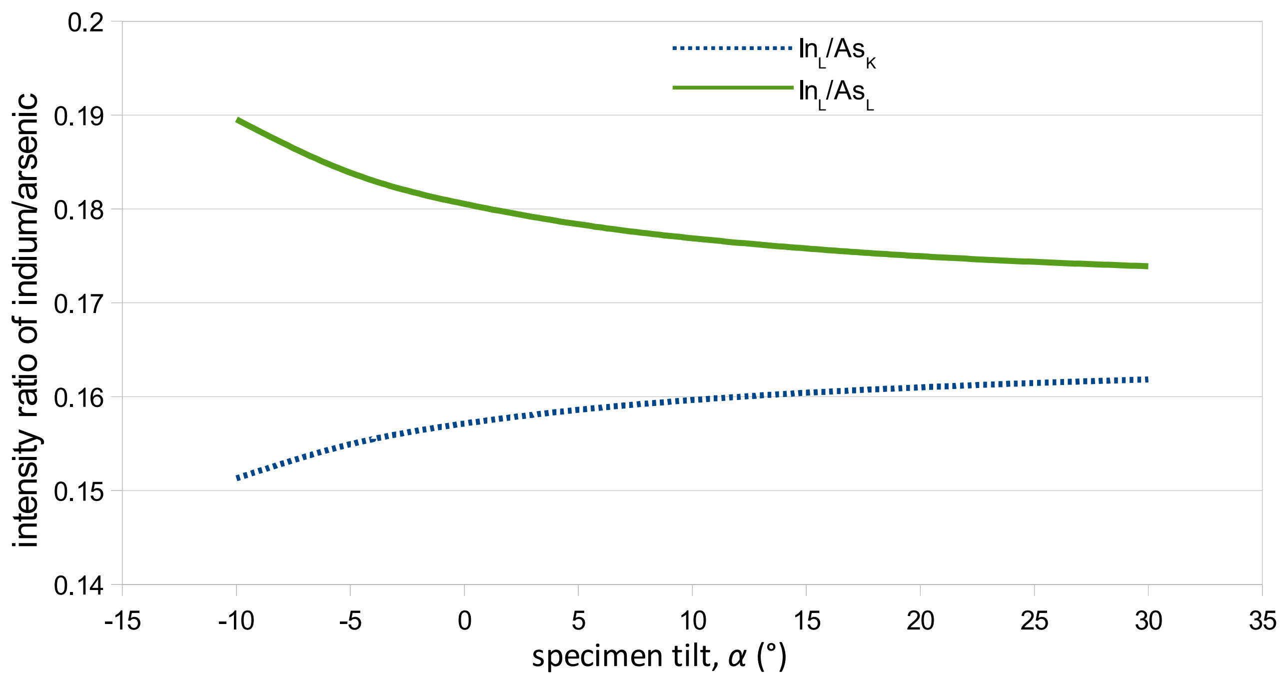

Figure 4.8.1.1: Example of typical plot. Simulation run in CASINO at 200keV beam energy with 10^8 electron trajectories, for 10nm of pure indium at the bottom surface of 60nm of GaAs (density = 5.316gcm^{-3}). $\theta = \alpha + 25°$.

Taking two ratios improves the method considerably. If the matrix material emits two X-rays, one of higher energy than the thin layer's X-ray line while the other is of lower energy, then taking the ratios of the two X-rays will converge towards a value in a manner distinctive to the structure of the sample, as seen in Figure 4.8.1.2. Here, there are three different geometries: where the thin layer is on top of the matrix, where the thin layer is embedded within the matrix and when the thin layer is below the entire matrix. It is obvious that when the thin layer is on top of the matrix, the lower energy ratio has a strong slope while the higher energy ratio has a very weak slope. The inverse is to some extent true when the thin layer is underneath the matrix, where the trend would become more pronounced if the matrix were to become thicker. It is worth noting that the situation when the thin layer is embedded within the matrix is distinguishable from the situation where the thin layer is underneath the matrix, in that the latter scenario would detect more of both high and low energy X-rays from the matrix.

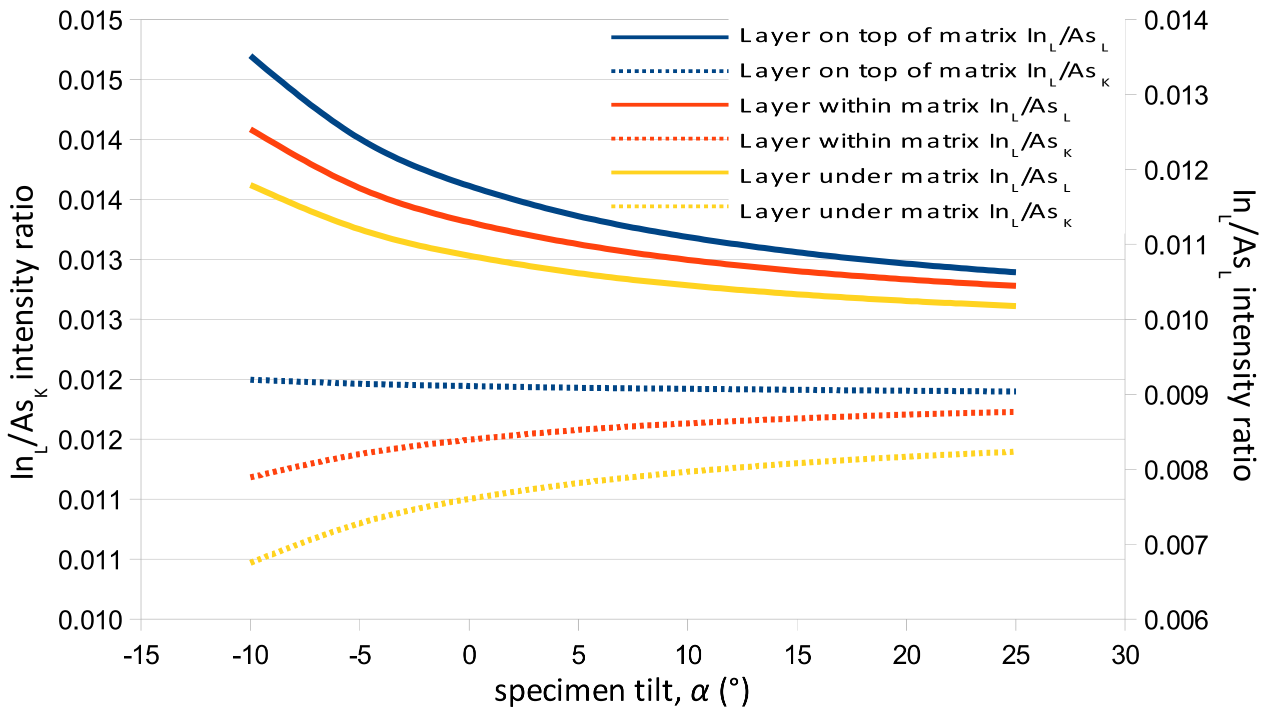

Figure 4.8.1.2: NISTMonte simulation of 1nm of InAs (density = 5.67gcm^{-3}) within a 99nm thick GaAs (density = 5.316gcm^{-3}) matrix. Layer is positioned on top (d = 0), within (d = 60nm) or under (d = 99nm) the matrix. Simulation run at beam energy 197keV with 10^7 electron histories. $\theta = \alpha + 25°$.

Figure 4.8.1.3 shows a comparison between NISTMonte and CASINO. Note that they are on different scales. It is already known that the simulation programs produce different absolute quantities of X-rays and so it is no surprise that their scale is different. Of particular interest is the fact that their curvature is different: NISTMonte seems to show a stronger slope than CASINO. Determining which, if either, is more accurate would require experimental calibration.

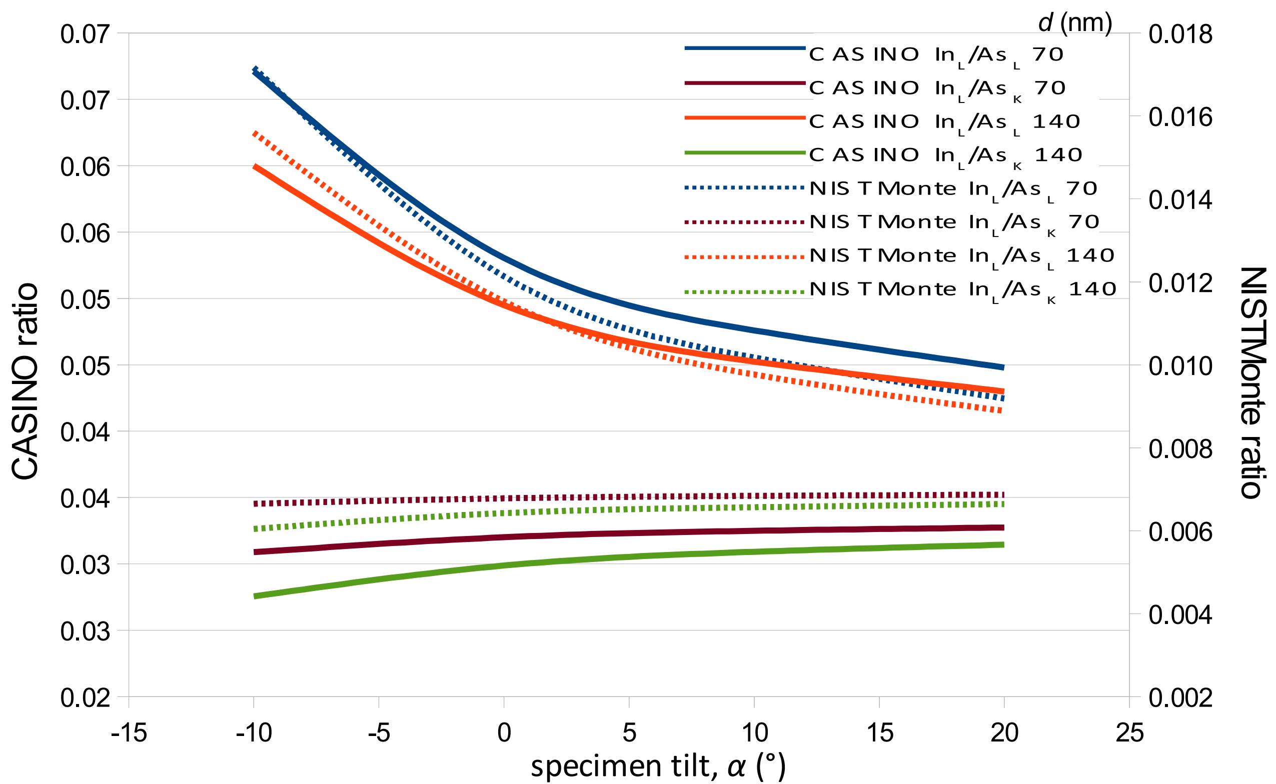

Figure 4.8.1.3: Comparison of simulation programs. $\theta = \alpha + 25°$. NISTMonte simulations run at beam energy 197keV, 10^7 electron histories, for a 8nm thick layer of $In_{0.24}Ga_{0.76}As$ (density = 6.0262gcm^{-3}) in a 424nm GaAs (density = 5.316gcm^{-3}) matrix, where the overlayer is as specified in the legend. CASINO simulations run at beam energy 197keV, 10^6 electron histories, for a 8nm thick layer of $In_{0.24}Ga_{0.76}As$ (density = 6.0262gcm^{-3}) in a 236nm GaAs (density = 5.316gcm^{-3}) matrix, where the overlayer is as specified in the legend.

4.8.2 Determination of the depth of a thin layer by matching absorption curves

The two methods presented in this subsection rely on the same principle as equation 4.1.1, that the degree of absorption changes predictably with changing take-off angle. The first method used a model to emulate the effects while the second uses simulations. In either case, the general idea is to find the modelled or simulated curve that best fits the experimental data and thereby matches the experimental sample composition and geometry.

4.8.2.1 Modelled absorption matching

The idea that the absorption changes with take-off angle can be approached from a different direction. If both the sample and the electron beam intensity are assumed to be constant then it is possible to use the ratio of X-ray intensities to determine, via comparison between modelled and experimental results, the depth of the layer and, ideally, the thickness of that layer.

Taking the ratio of the detected intensities for one specific X-ray line of intensity I and attenuation wavelength λ results in the following equation:

$$\frac{I_1}{I_2}=\frac{e^{\frac{-d}{\lambda*\sin(\theta_1)}}}{e^{\frac{-d}{\lambda*\sin(\theta_2)}}}$$ Equation 4.8.2.1.1

where $I_{1,2}$ are the X-ray intensities, $\theta_{1,2}$ the respective take-off angles, λ the attenuation wavelength described in section 4.5 and d is the depth of the layer. This equation can be used to plot a number of curves, each with a different assumed value of d. Matching the simulated to the experimental results could, in principle, yield the depth of the layer.

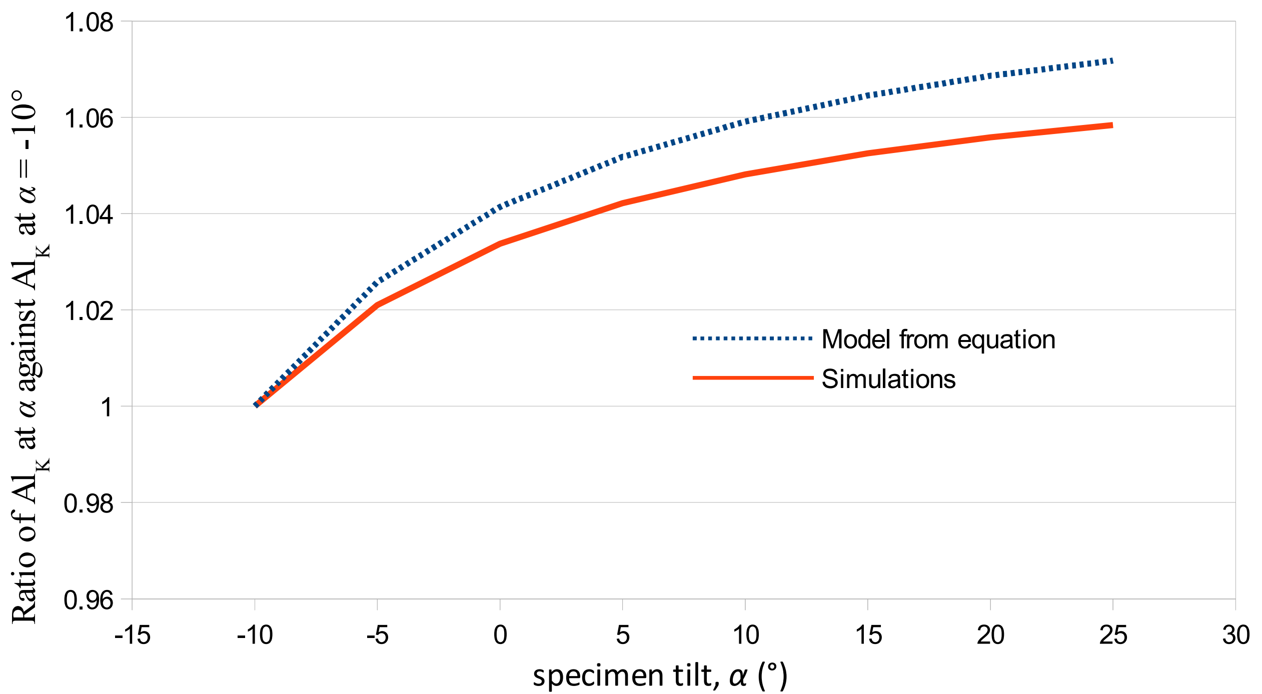

Figure 4.8.2.1.1: Comparison of simulation and model (equation 4.8.2.1.1). Simulation run in NISTMonte at beam energy 197keV with 10^7 electron histories. $\theta = \alpha + 25°$. Sample is comprised of 5nm of pure aluminium at the bottom surface of a 10nm thick GaAs (density = $5.316 gm^{-3}$) overlayer. λ = 369nm. Straggling correction applied to simulated data.

Figure 4.8.2.1.1 shows the result of such a comparison for 5nm of Al under 10nm of GaAs using λ = 369nm. It is clear that the curves are similar but the absolute values differ because of self-absorption in the layer.

Bringing the model closer to the results requires correcting for thin self-absorption in the layer. While this is generally regarded as negligible this appears not to be valid for this method. Correcting for this requires using the following equation:

$$\frac{I_1}{I_2}=\frac{\frac{e^{-\frac{d}{\lambda_{matrix}*\sin(\theta_1)}}*d}{d+\frac{t}{2}}+\frac{e^{-\frac{t}{\lambda_{material}*\sin(\theta_1)}}*\frac{t}{2}}{d+\frac{t}{2}}}{\frac{e^{-\frac{d}{\lambda_{matrix}*\sin(\theta_2)}}*d}{d+\frac{t}{2}}+\frac{e^{-\frac{t}{\lambda_{material}*\sin(\theta_2)}}*\frac{t}{2}}{d+\frac{t}{2}}}=\frac{e^{-\frac{d}{\lambda_{matrix}*\sin(\theta_1)}}*d+e^{-\frac{t}{\lambda_{material}*\sin(\theta_1)}}*\frac{t}{2}}{e^{-\frac{d}{\lambda_{matrix}*\sin(\theta_2)}}*d+e^{-\frac{t}{\lambda_{material}*\sin(\theta_2)}}*\frac{t}{2}}$$

Equation 4.8.2.1.2

where $I_{1,2}$ are the X-ray intensities, $\theta_{1,2}$ the respective take-off angles, $\lambda_{matrix,material}$ are the attenuation wavelengths (described in section 4.5) of the matrix and the layer, respectively, d is the depth of the thin layer and t is the thickness of the layer. This results in the improved curve shown in Figure 4.8.2.1.2, which is obviously superior in accuracy to that seen in Figure 4.8.2.1.1.

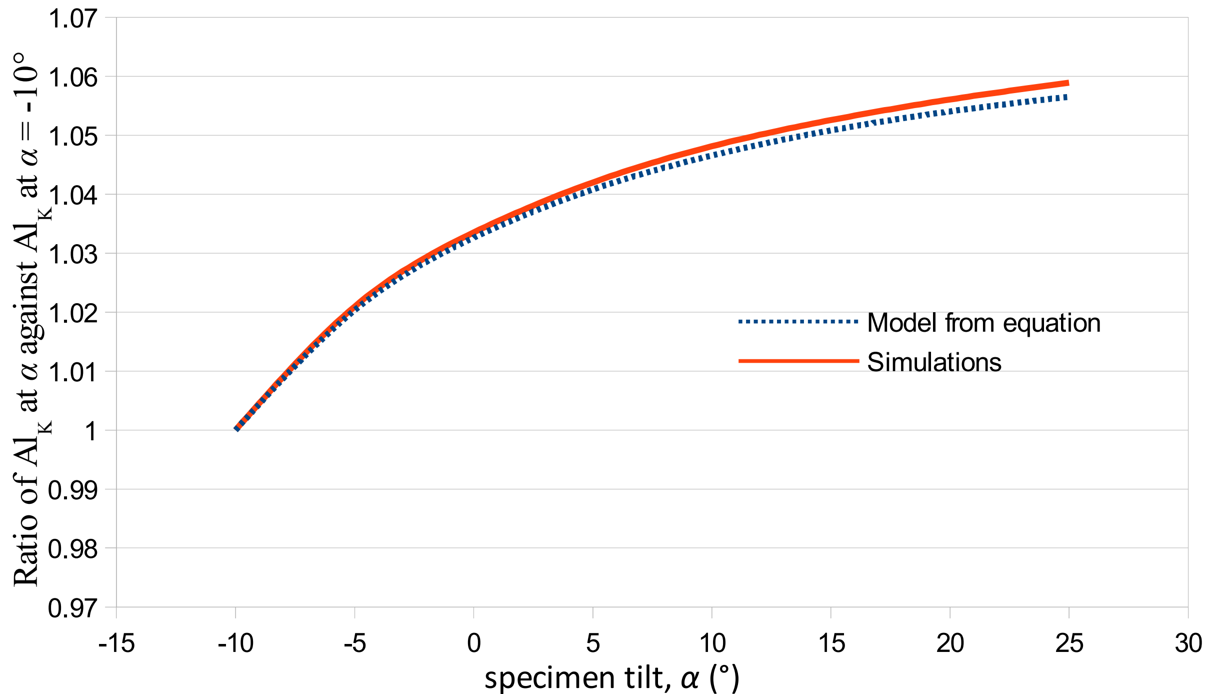

Figure 4.8.2.1.2: Comparison of simulation and model (equation 4.8.2.1.2). Simulation run in NISTMonte at beam energy 197keV with 10^7 electron histories. $\theta = \alpha + 25°$. Sample is comprised of 5nm of pure aluminium at the bottom surface of a 10nm thick GaAs (density = 5.316gm^{-3}) overlayer. λ = 369nm. Simulated data corrected for straggling.

This practice of dividing by another data point is acceptable in simulations where the data points always follow the expected trend, however, in an experimental analysis this is often not the case. If nothing else, statistical error will ensure that no individual data point is a suitable reference for normalising with respect to. The solution to this is to attempt to normalise with respect to each data point in a separate analysis, so that the final conclusion will have a number of results equal to the number of data points in the data set. Determining the values of d and t would be a matter of minimising some numerical value describing the difference between the model and the experimental curve. An obvious candidate would be the χ-squared goodness of fit (i.e. sum of squares (i.e. Σ (modelled value – experimental value)^2 over the entire range)).

4.8.2.2 Simulated absorption matching

The above method ('Modelled Absorption Matching') relies on both the model and the parameters being correct. Another way of approaching the same problem is to use simulations instead of the model of equation 4.8.2.1.2, as this considerably simplifies the problem from the user's perspective by removing the burden of ensuring that the model is correct, both in form and in its parameters. It would also theoretically allow for different geometries, such as where the thin layer is curved or inconsistent in some known way, such as a change in layer thickness or chemical composition. The disadvantage is that this approach is computationally intensive, as each data point must be simulated individually. By normalising a series of simulated curves, each with different overlayer thickness, to a particular experimental data point it is possible to observe how the resulting sum of squares between the simulated and experimental curves varies with overlayer thickness. If this variation has a minimum, then this closest match between the simulations and experiment is the overlayer thickness estimated by this method.

4.8.3 Curve Fit

This approach is built upon the same foundation as equation 4.1.1: as already mentioned, the procedure for calculating λ is to plot the natural log of the X-ray intensity against the effective thickness between the X-ray source and detector. Recognising that the effective thickness can be calculated by

$$t_{eff} = \frac{d}{\sin\theta}$$

where t_{eff} is the distance travelled through the sample between the X-ray point of origin and the detector, d is the depth of the thin layer and θ is the take-off angle. Taking into consideration the fact that take-off angle θ is under direct user control and therefore can be easily manipulated, it becomes clear that λ's definition as the inverse slope of a plot of $\log_e I$ vs. t_{eff} means that it is possible to fit the intensities to that slope by varying the assumed depth. This can be achieved iteratively by either the 'Detector Tilt' or 'Specimen Tilt' methods of λ calculation by inserting a value of d, observing how the calculated λ differs from the known value, then inserting another value of d based on that observation. This process would converge to the correct value for the depth.

Table 4.8.3.1 shows simulated results when using two different λ_{InL} values (5nm thick pure indium layer in GaAs, density = 5.316gcm^{-3}). These two values are from section 4.5.1, where they were calculated by the 'Specimen Tilt' and 'Variable Depth' methods. It is clear that the method functions reasonably well, better for 1970keV beam energy than for 197keV. Both beam energies are consistent in their slopes. While the higher energy results are better than those from lower energy, at 70.5nm, 90.5nm and 110.5nm depth with λ = 2796nm the result is fractionally outside the layer, indicating that an incorrect λ value provides erroneous results, regardless of the quality of the data. Unfortunately, the method does not yet contain an error estimate.

true input depth, d (nm)	fitted depth, d (nm), for:			
	λ = 2776nm (Variable depth)		λ = 2796nm (Specimen tilt)	
	U = 197keV	U = 1970keV	U = 197keV	U = 1970keV
10.5	10.8	10.5	10.9	10.6
30.5	31.0	30.5	31.2	30.8
50.5	51.2	50.5	51.6	50.9
70.5	71.3	70.5	71.9	71.1
90.5	91.4	90.5	92.1	91.2
110.5	111.5	110.5	112.3	111.3

Table 4.8.3.1: Comparison of d values calculated for two different λ values. Simulations run in NISTMonte for 10^7 electron histories. 'Specimen Tilt' method used. U is electron beam energy.

4.8.4 Piecewise curve fit

As already mentioned, the weakness of the above method is a reliance on minimal noise and data scatter. This is not always experimentally feasible, most commonly due to either insufficient counting statistics (leading to noise) or inconsistent sample composition such as the thin layer changing thickness or the chemical composition of the sample along the X-ray path changing (leading to data scatter). A potentially superior method would be to consider each data point separately and attempt to fit a curve that utilises only the most reliable points.

Given that a plot of natural log of the intensity against effective depth (i.e. ln I vs. $d / \sin(\theta)$) will be linear, it is simple to consider a data point and then use λ to calculate where the adjacent points should be. For example, for a data set that begins at +15° take off angle and increases by 5° to 50°, it would be possible to take the natural log of the intensity at the +25° data point and then calculate using λ the expected natural log of the intensities for +20° and +30°, as sketched in Figure 4.8.4.1.

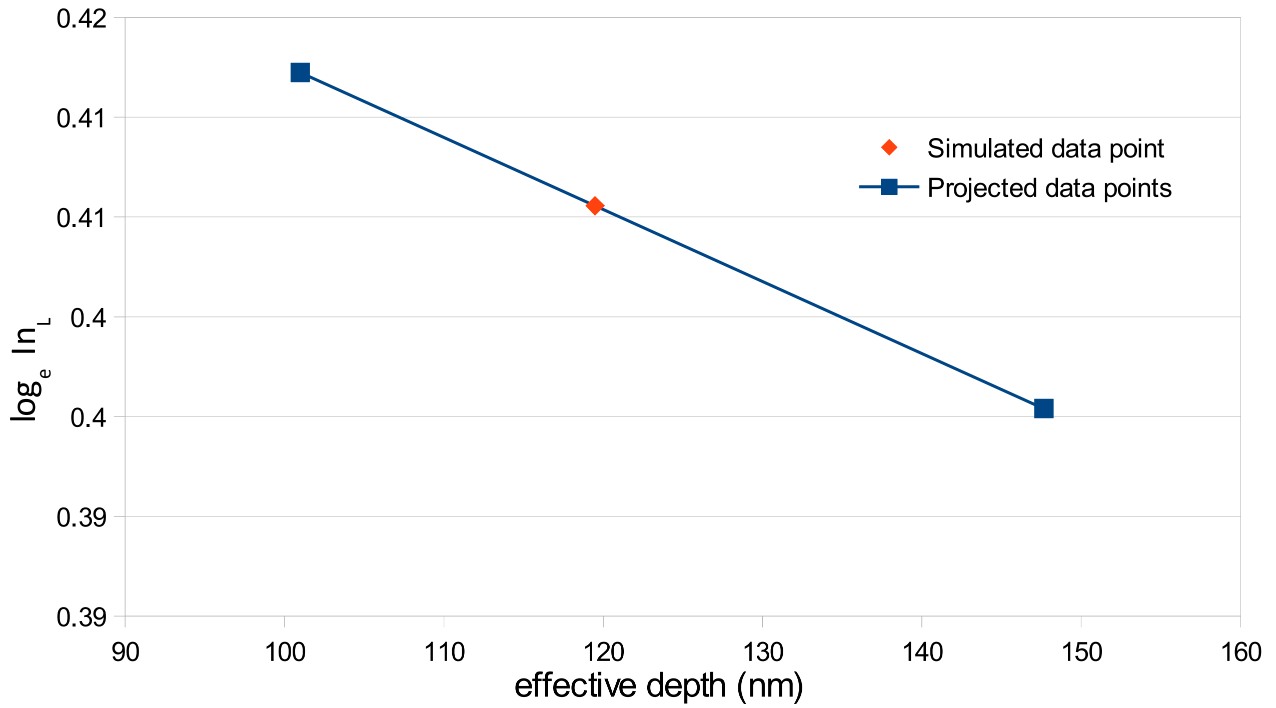

Figure 4.8.4.1: Demonstration of method: how λ (= 2770nm) can be used to plot a linear curve centred around a known data point. Effective depth = actual depth (d) / sin (take-off angle (θ)).

Doing the same for every data point would effectively give a series of linear plots, as shown in Figure 4.8.4.2.

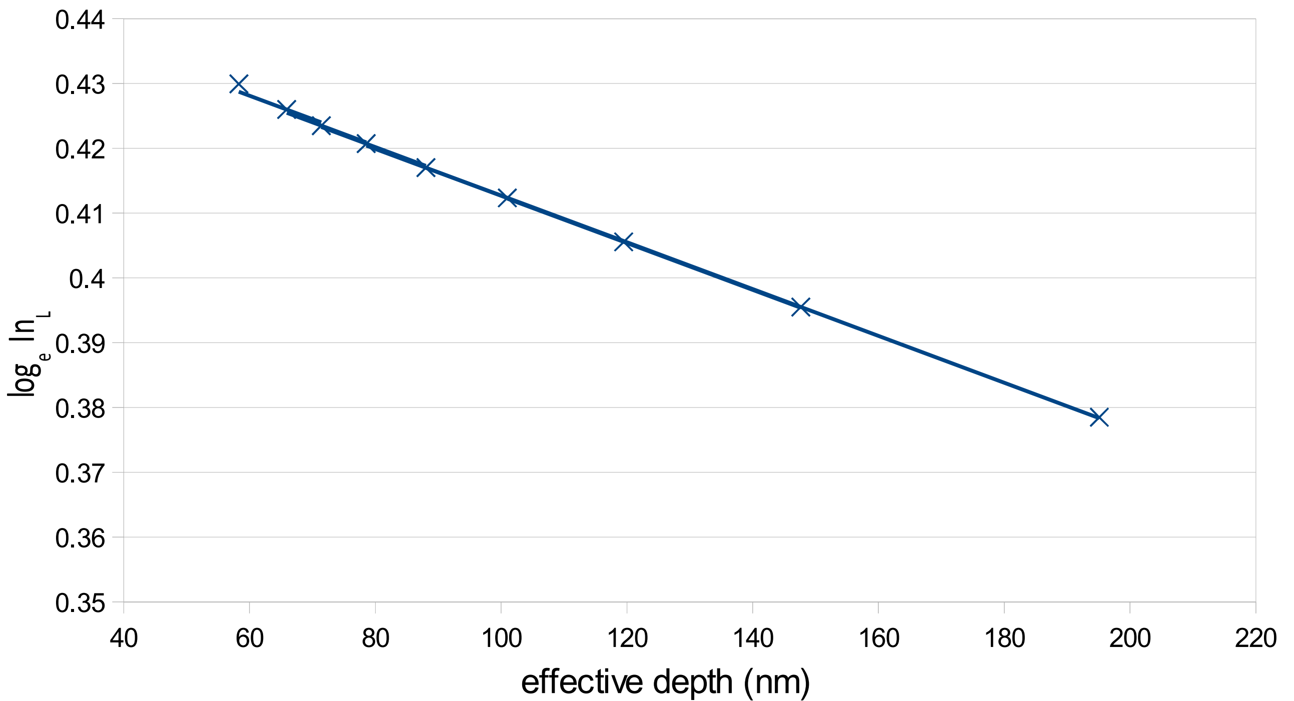

Figure 4.8.4.2: Extension of Figure 4.8.4.1 to an entire tilt series. λ = 2770nm. Effective depth = actual depth (d) / sin (take-off angle (θ)). d = 50.5nm. θ = 25°. Simulation run in NISTMonte at beam energy 197keV with 10^7 electron histories. Sample is comprised of 1nm of InAs (density =

5.67gcm^{-3}) at the bottom surface of a 50nm thick GaAs (density = 5.316gm^{-3}) overlayer.

Varying *d* will then cause the plots to change accordingly, which can be exploited to bring the curves together. The ideal would be to overlap the projected points with the actual, however doing so in every instance would mean that this method is not required (as the previous technique would function well enough) and so instead the user can attempt to get the best fit by eye.

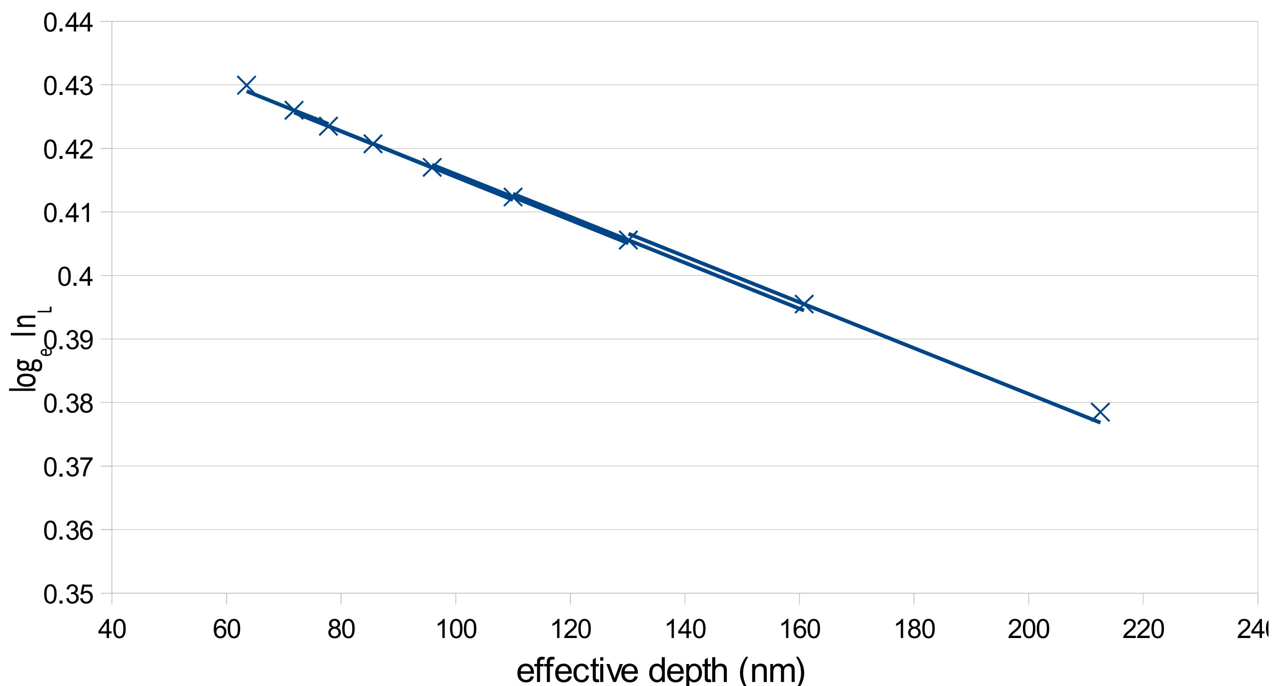

Figure 4.8.4.3:Complement to Figure 4.8.4.2, using d = 55nm to demonstrate the change. λ = 2770nm. θ = 25°. Effective depth = actual depth (d) / sin (take-off angle (θ)). Simulation run in NISTMonte at beam energy 197keV with 10^7 electron histories. Sample is comprised of 1nm of InAs (density = 5.67gcm^{-3}) at the bottom surface of a 50nm thick GaAs (density = 5.316gm^{-3}) overlayer.

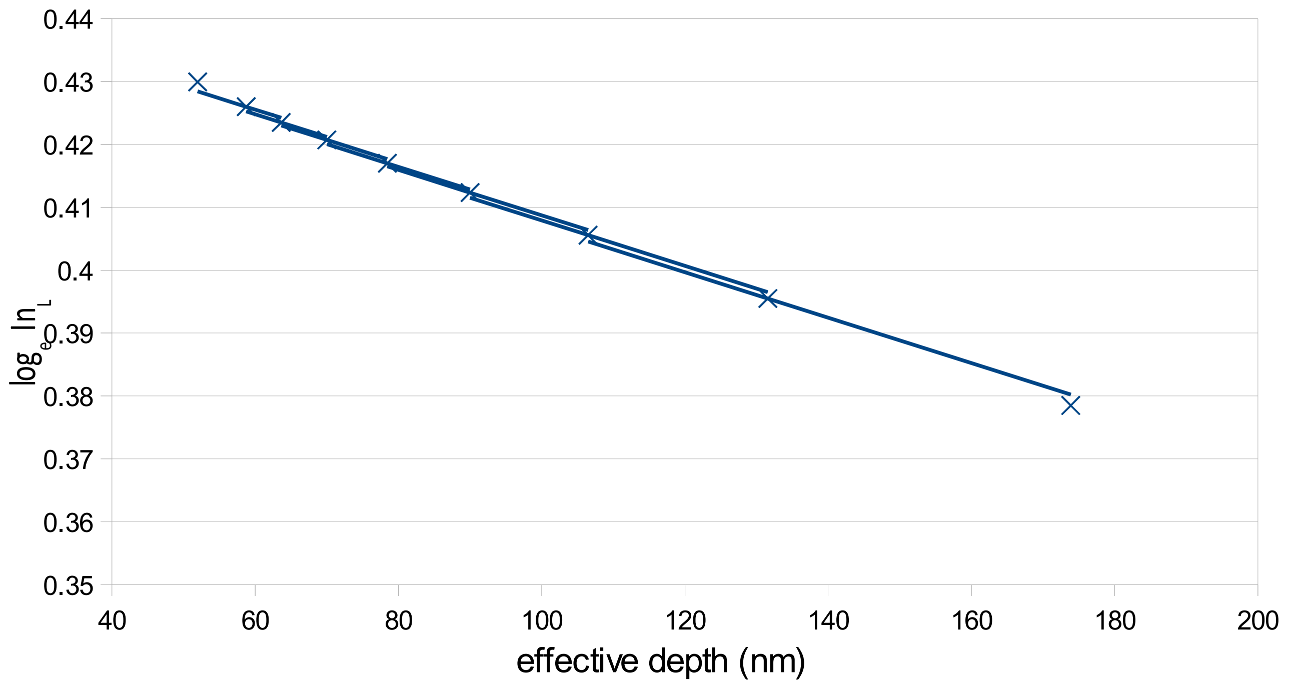

Figure 4.8.4.4: Complement to Figure 4.8.4.2, using d = 45nm to demonstrate the change. λ = 2770nm. θ = 25°. Effective depth = Actual depth (d) / sin (take-off angle (θ)). Simulation run in NISTMonte at beam energy 197keV with 10^7 electron histories. Sample is comprised of 1nm of InAs (density 5.67gcm^{-3}) at the bottom surface of a 50nm thick GaAs (density = 5.316gm^{-3}) overlayer.

The difference between Figure 4.8.4.3 and Figure 4.8.4.4 is very slight to the eye, despite a relative change of 20% of the true depth. This, unfortunately, means that the method is not sensitive enough to be useful experimentally, as a change in the order of magnitude in the estimated depth is required to cause a perceptible change in the graph. Note that applying a numerical means of comparing accuracy (such as summing the differences between all projected data points and their experimental counterparts) would transform this method into that seen in section 4.8.3.

4.9 Conclusion

The details of equation 4.1.1 were explored. In simulations, this method worked very well, giving distinct, well-defined Gaussian distributions even for very thin overlayers. This method was also shown to work in simulations for double and triple layer systems, being potentially sensitive to changes even when the additional layers are somewhat deeper than the first.

The means of calculating the variable λ was also discussed. Comparison of the different methods of calculation led to the conclusion that while the detector tilt method gives results closest to the mean, this seems to be a result of its large uncertainty. Even though the 'specimen tilt' method of calculating λ is not the exact equivalent of the 'variable depth' method, the difference is sufficiently small as to likely be negligible for experimental conditions. Looking at different materials saw that there are some trends that can be exploited: the constancy of the ratio of $\lambda_{InL}/\lambda_{SbL}$ seems especially interesting. It was also discovered that the user must be aware that fairly soft X-rays can see a change in λ due to the thickness of the thin layer: this could, in some cases, allow a user to determine the thickness of the layer.

Further, several other methods of determining the depth of thin layer, mostly extrapolations of equation 4.1.1, were discussed. In each case, the theoretical results seem promising, though their experimental efficiency was not discussed. In particular, the graphical methods ('Graphical comparison' and 'Piecewise curve fit') may be susceptible to variations in perception between users, while the remainder could suffer from statistical or over-sensitivity problems.

Comparison to existing methods (that described in section 2.6.2 would be one example) leads to the conclusion that in theory, these methods could be extremely useful, for example where tilting the sample is possible but changing the beam voltage to appreciable affect would not.

5 Experimental results for methods shown in Chapter 4

5.1 8nm thick $In_{0.24}Ga_{0.76}As$ layer embedded 95nm deep in a GaAs matrix

Figure 5.1.1 shows the EDX spectrum from a $In_{0.24}Ga_{0.76}As$ layer buried under 95nm of GaAs using 5° shielding by the sample holder, acquired over the course of an afternoon. This composition and layer thicknesses were confirmed by EDX analysis and imaging of the layer in a cross-sectional sample, as seen in Figure 5.1.3.

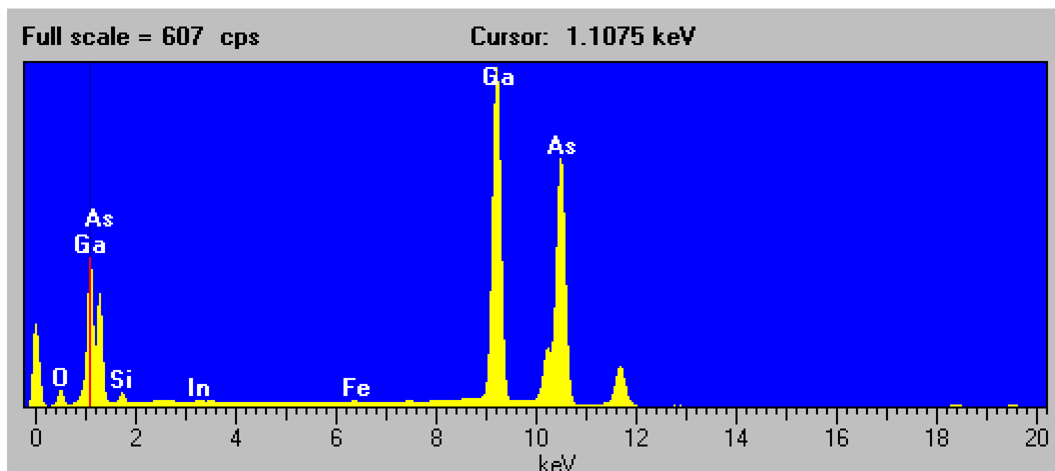

Figure 5.1.1: EDX spectrum for this experimental sample. 0° specimen tilt.

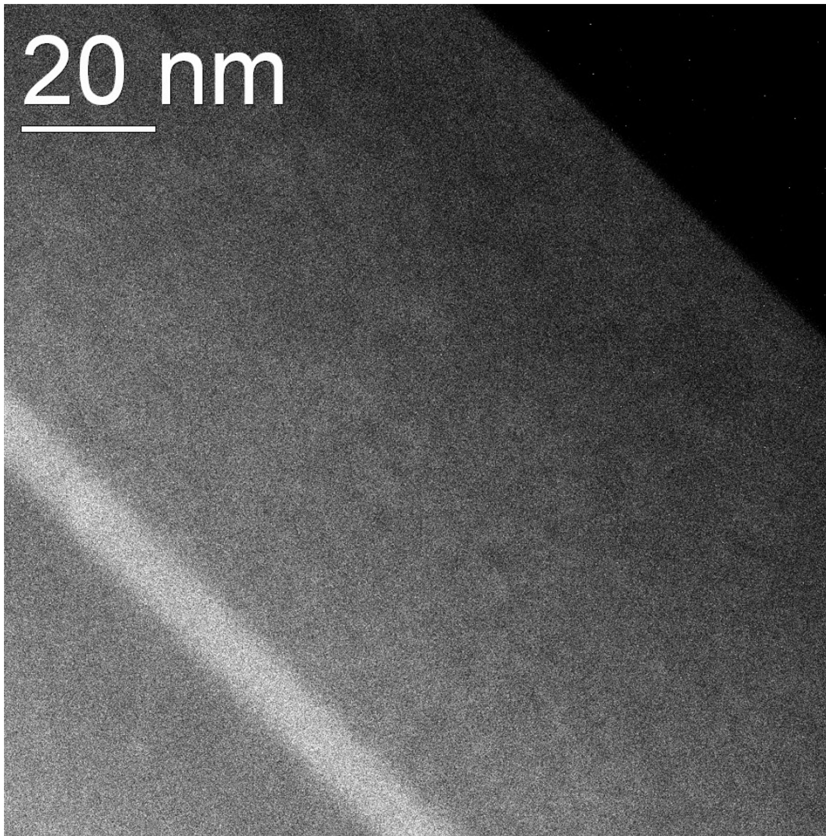

Figure 5.1.2: ADF-STEM of cross-sectional sample.

Figure 4.4.2 shows the livetime-corrected In_L intensity from this sample recorded in plan-view (top) geometry. Note that the corrections are sequential from top down (i.e. 'Tilt corrected' also has the livetime correction, while 'Shielding corrected' has all three corrections). It is clear that the general form but not the extent of the shielding corrected experimental curve matches the simulated data, albeit with considerable scatter. Note that several tilts have two readings, which generally lie within each other's error bars.

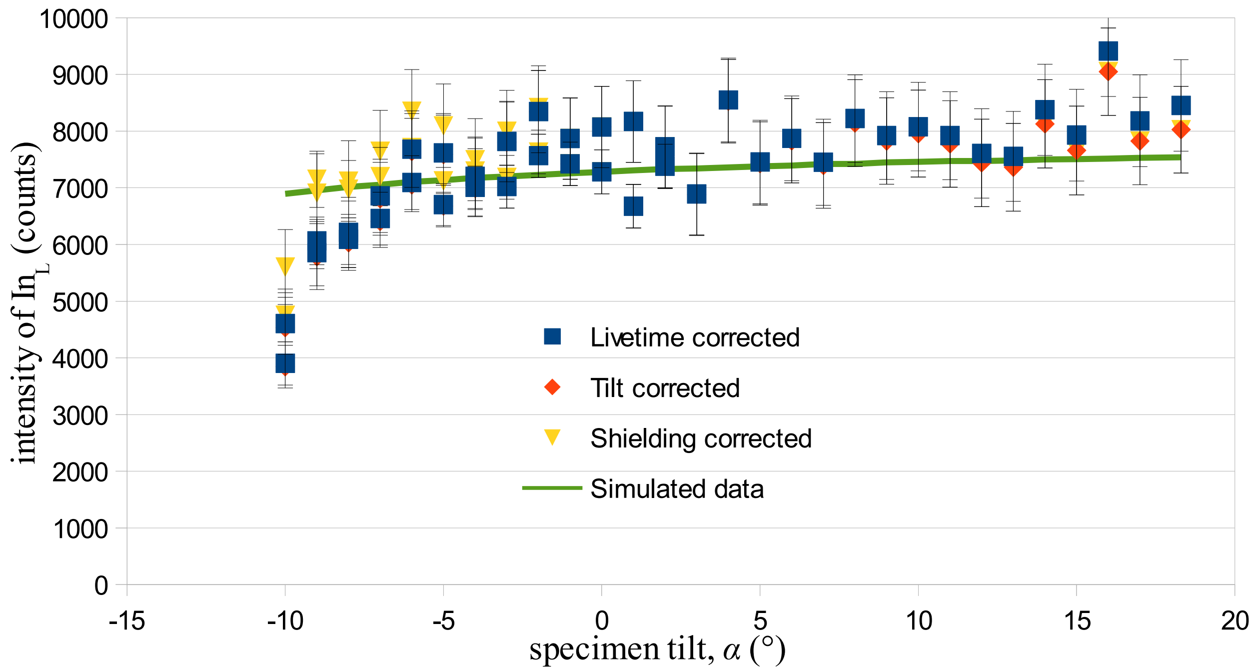

Figure 5.1.3: Experimental results from a GaAs sample with an 8nm $In_{0.24}Ga_{0.76}As$ embedded 95nm deep within. Note that when the data points from several ranges overlay each other for a significant range of sample tilts, most significantly for 'Tilt corrected', which is only particularly visible for greater than ~+12° tilt. Simulation normalised with respect to experimental 0° tilt data point. The simulated data has been corrected for tilt but not for shielding by the specimen holder. $\theta = \alpha + 25°$. Simulation run in NISTMonte at beam energy 197keV with 10^6 electron histories, for a 8nm $In_{0.24}Ga_{0.76}As$ layer at the bottom surface of a 94nm thick GaAs (density = 5.316gm^{-3}) overlayer.

5.1.1 Using equation 4.1.1

The result of applying equation 4.1.1 to calculate the depth of the $In_{0.24}Ga_{0.76}As$ layer solely from the above plan-view measurements is shown in Figure 5.1.1.1. It is clear that there is a tremendous amount of scatter, including many numerical results which are either negative (indicating that the slope is trending downward with increasing tilt) or measured in the microns: too large to be physically reasonable for an electron transparent sample. There could be a very slight maximum in the range of 100-120nm, though given the scatter and the number of physically impossible results this is not to be considered significant. Taking an average of all values between 0nm and 500nm gives 200.0±132.1, which is both far larger than the nominal and also has a relative error that is large enough that no meaningful conclusion can be drawn. Fitting a curve using the equation A * (1-e$^{(C+\text{offset})}$) and Excel's SOLVER function gives results that are more consistent but ranging from ~700nm to ~2nm, with no obvious means of differentiating which are correct.

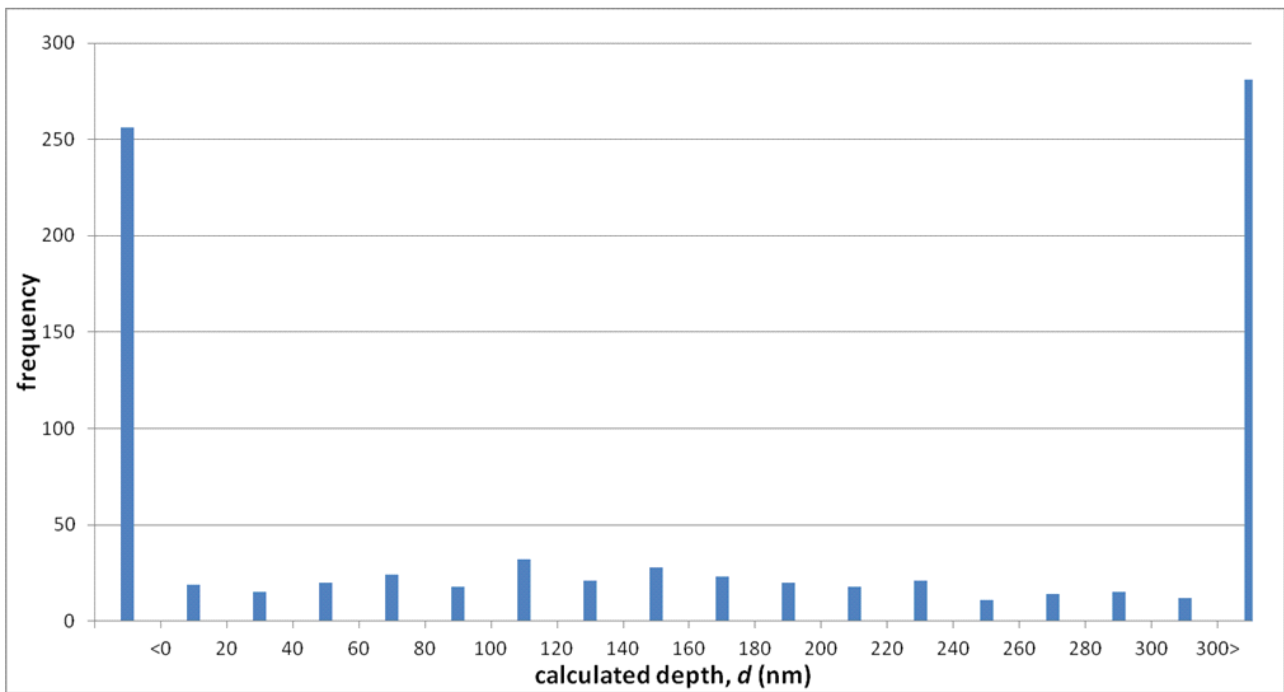

Figure 5.1.1.1: Histogram of calculated d from Figure 4.4.2. λ = 2525nm. Nominal d is 99nm. Average of all values between 0nm and 500nm = 200.0±132.1, where 45.5% of all data points fall into that range.

Attempting the analysis with different parameters for the shielding correction does not give appreciably better results.

Attempting to normalise with respect to As_K gives the results shown in Figure 5.1.1.2, where the detector efficiencies of In_L and As_K were estimated as 73% and 79%, respectively (Figure 2.3.1). Note that the λ is so different so as to follow the trend found in section 4.5.2, though using much smaller values does not produce results closer to the expectation. Again the scatter is large, this time without even a small maximum.

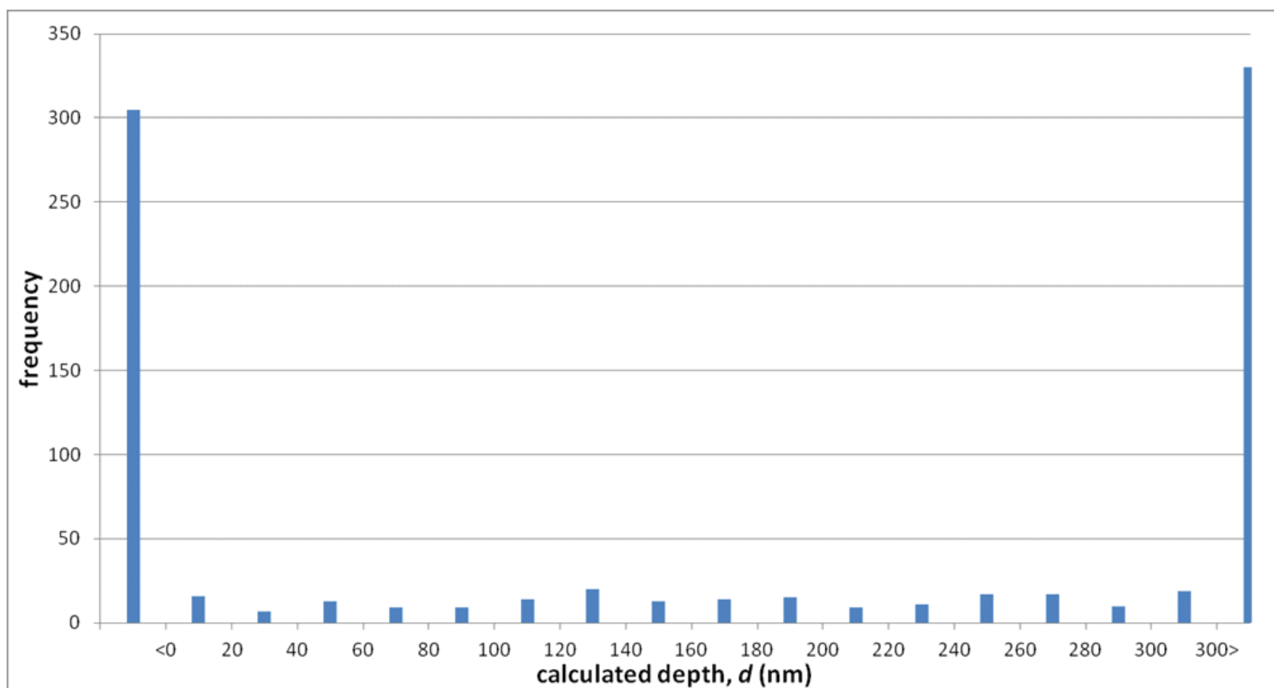

Figure 5.1.1.2: Histogram of calculated d using In_L/As_K from the sample in Error: Reference source not found. λ = 3900nm. Nominal d is 99nm. Average of all values between 0nm and 500nm = 233.8±132.4, where 33.8% of all data points fall into that range.

It is reasonable to conclude that despite the apparently correct trend of the data, no answer can be found using equation 4.1.1 for this sample. This is likely due to the large statistical error in the data. It should be noted that the total indium content, averaged over the sample thickness, was 0.9at% and as such this difficulty is not entirely unexpected.

5.1.2 Graphical Comparison

Figure 5.1.2.1 shows simulated results for different overlayer thicknesses using the ratios of In_L to As_K or In_L to As_L, where the thin layer is moved about within a matrix of thickness 424nm, where this thickness was arrived at as an estimate by comparison with simulations. This causes the distinctive change in the ratios seen in Figure 4.8.1.1. For reference, arsenic was chosen instead of gallium as the quantity of As is homogeneous throughout the sample, while the Ga concentration drops in the layer of interest: this drop would cause a slight, undesirable change in the ratio. The experimental In_L/As_L curve has too strong a slope to match any of the simulated curves: taking this result naïvely would imply that the layer is possessed of negative depth, which is impossible. It is worth considering that the total assumed thickness could be incorrect (in this case the total thickness was calculated using NISTMonte simulations of a KL intensity ratio (Chapter 6) for self-consistency), as this would indeed cause the slope to become stronger, bringing about a better match between experiment and simulations for In_L/As_L but worsening for In_L/As_K. While the InL/AsL curve does have a distinctive slope, there is too much scatter to be certain of matching a curve to a better accuracy than ~±100nm. The In_L/As_K shows far too much scatter to draw any conclusion at all. As seen in Figure 4.8.1.3, the slope of the simulations is in doubt. From this, it is possible that the NISTMonte In_L/As_L curve does not have a strong enough slope. If this is the case then the experimental In_L/As_L could be reasonable and not an issue with the experimental data.

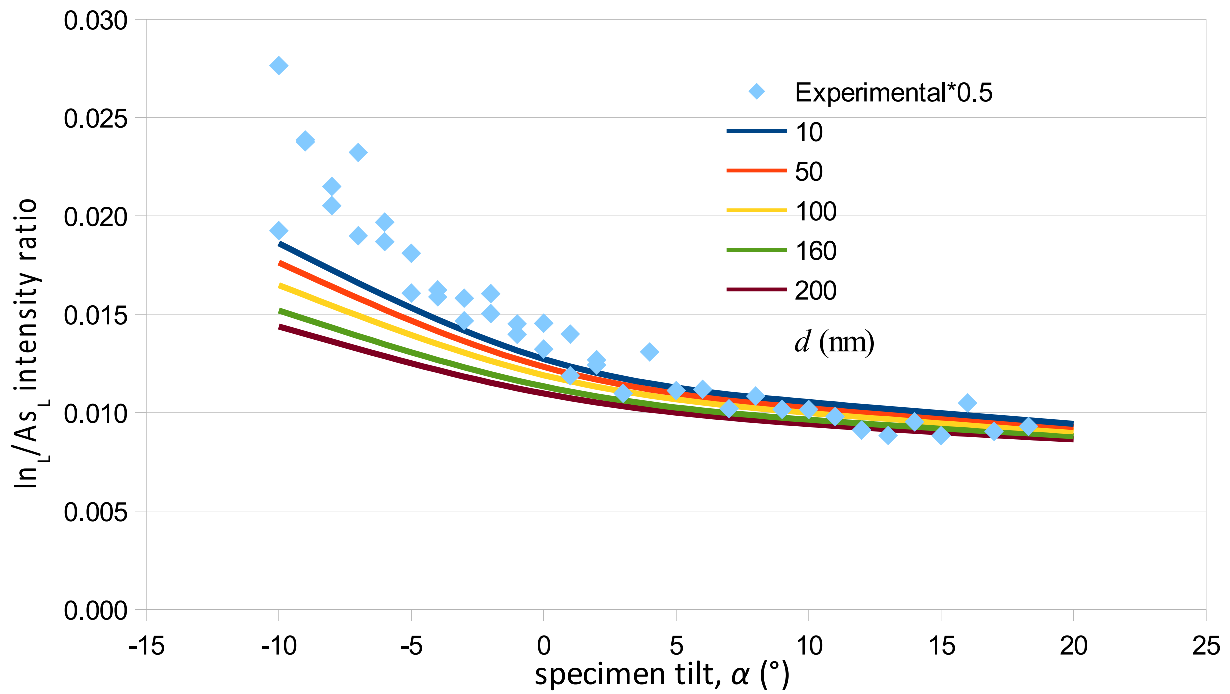

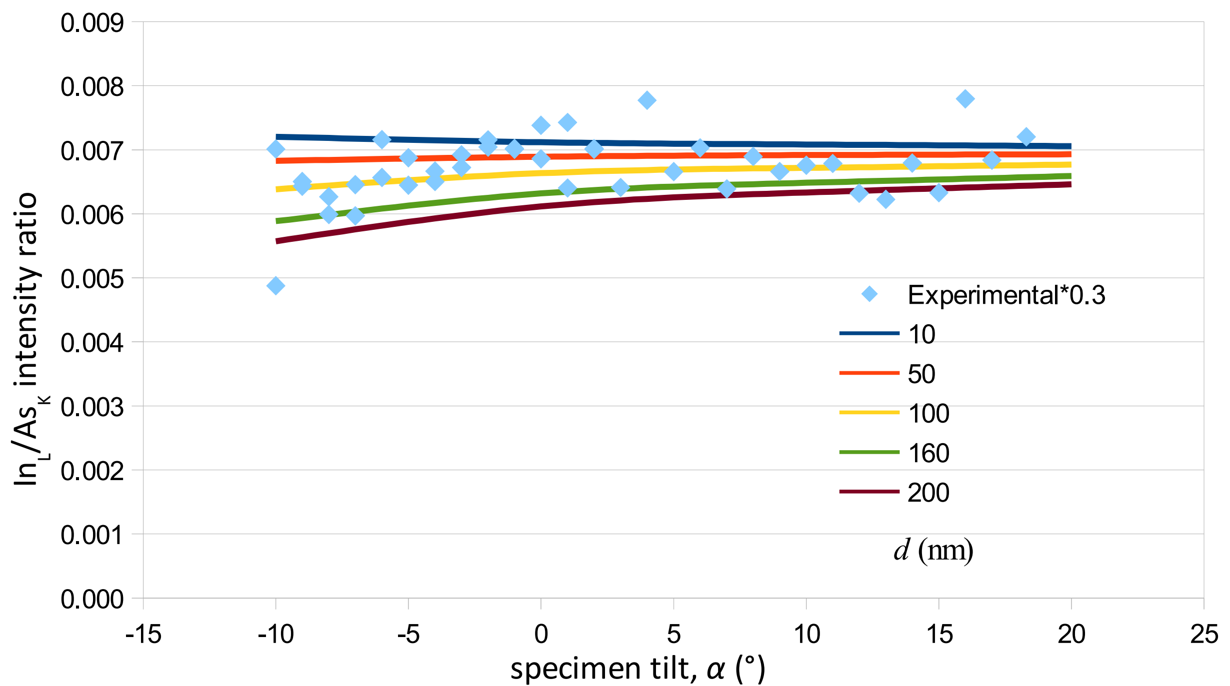

Figure 5.1.2.1: Results for 8nm $In_{0.24}Ga_{0.76}As$ with different overlayer thicknesses, with a nominal value of 95nm. Simulation run in NISTMonte at beam energy 197keV with 10^7 electron histories. $\theta = \alpha + 25°$. Simulated results run at beam energy 197keV, 10^6 electron histories, for a 424nm thick matrix GaAs (density = 5.316gcm^{-3}) with the overlayer thickness specified in the legend, $In_{0.24}Ga_{0.76}As$ (density = 6.0265gcm^{-3}) thin layer and specimen tilts between -10° and +20° in steps of 10°. Note that the experimental data was multiplied by a constant so as to arrive at the same scale as the simulations. Detector efficiencies were assumed to be for experimental data In_L: 73%, As_L: 68%, As_K: 0.79%.

5.1.3 Modelled Absorption Matching

Table 5.1.3.1 shows the result of equation 4.8.2.1.2 being applied to the data by automated trial and error through Microsoft Excel 2007's SOLVER functionality. To avoid local minima, the nominal values for both depth and thickness were given as the initial guesses. Both the In_L and In_L/As_K curves were used, where λ for In_L/As_K was calculated with respect to that of In_L according to the values described in 4.5.2. The most obvious fact is that the thickness of the layer seems to have no significant effect on the result, as attempting the analysis with either a varying or constant thickness does not materially change the result: this is a function of the fact that the λ values for the matrix and layer are very similar. The In_L results are fairly reasonable though too high, while the In_L/As_K results still posses the same cohesiveness as the In_L but are considerably too large. The outliers in the In_L data were taken as the -10°, -6° and +16° data points, as these were a factor of 2 larger than the others or gave a depth of near zero. The differences in the average results between In_L and In_L/As_K are the result of the difference in λ: reducing this difference by using a smaller value for In_L/As_K causes the difference to become smaller. Lowering λ, however, cannot be reconciled with that value determined in 4.5.

The overall trend for the In_L results to yield too high apparent depth values can be understood as either the result of using λ values that are themselves too high or that the experimental curvature of the slope in the experimental data is too strong for the nominal composition. λ has been calculated in multiple ways and as such is unlikely to be incorrect, and so it is the logical conclusion that the curvature is stronger than anticipated. Whether this is due to sample inconsistency, the nominal geometry being incorrect or some other factor not accounted for in the model is not currently clear.

	In_L, λ_{matrix} = 2525nm, λ_{layer} = 2602nm				In_L/As_K, λ_{matrix} = 3913nm, λ_{layer} = 4033nm			
Tilt normalised to (°)	depth of layer	thickness of layer	depth of layer	thickness of layer	depth of layer	thickness of layer	depth of layer	thickness of layer
-10	532.1	0.0	539.1	8	740.3	0.0	747.0	8
-9	162.0	0.0	166.4	8	518.9	0.0	524.5	8
-8	185.1	0.0	189.6	8	371.7	0.0	376.6	8
-7	124.2	0.0	128.3	8	246.0	0.0	250.4	8
-6	0.0	4.0	2.9	8	274.3	0.0	278.8	8
-5	125.6	0.0	129.7	8	324.9	0.0	329.6	8
-4	204.2	0.0	208.7	8	354.4	0.0	359.1	8
-3	178.5	0.0	182.9	8	377.3	0.0	382.1	8
-2	112.0	0.0	115.8	8	334.7	0.0	339.3	8
-1	204.9	0.0	209.4	8	441.9	0.0	446.9	8
0	212.9	0.0	217.4	8	545.4	153.4	490.0	8
1	269.5	77.5	245.1	8	553.4	157.8	495.6	8
2	248.0	72.7	226.1	8	524.2	146.4	470.5	8
3	193.8	56.3	177.0	8	487.8	138.4	438.1	8
4	273.5	0.0	278.3	8	467.2	132.3	420.9	8
5	176.9	47.7	163.6	8	414.0	0.0	419.1	8
6	210.2	0.0	214.8	8	390.7	0.0	395.7	8
7	119.0	0.0	123.0	8	458.4	0.0	463.6	8
8	263.6	0.0	268.5	8	500.4	0.0	505.8	8
9	195.3	0.0	199.9	8	483.1	0.0	488.3	8
10	222.8	0.0	227.5	8	485.1	0.0	490.3	8
11	179.2	0.0	183.6	8	401.8	0.0	406.8	8
12	96.8	0.0	100.6	8	478.5	0.0	483.7	8
13	83.2	14.3	81.0	8	493.3	0.0	498.6	8
14	268.0	0.0	272.9	8	529.8	0.0	535.2	8
15	156.0	0.0	160.2	8	640.7	171.2	574.3	8
16	571.4	153.7	506.1	8	442.2	0.0	447.2	8
17	206.0	0.0	210.5	8	402.9	0.0	407.8	8
18.3	263.7	0.0	268.6	8	333.0	0.0	337.6	8
Average depth with all data points	208.2±114.5		206.8±107.5		448.8±105.5		441.5±97.0	
Average depth with outliers removed	189.8±56		190.4±54.8		Not applicable		Not applicable	

Table 5.1.3.1: Result of applying equation 4.8.2.1.2 to a 8nm thick $In_{0.24}Ga_{0.76}As$ layer with a 95nm GaAs overlayer. λ_{layer} calculated using mass-absorption coefficient from XCOM [66] and density from NSM archive [67]. Note that a value of '0.0' means a value of 0.001, which was the minimum permitted to the function.

5.1.4 Simulated Absorption Matching

Figure 5.1.4.1 shows the above named method applied to the sample. Only a representative sample of the curves are shown. The scatter in the curves is predominantly from counting statistics, as the number of electron trajectories in each simulation was limited to produce an answer in a reasonable timeframe. Not all curves have a minimum: in Figure 5.1.4.1 the +12° tilt curve does not. A curve without a minimum would either be monotonically rising or monotonically falling. A rising curve implies that the actual overlayer thickness is smaller than the minimum simulated value for overlayer thickness while a falling curve would imply that the overlayer thickness is larger than the maximum simulated. In this data set, overlayer thicknesses between 2nm and 200nm were simulated, so a curve without a minimum would either mean an overlayer thickness of <2nm or a value far larger than 200nm. In both cases, these values would be omitted as the result of outliers, which can be justified by comparing experimental and simulated curves (not shown here).

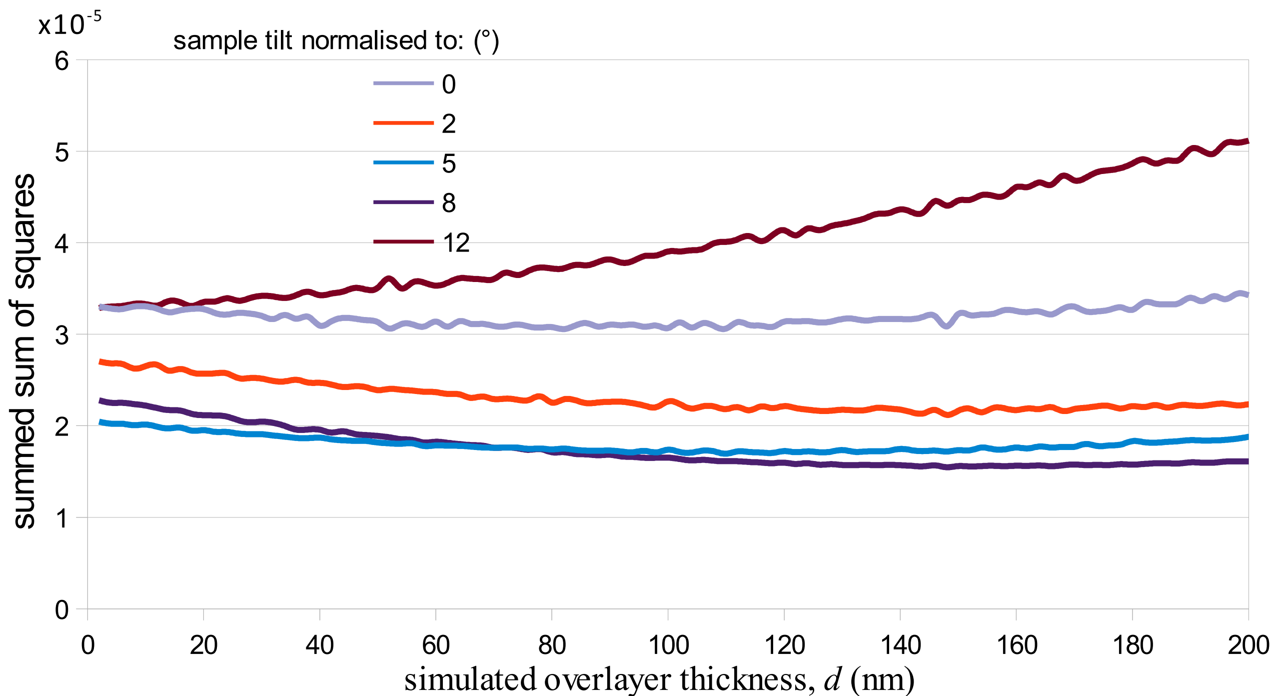

Figure 5.1.4.1: In_L/As_K summed sum of squares for 8nm $In_{0.24}Ga_{0.76}As$ layer under 95nm of GaAs. Simulated results run at beam energy 197keV, 10^6 electron histories, for thicknesses between 2nm and 200nm in steps of 2nm and specimen tilts between -10° and +17° in steps of 1°, followed by 18.3°. $\theta = \alpha + 25°$. Sample composition as described with GaAs (density = 5.316gcm^{-3}) and $In_{0.24}Ga_{0.76}As$ (density = (6.0265gcm^{-3}). Detector efficiencies In_L: 73%, As_K: 79%.

Table 5.1.4.1 shows the results of this analysis for both In_L and In_L/As_K. The raw 'base' data was smoothed by averaging over two ('Pairs') and three ('Triplets') data points. It is immediately apparent that the In_L results do not have many minima and those that do are almost uniformly larger than expected. Each of the In_L vs. overlayer thickness curves were monotonically falling, which implies that the In_L data indicates a much deeper layer than the nominal. The In_L/As_K results, however, give results that are fairly reasonable, with some (notably the -10° tilt) that do not give minima. The average of the results is fairly close to the nominal, though the error is very large. The fact that the two data sets do not agree implies that the statistical error, which is known to be large

and could produce a false positive for larger overlayer thicknesses, is possibly being counteracted by the As_K normalisation. Despite this, however, the In_L/As_K results are still subject to the extremely large variation that is inherent to this data set, and as such sees considerable inconsistency.

base data set			pairs data set			triplets data set		
specimen tilt, α, normalised to (°)	d (nm) from:		specimen tilt, α, normalised to (°)	d (nm) from:		specimen tilt, α, normalised to (°)	d (nm) from:	
	In_L	In_L/As_K		In_L	In_L/As_K		In_L	In_L/As_K
-10			-9.5			-9		
-9		104	-8.5		148	-8		162
-8		198	-7.5			-7		148
-7			-6.5		104	-6		104
-6	194	36	-5.5		60	-5		70
-5		102	-4.5		104	-4		80
-4		148	-3.5		80	-3		42
-3		76	-2.5	194	24	-2	198	26
-2	186	34	-1.5		18	-1		24
-1		84	-0.5		62	0		62
0		82	0.5		100	1		80
1		136	1.5		104	2		104
2		148	2.5		104	3		148
3		88	3.5		148	4		130
4		188	4.5		180	5		180
5	198	110	5.5		124	6	198	70
6		194	6.5		80	7		80
7		16	7.5		68	8		44
8	198	148	8.5		104	9		70
9		88	9.5		70	10		66
10		104	10.5		84	11		18
11		110	11.5		18	12		
12			12.5			13		
13		4	13.5		6	14		
14	198	104	14.5		6	15		126
15			15.5		158	16		126
16			16.5			17.1		
17		110	17.65		148	In_L/As_K mean:	89.1±46.5,	
18.3		194	In_L/As_K mean:	87.6±49.6		error of mean:	9.9	
In_L/As_K mean:	108.5±54.4		error of mean:	10.1				
error of mean:	11.1							

Table 5.1.4.1: Calculated overlayer thickness for the 8nm thick $In_{0.24}Ga_{0.76}As$ layer at the bottom surface of 95nm of GaAs. Blank cells are those with no minimum. 'Pairs' and 'Triplets' are the result of averaging over two or three experimental data points respectively in order to smooth the curve. Simulated results run at beam energy 197keV, 10^6 electron histories, for thicknesses between 2nm and 200nm in steps of 2nm and specimen tilts between -10° and +17° in steps of 1°, followed by 18.3°. $\theta = \alpha + 25°$. Sample composition as described with GaAs (density = 5.316gcm^{-3}) and $In_{0.24}Ga_{0.76}As$ (density = (6.0265gcm^{-3}). Detector efficiencies In_L: 73%, As_K: 79%.

A histogram of the data in Table 5.1.4.1 is shown in Figure 5.1.4.2. While the data is not perfectly Gaussian, the spread does crudely imply such a distribution and as such the data is likely scattered with some degree of randomness about the means given in Table 5.1.4.1.

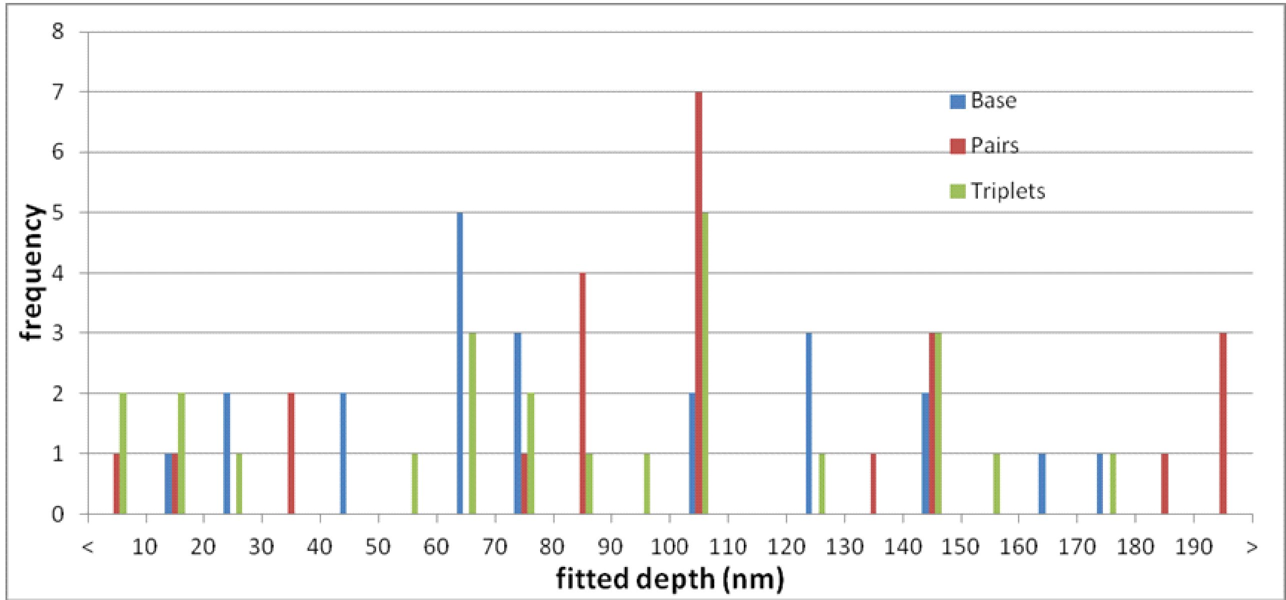

Figure 5.1.4.2: Histogram of data in Table 5.1.4.1. Known correct *d* = 99nm. Average overall: 95.3±50.6nm. Mean error of the mean: 6.0.

5.1.5 Curve Fit

The results from applying the 'Curve fit' method is shown in Table 5.1.5.1. As a test, both the In_L and In_L/As_K data were used. Further, the method was inverted in the third column, by inserting the correct *d* and calculating the resulting λ. The R^2 value indicates the quality of the resulting fit and as such the reliability of the result. It is obvious that the fit is extremely poor and that the calculated values are far from their nominal values. This is despite the fitted lines being visually similar to the experimental when plotted on a graph. Previously, incorrect values given by equation 4.1.1 could be interpreted as data scatter in each individual data point, however the fact that the slope of the curve appears incorrect implies that any correct answer from equation 4.1.1 would be due to chance.

	d at correct λ	λ at correct *d*	R^2
In_L	674.0	370.9	0.329
In_L/As_K	893.5	433.6	0.261

Table 5.1.5.1: Results from 'Curve fit' method.

5.1.6 Piecewise Curve Fit

Figure 5.1.6.1 shows the result of applying this method with a *d* of 99nm, while Figure 5.1.6.2 would be the same calculations performed with *d* = 129nm, for comparison. Both use the same set of data points (3°≥α≥17°), truncated for clarity. The two graphs are very similar, with the change

between them so small as to be imperceptible to the human eye, even with the 23% change seen here. In fact, a tremendous change in the assumed depth is required to introduce a sufficiently large difference so as to be visible to the user: approximately and order of magnitude would be sufficient in this case. The conclusion to be drawn is that while this method does not seem useful for discerning the exact value of the depth, it could give an order of magnitude estimate, which could be useful in some situations, such as for resolving conflicting data that implies a great variety in depths.

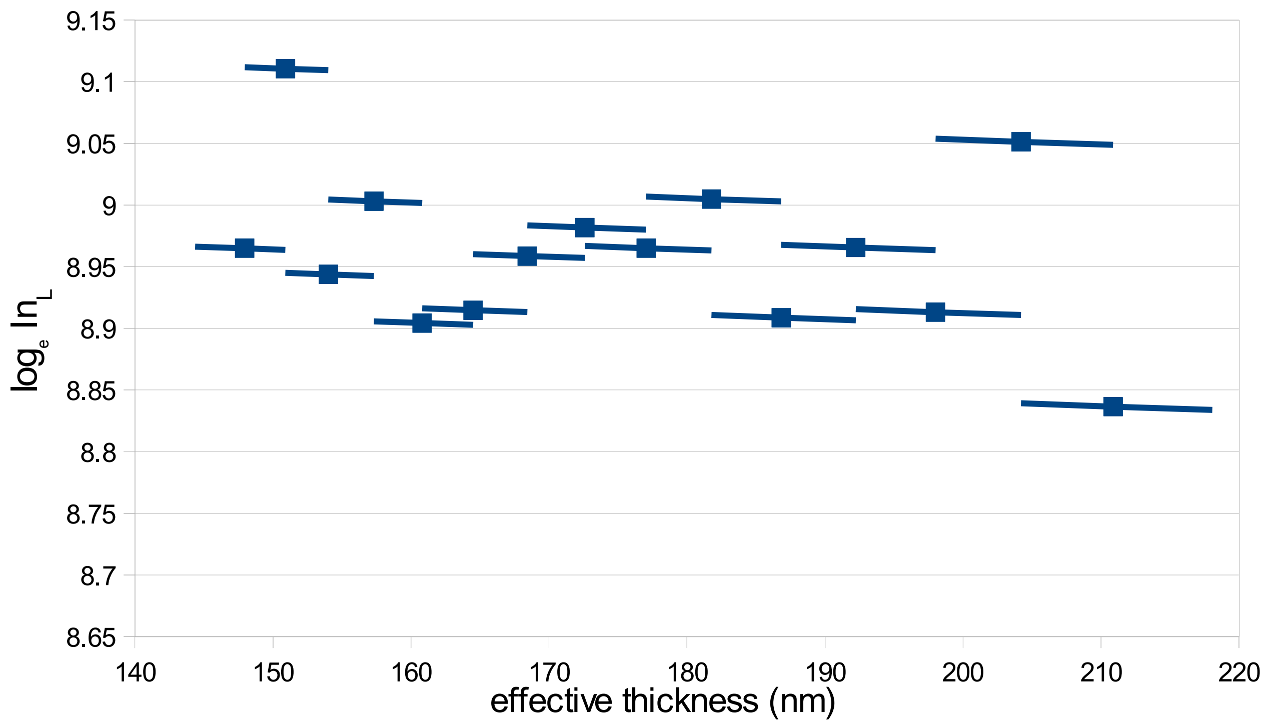

Figure 5.1.6.1: Result of piecewise curve fit method applied to this sample. $\lambda = 2525$, $d = 99$nm.

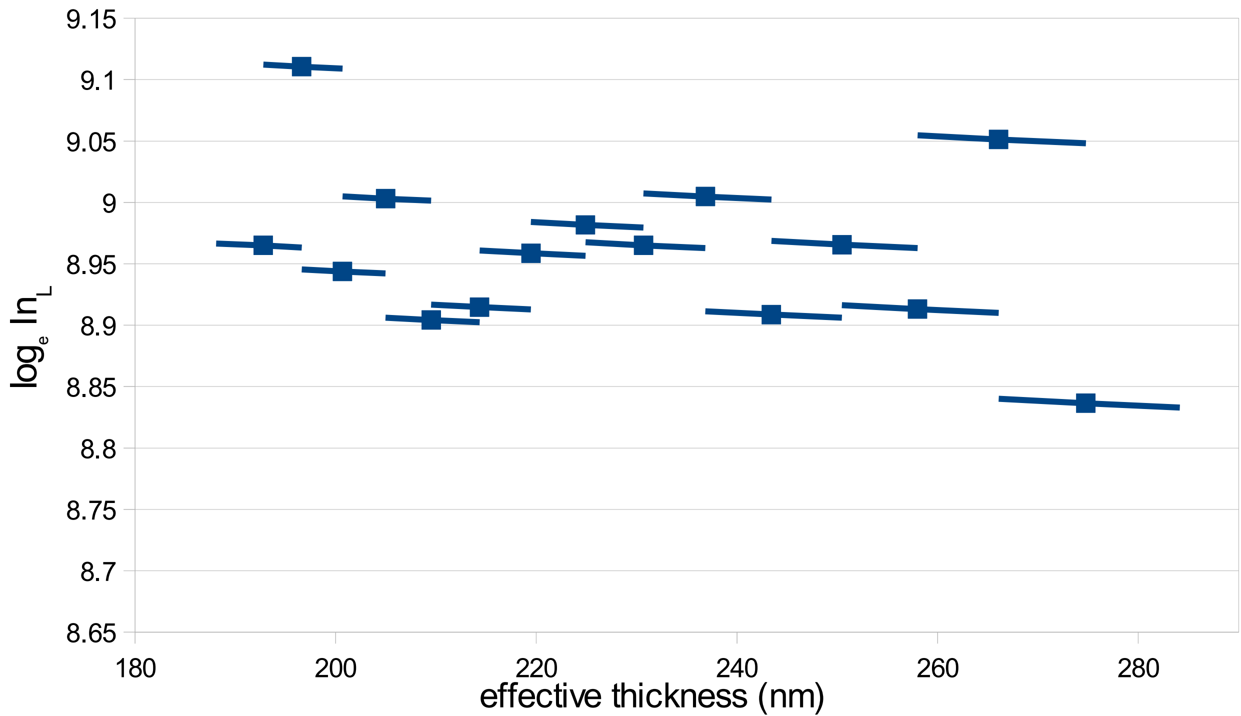

Figure 5.1.6.2: Result of piecewise curve fit method applied to this sample. $\lambda = 2525$, $d = 129$nm.

5.2 Second Sample

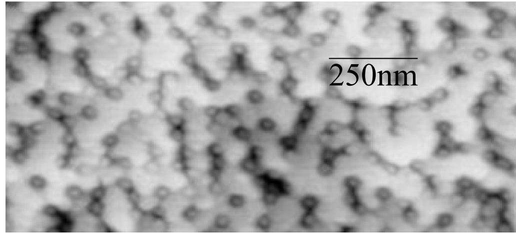

Figure 5.2.1: AFM topographical map of sample [68].

The second sample analysed was a 2nm InAs quantum well nominally embedded 6nm within a GaAs sample using 10° shielding by the sample holder. An AFM topographical map of this sample, shown in Figure 4.4.2, indicates that the capping is partial, so that the expected *d* would vary between 0nm and 6nm.

Whether such a shallow layer would produce enough change in X-ray intensity with changing take-off angle was studied in simulations, giving a calculated *d* shown in Figure 5.2.2 for different depths. It is clear that even such a small change as 2nm can, in theory, be detected.

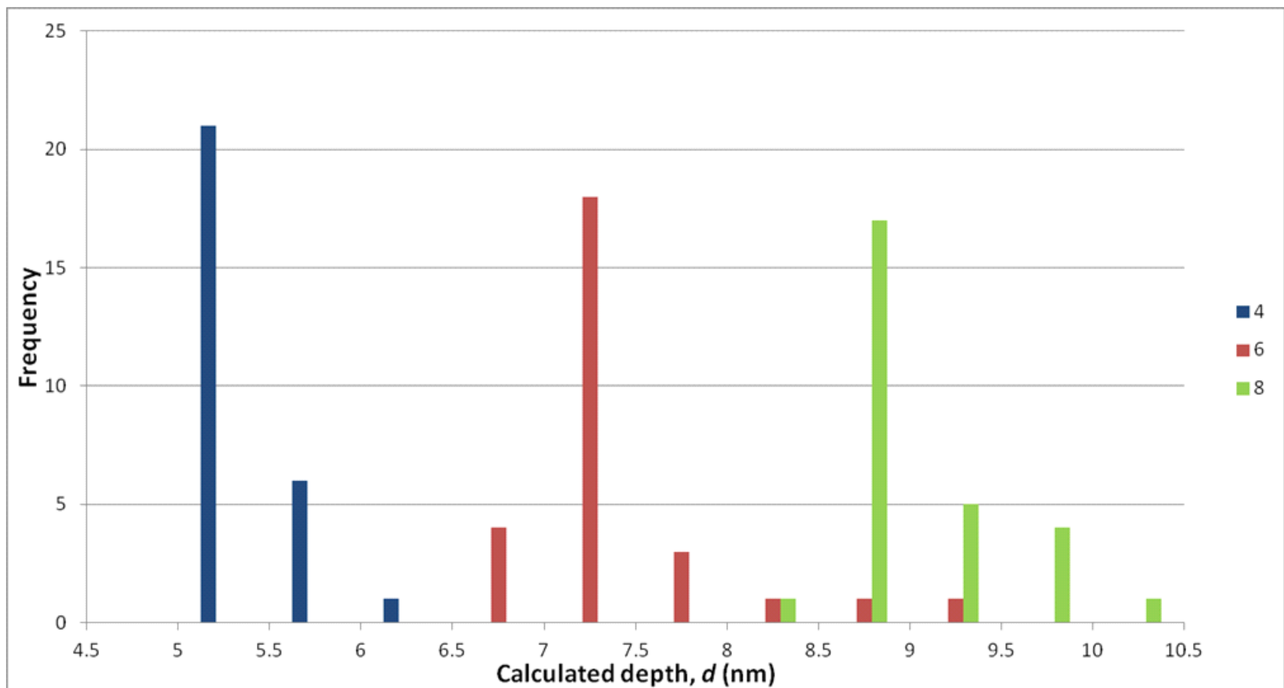

Figure 5.2.2: NISTMonte simulations of 2nm InAs (density = 5.67gcm^{-3}) at the bottom surface of 4, 6, 8nm of GaAs (density 5.316gcm^{-3}). λ = 2770nm. Specimen tilt range -10° to +20° in steps of 5°, where take-off angle is tilt + 25°. Beam energy 197keV and 10^7 electron histories.

Experimental X-ray data from this sample is shown in Figure 5.2.3. It is immediately apparent that, despite the error bars being relatively small, the curve does not match that expected from simulations. This can be attributed to the possibility that a slightly different region was illuminated by the beam when the sample was tilted. This would result in a different amount of absorption thereby violating one of the core assumptions.

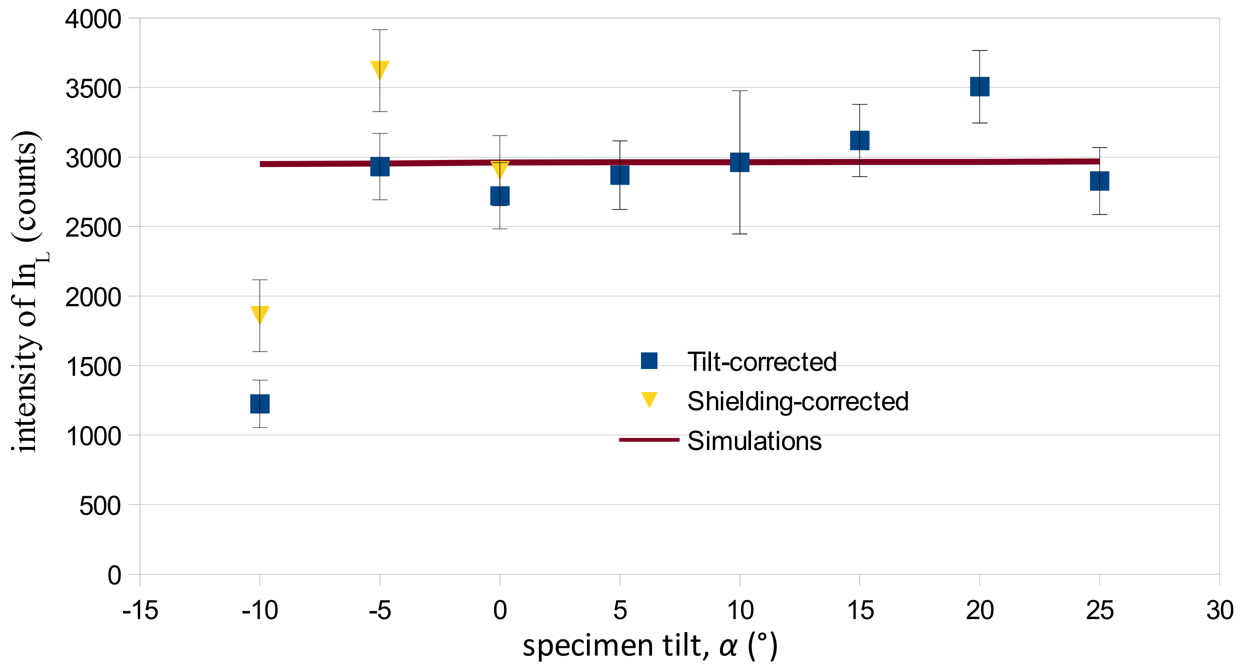

Figure 5.2.3: In_L intensity for a 2nm InAs nominally buried under 6nm of GaAs. $\theta = \alpha + 25°$. Simulated curve scaled with respect to +10° experimental data point, and is corrected for tilt but not shielding. Simulation run in NISTMonte at beam energy 197keV, 10^7 electron histories. Sample is comprised of 4nm of InAs (density = 5.67gcm^{-3}) at the bottom surface of 6nm of GaAs (density = 5.316gcm^{-3}). Note that the curvature of the simulations is not visible on this scale.

Applying equation 4.1.1 to the data of Figure 5.2.3 gives the results shown in Table 5.2.1. Obviously, these values are almost uniformly too large or negative, where neither category indicates a correct answer. Attempting the same analysis with different parameters for the shielding correction does not improve either the correctness nor the cohesiveness of the results.

		α_2 (°)						
		-5	0	5	10	15	20	25
α_1 (°)	-10	1791	751	589	555	566	654	414.03
	-5		-1002	-635	-429	-275	-54	-386
	0			-77	83	224	501	-62
	5				311	473	863	-54
	10					693	1292	-268
	15						2087	-989
	20							-4990

Table 5.2.1: Calculated *d* from the data in Figure 5.2.3. λ = 2525nm. Nominal *d* is approximately 6 to 8nm.

Using In_L/As_K gives the values shown in Table 5.2.2, which exhibit the same broad characteristics as Table 5.2.1.

		α_2 (°)						
		-5	0	5	10	15	20	25
α_1 (°)	-10	2862	1579	1258	1124	928	1071	626
	-5		-585	-374	-259	-402	-43	-672
	0			-53	32	-276	274	-718
	5				154	-459	478	-1069
	10					-1297	730	-1785
	15						3419	-2151
	20							-9396

Table 5.2.2: Calculated d using In_L/As_K from the sample in Figure 5.2.3. λ = 3900nm. Nominal d is approximately 6 to 8nm. The detector efficiencies of In_L and As_K were taken as 73% and 79%, respectively, from Figure 2.3.1.

Again, equation 4.1.1 has failed to provide a good result. In this case, the reason for this is likely the fact that the overlayer was of inconsistent thickness, which in turn caused both significantly different regions to be examined and a different amount and chemical composition of material for the resulting X-rays to travel through when the sample was tilted.

5.2.1 Graphical Comparison

As was seen in section 5.1.2, this method struggles to differentiate between small variations in overlayer thickness. As such, no meaningful result can be arrived at for this sample.

5.2.2 Modelled Absorption Matching

Table 5.2.2.1 shows the result of applying this method. It is plain that the results are inconsistent and do not provide any sort of useful answer.

	In_L, λ_{matrix} = 2525nm, λ_{layer} = 2602nm				In_L/As_K, λ_{matrix} = 3913nm, λ_{layer} = 4033nm			
Tilt normalised to (°)	depth of layer	thickness of layer	depth of layer	thickness of layer	depth of layer	thickness of layer	depth of layer	thickness of layer
-10	758.0	338.3	646.4	2	893.4	0.3	895.2	2
-5	314.4	315.2	312.9	2	431.9	0.0	433.2	2
0	846.3	213.3	728.5	2	1172.9	295.1	1009.0	2
2.5	414.6	0.0	416.0	2	574.8	0.0	576.1	2
5	993.5	243.2	791.1	2	1377.3	337.3	1095.5	2
7.5	691.4	185.7	597.7	2	953.9	228.1	827.8	2
10	198.2	57.7	178.3	2	275.2	83.8	246.7	2
12.5	829.9	212.1	710.6	2	1148.0	282.3	984.2	2
15	695.8	188.1	603.7	2	963.4	255.5	836.2	2
17.5	32.9	0.0	33.8	2	45.6	0.0	46.5	2
18.3	31463.6	0.0	1722.4	2	44447.7	0.0	2385.2	2

Table 5.2.2.1: Result of applying equation 4.8.2.1.2 to a 2nm thick InAs layer with a nominal 6nm

GaAs overlayer. λ_{layer} calculated using mass-absorption coefficient from XCOM [66] and density from NSM archive [67]. Note that a value of '0.0' means a value of 0.001, which was the minimum permitted to the function. Averages not included due to lack of meaning.

5.2.3 Simulated Absorption Matching

For this sample, this method gives results which are almost invariably larger than 100nm: the significant exception to this would be while matching to the In_L/As_K curve that was fitted to the experimental data rather than the experimental data itself. For this curve all of the results where 10nm, which is both consistent and remarkably close to the nominal. This is likely to be the result of applying so many different speculative corrections that one happens to function in the precisely correct way. While it is encouraging that one of the twenty four attempts succeeded this should not be taken as a guarantee of accuracy for future work.

5.2.4 Curve Fit

Equivalent to section 5.1.5, the 'Curve Fit' method was applied to this sample. Again, however, the results are poor. This is again a result of the experimental results not matching the expected, in addition to the poor fit implied by the low R^2 value.

	d at correct λ	λ at correct d	R^2
In_L	964.7	20.9	0.378
In_L/As_K	1690.4	18.5	0.356

Table 5.2.4.1: Results from 'Curve fit' method.

5.2.5 Piecewise Curve Fit

The conclusion from attempting this method is the same as with the previous sample: only order of magnitude changes provide perceptible changes, and as such no useful answer was arrived at.

5.3 Third Sample

A third sample, originally a GaAs matrix with two 11nm thick layers of InGaAs, one at the surface and another 100nm deep, was analysed using the holder that gives 5° shielding. This sample suffered considerable contamination by Al_2O_3 (composition confirmed by EDX and taken as stoichiometric on average) re-sputtering from the support of the specimen in the ion mill during the sample preparation, which results in a large Al_K signal that dominates all spectra of this sample. This means that the sample is very thick, with typical analysed areas being approximately 700-900nm thick, which contributes to bremsstrahlung and that much of the detector's time was spent collecting these Al_K X-rays, thereby reducing the number of In_L X-rays detected, which in turn worsens the signal-to-noise ratio of In_L. Both these effect contribute to a larger relative error. The advantage of this structure for the present study is that it presents a somewhat larger degree of absorption than the previous two samples, which should assist in giving more reliable results.

As seen in section 4.4, the correct *d* for a double layer system is some weighted average of the two individual layers. If the Al_2O_3 were not present, then the correct *d* would be approximately 65nm to 75nm.

A FIB lift-out was carried out to analyse the exact composition and size of the contamination, resulting in the SE image seen in Figure 5.3.1.

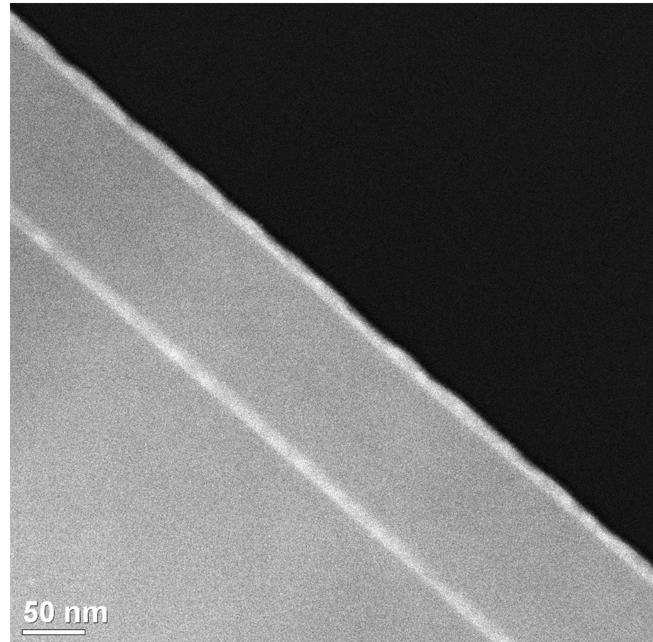

Figure 5.3.1: ADF-STEM images of sample. Note the difference in scale. The left image has two layers of platinum and copper deposited during the FIB lift-out, and do not exist in the sample analysed.

The In_L intensity from this sample is shown in Figure 5.3.2. The form of the curve is a good match to the general curvature seen in all simulations and the error bars are reasonably small. However, the fact that the simulations do not match the experimental data is not encouraging, as it implies some previously unforeseen factor or unexpected combination of existing factors. An example of this would be the possibility that tilting the sample is causing the area being examined to change significantly as a result of the sample thickness, instead of the minor change that is typically assumed.

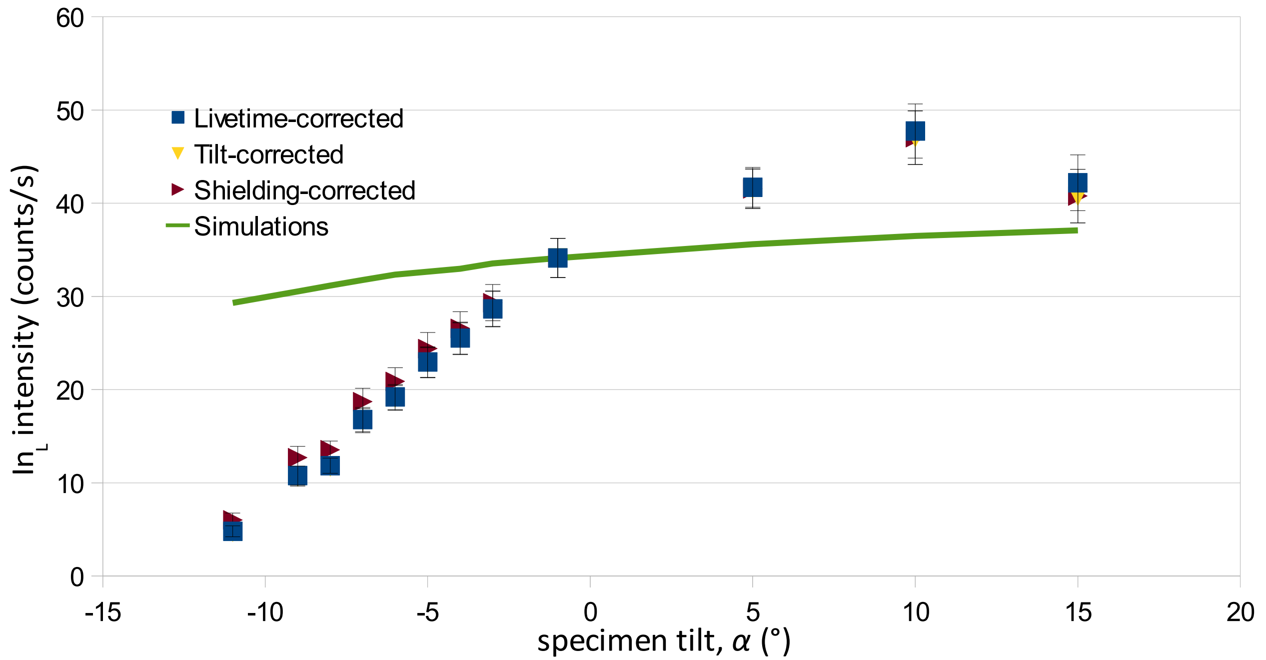

Figure 5.3.2: Experimental In_L data from a GaAs sample with a 11nm thick InGaAs layer at its surface and another buried 100nm deep. In addition, there is a 576nm Al_2O_3 layer on top of the GaAs. $\theta = \alpha + 25°$. Note that in this case there was such variation in the livetime that normalising to 1s livetime was chosen. Simulated curve scaled with respect to -1° data point, and is corrected for tilt but not shielding. Simulation run in NISTMonte at beam energy 197keV, 10^6 electron histories. Sample is comprised of two 11nm thick layers of InAs (density = 5.67gcm^{-3}) positioned at the surface and 100nm deep within a 200nm GaAs (density = 5.316gcm^{-3}) matrix which is itself capped by 576nm of Al2O3 (density = 4gcm^{-3}).

Calculating d directly from this data is not the correct approach. First, the additional absorption given by the Al_2O_3 must be either removed or otherwise accounted for.

Absorption can be modelled by the equation:

$$absorption = e^{\frac{-\frac{\mu}{\rho}\Big]_{spec}^{A} \rho t}{\sin\theta}} \qquad \text{Equation 5.3.1}$$

where $\frac{\mu}{\rho}\Big]_{spec}^{A}$ is the mass-absorption coefficient, ρ is the density, t is the thickness and θ is the take-off angle. Taking 402.8cm^{2}g^{-1} as the mass-absorption coefficient of Al_2O_3 and 4gcm^{-3} as the density, then the In_L curve after the absorption from the Al_2O_3 overlayer would be that shown in Figure 5.3.3. This curve remains of the kind expected from a thin layer, though there is a tremendous disagreement between experiment and simulation.

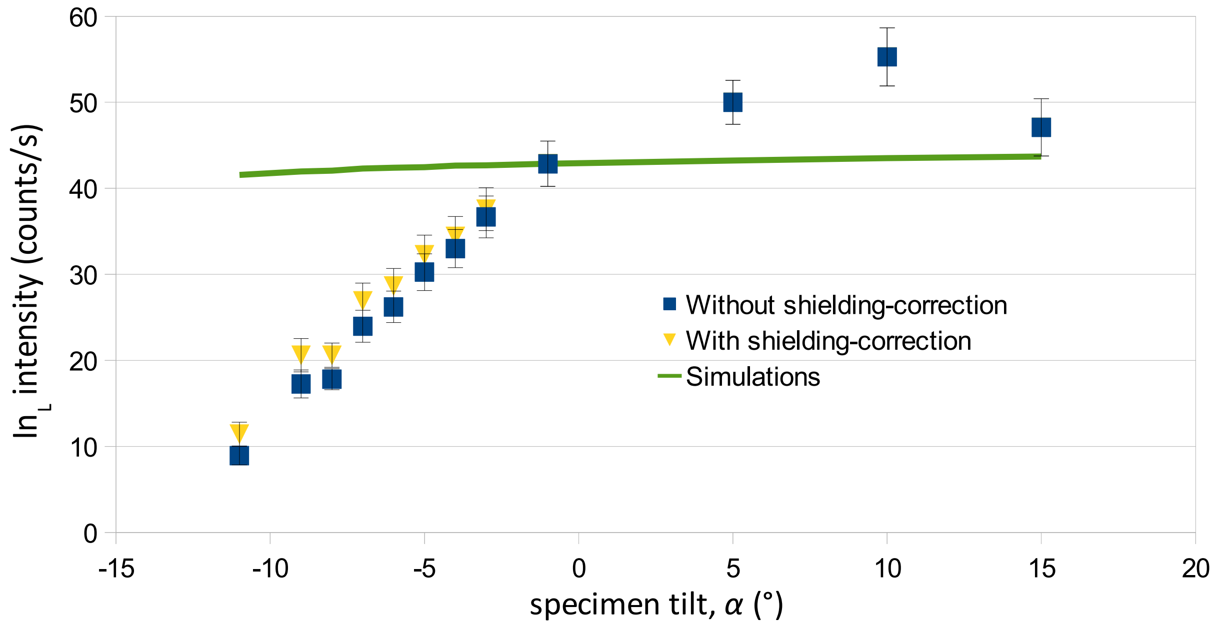

Figure 5.3.3: Figure 5.3.2 with the absorption effect from the Al_2O_3 overlayer removed. Simulated curve scaled with respect to -1° data point, and is corrected for tilt but not shielding. Simulation run in NISTMonte at beam energy 197keV, 10^6 electron histories. Sample is comprised of two 11nm thick layers of InAs (density = 5.67gcm^{-3}) positioned at the surface and 100nm deep within a 200nm GaAs (density = 5.316gcm^{-3}) matrix.

Applying equation 4.1.1 to the data in Figure 5.3.3 gives the results shown in Table 5.3.1. Again, there is no coherency, though it is encouraging that there are so few negative values. Too large values indicate that the slope is too strong, and so trial-and-error variation of the Al_2O_3 overlayer thickness (and therefore the modelled absorption) was attempted. In doing so, it was found that as the Al_2O_3 overlayer increases, the positive tilt values become negative (i.e. show downward slope) before the negative tilt data points give reasonable answer. From this, it is reasonable to conclude that the Al_2O_3 overlayer modelling is not the issue.

		α_2 (°)										
		-9	-8	-7	-6	-5	-4	-3	-1	5	10	15
α_1 (°)	-11	3493	2636	2955	2722	2685	2556	2496	2381	2051	1937	1639
	-9		549	2262	2021	2106	1991	1970	1900	1604	1520	1187
	-8			4192	2898	2757	2467	2363	2192	1758	1640	1258
	-7				1449	1910	1753	1769	1718	1395	1325	936
	-6					2424	1932	1900	1790	1387	1309	880
	-5						1386	1595	1588	1221	1170	713
	-4							1825	1670	1193	1142	641
	-3								1580	1079	1053	512
	-1									848	898	263
	5										986	-342
	10											-2157

Table 5.3.1: Calculated *d* values from the data of Figure 5.3.3 after removal of the effect of the Al_2O_3 contamination layer. λ = 2525nm. Nominal *d* is 65nm to 75nm.

Attempting to normalise with respect to As_K produces the results shown in Table 5.3.2. Again, there are no reasonable results.

		α_2 (°)										
		-9	-8	-7	-6	-5	-4	-3	-1	5	10	15
α_1 (°)	-11	2983	2314	2497	2440	2445	2392	2465	2499	2102	1941	1470
	-9		687	1870	1947	2059	2035	2192	2290	1828	1662	1101
	-8			3204	2698	2633	2480	2608	2636	1995	1783	1147
	-7				2131	2296	2181	2414	2502	1815	1607	922
	-6					2479	2210	2529	2601	1766	1543	790
	-5						1911	2559	2640	1652	1425	608
	-4							3272	2932	1608	1363	467
	-3								2737	1307	1114	163
	-1									650	635	-439
	5										609	-1563
	10											-4531

Table 5.3.2: Calculated *d* using In_L/As_K from the data of the sample used in Figure 5.3.3. λ = 3900nm. Nominal *d* is 65nm to 75nm.

In this case, the reason for the failure of equation 4.1.1 to produce the correct depth is less clear. The confounding variables are the Al_2O_3 overlayer and the double layer structure. If the presence of the second layer was distorting the results (if, for example, the second layer is only barely present at the bottom of the sample during one analysis then the slight changes in the area being examined as the sample is tilted could have caused the second layer to not exist in that second analysis) then there would be a strong, abrupt change in certain data points, however, such a change is not observed. The equation describing absorption is well understood and considered reliable and as such is unlikely to be the problem. Varying the Al_2O_3 overlayer thickness did not improve matters. A layer of contamination is not constant in thickness, and as such it is possible that this sample

violates the assumption concerning the amount of material that the X-rays travel through. This would be exacerbated by the fact that these X-rays would originate from a deep point within the sample and therefore even a slight change in take-off angle would cause them to travel through a significantly different region. This is not known with any certainty, however, and as such, the reason for this data set not producing good results is currently unknown.

5.3.1 Graphical Comparison

As with the previous sample, this method proved to be insufficiently sensitive to change in depth to give a useful answer.

5.3.2 Modelled Absorption Matching

This method, in its current form, cannot be applied to a sample with multiple thin layers or several different matrices. As such, no meaningful result can be acquired from this sample using this method.

5.3.3 Simulated Absorption Matching

Another sample that this was applied to was the InGaAs double layer system, previously studied in Figure 5.3.1. This sample possessed two 11nm thick InGaAs layers in a GaAs matrix, one at the surface and the other 100nm deep. Additionally, there was found to be a large Al_2O_3 contamination on the surface that had to be accounted for. As seen in Figure 5.3.2, the Al_2O_3 contamination proved to be a confounding variable and so in this case it was decided to hold the GaAs matrix constant and vary the thickness of the contamination. The results of this are shown in Table 5.3.3.1. It is clear that there is poor self-consistency. This implies that the data, despite seemingly falling on the correct curve, does not actually do so. It is possible that this could be due to a inconsistency in the thickness of the Al_2O_3 overlayer.

base data set			pairs data set			triplets data set		
specimen tilt, α, normalised to (°)	In_L	In_L/As_K	specimen tilt, α, normalised to (°)	In_L	In_L/As_K	specimen tilt, α, normalised to (°)	In_L	In_L/As_K
-11			-10			-9.33		
-9			-8.5	470		-8		
-8			-7.5			-7	455	
-7			-6.5			-6		
-6	645		-5.5			-5		
-5			-4.5			-4		
-4	645		-3.5			-2.67		
-3	710		-2			0.33		
-1	740		2			4.67		
5			7.5			10	600	
10			12.5		400			
15								

Table 5.3.3.1: Calculated Al_2O_3 overlayer thickness from an InGaAs in GaAs double layer system with Al_2O_3 contamination layer on the surface. Blank cells are those with no minimum. 'Pairs' and 'Triplets' are the result of averaging over two or three data points respectively in order to smooth the curve. Simulations carried out in NISTMonte for Al_2O_3 thicknesses between 300nm, 400nm, 450nm to 760nm in steps of 5nm and 800nm, beam energy 197keV, 10^6 electron histories. Sample comprised of two 11nm thick layers of InAs (density = 5.67gcm^{-3}) embedded at the surface and 100nm deep in a 200nm GaAs (density = 5.316gcm^{-3}) matrix, capped by a Al_2O_3 (density = 4gcm^{-3}) layer of varying thickness. Simulated tilts matched that of experimental. $\theta = \alpha + 25°$. Detector efficiencies In_L: 73%, As_K: 79%.

As with the modelled absorption match, this method does not see enough change from being applied to a 2nm InAs buried under 6nm GaAs to give meaningful answers.

5.3.4 Curve Fit

Table 5.3.4.1 shows the results of applying the curve fit method in an attempt to discover the effective depth of the two layer. A value for *d* of 66nm was chosen in accordance with that found in section 4.4. Despite the R^2 values being significantly higher, the calculated values are no more reasonable.

	d at correct λ	λ at correct d = 66nm	R^2
In_L	1831.9	91.0	0.901
In_L/As_K	1934.0	133.5	0.862

Table 5.3.4.1: Results from 'Curve fit' method, after manual correction for absorption.

5.3.5 Piecewise Curve Fit

Once again, this method does not show enough change with varied *d* to be useful for precision better than order of magnitude.

5.4 Conclusion

Three samples have been analysed using all the available methods, and it was found that only the absorption matching methods gave good answers, and that only once. Multiple attempts with the same samples (where only the best where included) do not show improvement. In some cases, the reason for this failure is obvious: statistical uncertainty or sample inconsistency. For the third sample, despite being a somewhat complex sample, good results could still have been reasonably expected. It is unclear why this was not found to be the case, though a likely culprit would be the necessity of manually correcting for absorption in the contamination layer, which could have introduced errors into the calculation.

Concerning the validity of the different methods, it is reasonable to say that the 'Graphical Comparison' and 'Piecewise Curve Fit' methods cannot give meaningful numerical results to better than the closest order of magnitude. 'Curve Fit' would require extremely accurate data with no outliers and as such presents little advantage over equation 4.1.1, while the two absorption matching methods do show some promise, even if only compared to the other methods.

Experimentally, other methods (such that described as section 2.6.2) have achieved much greater success than those attempted here.

While these results are not encouraging, it is possible that the failure to acquire correct results is a result of poor samples and/or data acquisition: the primary limitation to counting statistics was the time before sample drift causes an unacceptable change in the area being examined. As such, perhaps a sample of InSb, with a 10nm thick layer of either pure Al or AlAs buried approximately 50nm under the surface. Such a sample would give good counting statistics while simultaneously the X-ray of interest would be soft enough compared to the matrix material's density to experience significant absorption with changing take-off angle at that depth.

6 The use of EDX to determine sample thickness

6.1 Simulated Analysis

The basic principle of this method is straightforward: taking the ratio of two X-ray line intensities of the same element with different energies and therefore different absorption characteristics should yield a distinctive curve as a function of thickness. This dependence can then be used to determine the thickness of the sample from X-ray spectroscopy (if composition is homogeneous), removing the need to determine the sample thickness by some other method. This sample thickness can then be used to provide a more accurate absorption correction, which should generally give better accuracy in determining the chemical composition. Of course, accurate calculation of the sample thickness requires knowledge of the composition, which in turn requires the sample thickness: this problem can be overcome by iterating between the composition and the thickness.

The principle of this method is shown in Figure 6.1.1, using Ge_K and Ge_L in a simulated pure Ge sample. The distinctive trends seen here often arise: the intensity of the higher-energy X-ray (in this example, Ge_K) rises almost linearly with thickness up to at least several microns thickness while that of the lower-energy X-ray (Ge_L) begins roughly linear but saturates after a particular thickness, here approximately 1000nm. As X-ray generation is approximately linear with increasing thickness and a hard X-ray will not experience appreciable absorption, its intensity will rise almost linearly with thickness. For a lower energy X-ray this is not the case: while the rate of X-ray generation

does increase with thickness, those X-rays originating deeper within the sample will be absorbed before reaching the detector, giving rise to the saturation. The slight linear increase in Ge_L after saturation is due to a very few X-rays from deep in the sample reaching the detector (which will happen in very small numbers due to statistics) combined with backscattered electrons (both from the beam and those generated in the sample) generating X-rays at fairly shallow depths. Of course, absorption would eventually have such an effect on the higher energy X-ray line as well, though this would not occur until the sample were much thicker. In this case, the saturation of Ge_K is not visible at these thicknesses but a non-linearity is faintly visible, beginning at approximately 5000nm. This non-linearity can be understood as the result of the fact that it would be experiencing very little absorption regardless of thickness and so the detected intensity closely follows the number of X-rays generated, with the slight rise above the linear due to beam straggling increasing the X-ray fluorescence probability, beam spreading increasing the interaction volume exponentially with the increased thickness and the effects described above for Ge_L also applying to different extents for Ge_K. For the range of thicknesses present in typical TEM analysis, this trend (one X-ray almost linear, the other not) will likely hold for the intensity ratios both of many K/L pairs and (for heavier elements) L/M pairs.

As a consequence, the thickness dependence of the ratio is also rather universal in form, though the magnitude of its slope and the thickness from which it becomes approximately linear will depend on the material and X-ray energies. This means that assuming a linear relationship between the magnitude of the intensity ratio and the thickness is not valid for large thicknesses (several microns), though most experimental analysis is carried out for samples much thinner than this and so this non-linearity is not generally relevant. If deliberately using a thick sample to increase the accuracy of extrapolation then this non-linearity must be accounted for. Note that a homogeneous sample would be the most useful here, though any buried features of different materials could be ignored if sufficiently small.

As a note concerning the use of λ in previous chapters to denote the attenuation wavelength (i.e. the amount of material required to reduce the intensity of the X-ray line to 1/e), it could be considered logical to continue using the same concept here. Such is not the case, however, as previously matters such as beam spreading and backscattering could be legitimately neglected due to the extremely thin layers that the X-rays originated from while in this chapter the samples being examined are often very thick for TEM purposes.

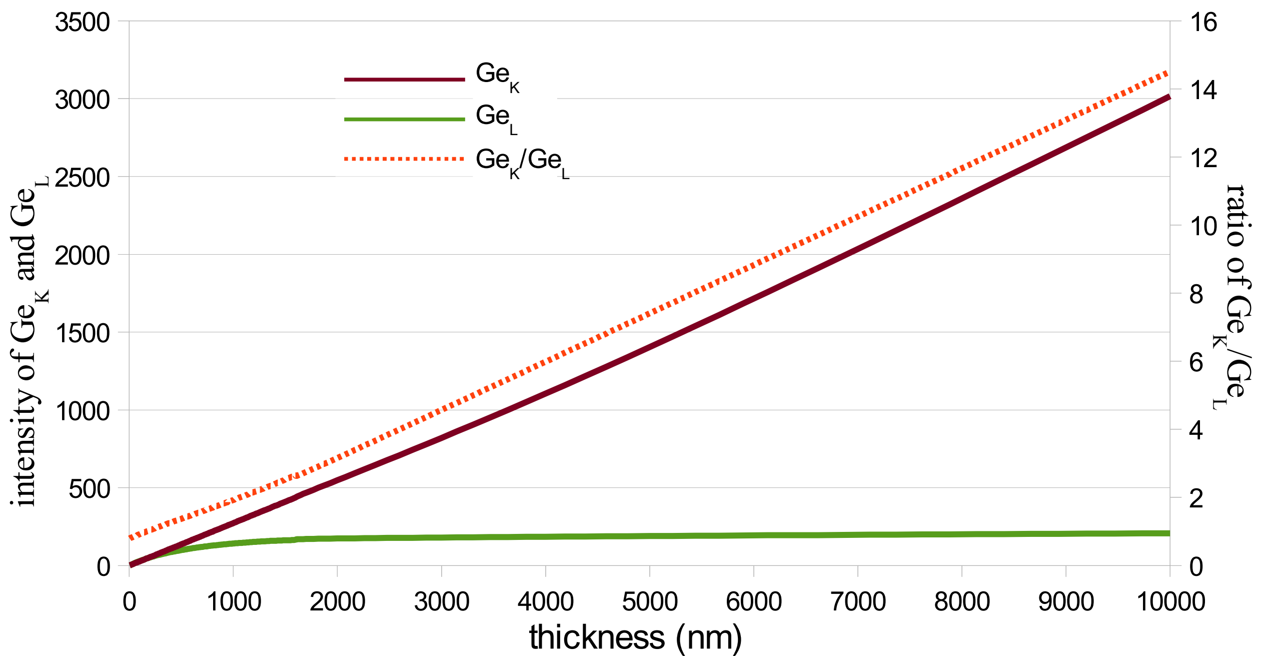

Figure 6.1.1: Simulation of result of K/L ratio method for germanium. 'Ratio' is against the right vertical axis. Simulation run in NISTMonte at beam energy 197keV, take-off angle 25° with 10^7 electron histories. Sample composition pure germanium lamella of varying thickness.

Figure 6.1.2 is the same as Figure 6.1.1 for a much smaller range of thicknesses. It is clear that the ratio is almost linear over the entire range of thicknesses. The plot not being linear would introduce considerable difficulty into the analysis, in that a linear curve would be much easier to assign values to from experimental measurements. It is worth noting that a linear curve would only require two data points to plot, though those two points would need to be very accurate.

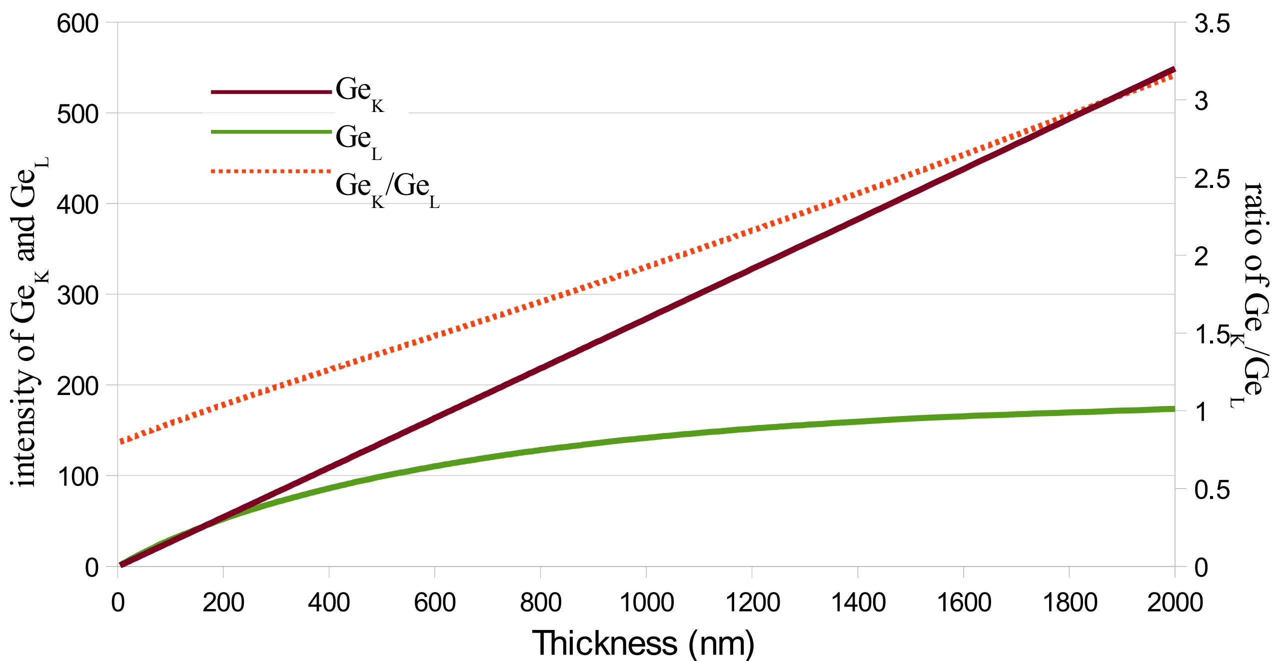

Figure 6.1.2: Magnification of Figure 6.1.1. 'Ratio' is against right vertical axis. Simulation run in NISTMonte at beam energy 197keV, take-off angle 25° with 10^7 electron histories. Sample composition pure germanium lamella of varying thickness.

Results for a GaAs sample from the Monte Carlo simulation programs NISTMonte and CASINO are shown in Figure 6.1.3. The As_K/As_L and Ga_K/Ga_L curves from both programs are similar, however there is a significant difference in the slopes. For a fairly typical TEM sample (i.e. $t \sim$ 100nm) the Ge_K/Ge_L intensity ratios from the two programs disagree significantly (NISTMonte predicts ~ 1 while CASINO gives ~1.4), a difference that vanishes at $t = 0$nm. The implication of this is that the two programs model absorption to different extents but that the fluorescence probability (at least of the X-rays in question) are similar. Determining which, if either, is closer to reality would require comparison to experimental data.

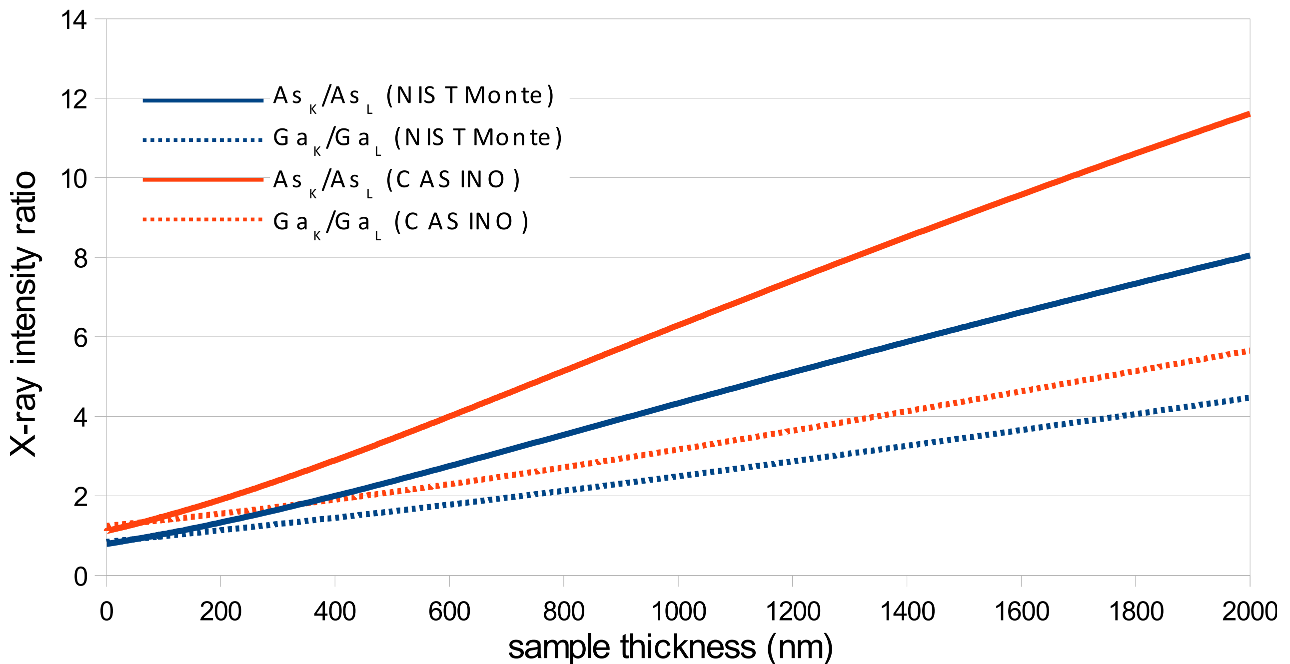

Figure 6.1.3: Comparison of NISTMonte and CASINO simulated results from GaAs sample. Both CASINO and simulations run at beam energy 197keV, take-off angle 20° with 10^7 electron histories. Sample GaAs (density = 5.316gcm^{-3}) lamella of varying thickness.

Figure 6.1.4 presents a further comparison between NISTMonte and CASINO. This is again for a homogeneous GaN sample. Here, the Ga_K/Ga_L intensities for both programs are plotted along with their normalised counterparts, where this normalisation is against the relevant 'absorption-less' intensity. This is to remove any difference in fluorescence probabilities between the two programs. It is clear that the form of both pairs of curves is different. Most obviously, the NISTMonte normalised curve has a larger absolute magnitude than its standard counterpart, while the reverse is true for CASINO. This implies that the absorption cross-section is significantly different for each program. The way that the two 'normalised' curves converge on approximately the same value while possessing significantly different slopes implies that their fluorescence probabilities are similar for low thickness but differ for higher thickness: this could be due to how beam straggling and spreading are modelled. It is interesting to note that despite the significant difference in the 'normalised' curves, the two non-normalised curves are fairly similar, implying that the different factors cancel out to some extent.

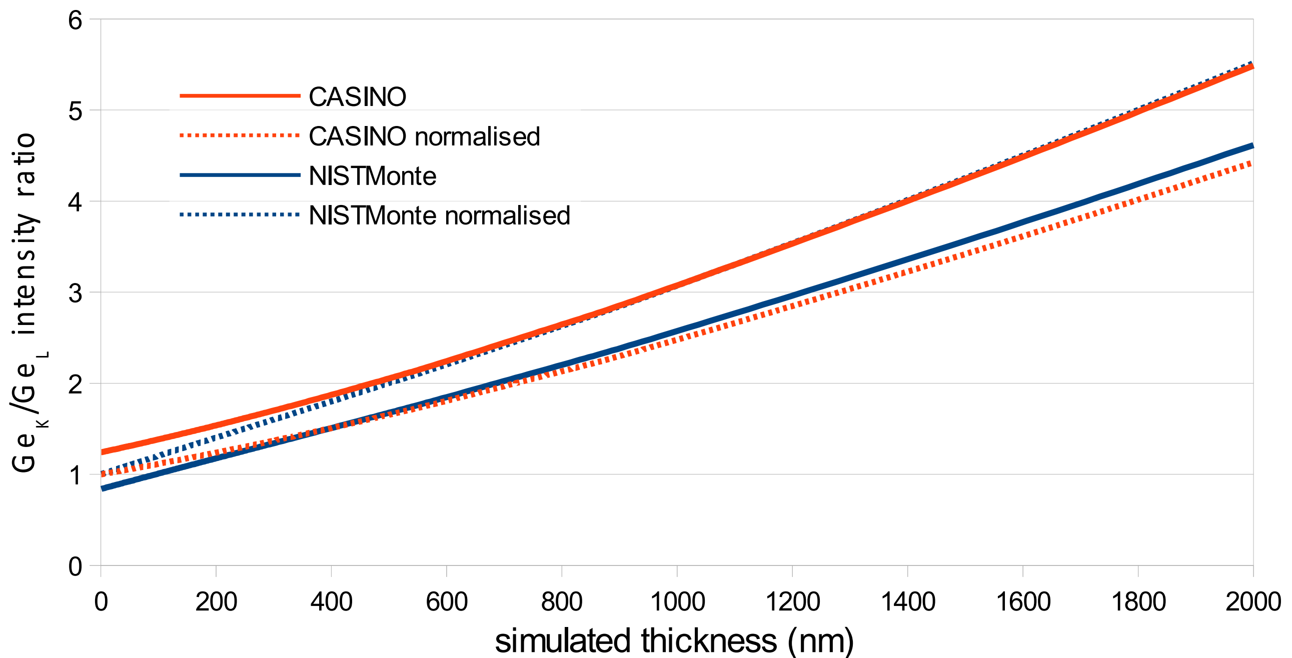

Figure 6.1.4: Comparison of NISTMonte and CASINO with absorption and without absorption for GaN. Both CASINO and NISTMonte simulations run at beam energy 197keV, take-off angle 25° with 10^6 electron histories. Sample composition GaN (density = 6.15gcm^{-3}) lamella of varying thickness.

To explore the usefulness of this method with different materials, an InP sample was simulated in NISTMonte. Figure 6.1.5 shows the simulated X-ray intensities over a large range of thicknesses. The expected trend is present: the highest energy X-ray (In_K) is only somewhat non-linear over most of the thickness range while those with lower energies begin with a linear rise but saturate at certain values, each of different particular thicknesses. Interestingly, the In_M curve rises quickly, tails off, then begins to rise again. This is the same effect as for Ge_L in Figure 6.1.1, only much more visible. A similar effect can be seen in the P_K and In_L curves. Interestingly, the In_K curve does not follow this general pattern, in that it has a slightly exponential form. Obviously, the difference is due to its much higher energy (24.2097keV) compared to In_L (3.2694keV). The form of the In_K is the same as Ge_K from Figure 6.1.1. Interestingly, the point at which the non-linearity begins being visible is the same for In_K as for Ge_K, despite their very different energies.

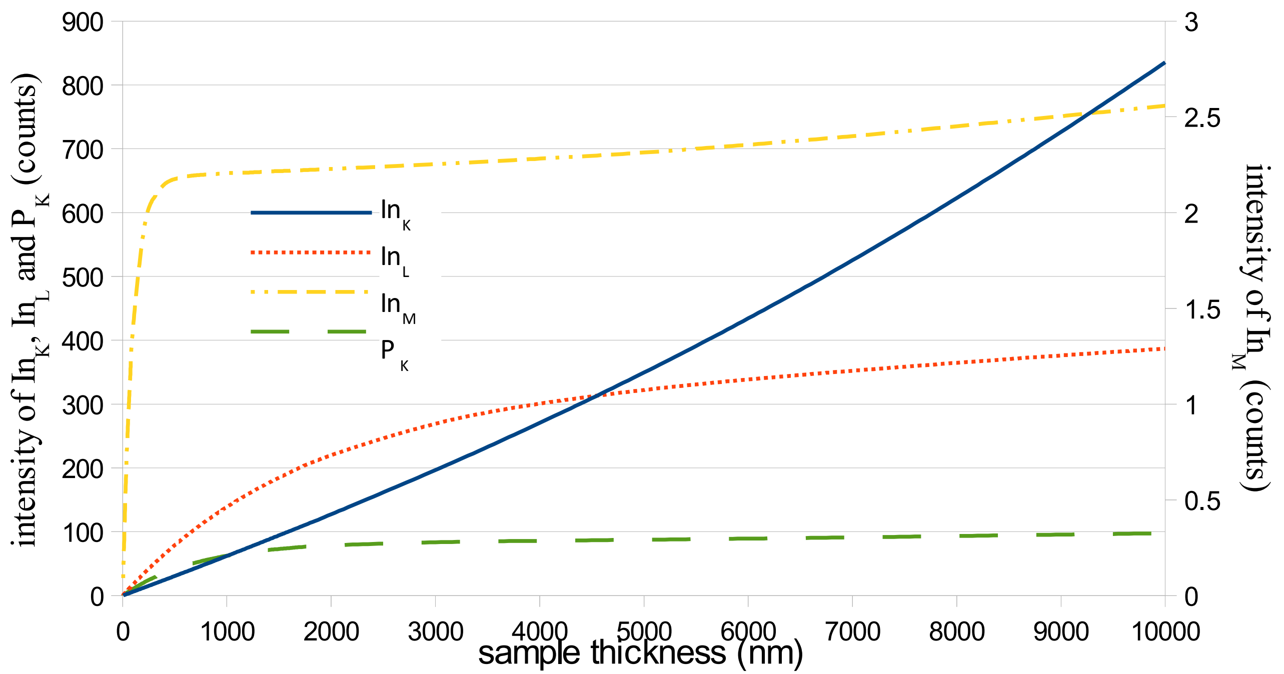

Figure 6.1.5: NISTMonte simulation for InP sample. In_M is plotted against the right vertical axis. Beam energy 197keV, take-off angle 25° with 10^6 electron histories. Sample InP (density = 5.12gcm^{-3}) lamella of varying thickness.

Figure 6.1.6 shows all possible intensity ratios from the indium lines of Figure 6.1.5. It is clear that the In_K/In_M intensity ratio is the closest to being linear, and as such would be the logical choice for determining thickness, assuming that the In_M intensity is readily detectable. This is due to the fact that a linear curve is much easier to interpolate from and is far more predictable than an exponential or polynomial curve.

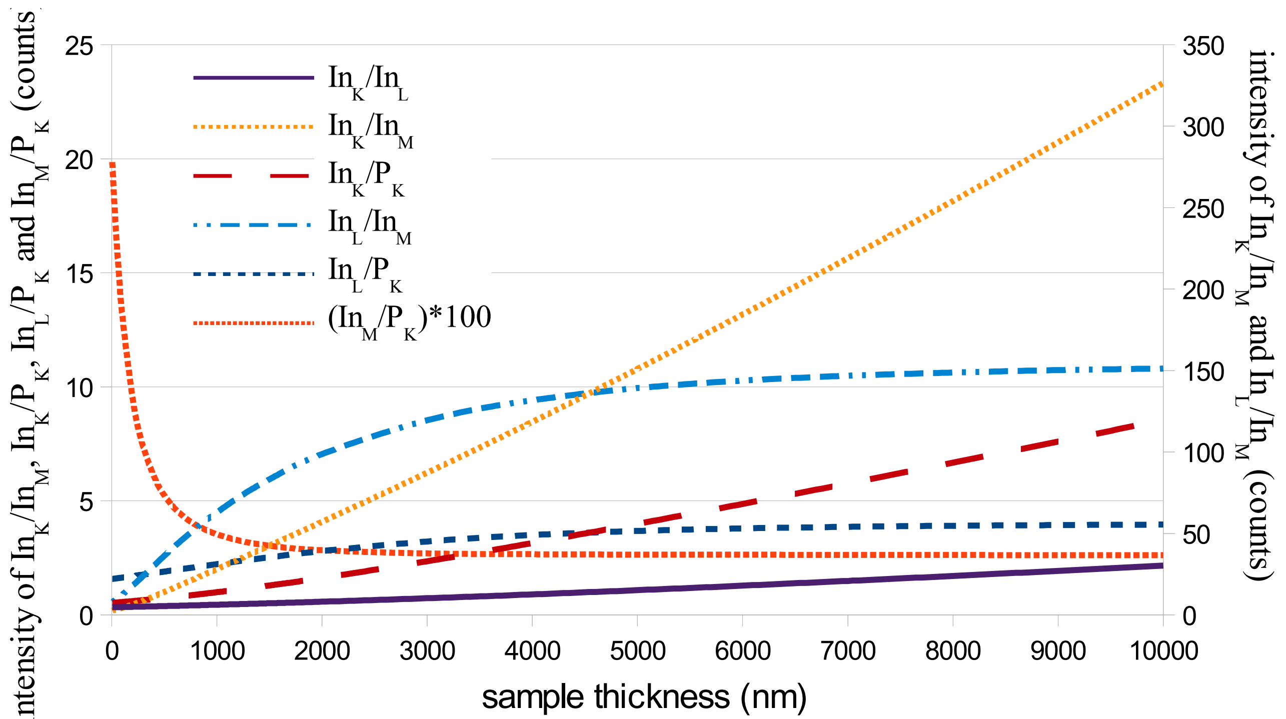

Figure 6.1.6: Comparison of ratios from Figure 6.1.5. In_K/In_M, In_L/In_M against right vertical axis. Beam energy 197keV, take-off angle 25° with 10^6 electron histories. Sample InP (density = $5.12gcm^{-3}$) lamella of varying thickness.

Figure 6.1.7 shows the results from a more complicated sample: InSb. Here, there are a total of six X-ray lines to detect, giving a large number of possible intensity ratios. This should prove sufficient to demonstrate validity for a complex sample.

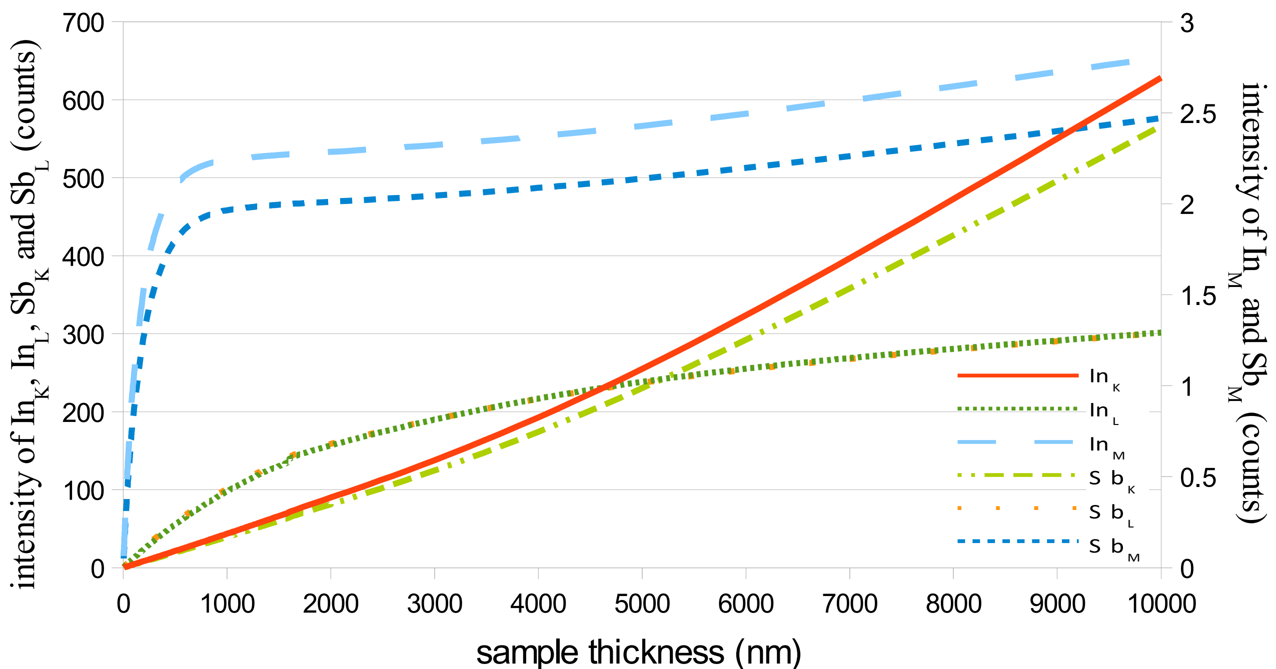

Figure 6.1.7: NISTMonte simulated X-ray intensities for InSb. In_M and Sb_M against right vertical axis. Beam energy 197keV, take-off angle 25° with 10^6 electron histories. Sample composition InSb (density = $5.775gcm^{-3}$) lamella of varying thickness.

Figure 6.1.8 shows all possible intensity ratios from Figure 6.1.7, both for different lines of each one element and between lines of different elements. Particularly interesting is the In_K/Sb_K ratio, which is effectively constant over the entire range of thickness. This can be attributed to their high line energies, in that neither experiences significant absorption over the relevant range. This can be compared to the In_L/Sb_L and In_M/Sb_M ratios which exhibit similar behaviour but with an initial non-linear thickness behaviour. This difference in behaviour is due to the fact that the L or M-lines do experience significant absorption, to very similar but not quite identical extents, which causes a difference in the change of intensity with increasing sample thickness. Presumably, a similar trend would be visible for the In_K/Sb_K ratio if the sample were made thick enough.

As a rule, it is wise to avoid relying on a ratio that uses X-rays from two different elements to measure thickness, as while the sample as a whole is stoichiometric there could be some local change of the concentration of one element which would bias the result (e.g. surface oxidation will mean small thicknesses could give different results). There is the further difficulty that in non-stoichiometric materials (either local impurity or characteristic of the material) there is an additional uncertainty introduced that would in turn be passed onto the final thickness calculation.

The In_K/Sb_L ratio is very similar in form to the In_K/In_L and Sb_K/Sb_L ratios, which is again no surprise given their similar energies. This pattern holds for all the intra- and inter-element ratios. In principle, this similarity could be exploited by varying the composition of a theoretical sample of e.g. $InGa_{1-x}Sb_x$ until all the ratios agree on thickness.

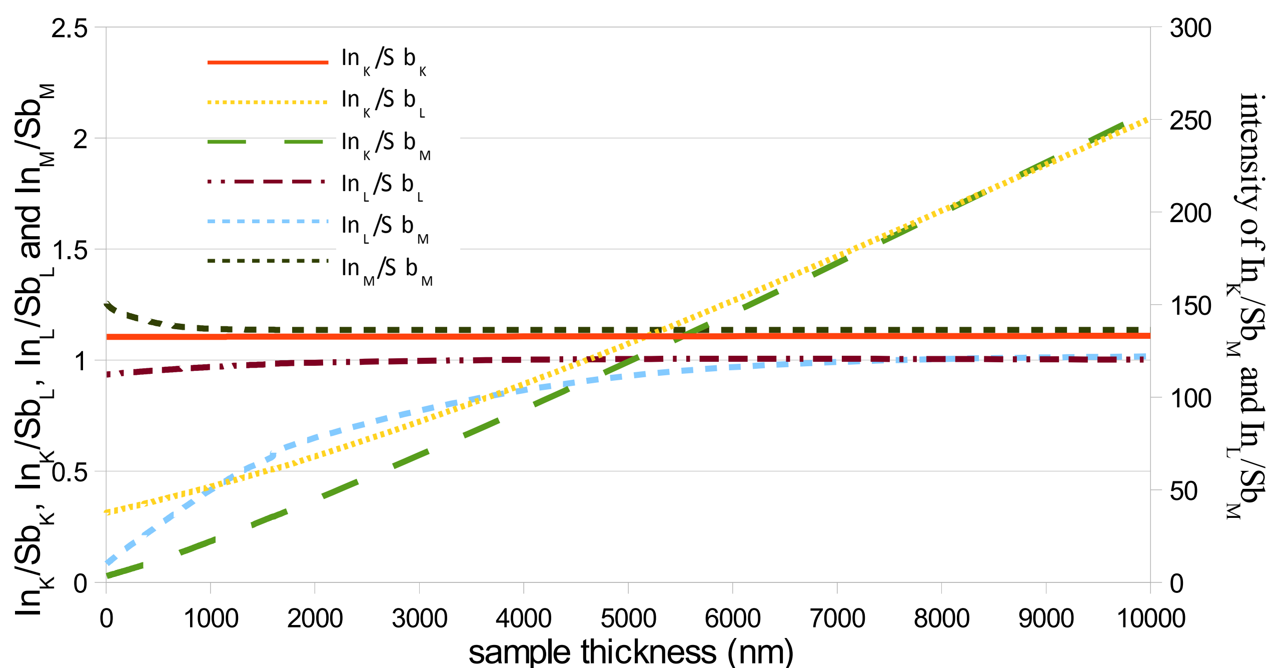

Figure 6.1.8: Comparison of In_x/Sb_y ratios from Figure 6.1.7. In_K/Sb_M and In_L/Sb_M against right vertical axis. Beam energy 197keV, take-off angle 25° with 10^6 electron histories. Sample composition InSb (density = 5.775gcm^{-3}) lamella of varying thickness.

Figure 6.1.9 and Figure 6.1.10 show the intensity ratios within In and Sb. The degree of similarity is to be expected, since both elements have X-ray families that are similar in their energy spread relative to other X-rays within the same family.

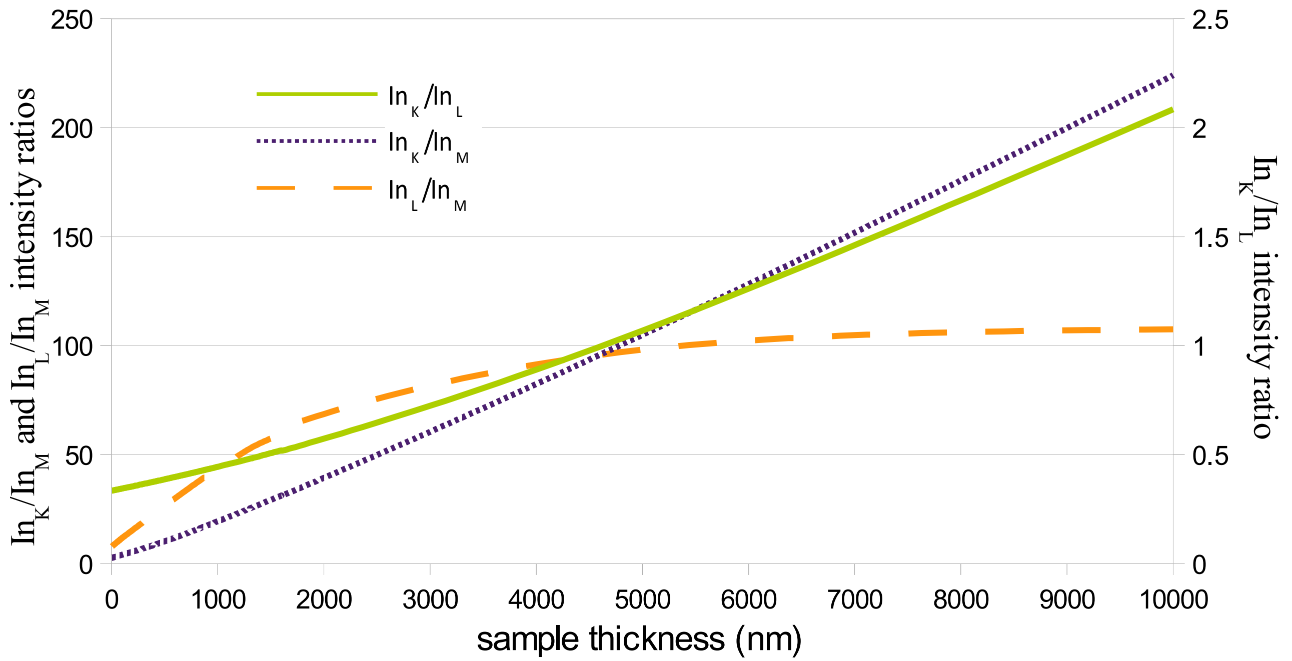

Figure 6.1.9: Comparison of In_x/In_y ratios from Figure 6.1.7. In_K/In_L against right vertical axis. Beam energy 197keV, take-off angle 25° with 10^6 electron histories. Sample composition InSb (density = 5.775gcm^{-3}) lamella of varying thickness.

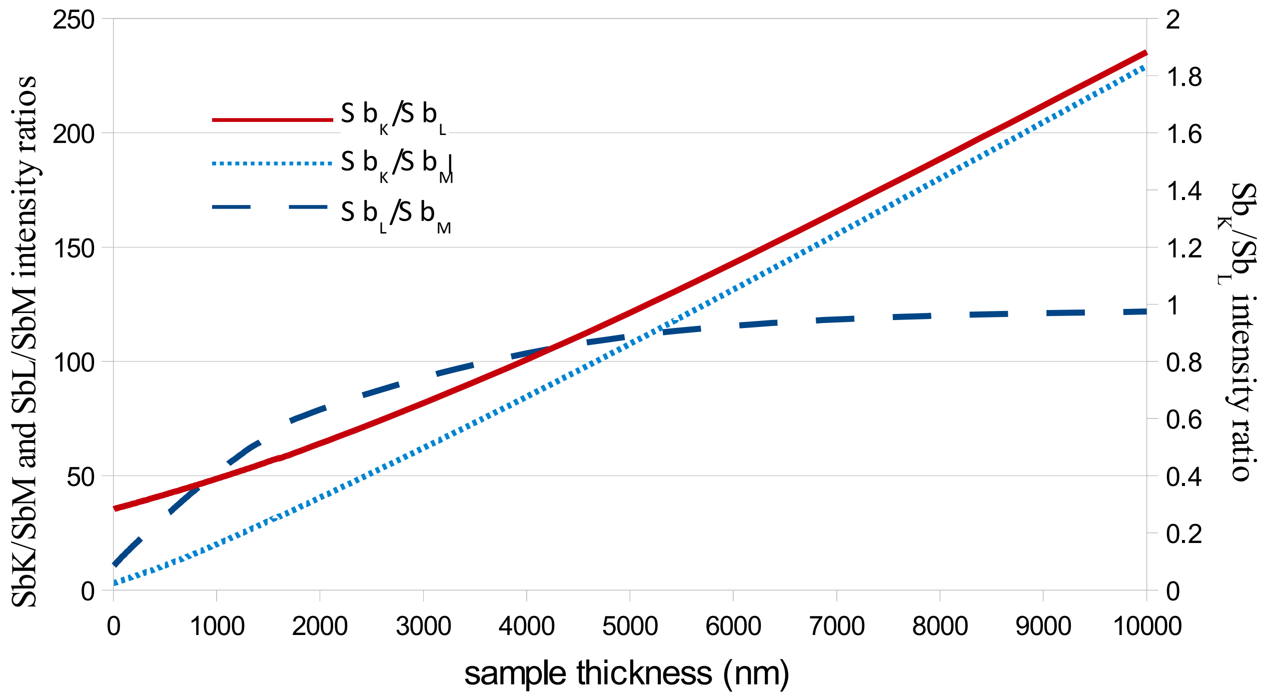

Figure 6.1.10: Comparison of Sb_x/Sb_y ratios from Figure 6.1.7. Sb_K/Sb_L against right vertical axis. Beam energy 197keV, take-off angle 25° with 10^6 electron histories. Sample composition InSb (density = 5.775gcm^{-3}) lamella of varying thickness.

6.2 Experimental Analysis

Figure 6.2.1 shows the In line intensity ratios resulting from a experimental InP sample, where the ratios are plotted against detector deadtime instead of thickness. This is due to the fact that sample

thickness must be measured independently, but deadtime is a product of analysis that is both well-defined (i.e. small-error) and is self-consistent. It is thought that deadtime directly correlates with thickness to some extent, as increased thickness causes an increase in X-rays detected which in turn increases deadtime. This graph could be considered a scaled equivalent of the simulated data in Figure 6.1.6, where deadtime of unity would be equal to that thickness at which the detector saturates. Comparing the two figures, it is obvious that there are significant differences. It is worth noting that a difference in the absolute value of the ratios is to be expected: of concern is a difference in form of the curves. Of note is that the spectra could not be analysed with the available ISIS software and so intensity values were extracted manually, using linear interpolation to subtract the background and Gaussian fits to remove the O_K and C_K peaks that straddle the In_M characteristic peak. The consequence of this is that all error bars are simple Poisson statistics (i.e. $n/\sqrt{n}$) and that the general quality of the data is likely to be inferior compared to that extracted with dedicated software.

The In_K/In_L curves could match, as the linear rise seen in the simulation may also be present in the experimental result, however the scatter and the error preclude any reasonable conclusion. In_K/In_M matches better, with a slight non-linearity at high deadtime that is mirrored by the simulated curve at high thickness. In_L/In_M does not match, as the experimental curve shows a trend similar to In_K/In_M that is significantly beyond the error bars. In_K/P_K could be a partial match at high deadtime: a very slight rise might exist for the curves after the cluster at low deadtime. In_L/P_K does not match in form, but as this curve is expected to be fairly constant it is difficult to be certain. In_M/P_K could be a match, albeit with considerable scatter. In summary, three experimental curves from this InP sample show partial matches in form with their simulated counterparts, two do not match at all and one gives a good match.

In a system where there are multiple good matches between simulated and experimental (or two experimental data sets where one is very well understood) it would in principle be possible to compare the inflexion points and thereby match deadtime to thickness for that particular detector processing time. This is not possible for the available data set, as the match is not sufficient.

Using the total X-ray counts from the entire spectrum instead of the detector deadtime resulting in a similar but inferior fit, primarily due to the fact that the data points were not so distributed along the x-axis but clustered to one side.

Further analysis will be carried out in Chapter 7.

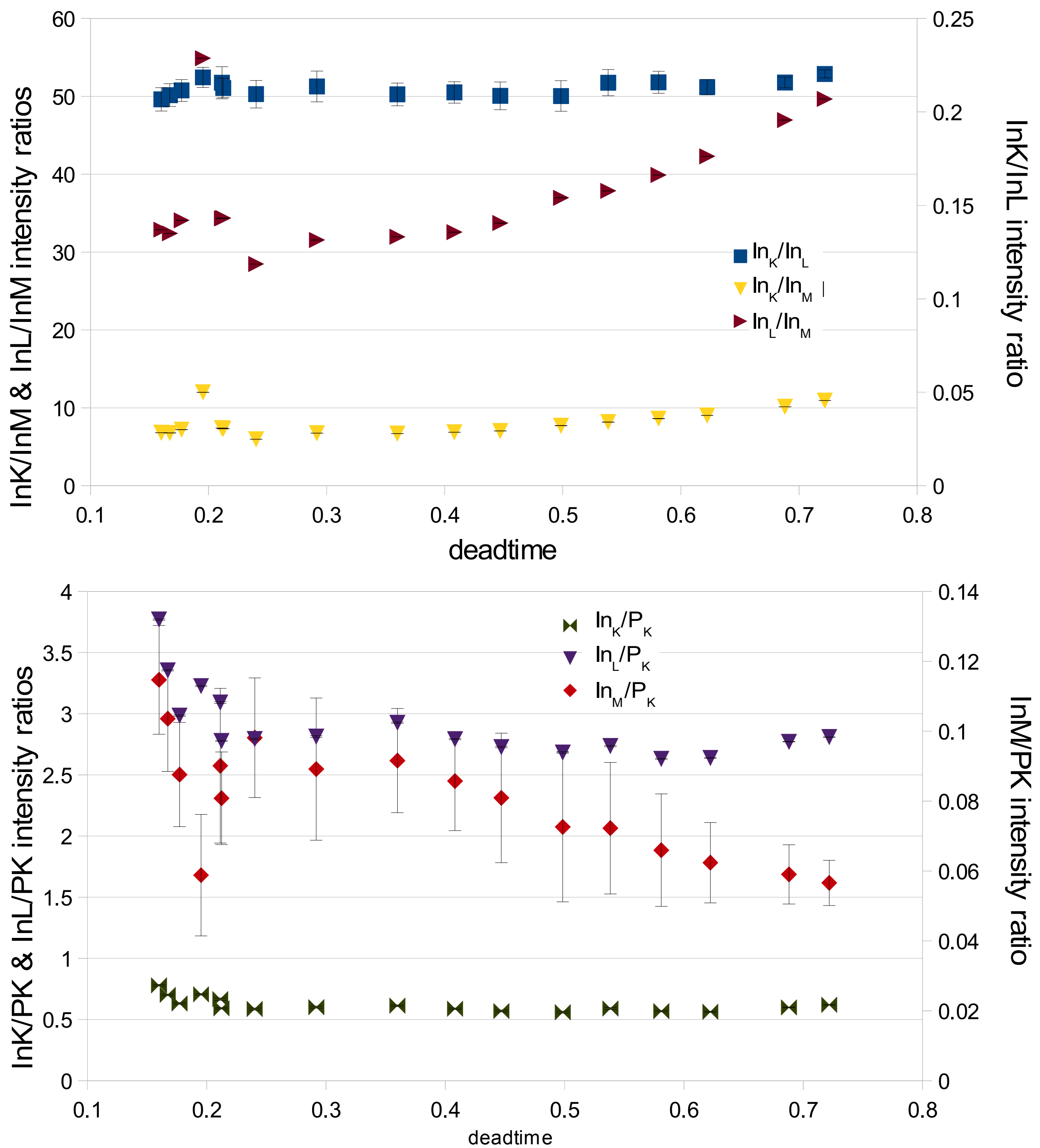

Figure 6.2.1: InP experimental data. Detector efficiencies were taken as In_K: 89%, In_L: 73%, In_M: 41%, P_K: 69% (Figure 2.3.1). These were calculated for the strongest line in each family and assumed to apply to the entire peak.. Refer to Figure 6.1.6 for simulated comparison.

Figure 6.2.2 shows a comparison between simulated and experimental results for a FIB-prepared GaAs lamella. The numerical values for a linear least-squares fit are included in Table 6.2.1. The experimental result for the As_K/As_L ratio agrees better with NISTMonte than CASINO, while the reverse is true for Ga_K/Ga_L. While this is not conclusive, it does imply that neither program can be relied upon to give sufficiently accurate results for all X-ray lines in all materials. The other fact of note is that the R^2 of both experimental data sets is fairly close to unity, which implies that the linearity assumption is valid at these thicknesses.

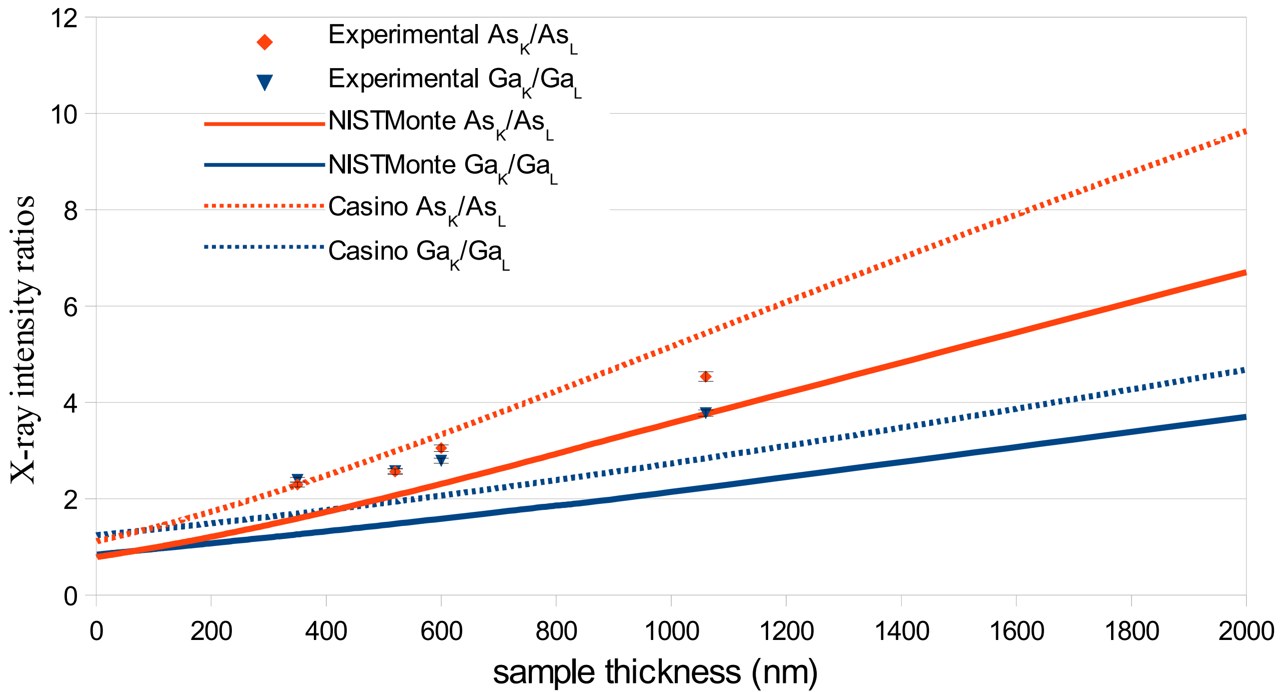

Figure 6.2.2: Comparison of experimental to simulated X-ray intensity ratios for a GaAs FIB lamella, where the thickness was estimated from SEM imaging. Detector efficiencies As_K: 79%, As_L: 68%, Ga_K: 77%, Ga_L: 64%. Note that both the 350nm experimental data points are overlaying each other. Take-off angle 25°, 10^7 electrons trajectories, beam energy 197keV.

X-ray intensity ratio	slope ($x10^{-3}$)	intercept	R^2
As_K/As_L (Experimental)	3.3±0.3	1.1±0.2	0.984
As_K/As_L (CASINO)	4.25±0.04	0.97±0.03	0.998
As_K/As_L (NISTMonte)	2.92±0.05	0.70±0.03	0.999
Ga_K/Ga_L (Experimental)	2.02±0.16	1.60±0.11	0.987
Ga_K/Ga_L (CASINO)	1.65±0.03	1.17±0.01	0.994
Ga_K/Ga_L (NISTMonte)	1.40±0.02	0.81±0.01	0.998

Table 6.2.1: Linear least-squares regression fits of the data in Figure 6.2.2.

Figure 6.2.3 shows a comparison of three different experimental samples, two wedges and a FIB lamella (where the lamella is the same data used in Figure 6.2.2). Note the double-log scale. It is plain that all three follow the same general curvature, however the fact that the lamella sits between the two wedges does not assist in determining to what extent the shape of a wedge affects its absorption characteristics.

Comparing the simulation to the three experimental data sets, it is clear that, apart from some outliers, the form of the curves are similar. The two 10nm data points deviating from the expected curve is not a surprise: such thicknesses are difficult to measure and are also susceptible to effects such as specimen warping and surface oxidation. The second wedge's 10000nm data point is much lower than expectation: this is unlikely to be a case of incorrect thickness (as it would have to be an order of magnitude smaller to match the curve) and could be due to the detector having difficulties

at such high thickness and therefore high countrate. It could also be due to a parallax effect, as the specimen would no longer the electron transparent at such a high thickness. The remaining two obvious outliers, 1000nm and 1400nm from the second wedge, cannot be so readily explained. It is possible that if the wedge was imperfectly cleaved then there would be bulges or depressions that would give much larger absorption than the expected. The fact that the value between them, 1200nm, is slightly lower than expected implies that this could be the case.

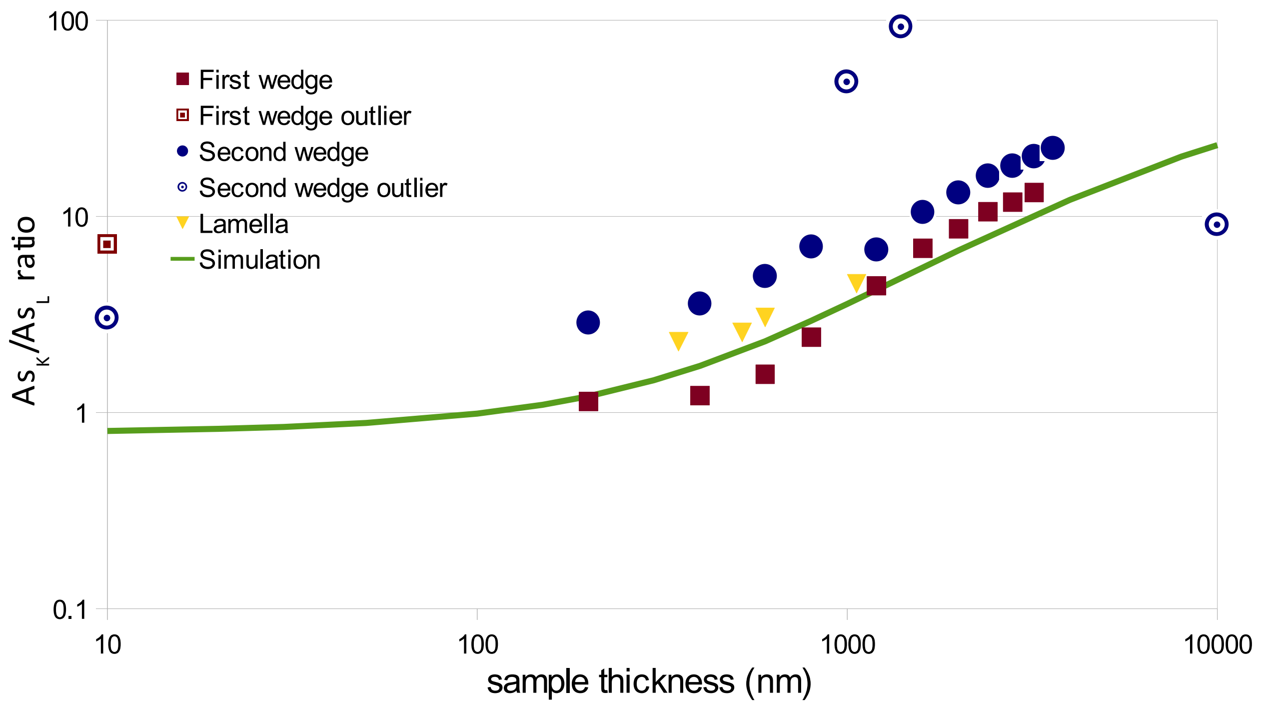

Figure 6.2.3:Experimental comparison of three different samples. Note the double-log scale. Simulation was run in NISTMonte for beam energy 197keV, 10^7 electron histories, with a GaAs (density = 5.316gcm^{-3}) lamella of varying thickness with take-off angle 25°. Detector efficiencies As_K: 79%, As_L: 68%, Ga_K: 77%, Ga_L: 64%. Note that the thickness of the two 10nm data points is not well known, and could vary by as much as 50%.

Table 6.2.2 contains the calculated parameters from least-squares fitting third order polynomials to the curves in Figure 6.2.3, with the exception of the lamella data set, which does not posses enough data points to justify a second order polynomial fit. These fits are justified by the simulated data.

This analysis will be continued in Chapter 7.

	y-intercept	R^2
First wedge (all data points)	2.5±0.4	0.971
First wedge (outliers removed)	1.1±0.2	0.997
Second wedge (all data points)	-2±12	0.170
Second wedge (outliers removed)	1.8±0.7	0.993
Lamella	1.1±0.2	0.984
Simulation	0.69±0.04	0.9997
Combined (all data points)	-1±6	0.112
Combined (outliers removed)	0.6±1.9	0.772

Table 6.2.2: Least-squares regression of the curves in Figure 6.2.3. First wedge outlier is the 10nm data point. Second wedge outliers are 10nm, 1000nm, 1400nm and 10000nm data points. 'Combined' is all data sets analysed together, where the outliers are those specified in the individual sets.

Much of the method of taking the ratio of two X-rays to determine the thickness of the sample has already been explored [9], with further details on how it can be used for more accurate quantification. The new aspects covered here is the discussion of the merits of using deadtime (or total X-ray intensity) as a measure of thickness. A further improvement will be detailed in Chapter 7.

6.3 Method for Determination of Thickness by Varying Take-off Angle

The change in the strength of absorption of an X-ray line with changing take-off angle is mathematically predictable. This predictability can be exploited in homogeneous samples to determine the thickness of the sample by taking a series of spectra at different take-off angles. The advantage of this method compared to the K/L ratio is that it does not require either two X-ray lines from the same material or known sample composition. This is most obviously useful for those elements which do not possess an L-line (i.e. Z≤10) or those whose L-line cannot be readily quantified with today's technology (E≤200eV). The disadvantage is that multiple data points are necessary, which in turn requires a stable beam intensity and insignificant sample drift or damage and does not allow enhanced quantification from one spectrum alone.

A commonly accepted method to calculate the absorption factor is that used in the Cliff-Lorimer ratio method, below:

$$a=\left(\frac{\left.\frac{\mu}{\rho}\right]_{spec}^{A}}{\left.\frac{\mu}{\rho}\right]_{spec}^{B}}\right)\left(\frac{1-e^{-\left.\frac{\mu}{\rho}\right]_{spec}^{B}\rho\, t\arcsin(\theta)}}{1-e^{-\left.\frac{\mu}{\rho}\right]_{spec}^{B}\rho\, t\arcsin(\theta)}}\right)$$

where $\left.\frac{\mu}{\rho}\right]_{spec}^{A}$ is the mass-absorption coefficient in cm^2g^{-1}, ρ is the density in gcm^{-3}, t is the thickness in m and θ is the take-off angle in degrees. For the same X-ray line at two different take-off angles θ_1 and θ_2 this reduces to:

$$\frac{I_1}{I_2}=\left(\frac{1-e^{-\left.\frac{\mu}{\rho}\right]_{spec}^{B}\rho\, t\arcsin(\theta_2)}}{1-e^{-\left.\frac{\mu}{\rho}\right]_{spec}^{B}\rho\, t\arcsin(\theta_1)}}\right) \quad \text{Equation 6.3.1}$$

This would result in a graph similar to Figure 6.3.1, where each curve is for a different thickness. Comparing experimental results to similar curves would allow the user to determine the thickness by finding the closest match.

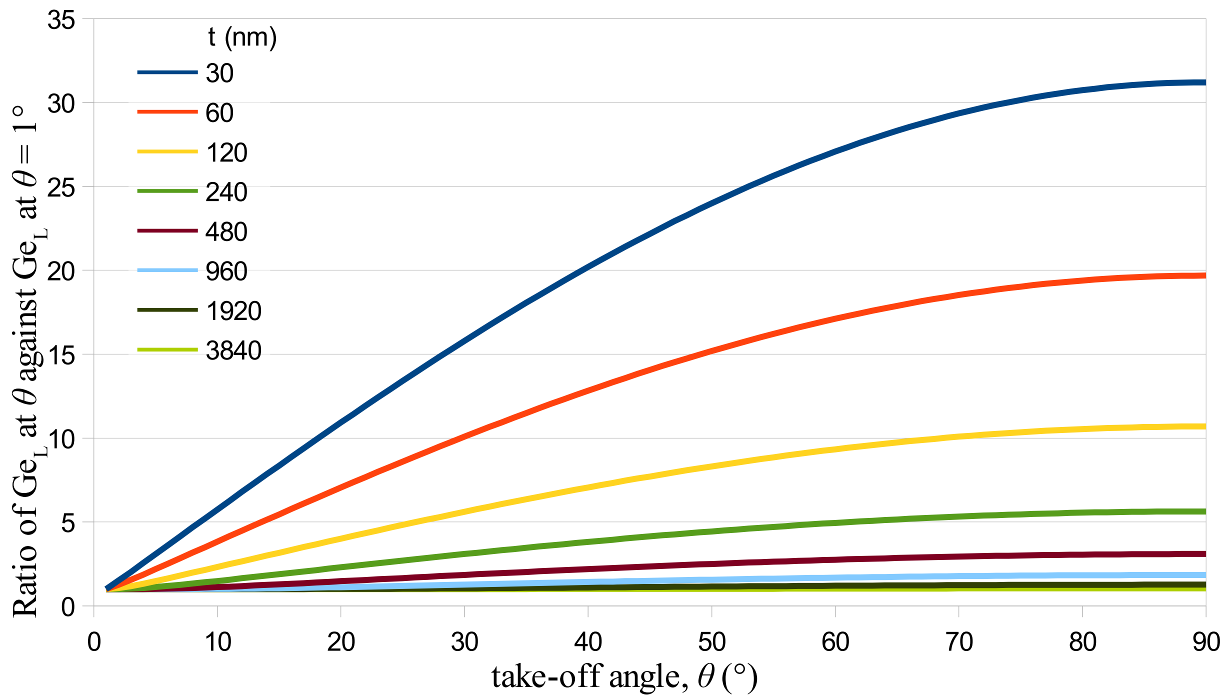

Figure 6.3.1: Result of equation 6.3.1 for Ga_L in GaAs for different thicknesses. $\left.\frac{\mu}{\rho}\right]_{spec}^{A}$ = $1532 cm^2 g^{-1}$, $\rho = 5.32 gcm^{-3}$.

Figure 6.3.1 shows that for a large change in take-off angle there is a very significant difference in Ga_L intensity between different thicknesses, thereby allowing the user to readily distinguish between thicknesses. Note that this does not apply when the sample is beyond a certain critical thickness, as the X-rays would reach a 'saturation point' beyond which additionally generated X-rays would be mostly absorbed by the sample, regardless of take-off angle.

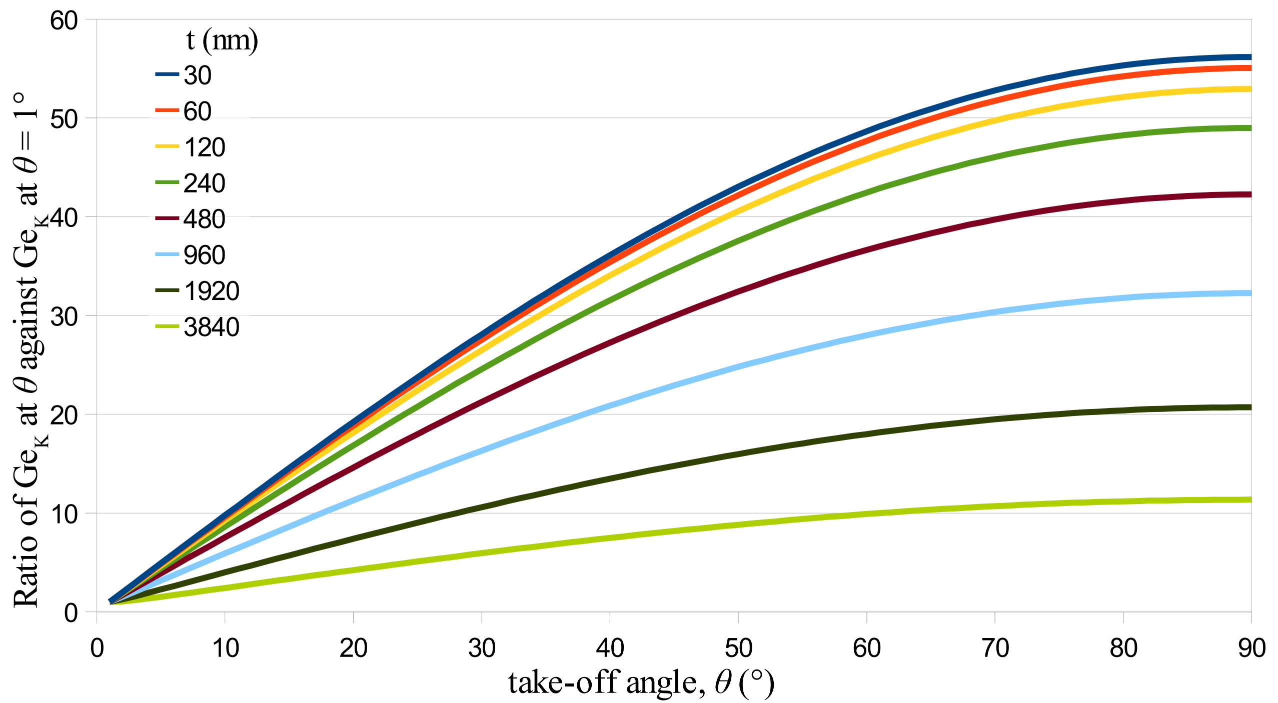

Figure 6.3.2: Result of equation 6.3.1 for Ga_K in GaAs for different thicknesses. $\left.\frac{\mu}{\rho}\right]^{A}_{spec}$ = 44.87cm^{2}g^{-1}, ρ = 5.32gcm^{-3}.

Figure 6.3.2 is an equivalent to Figure 6.3.1 with Ga_K instead of Ga_L. It is clear that while the overall form of the curves is the same their response to increasing thickness is much weaker, and it is the low thicknesses that see little difference in Figure 6.3.2 as opposed to the high thicknesses seen in Figure 6.3.1. This implies that a sample with a number of X-rays with energy values covering a large range of energies could use this method to estimate thickness, as if one X-ray line will not work then another would. Obviously, different lines could then be used for a self-consistency check. For example, the above simulations imply that such cross-checking could be carried out for sample thicknesses of between approximately 120-480nm.

In summary, the advantage of this method is the lack of requirement for either two clearly defined X-ray lines from the same element or known sample composition. The drawbacks is a need for several data points acquired with a constant beam intensity of the same region without significant sample drift or damage.

7 An improvement to the Cliff-Lorimer *k*-factors

7.1 Simulated Analysis

As already mentioned, the Cliff-Lorimer ratio method uses the following equation for quantification:

$$X_j = \frac{\dfrac{I_j a_j k_j e_j}{A_j}}{\sum_n \dfrac{I_n a_n k_n e_n}{A_n}} \quad \therefore \quad \frac{X_j}{X_i} = \frac{\dfrac{I_j a_j k_j e_j}{A_j}}{\dfrac{I_i a_i k_i e_i}{A_i}} = \frac{I_j a_j k_j e_j}{I_i a_i k_i e_i}\frac{A_i}{A_j} \qquad \text{Equation 7.1.1}$$

where $X_{j,i}$ are compositions, $I_{j,i,n}$ X-ray intensities, $a_{j,i,n}$ the absorption correction, $k_{j,i,n}$ the k-factors, $e_{j,i,n}$ the detector efficiencies at the relevant energies, $A_{j,i,n}$ the atomic weight, n every element in the sample and i,j two elements of interest. The absorption correction a and the k-factor are defined relative to another. Taking a and k as relative to a_i and k_i causes Equation 7.1.1 to simplify to

$$\frac{X_j}{X_i} = \frac{I_j a_j k_j e_j}{I_i e_i}\frac{A_i}{A_j} \quad \therefore \quad a_j k_j = \frac{X_j}{X_i}\frac{I_i e_i}{I_j e_j}\frac{A_j}{A_i} \qquad \text{Equation 7.1.2}$$

Using this method means that the k-factor and the absorption correction cannot be separated. Therefore, arriving at a value for one can be accomplished by setting the other to a specific value: the most obvious way to do this is to drive the absorption correction to unity, as this can be done through extrapolating to zero thickness. As such, arriving at correct values for either variable is difficult. However, this can be accounted for by taking a series of measurements at different sample thicknesses, as doing so would result in a series of monotonic data points as seen in Figure 7.1.1. This can be used in two ways: by extrapolating the value to zero a value of the k-factor without the effect of absorption can be estimated and the product of the absorption and k-factor, which may be called an effective k-factor k_{eff}, can be determined from knowledge of the thickness. This is superior to the current generally accepted method of calculating a value for the k-factor and estimating the absorption correction from sample density and thickness. Of course, knowledge of the sample thickness is necessary for this method to function: this knowledge can be acquired using the same data set using the method described in Chapter 6. It is worth noting that the form of the curve seen in Figure 7.1.1 is not universal, though such curves are always monotonic. It is also worth noting that this method would apply to a sample that is not homogeneous, if the inhomogeneity is sufficiently small.

[CLARIFY CONNECTION TO ZAF METHOD]

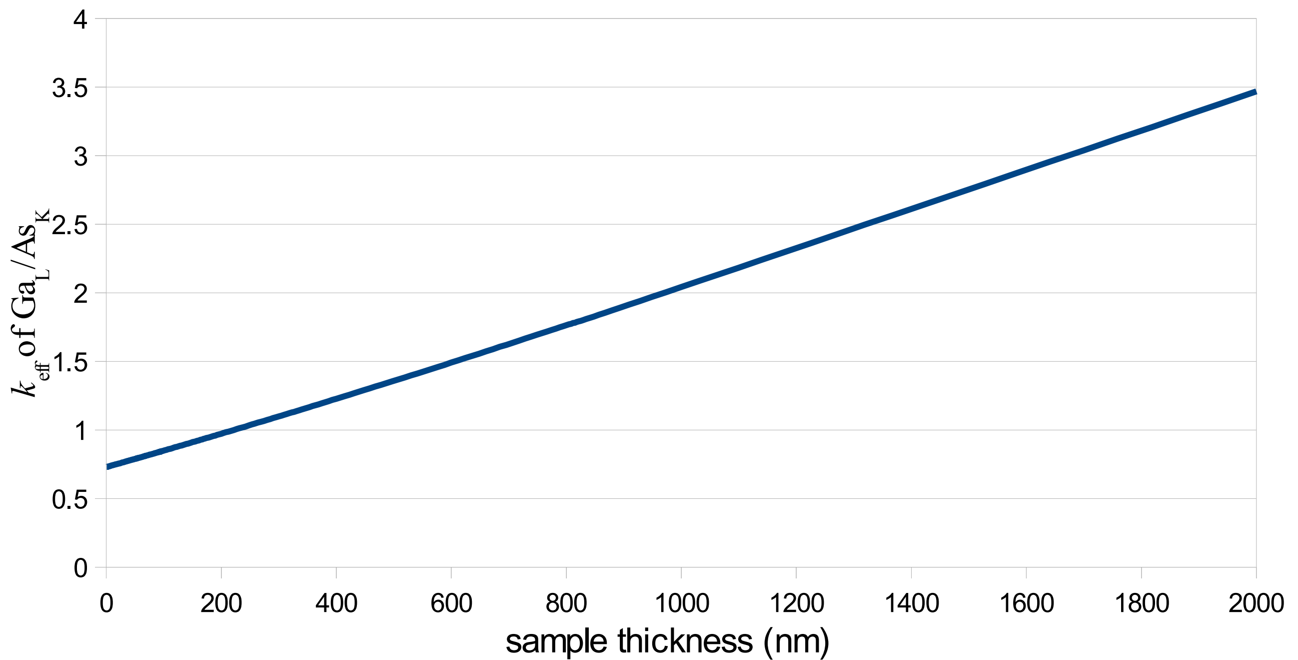

Figure 7.1.1: k_{eff} of Ga_L with respect to As_K. Simulation run in NISTMonte at beam energy 197keV, take-off angle 20° with 10^7 electron histories. Sample composition GaAs (density = 5.316gcm^{-3}) lamella of varying thickness.

Figure 7.1.2 shows a comparison between the results from NISTMonte and CASINO. Both k_{eff} are with respect to Si_K. The curves from Ge_K are clearly very similar, with only a slight difference between their absolute values and slopes. The CASINO Ge_L curve is similar to the two Ge_K curves in slope, with, the difference being the absolute magnitude. The NISTMonte Ge_L curve, however, has a very different slope and *y*-intercept, though it does agree with CASINO at high thickness. It is difficult to be certain which of the two is correct. Given the very different energies of Ge_K and Ge_L a change in the slope would be expected, which agrees with NISTMonte, however, such a similarity in *y*-intercept would not be expected. This will be discussed in more detail in Figure 7.2.5. A large difference at low thicknesses that grows smaller with increasing thickness implies that there is a difference in the rate of X-ray production for that line that is being counterbalanced by the effect of different levels of absorption modelled.

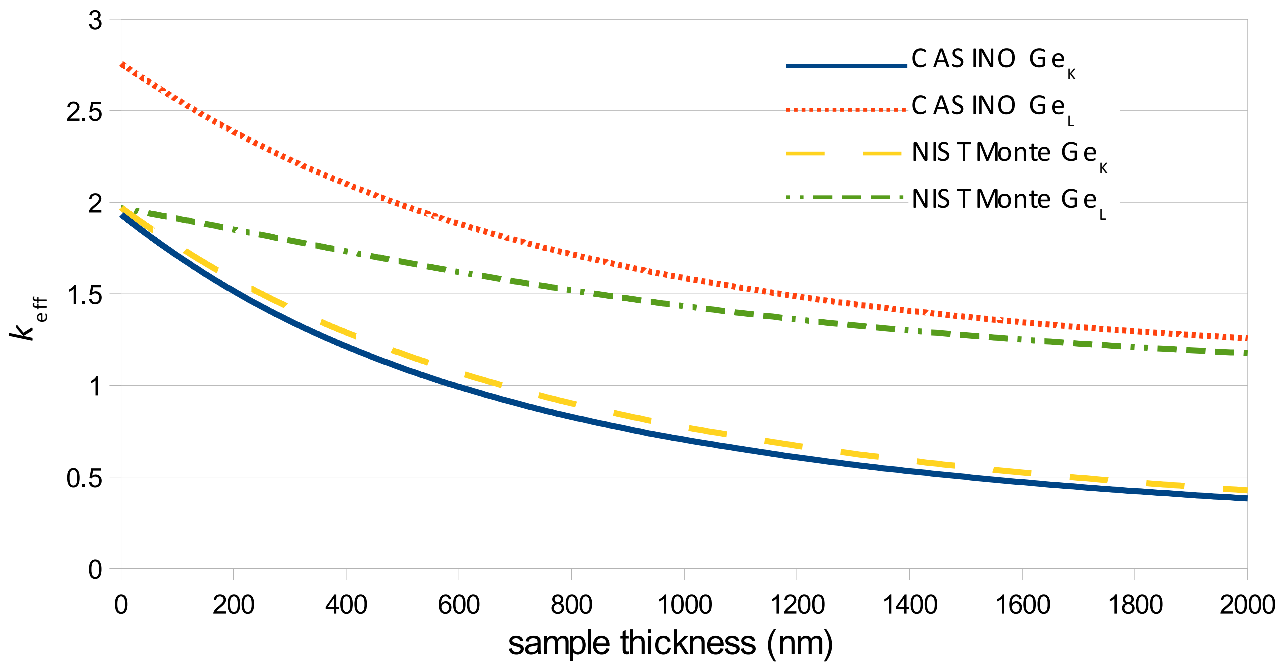

Figure 7.1.2: Comparison of k_{eff} resulting from CASINO and NISTMonte simulations. NISTMonte simulation: beam energy 197keV, take-off angle 25° with 10^6 electron histories. CASINO simulation: beam energy 200keV, take-off angle 25° with 10^6 electron histories. Sample composition $Si_{0.54}Ge_{0.46}$ (density = 3.71gcm^{-3}) lamella of varying thickness.

Figure 7.1.3 shows the calculated k_{eff} with respect to In_K for an InP binary system. The In_M curve seems almost linear, with a very slight curve at low thickness, while both the In_L and P_K curves have obvious non-linearities that extend into micron thicknesses. Obviously, this would be problematic for attempts to calculate the absorption-less *k*-factor, as while the form of the experimental curve will likely correspond to simulations the strength of the slope may not, meaning that multiple measurements in the non-linear regions would be necessary for accurate extrapolation.

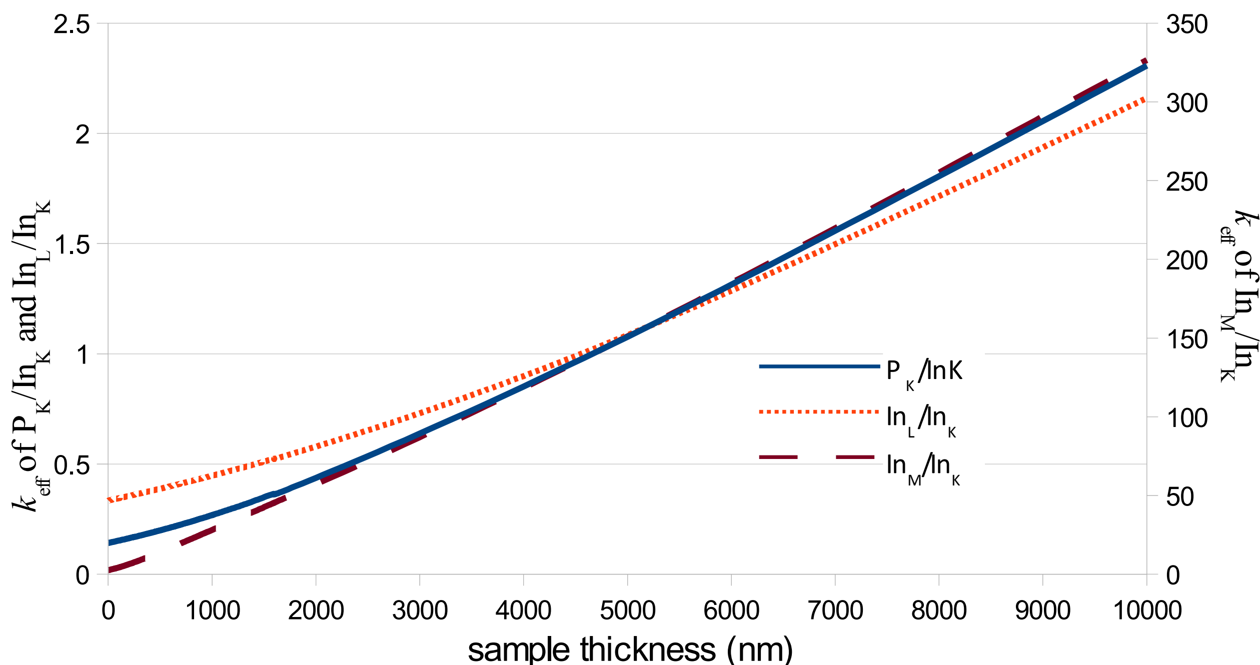

Figure 7.1.3: NISTMonte simulated results for InP sample. In_M/In_K is plotted against the right vertical axis. Beam energy 197keV, take-off angle 25° with 10^6 electron histories. Sample InP (density = $5.12 gcm^{-3}$) lamella of varying thickness.

Figure 7.1.4 shows the calculated k_{eff} for all X-rays in the binary InSb system, calculated with respect to Sb_K. In_M and Sb_M both show slight non-linear behaviour followed by a linear region: given their similar energies this is to be expected. In_L and Sb_L also share a trend for much the same reason. In_K is effectively horizontal: this is a function of energy similar to Sb_K.

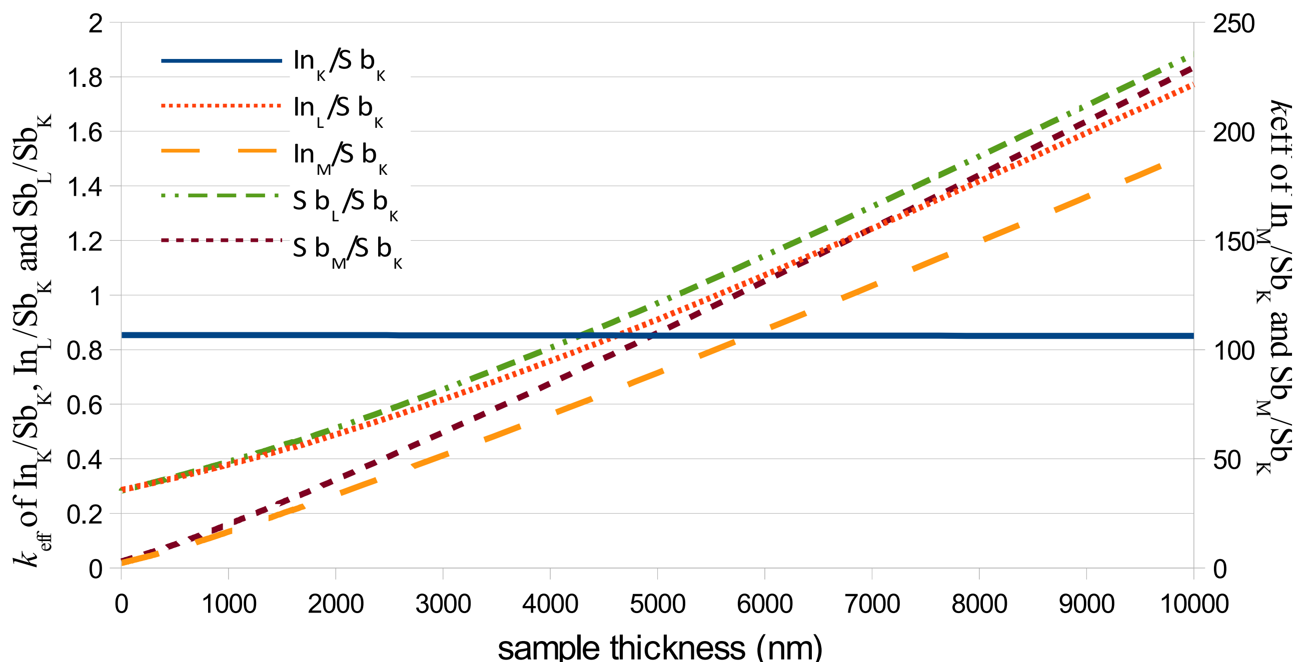

Figure 7.1.4: NISTMonte simulated X-ray intensities for InSb. In_M/Sb_K and Sb_M/Sb_K against right vertical axis. Beam energy 197keV, take-off angle 25° with 10^6 electron histories. Sample InSb (density = $5.775 gcm^{-3}$) lamella of varying thickness.

Figure 7.1.5 is the same system as Figure 7.1.4 where all lines are calculated with respect to In_K instead of Sb_K. Given the comparatively similar energies of In_K and Sb_K it is no surprise that the same trends hold.

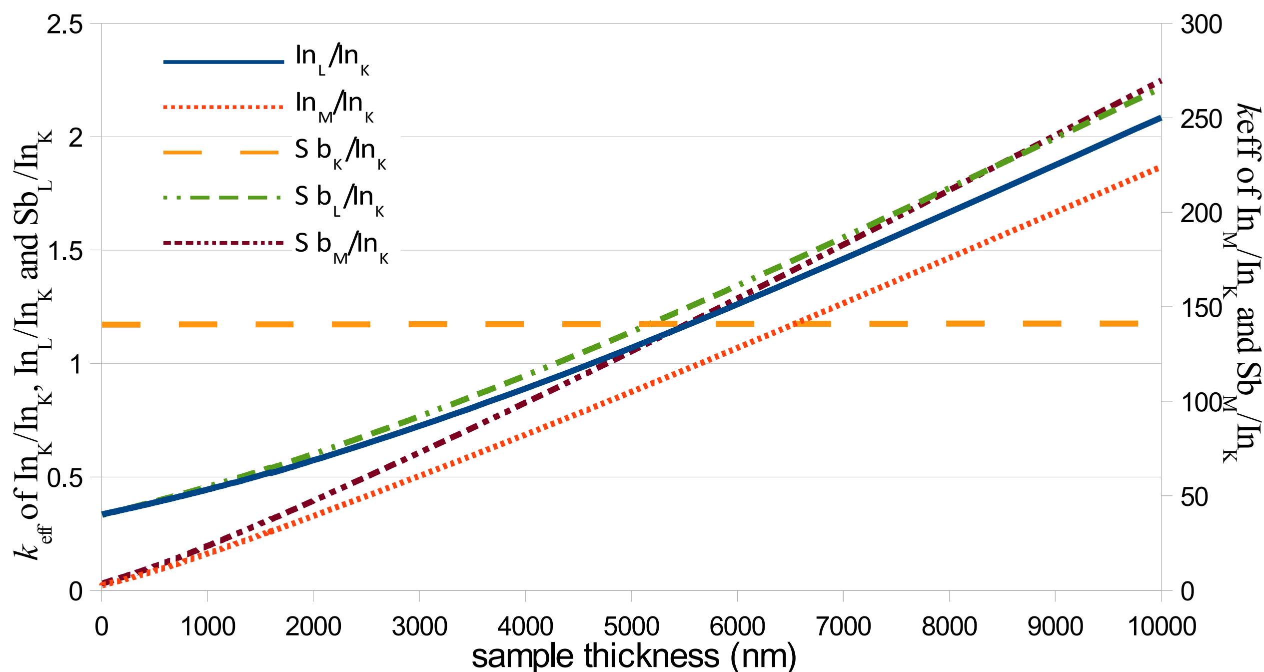

Figure 7.1.5: NISTMonte simulated X-ray intensities for InSb. In_M/In_K and Sb_M/In_K against right vertical axis. Beam energy 197keV, take-off angle 25° with 10^6 electron histories. Sample composition InSb (density = 5.775gcm^{-3}) lamella of varying thickness.

Figure 7.1.6 shows data again for the InSb system, this time calculated with respect to In_L. This line would experience significantly more absorption than either In_K or Sb_K, and as such would result in very different calculated trends. This time, it is the Sb_L line that is almost horizontal, a function of its energy similar to In_L. It is worth noting that, unlike the In_K curve in Figure 7.1.4, this curve is not completely horizontal as a function of the slightly different absorption that In_L and Sb_L experience, where this trend would presumably also be visible for the In_K of Figure 7.1.4 if the thickness was increased sufficiently. The curves of In_M and Sb_M, being absorbed more strongly than In_L, begin with a strong increase (which would translate to a decrease in relative intensity) and then level off: this would be due to most additional X-rays generated by greater thickness being self-absorbed by said greater thickness. In_K and Sb_K show the opposite trend as a result of being much higher in energy than In_L.

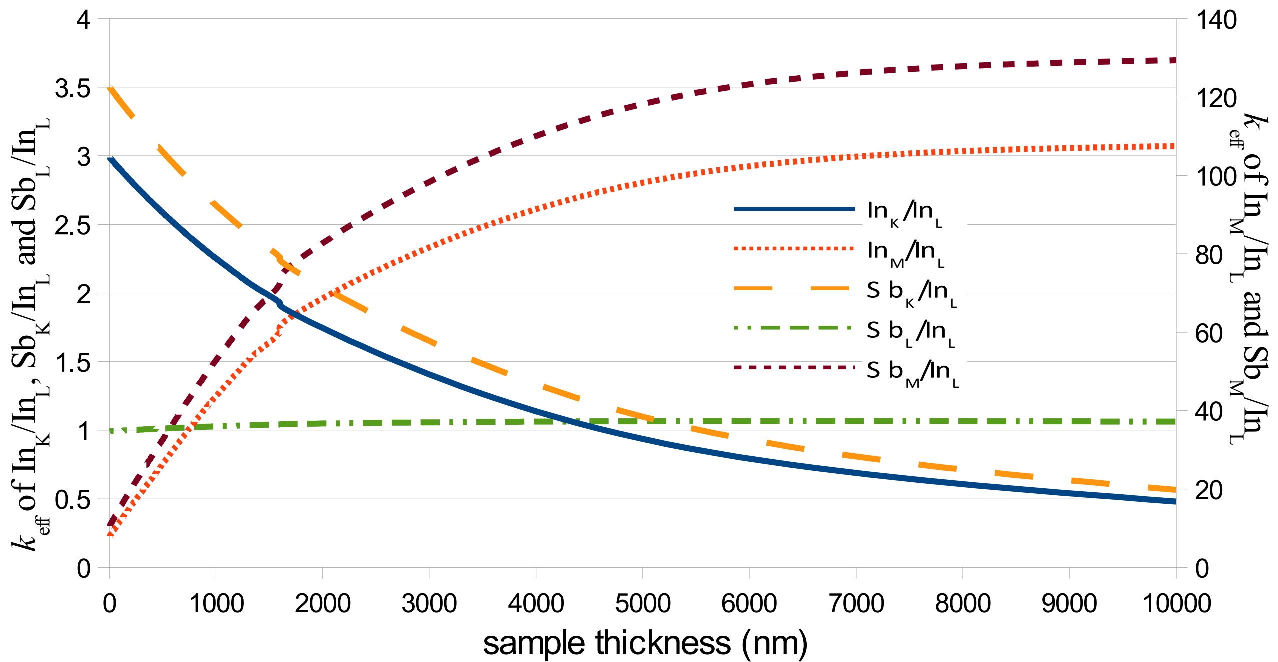

Figure 7.1.6: NISTMonte simulated X-ray intensities for InSb. In_M/In_L and Sb_M/In_L against right vertical axis. Beam energy 197keV, take-off angle 25° with 10^6 electron histories. Sample composition InSb (density = 5.775gcm^{-3}) lamella of varying thickness.

Given that higher energy X-rays (like In_K and Sb_K) give a much more linear curve (as seen in Figure 7.1.4 and Figure 7.1.5) compared to X-rays of lower energy (like In_L) it would be reasonable to ask why investigate such curves at all. The chief advantages would be availability, statistics and whether the change due to absorption is desirable: the detection efficiency of a Si(Li) detector at the energies of harder X-rays is significantly less than that of softer X-rays, which could mean significantly inferior counting statistics if this loss of intensity due to detector efficiency is greater than the gain from decreased absorption. If the intent is to arrive at the sample thickness, then certain combinations of X-rays would be unsuitable as there would be very little change (e.g. Sb_L / In_L in Figure 7.1.6), though such curves would be ideal for determining chemical composition as they are almost independent of sample thickness. It is also worth noting that a lower energy X-ray may be selected as the comparator simply because the highest energy X-ray may be emitted from a material that is of low concentration in the sample, such as In_K from $In_{0.1}Ga_{0.9}As$.

The primary difficulty in extrapolating from a few data points in a non-linear curve is that the slope and the point of transition from non-linear to linear are both critical to analysis and difficult to measure with good accuracy. As such, a method that reduces the problem to a simple linear extrapolation would be useful. Noting that in Figure 7.1.6 the In_M and In_K curves are inverse functions implies that some manner of combination might lead to a linear curve. An obvious way to do this is to take their ratio, which results in the curve seen in Figure 7.1.7. The extent to which this curve is linear can be judged by its linear least-squares R^2 value of 0.9972. It is worth noting that this curve could still be extrapolated to zero so as to arrive at a *k*-factor without absorption, but the resulting value would be the weighted sum of the two relevant *k*-factors, which would require knowledge of one in order to extract the other.

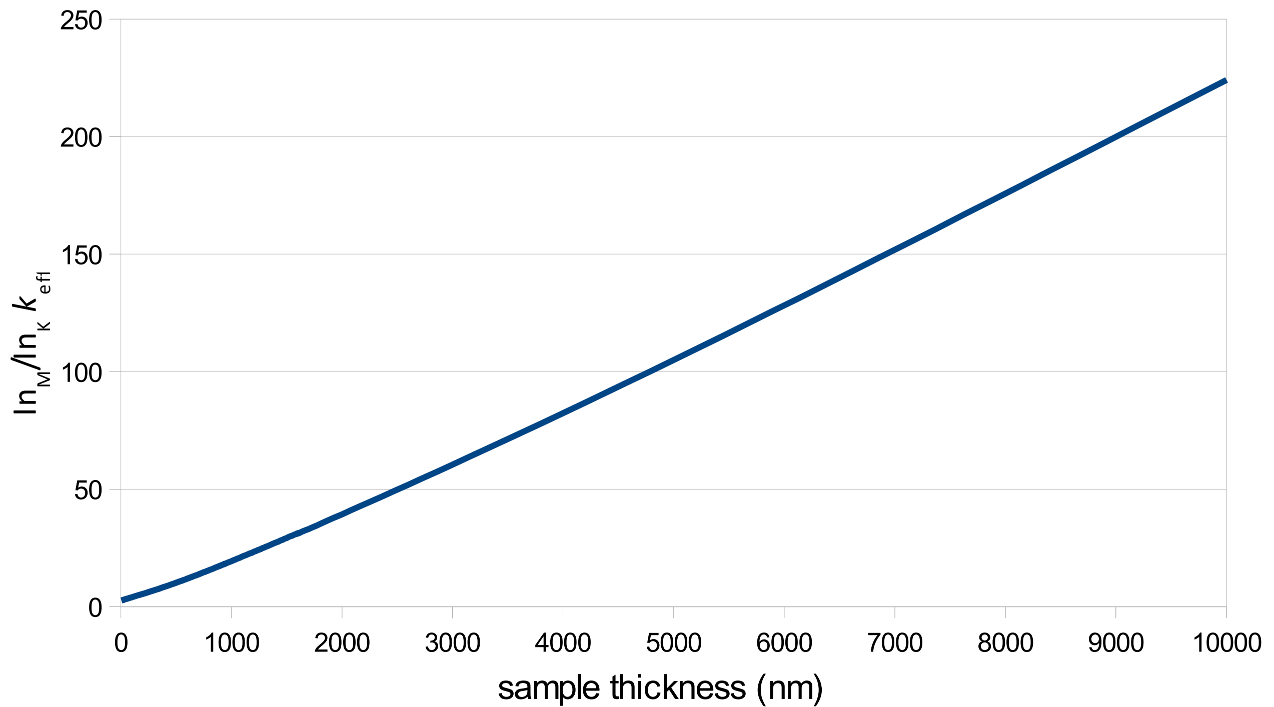

Figure 7.1.7: NISTMonte simulated X-ray intensities for InSb. Beam energy 197keV, take-off angle 25° with 10^6 electron histories. Sample InSb (density = 5.775gcm^{-3}) lamella of varying thickness.

Given that the In_M and In_K curves in Figure 7.1.6 are of different orders of magnitude it is clear that simple addition will not suffice, however a weighted sum could do instead. This can be done by following this equation:

$$I = \frac{I_M}{w_M} + \frac{I_K}{w_K} \quad \text{Equation 7.1.3}$$

where I is the resulting intensity (hopefully linear with thickness), I_M and I_K are the low and high X-ray energy intensities respectively and w_M and w_K are their respective weights. Using trial and error for simulated curves it was found that the most linear result is when $w_K = 1$ and $w_M = 55.22$, resulting in the curve displayed in Figure 7.1.8. Linear least-squares analysis gives this curve an R^2 value of 0.9916. Depending on what experimental data points are available, this could be favourable compared to the exponential curves seen in Figure 7.1.6 and could be superior to the curve seen in Figure 7.1.7 if the two intensities chosen for this analysis are not scaled opposites, since a ratio would not necessarily result in a linear curve while a weighted sum might.

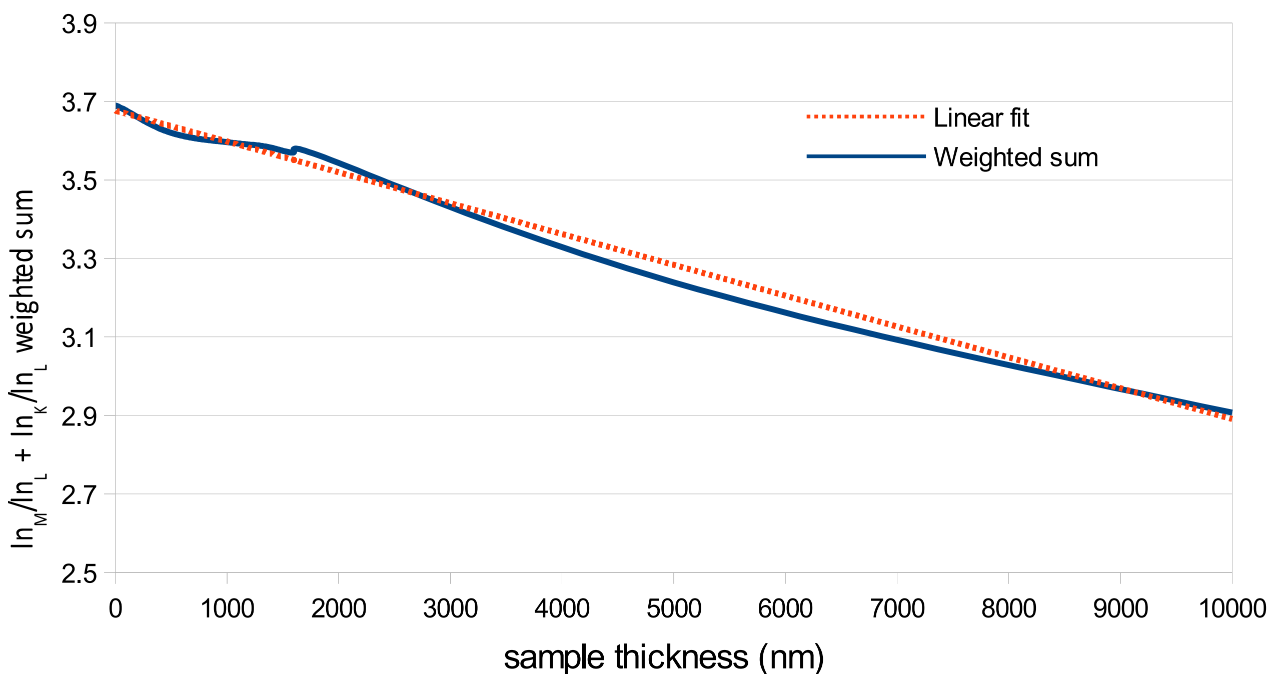

Figure 7.1.8: Weighted sum of In_M/In_L and In_K/In_L in InSb. NISTMonte simulation run at beam energy 197keV, take-off angle 25° with 10^6 electron histories. Sample InSb (density = 5.775gcm^{-3}) lamella of varying thickness.

Calculating the corrected *k*-factor from this method would then be a simple matter of subtracting the additional *k*-factor from the extrapolated intercept.

The only samples considered up to this point are binary in composition. Many samples, however, would be comprised of three or more materials: the prior derivation holds true in this case, where the presence of the additional elements can be ignored for the purposes of the calculation. It is worth noting that the k_{eff} for values above $t = 0$ will be different, but that for $t = 0$ it will be the same. The validity of this approach is shown in Figure 7.1.9, which shows that varying the indium concentration in $In_xGa_{1-x}As$ can be properly accounted for to give the same *y*-intercept.

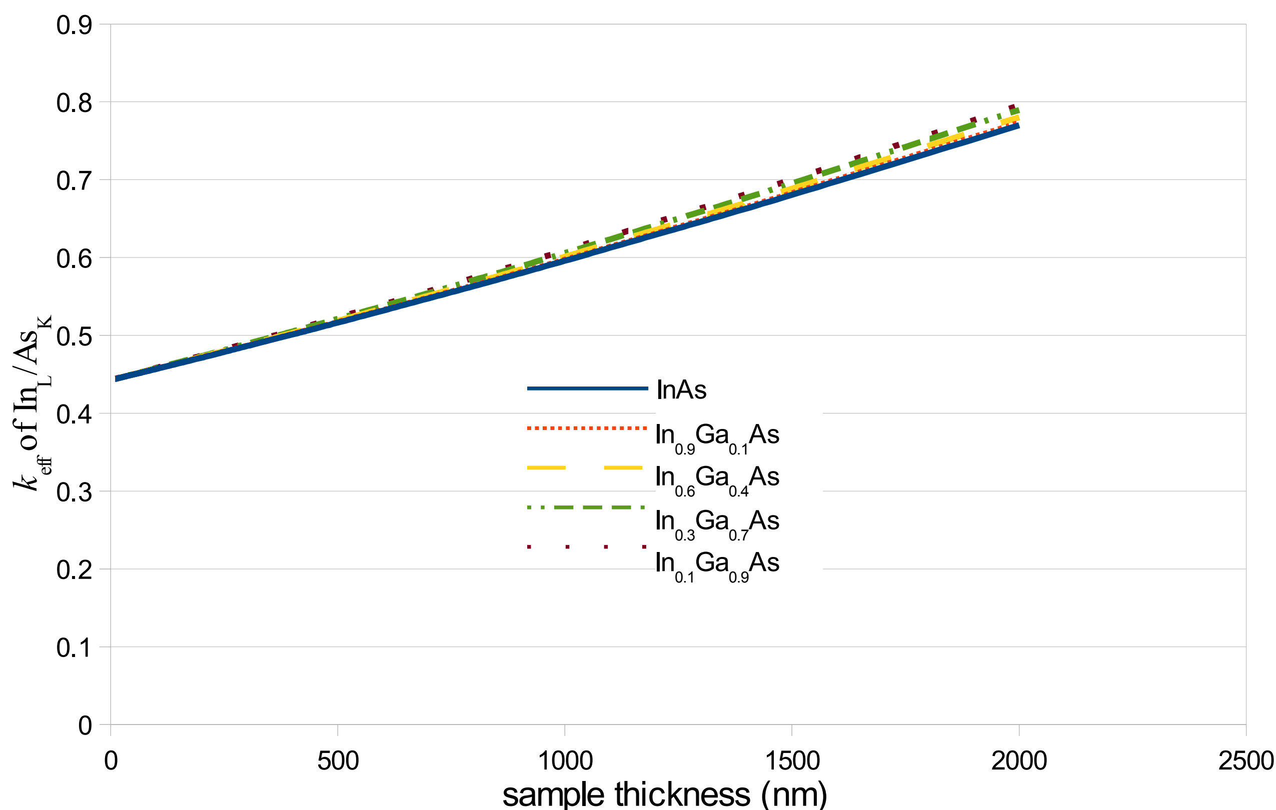

Figure 7.1.9: NISTMonte simulation of $In_xGa_{1-x}As$ of various compositions. Beam energy 197keV, take-off angle 25° with 10^6 electron histories. Material densities given by linear interpolation between InAs (density = 5.67gcm^{-3}) and GaAs (density = 5.316gcm^{-3}).

In principle, this means that several corrected *k*-factors could be derived from a single sample. The difficulty with this is twofold: reduced counting statistics for individual lines compared to if they were analysed in a binary sample (since all available lines 'compete' for detector processing time) and uncertainty in knowledge of the composition. In many binary samples, a certain composition can be assumed with a fair degree of accuracy (a Type III and Type V sample would be 1:1, for example) however such would not be the case for a sample with more elements. Counting statistics is unlikely to be a problem, as analysis time can be devoted in full to a single sample rather than needing to split between two or more samples: this would likely offset any increase in error due to background subtraction. The composition issue would likely introduce significant errors: this could be partially mitigated by an iterative approach, cycling back and forth between the composition, sample thickness at that particular point (possibly aided by that discussed in Chapter 6) and fitting to modelled or simulated curves. Other than convenience, this approach would have the advantage of producing self-consistent *k*-factors.

7.2 Experimental analysis

The first experimental sample to be analysed is the GaAs lamella previously seen in Figure 6.2.2. As already mentioned, extrapolating the value to zero thickness gives the *k*-factor value, as seen in Figure 7.2.1. Given that there are only a few data points and that they lie along a fairly straight line, a linear least-squares regression seemed the best choice. The results of this analysis is shown in Table 7.2.1, along with the nominal values extracted from the LINK ISIS software. The R^2 values are uniformly high and the relative errors comparatively low. Compared to the currently accepted values the absorption-less *k*-factors are significantly different, with all but the Ga_K/As_K ISIS values

being smaller than their corrected counterpart. The reason for why this is not clear: it could be that the ISIS values were calculated with an excessive correction for absorption and therefore gave values that are too low.

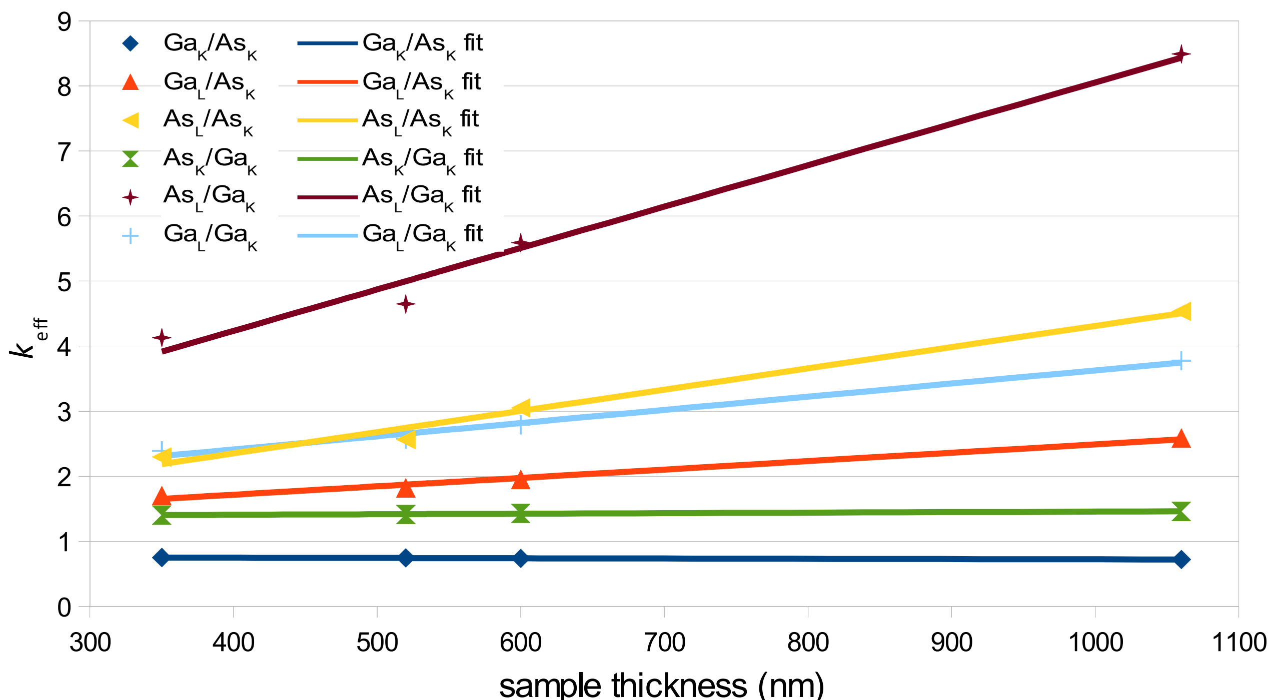

Figure 7.2.1: Experimental data from GaAs lamella. Estimated detector efficiencies As_K: 79%, As_L: 68%, Ga_K: 77%, Ga_L: 64%.

	y-intercept	R^2	ISIS value
Ga_K/As_K	0.764±0.003	0.975	0.88
Ga_L/As_K	1.20±0.07	0.987	0.90
As_L/As_K	1.4±0.3	0.984	0.89
As_K/Ga_K	1.38±0.01	0.977	1.14
As_L/Ga_K	1.7±0.4	0.984	1.02
Ga_L/Ga_K	2.32±0.16	0.987	1.03

Table 7.2.1: Least-squares linear regression of the data in Figure 7.2.1.

Plotting k_{eff} against thickness is not the only method for correcting the *k*-factor. Another viable method is to plot it against a K/L ratio, such as those seen in Chapter 6. In this case, to give the correct *k*-factor without absorption value the curve must not extrapolated to the *y*-intercept but instead to some value of the K/L ratio that corresponds to zero thickness. This value can be determined from the same data set to provide a self-consistent result. It is worth noting that this approach would exclude the calculation of certain *k*-factors, as plotting the k_{eff} of a pair of X-rays against its own K/L ratio is not meaningful. The data of Figure 7.2.1 is plotted against As_K/As_L and Ga_K/Ga_L in Figure 7.2.2: plainly the same trends are followed.

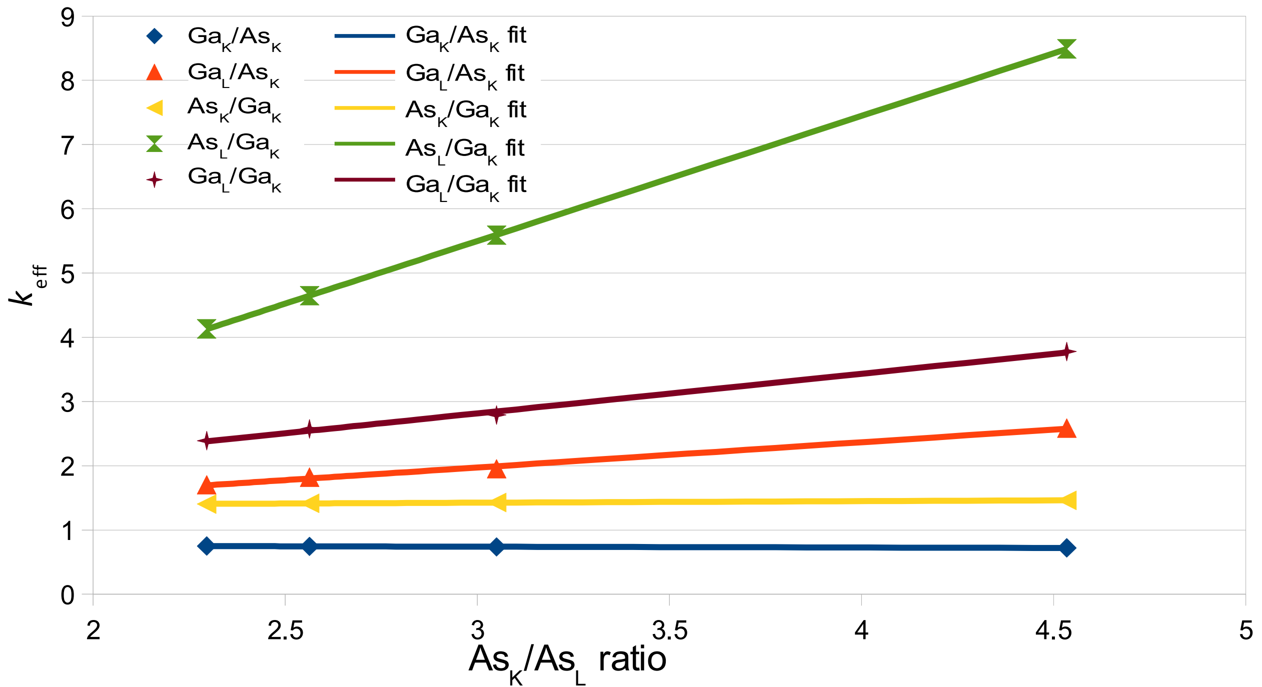

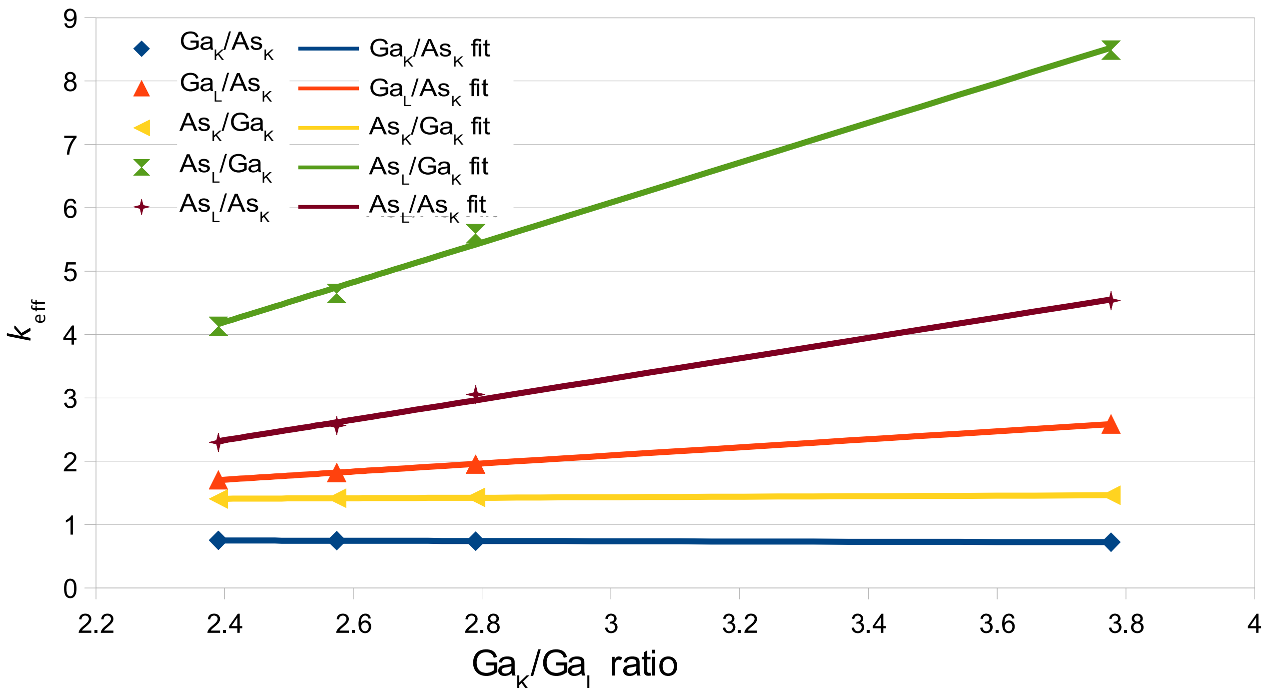

Figure 7.2.2: Figure 7.2.1 data plotted against As_K/As_L and Ga_K/Ga_L. Estimated detector efficiencies As_K: 79%, As_L: 68%, Ga_K: 77%, Ga_L: 64%.

The linear least-squares regression results of the curves shown in Figure 7.2.2 are displayed Table 7.2.2. It is clear that plotting against either As_K/As_L or Ga_K/Ga_L gives similar results, with only minor changes in both the error of the results and the R^2 and the calculated k_{eff} at t=0 being the same in both cases. There is no clear trend as to which is superior, though perhaps the As_K/As_L fits have, on average, a slightly higher R^2. Of particular interest is comparing these results to those found in Table 7.2.1: the answer calculated using the K/L ratios almost uniformly have lower relative error and R^2 values closer to unity than those calculated with respect to sample thickness. In a sample of this nature, where the data is well-behaved, this approach may well not be necessary, however, if there is more scatter or other problems with the data then the increased self-consistency could give

far greater benefits. Comparing the corrected *k*-factors with those given by the ISIS software, there are some changes particularly in the softer X-rays (As_L and Ga_L). This is as expected, as a softer X-ray is more susceptible to absorption and hence removing absorption would change the values to a greater extent.

		k-factor at t=0	R^2	ISIS values
plotted against As_K/As_L	Ga_K/As_K	0.766±0.002	0.980	0.88
	Ga_L/As_K	1.20±0.08	0.995	0.90
	As_K/Ga_K	1.382±0.004	0.983	1.14
	As_L/Ga_K	1.7±0.4	1.000	1.02
	Ga_L/Ga_K	1.61±0.12	0.996	1.03
		k-factor at t=0	R^2	ISIS values
plotted against Ga_K/Ga_L	Ga_K/As_K	0.765±0.002	0.964	0.88
	Ga_L/As_K	1.20±0.07	1	0.90
	As_K/Ga_K	1.390±0.004	0.968	1.14
	As_L/Ga_K	1.7±0.4	0.996	1.02
	As_L/As_K	1.05±0.18	0.996	0.89

Table 7.2.2: Linear least-squares regression of data in Figure 7.2.2 where the KL ratio corresponding to t=0 was taken from Figure 6.2.2.

An example of a data set which is not well-behaved when plotted with respect to sample thickness would be either of the two 'wedge' data sets shown in Figure 6.2.3. This behaviour is most apparent in ratios other than As_K/As_L which had not been plotted previously. Plotting k_{eff} for different X-ray lines against sample thickness illustrates this issue, as seen in Figure 7.2.3. It is plain that in some cases, such as the Ga_K/As_K or As_L/Ga_K curves, neither a linear nor a second order polynomial fit will suffice. In other curves this is less obvious, such as the Ga_L/Ga_K, which has a slight curvature at high thicknesses and a strong curve in the other direction at low thickness.

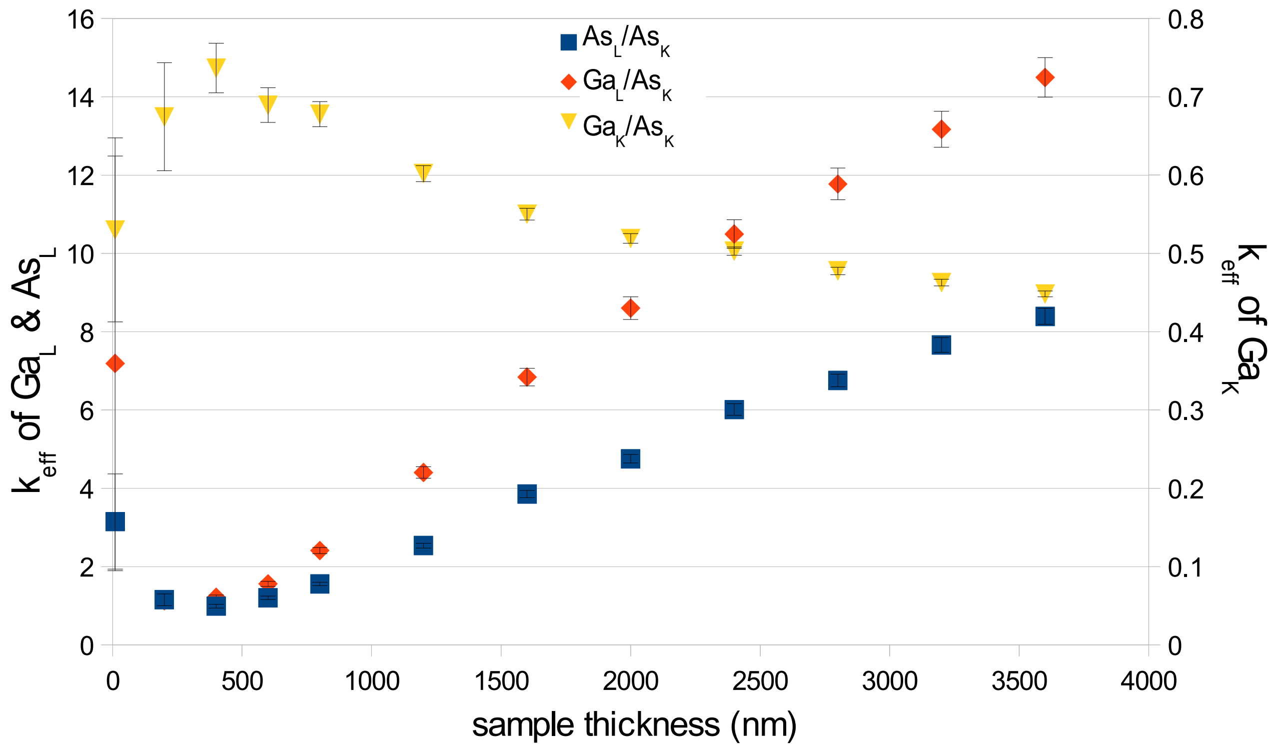

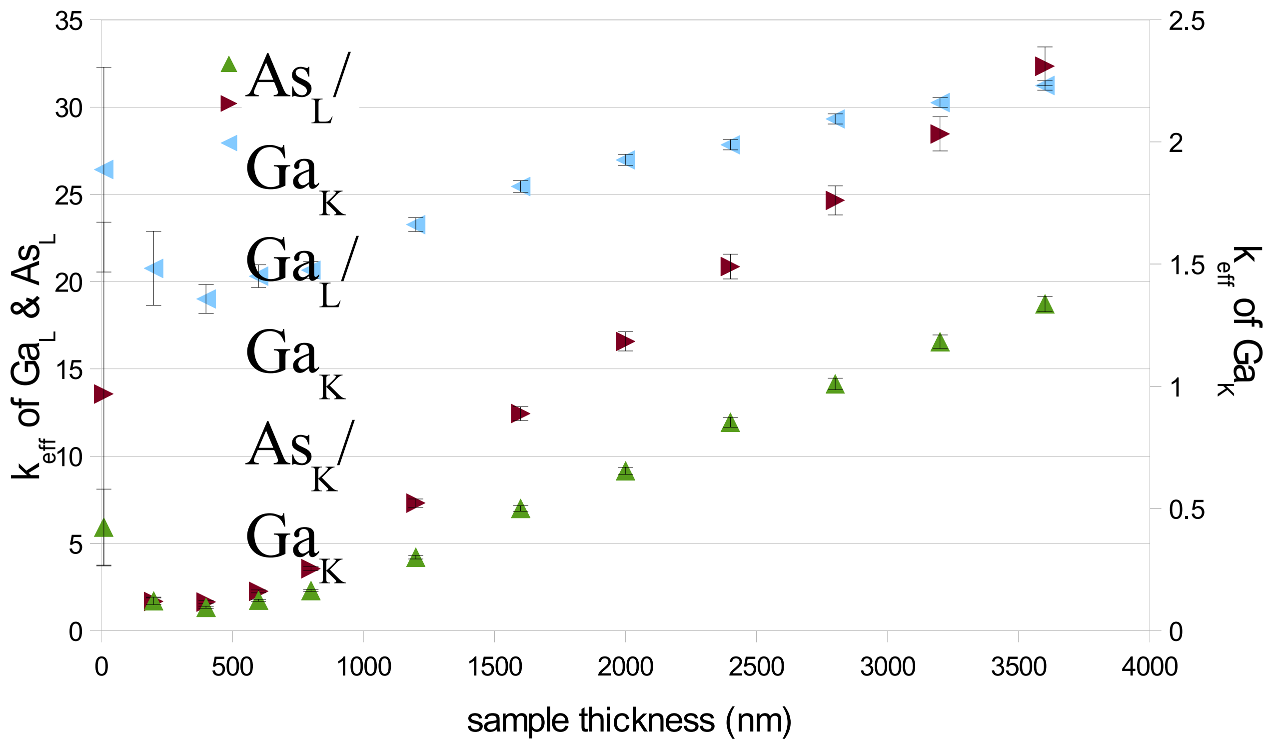

Figure 7.2.3: Various k_{eff} for a GaAs cleaved wedge. Detector efficiencies As_K: 79%, As_L: 68%, Ga_K: 77%, Ga_L: 64%.

Plotting the same curves against a KL ratio, however, gives a much superior plot, as seen in Figure 7.2.4. These curves are significantly more linear than those seen in Figure 7.2.3 and therefore are better suited for extrapolation.

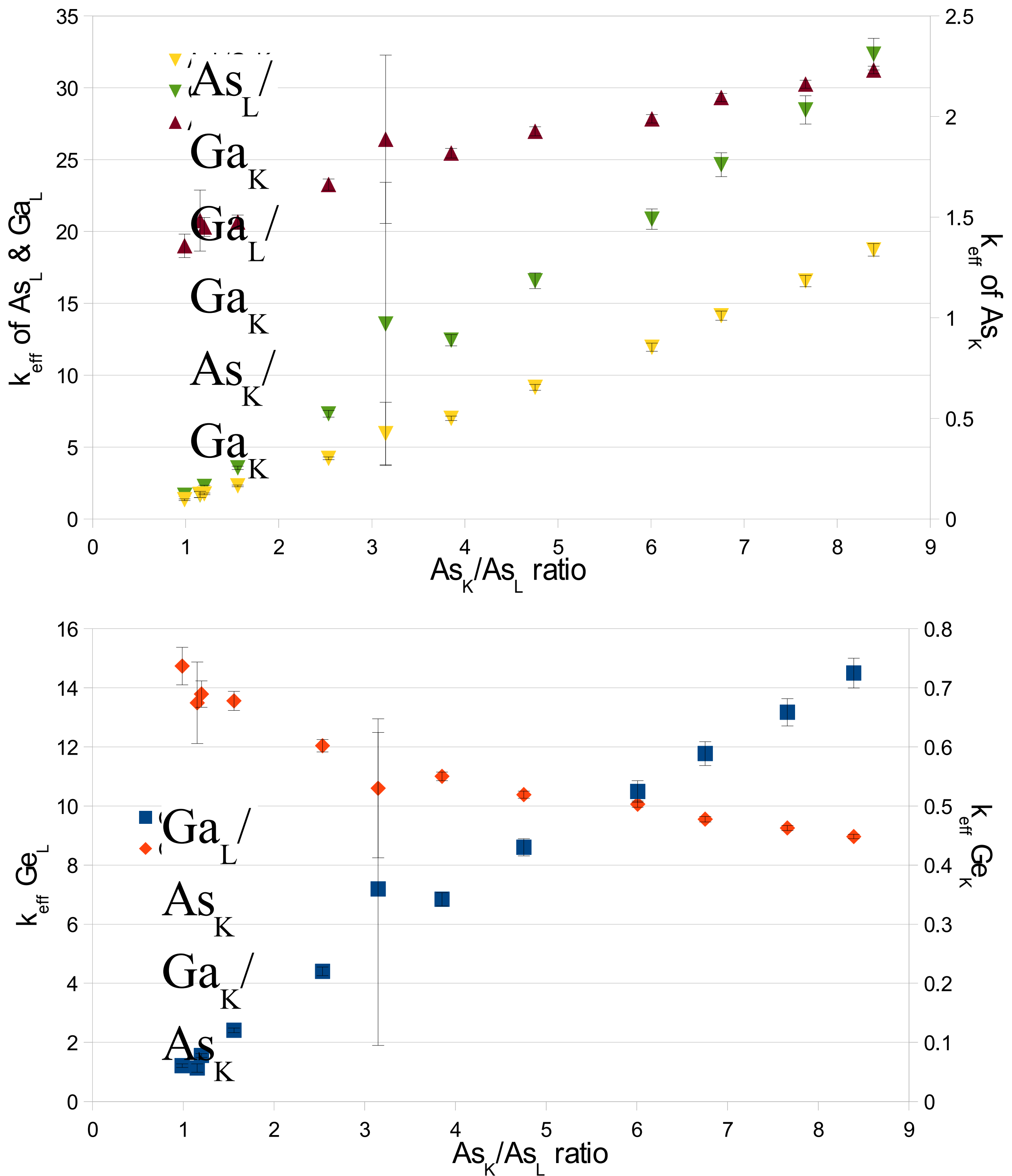

Figure 7.2.4: Wedge As_K/As_L and Ga_K/Ga_L data plotted against thickness.

Calculating a corrected *k*-factor using this method is extremely dependent on first acquiring a correct value for the KL that corresponds to zero thickness. For this sample, this proved to be difficult: the As_K/As_L at t=0 possess large error bars. However, it is also possible to use external data for this purpose: Table 7.2.3 contains the results for corrected k-factors taken with respect to thickness, then with respect to AsK/AsL where the KL ratio corresponding to zero thickness was first taken from the data set and then from the lamella of Figure 7.2.1. First, note that some the values calculated with respect to thickness are of good quality, such as As_K/Ga_K or Ga_K/As_K. In other

cases, however, the fit is considerably worse such as Ga_L/Ga_K or Ga_L/As_K. Looking at the values calculated with respect to As_K/As_L the trend is different, with curves that had low error before gaining large uncertainty, such as As_K/Ga_K, while those that were previously uncertain see a decrease in error. Those values calculated with the lamella KL ratio at t=0 show superior relative error, which is to be expected. This inversion of the error characteristic is a function of the plots: those curves plotted against As_K/As_L are much more linear and hence much better suited to extrapolation, but are also subject to the error in the KL ratio that corresponds to zero thickness. The lesson to be learned in that correctly and accurately calculating the KL ratio that corresponds to zero thickness is critical. It is worth noting that there is no reason why both methods cannot be used, with some k_{eff} being calculated against sample thickness and others against KL ratio.

		corrected *k*-factor	R^2	ISIS values
against thickness	As_L/As_K	1.4±0.5	0.924	0.89
	Ga_L/As_K	2.5±1.3	0.850	0.90
	Ga_K/As_K	0.66±0.04	0.679	0.88
	As_L/Ga_K	2.4±1.1	0.942	1.02
	Ga_L/Ga_K	5±3	0.890	1.03
	As_K/Ga_K	1.54±0.10	0.765	1.14
	Corrected *k*-factor:	using self-consistent KL ratio for t=0	using lamella KL ratio for t=0	R^2
against As_K/As_L	Ga_L/As_K	2.1±1.2	1.3±0.5	0.990
	Ga_K/As_K	2.1±1.0	1.5±0.4	0.958
	As_L/Ga_K	1.48±0.09	1.42±0.03	0.999
	Ga_L/Ga_K	0.68±0.04	0.70±0.02	0.990
	As_K/Ga_K	3±2	1.8±0.8	0.968

Table 7.2.3: Corrected k-factors for the data shown in Figure 7.2.4.

The previously shown sample were all possessed of a 1:1 composition. Correcting for binary compounds with a different composition can also be done. To demonstrate this, a $Si_{0.54}Ge_{0.46}$ sample was analysed, with the resulting intensities shown in Figure 7.2.5. It is readily perceptible that the simulations broadly follow the experimental results, however NISTMonte matches the Ge_K/Si_K curve better than CASINO while the reverse is true for Ge_L/Si_K, where the CASINO curve's slope matches fairly well. In this case, no measurement of sample thickness was undertaken.

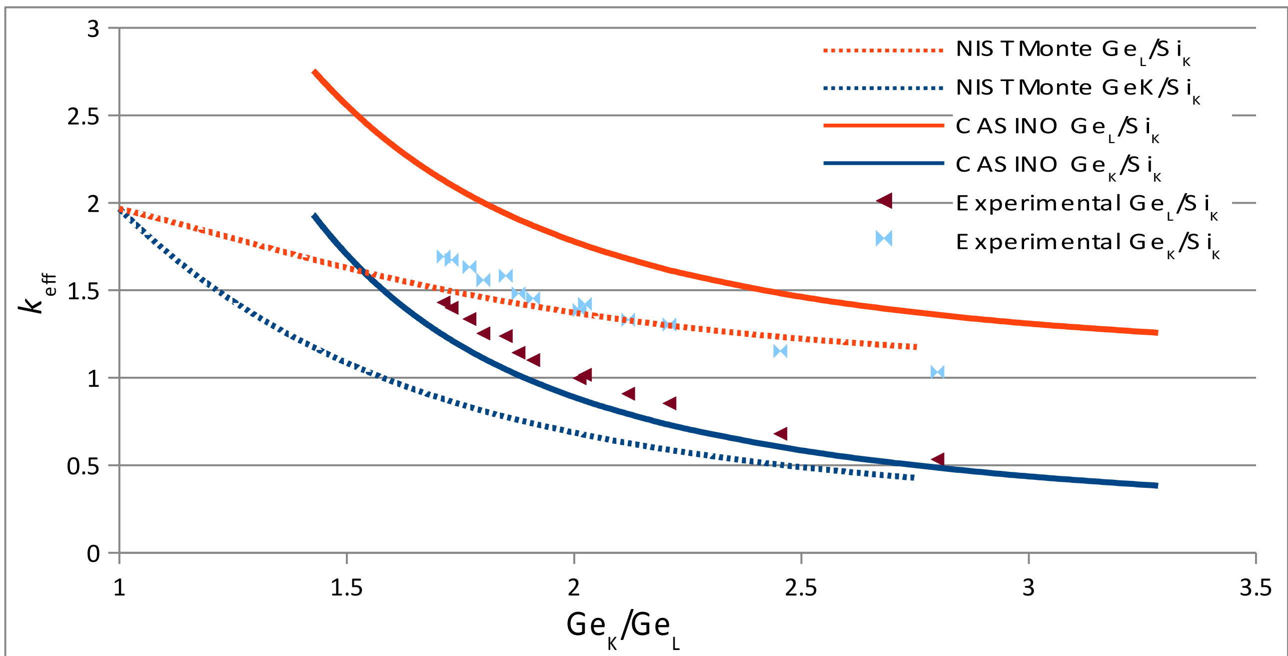

Figure 7.2.5: $Si_{0.54}Ge_{0.46}$ experimental to simulation comparison. NISTMonte simulation: beam energy 197keV, take-off angle 25° with 10^6 electron histories. CASINO simulation: beam energy 200keV, take-off angle 25° with 10^6 electron histories. Simulated sample composition $Si_{0.54}Ge_{0.46}$ (density = 3.71gcm^{-3}) lamella of varying thickness. Estimated detector efficiencies Si_K: 70%, Ge_L: 64%, Ge_K: 77%.

Using a value for the KL ratio at t=0, determined previously, of 1.3±0.05, the corrected k-factors are shown in Table 7.2.4. Clearly, the fits are of good quality and produce little error. This is, it is worth noting, a well-behaved data set, in that both curves are well defined with no outliers. It does, however, serve to indicate that a good fit and accurate knowledge of the KL ratio at t=0 can give very accurate results.

	corrected *k*-factor	R^2	ISIS value
Ge_L/Si_K	$2.15\pm^{0.07}_{0.06}$	0.982	1.654
Ge_K/Si_K	2.13±0.09	0.992	1.609

Table 7.2.4: Second order polynomial least-squares regression k_{eff} at t=0 for the data in Figure 7.2.5.

As already mentioned, k_{eff} can be plotted with respect to any scale that represents sample thickness. Previously, this was the KL ratio, however other scales such as detector deadtime would also function. Shown in Figure 7.2.6 is the results from a InP sample plotted against deadtime from the same sample as that shown in Figure 6.2.1. As a reminder, this data was extracted manually and as such the error is purely Poisson statistics and the general quality is lower than that given by dedicated software.

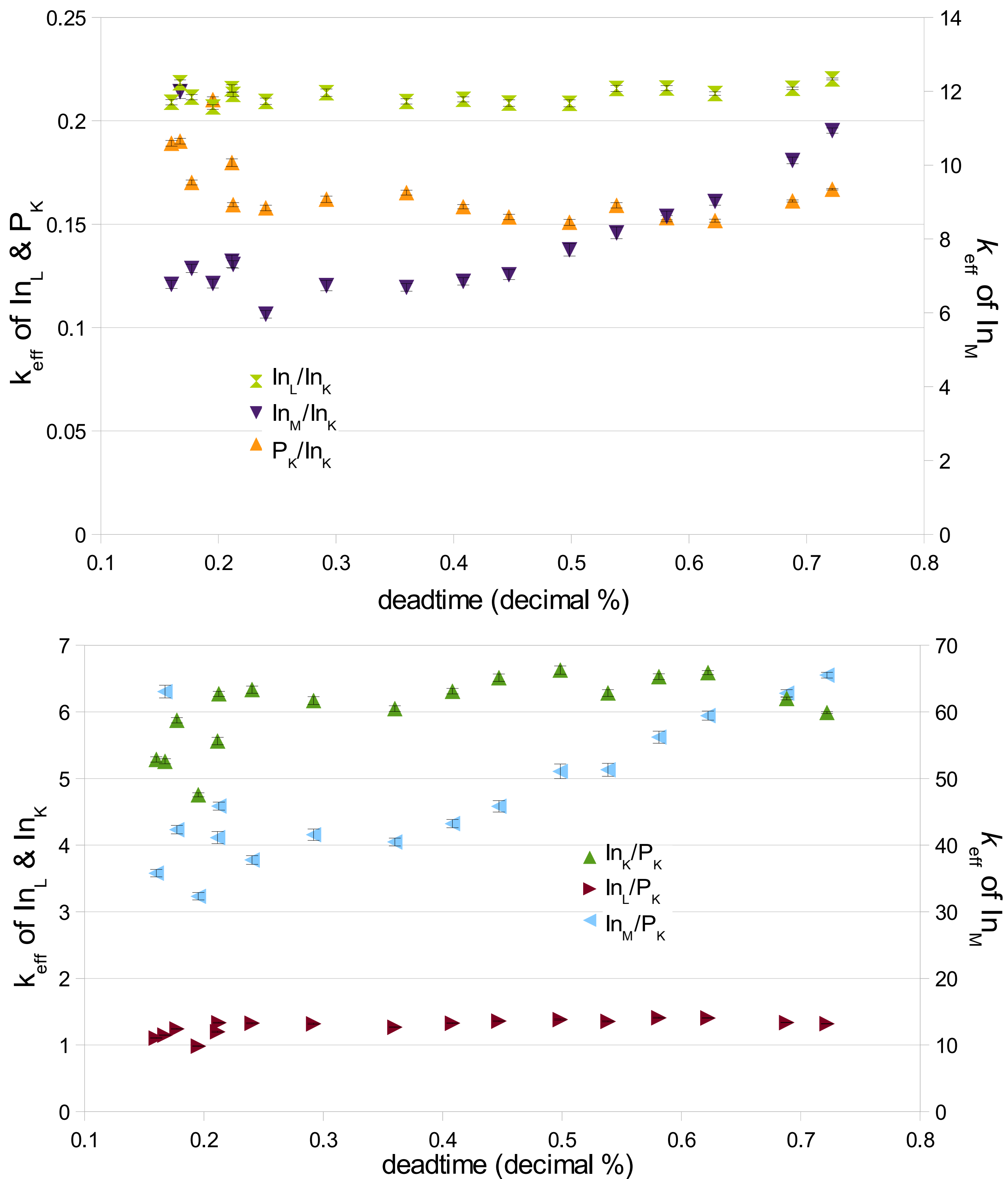

Figure 7.2.6: InP k_{eff} against deadtime. Detector efficiencies were taken as In_K: 89%, In_L: 73%, In_M: 41%, P_K: 69% (Figure 2.3.1).

The second order polynomial fits from Figure 7.2.6 are shown in Table 7.2.5. The R^2 value for each fit is significantly lower than could be desired, though the relative error is generally good. Unfortunately, ISIS only contains the *k*-factors for In_L and P_K and so no other comparison is possible. Without pre-existing k-factors to compare to it can only be said that the fits are not of very good quality.

	k_{eff} at t=0	R^2	ISIS values
In_K/P_K	4.1±0.5	0.627	
In_L/P_K	0.90±0.10	0.609	1.822
In_M/P_K	52±9	0.632	
In_L/In_K	0.219±0.004	0.399	
In_M/In_K	11.2±1.7	0.532	
P_K/In_K	0.23±0.02	0.582	

Table 7.2.5: Second order least-squares regression results from the data shown in Figure 7.2.6.

In comparison, these k_{eff} were plotted against In_K/In_L, In_K/In_M and In_L/In_M to determine whether this would improve either the error or the R^2. Using a second order polynomial fit for the three ratios above to determine at what ratio value the deadtime reaches zero (since this would correspond to zero thickness), excluding the 0.195 deadtime data point as an outlier, gives the values shown in Table 7.2.6. Many of the fits were very poor ($R^2 < 0.3$) and so no meaningful k_{eff} could be calculated for them. In opposition to the expected, only a few fits are superior to their deadtime counterparts seen in Table 7.2.5. This can be interpreted as deadtime already being a scale of sample thickness that is fairly accurate, and attempting to improve this by using the intensity ratio does not always help. Note that the deadtime is known very accurately, while sample thickness must be measured some other way, which implies that the error in k_{eff} when measured against sample thickness is a function of uncertainty of the sample thickness measurement. Interestingly, the best quality fits are when plotted against In_L/In_M neither of the intensity ratios involving In_K are superior. This could be the result of In_K being such high energy that it has a low detector efficiency.

		k_{eff} at t=0	R^2	ISIS values
Against In_K/In_L	In_K/P_K		0.225	
	In_L/P_K		0.269	1.822
	In_M/P_K	$51 \pm^{18}_{8}$	0.607	
	In_M/In_K	$8 \pm^{4}_{1.2}$	0.735	
	P_K/In_K		0.255	
		k_{eff} at t=0		
Against In_K/In_M	In_K/P_K		0.211	
	In_L/P_K		0.227	1.822
	In_M/P_K	$55 \pm^{6}_{3}$	0.889	
	In_L/In_K	$0.21 \pm^{1.81x10^{-3}}_{9x10^{-4}}$	0.652	
	P_K/In_K		0.190	
		k_{eff} at t=0		
Against In_L/In_M	In_K/P_K		0.189	
	In_L/P_K		0.194	1.822
	In_M/P_K	$55 \pm^{5}_{3}$	0.878	
	In_L/In_K	$0.21 \pm^{1.6x10^{-3}}_{0.8x10^{-3}}$	0.594	
	In_M/In_K	$8.6 \pm^{0.9}_{0.4}$	0.997	
	P_K/In_K		0.166	

Table 7.2.6:Second order polynomial fit results for various k_{eff} in InP.

7.2.1 Conclusion

A method for both accurately accounting for absorption and correcting *k*-factors has been discussed. This method has been shown to apply in simulations to a variety of different samples and compositions. Further, a means by which this method can be utilised without a direct reliance on knowledge of sample thickness has also been expanded upon.

Experimentally, both the original method and expanded form have been shown to work in some cases. Indeed, the GaAs wedge sample demonstrated that a dual effect could function well, with some k_{eff} being calculated with respect to sample thickness and other in terms of KL ratio. Further, it was shown that to some extent detector deadtime can serve as a viable replacement for thickness, in some cases proving superior to the X-ray intensity ratio method.

8 Conclusion

The Monte Carlo simulation programs compared led to the conclusion that CASINO appears to give the best absorption values, though all four programs used followed the same trends. The bulk of the simulations were run in NISTMonte for speed and ease of use.

The use of the equation to calculate the depth of a thin layer was explored in some detail. While it was found to work very well in simulations, attempts to apply it to experimental data uniformly met with failure. This appears to be primarily due to counting statistics and sample inconsistencies, where both are more strenuous to achieve to the required accuracy than initially assumed. Calculation of the variable λ was examined with the intent of determining its associated difficulties. Several issues were found: the fact that the different methods of calculating λ provide different results, how normalisation changes the effective λ value and the sometimes strong effect of self-absorption in the thin layer. It was also discovered that the value of λ for one material can sometimes be used to estimate that of another material, such as In_L and Sb_L. It was found that a sample with multiple thin layers behaves much like that with a single thin layer at some intermediate depth, though this could see an increase in the statistical error of the result.

The five other methods of Chapter 5 for the determination of the depth of a thin layer were also discussed. Here, it was found that both the graphical methods can only be used to give a general estimate of the depth, as they are insufficiently sensitive for meaningful numerical results. The 'curve fit' approach gave results that were incorrect by orders of magnitude: given that this method is built on the principle of calculating λ from equation 4.1.1 this implies that experimental calculation of this critical parameter would be more difficult than first thought. Both the 'absorption matching' methods gave coherent results, though these results are very different. This appears to be a matter of the input parameters: which, if either, is correct is not clear.

A method of calculating the thickness of a sample from a ratio of two X-rays was discussed. It was discovered that certain X-ray intensity ratios allow direct calculation of the chemical composition by virtue of being near-unchanged with thickness. Further, it is possible to use spectra that have been gathered with knowledge of some other measure of sample thickness, such as detector deadtime. A theoretical method for calculating the thickness of a sample by analysis of the same region at different take-off angles was also discussed, though no reliable experimental data was available to test this approach.

Finally, a method for calculation of effective *k*-factors that include the absorption effectwas discussed. It was found that this method can be attempted with respect to other measures of thickness that also vary with sample thickness, such as detector deadtime or the ratio described above. In the case of the X-ray intensity ratio, a much improved value can result, as the curves become far more self-consistent, which in turn improves the accuracy of any fit. Taking this method with respect to detector deadtime appears to give an improved result compared to the X-ray intensity ratio, though whether this is a function of the sample differing from the expected geometry or a general trend is unknown.

8.1 Applications

Obviously, the most sophisticated methods are useless if there is no need for them. Clearly, equation 4.1.1 and its associated methods are useful for any situation where there is a thin layer embedded within a matrix, such as a quantum domain structure (i.e. well, wire or dot). Such semiconductor

structures are exceptionally useful in that they present novel characteristics, particularly in terms of bandgap and therefore electromagnetic properties. At present, there appears to be no other method which does this in a TEM, and as such there are comparatively few situations presented in the literature where such a method would be useful [69][70][71][72][73][74][75][76]. Further, the same principle could be applied to other fields such as X-Ray Fluorescence (XRF) or Particle Induced X-ray Emission (PIXE), which stimulate X-ray emission by means other than electrons. Details may differ (for example, XRF would experience the equivalent effect to beam straggling as a reduction in X-ray generation, as the 'waves' used do not lose energy gradually in the same way as electrons), and as such simulations with the appropriate software would be necessary to discover the extent of the differences, but the fundamental concept should remain sound.

The 'K/L ratio' method can be utilised in any sample with at least one element whose $Z \geq 20$. The usefulness would be to either acquire the specimen thickness for its own value or use that knowledge of the thickness to more accurately correct for absorption. Obviously, this situation is common [77][78][79][80][81][82][83][84][85][86][87][88].

The 'k-factor' is useful in any situation where the Cliff-Lorimer ratio method is used. It can also be used to complement the 'K/L ratio' method, in that once the thickness has been determined the absorption can be arrived at through interpolation [26][89][90][91]. In principle, this could also be utilised in a SEM, if there is sufficient knowledge of the interaction volume to give an 'effective' thickness.

Obviously, there are far more situations where these techniques could be useful: those listed here are only a small fraction for brevity.

8.2 Further work:

For further work, I would recommend the following:

For equation 4.1.1, attempting the analysis of a sample with a fairly thick layer (e.g. 10nm) of some element which possesses a soft X-ray (e.g. aluminium) embedded somewhat shallowly (~50nm) within a matrix of some material which does not produce characteristic X-rays that would interfere with the X-ray of interest and of sufficient absorption cross-section that it would provide strong absorption (e.g. InSb). Ideally, this could be carried out in a microscope that is equipped with an SDD for the higher resolution at the expected countrate, provided that this countrate can be utilised without damaging the sample during analysis. Of note is that the thin layer should be fairly shallow, as this would present the smallest change in the region that the generated X-rays travel through on their way to the detector. Such an analysis must have sufficient livetime to ensure that statistical error would not mitigate the accuracy of the results. Further note that self-absorption in the layer must be accounted for.

Be sure to apply the two 'absorption matching' methods to the data gathered from the above sample. In theory, the results should match. If they do not, attempt to discover why.

It has been suggested that a spherical particle could be used instead of a layer to remove interaction-volume effects. This would work, provided that the beam is significantly wider than the sample. The disadvantage would be an increased number of X-rays from the matrix which would still suffer from these effects and as such could not be used as a correction for such things an uncertainty in the beam electron density. Despite this disadvantage, an experiment with a spherical particle could be

used in place or in addition to that described above, with similar parameters. Note that multiple particles or nanocomposites would likely function in a manner analagous to the multiple layers discussed in section 4.4, and as such would give no particular advantage.

The correction for shielding by the sample holder is heavily reliant on accurate parameters for the sample holder (the cut-off angle). Acquiring this parameter to a high degree of accuracy would be beneficial, as the distinctive curve seen in the X-ray intensity as a function of sample tilt is to a significant extent the result of this shielding effect. This could be done by mounting the sample holder in some manner of apparatus which would hold it steady while simultaneously allowing it to be rotated with a high degree of precision. Then, a laser could be aimed at the centre of where the sample is placed. From there, it would be a simple matter of rotating the sample holder until the laser is obscured. What has already been done is a somewhat low-precision form of this.

Devise and carry out an experiment with the above improved shielding cut-off angle and some means of measuring exactly which region of the sample is being examined relative to the edge of the specimen holder. Otherwise, the exact position of the area being examined could have an effect on the degree of shielding.

Perform an experiment with a holder that has no shielding at all: while it is thought that shielding has been properly modelled it would be wise to be certain of this.

Further, it would be wise to explore the assumption that the detector is a single point: can equation 4.1.1 be extended to have a range of take-off angles? What about an annular detector, which has a tremendous solid angle?

Investigate the consequences of using a detector with a take-off angle far from that used in this project (25°). What about multiple detectors, or those with an unusual shape?

Could equation 4.1.1 be utilised in conjunction with the $\varphi(\rho z)$ method to give better correction for absorption? If nothing else, fitting to the X-ray generation vs. depth curve could give better results if several experimental curves with differing take-off angles were used for one sample.

Extend the 'curve fit' methods by plotting a single curve of ln (X-ray intensity) against $1/\sin(\theta)$. A linear fit of this would, in principle, give the ratio of d/λ. This was not done due to time constraints.

Apply the varying take-off angle method of chapter 6 to a reliable experimental sample to explore its validity.

Continue attempting to explore the validity of the the method of chapter 7 when applied to indirect means of measuring the sample thickness, such as detector deadtime and X-ray intensity ratios.

Confirm that the effective k-factors measured against indirect measures for thickness can be extended to other methods of quantification (such as Watanabe's ζ method).

9 References

[1]:Williams D.B. & Carter C.B.,Transmission Electron Microscopy , 2009,2,Springer Science Business Media
[2]:Ritchie, N.W.M., DTSA II, Retrieved January 2014, http://www.cstl.nist.gov/div837/837.02/epq/dtsa2/
[3]:Garratt-Reed A.J. & Bell D.C.,Energy-Dispersive X-ray Analysis in the Electron Microscope , 2003,,Garland Science
[4]:Boon G. & Bastin G.,Quantitative Analysis of Thin Specimens in the TEM using a phi-rho-z Model, 2004,Microchim. Acta.,147,125-133
[5]:Horny P., Lifshin E., Campell H. & Gauvin R.,Development of a New Quantitative X-ray Microanalysis Method for Electron Microscopy, 2010,Microsc. Microanal,16,821-830
[6]:Cliff, G.; Lorimer, G.W.,The quantitative analysis of thin specimens,March 1975,Journal of Microscopy,103,203-207
[7]:Watanabe M., Horita Z. & Nemoto M.,Absorption correction and thickness determination using the zeta factor in quantitative X-ray microanalysis, 1996,Ultramicroscopy,,187-198
[8]:Morris P.L., Ball M.D. & Statham P.J., , 1980,IOP Conference Series No. 52,
[9]:Horita Z., Ichitani K., Sano T. & Nemoto M.,, 1989,Phil. Mag. A,59,939
[10]:Fujita T., Watanaby M., Horita Z. & Nemoto M.,Advanced form of zeta-factor method in analytical electron microscopy,May 1999,Journal of Electron Microscopy,48,561-568
[11]:Watanabe M. & Williams D.B.,The quantitative analysis of thin specimens: a review of progress from the Cliff-Lorimer to the new zeta-factor methods, 2006,Journal of Microscopy,221,89-109
[12]:Cappellen E.V. & Doukhan J.C.,Quantitative transmission X-ray microanalysis of ionic compounds, 1994,Ultramicroscopy,53,343-349
[13]:Zhuang L.B., Bao S.X., Wang R., Li S.L., Ma L.L. & Lv D.C., Thin Film Thickness Measurement using Electron Probe Microanalyzer, 2009,2009 International Conference on Applied Superconductivity and Electromagnetic Devices,
[14]:Popova T.B., Bakaleinikov L.A., Flegontova E.Yu., Shakhamin A.A. & Zamoryanskaya M.V.,Electron Probe Microanalysis of Heterostructures with Nanolayers, 2011,Semiconductors,45,260-264
[15]:Ng F.L., Wei J., Lai F.K. & Goh K.L.,Metallic thin film depth measurements by X-ray microanalysis, 2006,Applied Surface Science,252,3972-3976
[16]:Peiner E., Hansen K. & Schlachetzki A.,Thickness control of InP and In0.53Ga0.47As thin films by energy-dispersive X-ray spectrometry, 1995,Thin solid films,256,143-147
[17]:Horita Z., Sano T. & Nemoto M.,An extrapolation method for the determination of Cliff-Lorimer KAB factors at zero foil thickness,September 1986,Journal of Microscopy-Oxford,143,215-231
[18]:Horita Z., Sano T. & Nemoto M,Simplification of X-ray absorption correction in thin-sample quantitiative analysis, 1987,Ultramicroscopy,21,271-276
[19]:Horita Z., Sano T. & Nemoto M,A new form of the extrapolation method for absorption correction in quantitative X-ray microanalysis with the analytical electron microscope, 1991,Ultramicroscopy,35,27-36
[20]:Westwoo A.D., Michael J.R. & Notis M.R.,Experimental-determination of light-element k-factors using the extrapolation technique - oxygen segregation in aluminum nitride,September 1992,Journal of Microscopy-Oxford,167,287-302
[21]:Eibl O.,New method for absorption correction in high-accuracy, quantitative EDX microanalysis in the TEM including low-energy X-ray lines, 1993,Ultramicroscopy,50,179-188
[22]:Eibl O.,Application of a new method for absorption correction in high-accuracy, quantitative EDX microanalysis in the TEM: analysis of oxygen in CuO-based high-Tc superconductors,

1993,Ultramicroscopy,50,189-201
[23]:Eibl O., Schultheiss S., Blitgen-Heinecke P., Schraermeyer U.,Quantitative chemical analysis of ocular melanosomes in the TEM, 2006,Micron,37,262-276
[24]:Birajdar B., Peranio N. & Eibl O., Advanced electron microscopy methods for the analysis of MgB2 superconductor, 2007,J. Phys.: Conf. Ser.,97
[25]:Birajdar B., Peranio N. & Eibl O.,Quantitative electron microscopy and spectroscopy of MgB2 wires and tapes, 2008,Supercond. Sci.Technol.,21,
[26]:Gusenbauer C., Ashraf T., Stangl J., Hesser G., Plach T., Meingast A., Kothleitner G. & Koch R.,Interdiffusion in Huesler film epitaxy on GaAs(001), 2011,Phys. Rev. B,83,
[27]:Kunle M., Janz S., Nickel K.G. & Eibl O.,Changes in chemical composition and nanostructure of SiC thin films prepared by PECVD during thermal annealing, 2011,Phys. Status Solidi A,208,1885-1895
[28]:Roder A. & Bauer H.-D.,Analytical transmission electron microscopy in the nanometer-region, 1994,Fresenius J. Anal. Chem.,349,122-130
[29]:Statham P.J. & Ball M.D.,, 1980,Microbeam Analysis,,165-168
[30]:Tekin A., Uguz A. & Martin J.W.,Rapid Method for the Detrmination of TEM Foil Thickness, 1990,Materials Characterization,25,99-107
[31]:Craven A.J. & Adam P.F., , 1984,Proe. 8th European Congress on ElectronMicroscopy,
[32]:Garret-Reed A.J. & Furdanowicz W., , 1988,EMAG 87,
[33]:Khan K.M., Nicholson W.A.P., Pediani J.D. & Elder H.Y., , 1989,EMAG-MICRO-89 lOP Conf.Ser. No. 98,
[34]:Lorimer G.W., Cliff G. & Clark N.J. , Developments in Electron Microscopy and Analysis, 1976,Inst. Phys. Conf. Ser.,36
[35]:Horita Z., Ichitani K., Sano T. & Nemoto M.,Minimization of the overestimation of thin foil thickness in the contamination spot separation method, 1986,Scripta Metallurgica,20,381-384
[36]:Pan Z., Davies C.K.L. & Stevens R.N.,Measurement of foil thickness in transmission electron microscopy, 1994,Journal of Materials Science,29,1920-1924
[37]:Horita Z., Ichitani K., Sano T. & Nemoto M.,Applicability of the differential X-ray absorption method to the determinations of foil thickness and local composition in the analytical electron microscope,May 1989,Philosophical Magazine A-Physic of Condensed Matter Structure Defects and Mechanical Properties,59,939-952
[38]:Armigliato A., Balboni R. & Rosa R.,Quantitative Thin-Film X-ray Microanalysis by STEM/HAADF: Statistical Analysis for Precisionand Accuracy Determination, 2006,Microsc. Microanal,,318-321
[39]:Loukanov A., Kamasawa N., Danev R., Shigemoto R. & Nagayama K.,Immunolocalization of multiple membrane proteins on a carbon replica with STEM and EDX, 2010,Ultramicroscopy,,366-374
[40]:Zak M., Laval J.Y., Dluzewski P.A., Kret S. Yam V., Bouchier D. & Fossard F.,Influence of the Si cap layer on the SiGe islands morphology, 2009,Micron,,122-125
[41]:Nath, S.; Ghosh, S. K.; Kundu, S.; Praharaj, S.; Panigrahi, S.; Basu, S.; Pal, T.,, 2005,Materials Letters,59,3986 – 3989
[42]:Kim, J.-H.; Bryan, W. W.; Lee, T. R.l,Preparation, Characterization, and Optical Properties of Gold, Silver,and Gold-Silver Alloy Nanoshells Having Silica Cores, 2008,Langmuir,24,
[43]:Vaidya, S.; Patra, A.; Ganguli, A. K. ,Core–shell nanostructures and nanocompositesof Ag@TiO2: effect of capping agent and shell thicknesson the optical properties, 2010,J Nanopart Res,12,1033–1044
[44]:Pyne, S.;Sarkar, P.; Basu, S.; Sahoo, G. P.; Bhui, D. K.; Bar, H.; Misra, A.,Synthesis and photo physical properties of Au @ Ag(core @ shell) nanoparticles disperse in poly vinyl alcoholmatrix, 2011,J Nanopart Res,13,1759–1767
[45]:Fernandez, A.; Rojas, T. C.,Microstructural and Chemical Characterisation of Metal Particles

Nanostructures, 2003,Materials Transactions,44,2055 - 2061
[46]:Ivetic T., Nikolic M.V., Parakevopulos K.M. Pavlidou E., Zorba T.T. Nikolic P.M.; Ristic M.M.,Combined FTIR and SEM-EDS study of Bi2O3 doped ZnO–SnO2ceramics, 2008,Journal of Microscopy,232,498-503
[47]:West G.D. & Thomson R.C.,Combined EBSD/EDS tomography in a dual-beam FIB/FEG–SEM, 2009,Journal of Microscopy,,442-450
[48]:Laszcz A., Czerwinski A., Ratajcak J., Szerling A., Phillipp F., van Aken P.A. & Katcki J.,Transmission electron microscopy characterization of Au/Pt/Ti/Pt/GaAs ohmic contacts for high power GaAs/InGaAssemiconductor lasers, 2010,Journal of Microscopy,,347-351
[49]:de Vrieze E., Heijnen L., Metz J.R. & Flik G.,Evidence for a hydroxyapatite precursor in regenerating cyprinid scales, 2012,J. Appl. Ichthyol,,388-392
[50]:Tokarz A., Wieczorek P., Lis A.K. & Morgiel J.,Microstructure of electrodeposited NiFe/Cu multilayers, 2010,Journal of Microscopy,,456-460
[51]:Hunsche M. & Noga G.,Applicability of the energy dispersive x-ray microanalysis forquantification of irregular calcium deposits on fruit and leaf cuticles, 2008,Journal of Microscopy,232,453-462
[52]:Beltrami D., Calestani D., Maffini M., Suman M., Melegari B., Zappettini A., Zanotti L., Casellto U., Careri M. & Mangia A.,Development of a combined SEM and ICP-MS approachfor the qualitative and quantitative analyses of metalmicroparticles and sub-microparticles in food products, 2011,Anal. Bioanal. Chem.,401,1401-1409
[53]:Mobus G, Doole R.C. Inkson B.J.,Spectroscopic electron tomography, 2003,Ultramicroscopy,96,433-451
[54]:Kirk R.G., Gates M.E., Provance A.J. & Lee P.,Quantitative X-ray Images Calculated on the Basis ofMass and Volume, 1997,Microsc. Microanal.,3,512-519
[55]:Bourdelle F., Parra T., Beyssac O., Chopin C. & Moreau F.,Ultrathin section preparation of phyllosilicates by Focused Ion Beam milling forquantitative analysis by TEM-EDX, 2012,Applied Clay Science,59-60,121-130
[56]:Servanton G., Pantel R., Juhel M. & Bertin F.,Two-dimensional quantitative mapping of arsenic in nanometer-scalesilicon devices using STEM EELS–EDX spectroscopy, 2009,Micron.,40,543-551
[57]:Tian W.H., Horita Z., Sano T. & Nemoto M.,An Application of the Differential X-ray-absorption Method to Thickness Measurement in Precipitate-containing Ni3(Al,Ti) and TiAl Compounds ,June 1993,Philosophical Magazine B - Physics of Condense Matter Statistical Mechanics Electronic Optical and Magnetic Properties,67,811-822
[58]:Kuimalee S., Chairuangrsi T., Pearce J.T.H., Edmonds D.V., Brown A.P. & Brydson R.M.D.,Quantitative analysis of a complex metal carbide formed during furnace coolingof cast duplex stainless steel using EELS and EDS in the TEM, 2010,Micron.,41,423-429
[59]:Malac M. & Egerton R.F.,Calibration Specimens for Determining Energy-DispersiveX-ray k-Factors of Boron, Nitrogen, Oxygen, and Fluorine, 1999,Microsc. Microanal.,5,29-38
[60]:Longo D.M., Howe J.M. & Johnson W.C.,Experimental method for determining Cliff-Lorimer factorsin transmission electron microscopy (TEM) utilizing stepped wedge-shaped specimens prepared by focused ionbeam (FIB) thinning, 1999,Ultramicroscopy,80,85-97
[61]:Joy D.C.,An Introduction to Monte Carlo Simulations, 1991,Scaccing Microscopy,5,329-337
[62]:Joy D.C.,A Database on Electron-Solid Interactions, 1995,SCANNING,17,270-275
[63]:Metropolis, N. and Ulam, S,The Monte Carlo Method,September 1949,Journal of the American Statistical Association,44,335-341
[64]:Maurice F.,Monte-Carlo Technique in Microanalysis, 1972,Journal of Microscopy-Oxford (French),,
[65]:Rickerby, D.G. and Thiot, J.F.,, 1994,Mikrochmica Acta,114,421
[66]:Faucheu, J., et al.,Latex Imaging by Environmental STEM: Application to the Study of the

Surfactant Outcome in Hybrid Alkyd/Acrylate Systems., 2009,Langmuir,25,10251-10258
[67]:Grillon F.,Low Voltage Contrast with an SEM Transmission Electron Detector, 2006,Microchim Acta,155,157-161
[68]:Hovington, P., Drouin, D. and Gauvin, R. ,CASINO : A New Monte Carlo Code in C Language for Electron Beam Interaction —Part I: Description of the Program., 1997,Scanning,19,1-14
[69]:Drouin, D., Hovington, P. and Gauvin, R.,CASINO : A New Monte Carlo Code in C Language for Electron Beam Interactions—Part II : Tabulated Values of the Mott Cross Section, 1997,Scanning,19,20-28
[70]:Hovington, P., et al.,CASINO: A New Monte Carlo Code in C Language for Electron Beam Interactions—Part III : Stopping Power at Low Energies, 1997,Scanning,19,29-35
[71]:Drouin, D., et al.,CASINO V2.42—A Fast and Easy-to-use Modeling Tool for Scanning Electron Microscopy and Microanalysis Users, 2007,Scanning,29,92-101
[72]:Choel, M., Deboudt, K. and Flament, P.,Evaluation of Quantitative Procedures for X-ray Microanalysis of Environmental Particles, 2007,Microscopy Research and Technique,70,996-1002
[73]:El Gomati, M.M., et al.,Theory Experiment Comparison of the Electron Backscattering Factor from Solids at Low Electron Energy (250–5,000 eV), 2008,Scanning,30,2-15
[74]:SmallWorld, , 2014, http://www.small-world.net/efs.htm
[75]:Roux, S., et al.,Determination of paper filler Z-distribution by low-vacuum SEM and EDX, 2008,Journal of Microscopy,229,44-59
[76]:Van Eerdenbrugh, B., et al.,Alternative matrix formers for nanosuspension solidification: Dissolution performance and X-ray microanalysis as an evaluation tool for powder dispersion., 2008,European Journal of Pharmaceutical Sciences,35,344-353
[77]:Carlton, R.A., Lyman, C.E. and Roberts, J.E.,Accuracy and Precision of Quantitative Energy-Dispersive X-Ray Spectrometry in the Environmental Scanning Electron Microscope, 2004,Scanning,26,167-174
[78]:Ritchie, N.W.M., , 2005,Surf. Interface Anal.,37
[79]:Scott, K. & Ritchie, N.W.M.,Analysis of 3D elemental mapping artefacts in biological specimens using Monte Carlo simulation, 2009,Journal of Microscopy,233,331-339
[80]:Ritchie, N.W.M.,Using DTSA-II to Simulate and Interpret Energy Dispersive Spectra from Particles., 2010,Microsc. Microanal.,16,248-258
[81]:Baro, J.; Sempau J.; Fernandez-Varea, J.M., Salvat,F.,PENELOPE: an algorithm for Monte Carlo simulation of thepenetration and energy loss of electrons and positrons in matter, 1995,Nucl. Instrum. Meth. B,100,31–46
[82]:Salvat, F.; Fernandez-Varea, J.M.; Sempau, J., , 2014, http://www.oecd-nea.org/dbprog/courses/penelope-2011.pdf
[83]:Statham, P.; Llovet, X.; Duncumb, P., Systematic discrepancies in Monte Carlo predictions ofk-ratios emitted from thin films on substrates, 2012,IOP Conf. Series: Materials Science and Engineering,32
[84]:Walther, T., Comparison of experimental and theoretical X-ray intensities from (In)GaAs specimens investigated by energy-dispersive X-ray spectroscopy in a transmission electron microscope., 2010,,209
[85]:Walther, T., , 2008,J. Phys.: Conf. Ser.,209
[86]:Berger, M.J.; Hubbell, J.H.; Seltzer, S.M.; Chang, J.; Coursey, J.S.; Sukumar, R.; Zucker D.S.; Olsen, K., http://www.nist.gov/pml/data/xcom/index.cfm/, 2014,
[87]:Ioffe Physical Technical Institute, , January 2014, http://www.ioffe.ru/SVA/NSM/Semicond/index.html
[88]:Liew, S.L.; Walther, T., Irsen S.; Hopkinson, M.; Skolnick, M.S.; Cullis A.G., , 2008,Springer Proc. in Physics,120

10 Appendix

What follows is the derivation of the degree of shielding caused by tilting the sample holder or moving the detector. The previously known variables are the collection angle, Ω, the natural take-off angle (i.e. the angle at which the detector is fixed with respect to the horizontal), θ, the degree of specimen tilt, α, the area of the detector, A, and the angle at which the sample holder is assumed to cut off all X-rays, σ. This derivation could be used with different initial known variables, with appropriate extension.

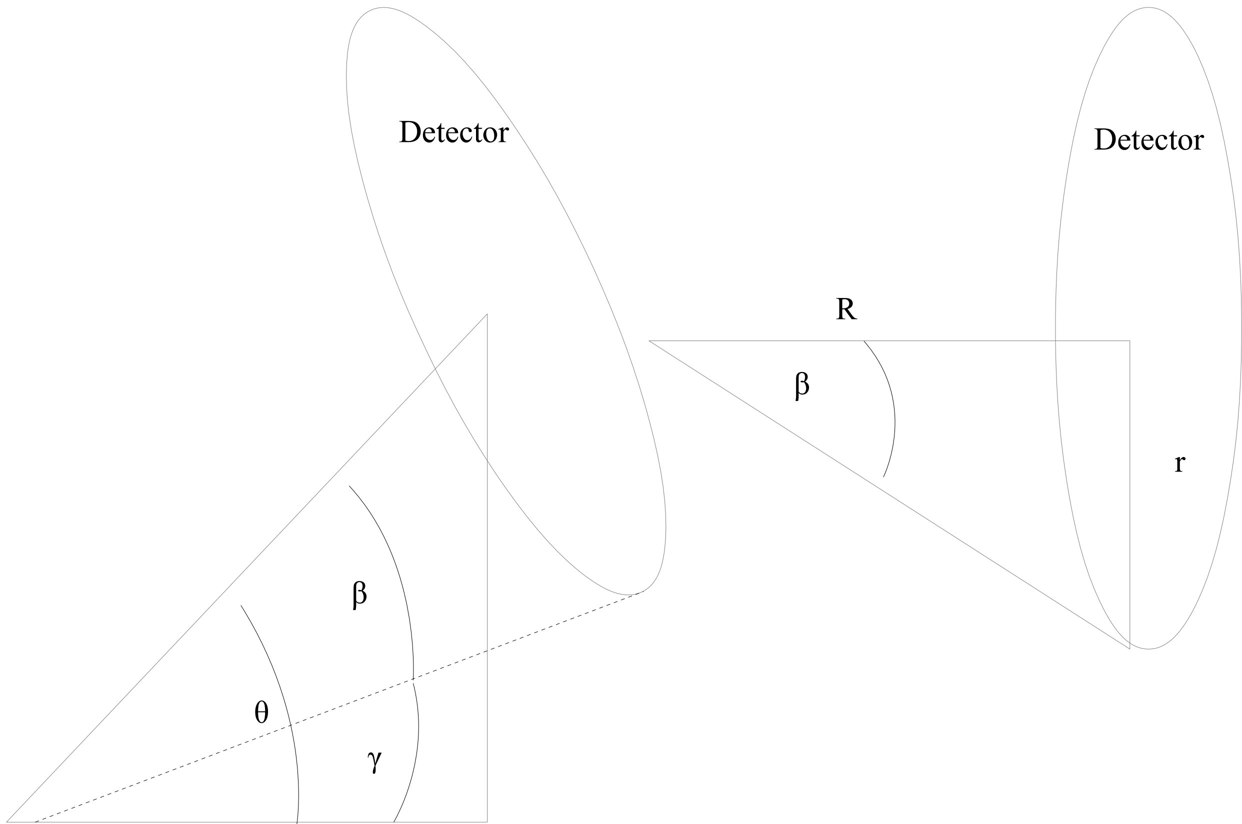

Figure 10.1: Diagram showing relevant variables. Note that neither diagram accounts for a change in specimen tilt, α.

The collection angle Ω is defined in terms of steradians (srad). Given this, the distance between the sample and the detector, R, can be calculated as the radius of the hypothetical sphere that the steradian unit envisions. The distance between sample and detector can be calculated from the definition:

$$\Omega = \frac{A}{R^2} \therefore R = \sqrt{\frac{A}{\Omega}}$$

where A is the area of the detector and R is the radius of the hypothetical sphere and hence the distance between sample and detector.

The radius of the detector (which is assumed to be perfectly circular) is simply given by $r = \sqrt{\frac{A}{\pi}}$.

β, half the two dimensional angle covered by the detector, is given by $\beta = \tan^{-1}(r/R)$ and γ, the angle between the horizontal and the bottom of the detector is $\gamma = \theta - \beta$

The first step is to calculate the angle shielded, measured from the bottom of the detector for simplicity: $\sigma - \alpha - \gamma$

This can then be expressed as the distance from the bottom of the detector that is shielded, r_s:

$$r_s = r - R \cdot \tan(\beta - (\sigma - \alpha - \gamma))$$

It is then possible to calculate the area of the (circular) detector that is part of the segment described by r_s, A_s:

$$A_s = r^2 \cdot \cos^{-1}\left(\frac{r - r_s}{r}\right) - (r - r_s) \cdot \sqrt{(2 \cdot r \cdot r_s - r_s^2)}$$

From there, it is a simple matter to calculate the fraction of the detector that is exposed:

$$multiplier = \frac{A - A_s}{A}$$

which would be multiplied with simulated results to bring them in line with experiment, or divide experimental results by this value to arrive at the expected value without shielding.

In the case of the specific detector used to gather the experimental results of this project, the following values were used:

Ω	0.12	srad
θ	25	degrees
σ	10 or 5	degrees
A	30	mm^2

The values for α are set in each individual experiment.